

Copyright
by
Bryan Russell Wygant
2020

**The Dissertation Committee for Bryan Russell Wygant Certifies that this is the
approved version of the following Dissertation:**

**Electrochemical Materials for the Production and Storage of Renewable
Energy**

Committee:

Charles Buddie Mullins, Supervisor

Richard M. Crooks

Sean T. Roberts

Livia S. Eberlin

Edward T. Yu

**Electrochemical Materials for the Production and Storage of Renewable
Energy**

by

Bryan Russell Wygant

Dissertation

Presented to the Faculty of the Graduate School of

The University of Texas at Austin

in Partial Fulfillment

of the Requirements

for the Degree of

Doctor of Philosophy

The University of Texas at Austin

May 2020

Dedication

To my parents Roger and Elaine, my sister Tonya, my grandparents Gordon and Joyce,
and to all of my friends and family who have helped me along the way.

Acknowledgements

I would like to begin by expressing my sincere thanks to my advisor, Professor C. Buddie Mullins, for his continuous support, mentorship, and guidance during my journey through my doctoral studies. With his cheerful attitude and can-do attitude, he helped me find my path and stay the course, and it has been a pleasure to work with him these past years.

Equal thanks is due to my parents, Roger and Elaine, for their love and support throughout the years. They helped to foster my love of science from an early age, and their guidance and support has helped shape me into the scientist, and more importantly person, that I am today. Of course, I must also thank my sister, Tonya, for helping to keep me grounded and humble through the years, and for always being there when I need her. Special thanks also goes to my grandparents, Gordon and Joyce, for the many enjoyable conversations, support, and love that they have always provided.

I was fortunate enough to work with many talented people during my studies, and I can't begin to express how much the friendship and support of my labmates and classmates has meant to me. Melissa Meyerson has done more than anyone to help keep me pointed in the right direction, both inside and outside of the lab, and I can't believe how lucky I've been to have her come into my life. Working together with Niyi Mabayoje was one of the highlights of my studies, and I will continue to look back fondly on the many hours we spent in the lab debating the finer points of electrocatalysis. Likewise, Edward Evans' sense of humor was always a welcome ray of sunshine in the lab and our conversations never failed to leave me feeling better than I did before. The many hours that I spent talking science, music, and everything else with Geoff Geberth

were also a source of great pleasure for me, and I'm grateful for his friendship. The undergraduate researchers who have worked with me through the years, Alex Ye, Anna Poterek, Quyen Vu, David Abbot, and the others, also deserve to be recognized for all of their help in the lab, as well as their patience with my sometimes haphazard mentorship. Thank you, as well, to Alex Rettie, Will Chemelewski, Sean Wood, Kyle Klavetter, and the other senior graduate students who helped me find my footing and take my first steps into the lab when I first arrived in Austin. And of course, thank you to Ryan Ciufo, Josh Pender, Kenta Kawashima, Rodrigo Rodriguez, and all of the other members of the Mullins Lab with whom I have worked side-by-side through the years.

Outside of the Mullins Lab, much thanks is due to the wonderful collaborators at Austin who helped me through the years. First and foremost is Dr. Andrei Dolocan, whose enthusiasm and insight is responsible for much of my work into perovskite photovoltaics; our numerous conversations on topics big and small, scientific and mundane, were a highlight of my time working at Austin. I must also express my gratitude to the other managers at TMI, Dr. Raluca Gearba, Dr. Karalee Jarvis, Dr. Hugo Celio, and the others, for all of their help and expertise through the years that made my own research possible. Last but not least, thank you to Shak McDonald and Adam Kennedy for all of their fabrication help and delightful conversation through the years, and for helping me create all the things I needed to pursue my work.

Finally, to all of the friends and family who I haven't had the space to mention here individually, thank you for everything. Your support has meant the world to me, and I couldn't have done it without you.

Abstract

Electrochemical Materials for the Production and Storage of Renewable Energy

Bryan Russell Wygant, Ph.D.

The University of Texas at Austin, 2020

Supervisor: Charles Buddie Mullins

The production of electricity from renewable sources, including solar power, is increasingly important as our society seeks to move to cleaner energy sources. Organolead halide perovskites, a class of thin film photovoltaic (PV) materials, are an exciting competitor to traditional Si devices, but suffer from poor material stability. Further, PV power is intermittent, creating a need for efficient energy storage during times when solar power is unavailable. H₂ gas, produced via electrochemical water electrolysis, is a promising way to store this energy in chemical bonds but efficient electrocatalysts are required to drive the reaction. This need for electrocatalysts is particularly acute for the complementary oxygen evolution reaction (OER), the rate-limiting half reaction of electrolysis. Here, we address both halves of the renewable energy problem above, production and storage, and study how the chemistry of PV and OER electrocatalyst materials impacts electrochemical performance and material stability. In regard to production, we studied the performance and stability of quasi-2D Ruddlesden-Popper phase (RPP) perovskites under humid conditions. We found that RPP

perovskites are more stable than typical 3D perovskites due to a unique moisture-driven disproportionation mechanism that passivates and protects the surface of the RPP perovskite. This process can also result in the formation of discrete RPP crystallites within the bulk of a perovskite film or device. We also found that changing the composition of the RPP perovskite enables control of the halide diffusion barrier, further impacting material stability. We next investigated energy storage, and studied how elemental composition affected the performance of two transition metal-based OER electrocatalysts. We found that for a Co-containing oxide perovskite, changes in the crystal structure of the catalyst from hexagonal to orthorhombic had little effect on OER performance, while adding small amounts of Fe improved catalytic behavior. Likewise, we found that the addition of Se to a nickel sulfoselenide material improved OER performance, even though the sulfoselenide material itself oxidizes during electrocatalysis to produce a catalytically-active nickel (oxy)hydroxide surface. Altogether, our work highlights the importance chemical composition when studying the material stability and electrochemical performance of both PV and electrocatalytic materials for renewable energy applications.

Table of Contents

List of Tables	xiv
List of Figures	xv
Chapter 1: Introduction to Renewable Energy Production and Storage	1
1.1 Opening Remarks and Organolead Halide Perovskites	1
1.2 Transition Metal-Based Oxygen Evolution Reaction Electrocatalysts.....	5
1.3 Overview of Chapters	10
1.4 References.....	11
Chapter 2: Introduction to Perovskite Photovoltaics	14
References.....	16
Chapter 3: Probing the Degradation Chemistry and Enhanced Stability of 2D Organolead Halide Perovskites	17
3.1 Introduction.....	17
3.2 Experimental.....	20
3.2.1 Device and Film Fabrication.....	20
3.2.2 Electrochemical Testing.....	23
3.2.3 Physical Characterization.....	23
3.3 Results and Discussion	25
3.3.1 X-ray Diffraction Spectroscopy	26
3.3.2 Photoluminescence Spectroscopy	27
3.3.3 ToF-SIMS Device Profiling.....	34
3.3.4 C ₆₀ /Perovskite Interface Studies	37
3.3.5 Inorganic Profile Analysis	39

3.3.6 Organic Profile Analysis.....	42
3.3.7 Isotope Studies	43
3.3.8 Mechanism of nBA-MAPI Degradation	48
3.4 Conclusions.....	51
3.5 References.....	52
Chapter 4: Moisture-Driven Formation and Growth of Quasi-2D Organolead Halide Perovskite Crystallites	57
4.1 Introduction.....	57
4.2 Experimental.....	60
4.2.1 Film Fabrication and Moisture Exposure	60
4.2.2 Instrumental Characterization	62
4.3 Results and Discussion	64
4.3.1 XRD Analysis	64
4.3.2 AFM Analysis of Film Surface.....	67
4.3.3 Bulk Photoluminescence Spectroscopy	71
4.3.4 Fluorescence Microscopy Analysis	75
4.3.5 ToF-SIMS/AFM	78
4.3.6 Proposed Crystal Growth Mechanism	82
4.4 Conclusions.....	86
4.5 References.....	87
Chapter 5: The Effects of Alkylammonium Choice on the Stability and Performance of Quasi-2D Organolead Halide Perovskites	92
5.1 Introduction.....	92
5.2 Experimental.....	95

5.2.1 Film Fabrication.....	95
5.2.2 Device Fabrication.....	96
5.2.3 Device Testing	97
5.3 Results and Discussion	99
5.3.1 Electrochemical Testing and Stability	99
5.3.2 XRD Analysis	102
5.3.3 PL Analysis.....	105
5.3.4 ToF-SIMS Analysis	110
5.3.5 UV-Vis Halide Mobility Analysis	116
5.4 Conclusions.....	120
5.5 References.....	121
Chapter 6: Introduction to Transition Metal-based Oxygen Evolution Reaction Electrocatalysts	125
References.....	128
Chapter 7: Structural and Catalytic Effects of Iron- and Scandium-Doping on a Strontium Cobalt Oxide Electrocatalyst for Water Oxidation.....	130
7.1 Introduction.....	130
7.2 Experimental.....	133
7.2.1 Materials	133
7.2.2 Materials Synthesis	133
7.2.3 Electrode Preparation.....	135
7.2.4 Material Characterization.....	135
7.2.5 Electrochemical Characterization	136
7.3. Results and Discussion	137

7.3.1 XRD Analysis	137
7.3.2 XPS Analysis	143
7.3.3 SEM Analysis	148
7.3.4 TEM Analysis	149
7.3.5 Cyclic Voltammetric Testing.....	155
7.3.6 Stability Testing.....	159
7.4. Conclusions.....	161
7.5 References.....	161
Chapter 8: Effect of Selenium Content on Nickel Sulfoselenide-Derived Nickel (Oxy)hydroxide Electrocatalysts for Water Oxidation	167
8.1 Introduction.....	167
8.2 Experimental.....	169
8.2.1 NiS _x Se _y Electrocatalyst Synthesis.....	169
8.2.2 Electrocatalyst Ink and Electrode Preparation.....	170
8.2.3 Electrochemical Testing.....	171
8.2.4 Physical Characterization.....	172
8.3 Results and Discussion	174
8.3.1 X-ray Diffraction Spectroscopy and Scanning Electron Microscopy.....	174
8.3.2 Electrochemical Characterization	177
8.3.3 X-ray Photoelectron Spectroscopy	184
8.3.4 Transmission Electron Microscopy	189
8.4 Conclusions.....	194
8.5 References.....	195

Chapter 9: Conclusions and Future Work.....	200
9.1 Conclusions of Presented Work.....	200
9.2 Future Directions	202
Appendix A: Supporting Information for Chapter 3.....	205
A.1 Supplemental Discussions	205
A.1.1 Hydrophobicity of quasi-2D perovskite materials	205
A.1.2 Spectroscopic and physical effects of nBA-MAPI disproportionation	208
A.1.3 Water diffusion and damage at the perovskite/PEDOT:PSS interface.....	212
A.2 Tables	214
A.3 Figures.....	215
A.4 References	234
Appendix B: Supporting Information for Chapter 4.....	237
Appendix C: Supporting Information for Chapter 5.....	247
Appendix D: Supporting Information for Chapter 7.....	267
D.1 Tables	267
D.2 Figures.....	269
Appendix E: Supporting Information for Chapter 8	286
E.1 Figures	286
E.2 References	299
Works Cited	300

List of Tables

Table 7.1: The ratio of the atomic percent of Sr and B-site cation (Co, Fe, Sc) present on the SCO surface.	146
Table 8.1 Gravimetric overpotential, BET-derived overpotential, and BET surface areas of NiS_xSe_y composites	183
Table A.1: Performance metrics from electrochemical tests of MAPI, nBA-MAPI, and 2D/3D MAPI devices. Average values from a single batch of devices are reported with a standard deviation, while champion device values are included in parentheses.	214
Table D.1 Tolerance values for the seven selected SCO samples examined in this study. t shows a transition to unity with increasing concentrations of both Fe and Sc dopants.	267
Table D.2 Atomic percentage of Fe and Sc dopants as measured using XPS, and the binding energy of the 2p 3/2 peaks both elements.....	267
Table D.3 FWHM and Co 2p 3/2 binding energies for the Fe-SCO samples. As iron concentration increases, the FWHM of the peak increases as well.	268
Table D.4 OER mass activities of several perovskites. LaNiO_3 , $\text{LaNi}_{0.75}\text{Fe}_{0.25}\text{O}_3$, LaCoO_3 , and LaMnO_3 are all supported on N-doped carbon on a glassy carbon rotating disk electrode.....	268

List of Figures

- Figure 1.1** Model of the crystal structure of a cubic organolead halide perovskite. The A-site (red) is a monovalent cation which is typically an alkylammonium species, the B-site (blue) is a divalent metal cation such as Pb^{2+} , and the X-site (green) is a halide species.3
- Figure 1.2** Model of the crystal structures of a series of quasi-2D organolead halide perovskites with different n -phases a cubic organolead halide perovskite with the generic formula $\text{A}'_2\text{A}_{n-1}\text{B}_n\text{X}_{3n+1}$. Here, the A'-site is a long alkylammonium species, the A-site is a monovalent organic cation, the B-site is a divalent metal cation, and the X-site is a halide species.5
- Figure 1.3** Actual and predicted electricity generation by fossil fuel-fired power plants for a municipality in California, showing the impact of adding increasing amounts or renewably-generated electricity to the grid. Because most renewable energy is available during the day rather than night, increased quantities of renewable-derived electricity will require more extreme production ramps (after 3 pm) from fossil fuel-fired plants to meet peak demand (around 8 pm). Image adapted from source 16.6
- Figure 1.4** Diagram of a typical water electrolyzer system. Electricity, here provided by intermittent renewable sources, powers the oxygen evolution reaction (OER) at the anode and the hydrogen evolution reaction, (HER) at the cathode. Both electrodes are submerged in an aqueous electrolyte solution, typically strongly acidic or basic.8

Figure 2.1 The architectures of typical (a) n-i-p and (b) p-i-n organolead halide perovskite devices. Both devices contain an intrinsic perovskite photoabsorbing layer, an n-type electron-selective electron transport material (ETM), and a p-type hole-selective hole transport material (HTM).	15
Figure 3.1: a) Crystal structure of an $n = 4$ nBA-MAPI perovskite (blue), with sheets composed of 3D MAPI perovskite (red) separated by A' n -butylammonium ions. b) Graphical representation of proposed 2D/3D MAPI structure, where a thin layer of nBA-MAPI is coated on the surface of the 3D MAPI.	18
Figure 3.2: Normalized power conversion efficiency (PCE) of MAPI, nBA-MAPI, and 2D/3D MAPI devices following exposure to 78% RH over the course of 48 hours, showing the decrease in PCE for all devices as they degrade.	26
Figure 3.3: Fluorescence spectra for the front and back of a) MAPI and b) nBA-MAPI films, before and after exposure to 78% relative humidity for 8 hours. c) Normalized difference plot for the front-side spectra for both films. nBA-MAPI shows the growth of $n = 3$ and ∞ peaks, as well as the loss of the $n > 5$ peak, while little change visible in the MAPI spectra.	28
Figure 3.4: a) Cross sectional TEM image of a typical nBA-MAPI device with layers labeled. b) Full negative-mode ToF-SIMS depth profiles for fresh MAPI (top), nBA-MAPI (middle) and 2D/3D MAPI (bottom) devices with characteristic species chosen to represent different layers and color-coded to the bar at top.	36

Figure 3.5: a) ToF-SIMS depth profile of OH^- before and after exposure to humidity.

The peak at the hydration region in blue shifts slightly and decreases in intensity, indicating a loss of hydrated water b) proposed degradation scheme for MAPI with three separate hydration steps. Steps 2 and 3 produce liquid water, which could then be removed via vacuum, producing the decrease observed in a).38

Figure 3.6: Negative-mode ToF-SIMS depth profiles of (a) MAPI, (b), nBA-MAPI, and (c) 2D/3D MAPI devices, before and after exposure to humidity, near the C_{60} /perovskite interface; the blue box represents the hydration region in each device. The top profiles show the changes to the C_{60} (C_9^-) and perovskite (PbI_2^-) with exposure; nBA-MAPI and 2D/3D MAPI show little change, while MAPI shows the formation of a new peak in the hydration region. The bottom profiles show changes to N- and H-containing organic species (C_2N^- and CH_2^- , respectively). A clear peak in both ions is visible at 7500 s, within the hydration region in (a), while neither nBA-MAPI nor 2D/3D MAPI show any increase in these species. Such species are indicative of the formation of degraded hydrated MAPI species.40

Figure 3.7: ToF-SIMS depth profiles of OH^- and OD^- before and after exposure to D_2O vapor in (a) MAPI and (b) nBA-MAPI devices near the C_{60} /Perovskite interface. MAPI (a) exhibits the formation of an OD^- hydration feature (blue box) after exposure, while nBA-MAPI (b) does not. The OD^- peak in (a) is due to the formation of hydrated species at the perovskite surface which have formed during reaction with the D_2O vapor, remaining stable under vacuum.44

Figure 3.8: Deuterated methylammonium derivatives ($D = 1-3$, i.e. $D1 = \text{CNH}_5\text{D}^+$) and PbI^+ for (a) MAPI and (b) nBA-MAPI devices exposed to D_2O vapor for 1 hour. The total ion counts, and therefore abundance, of the derivatives decreases as the level of deuteration increases. c) Simple exchange pathway for the deuteration of methylammonium species; the rate of the H/D exchange reaction slows with the extent of deuteration, therefore high concentrations of D2 and D3 require longer exposure times. d) Total integrated yield of the deuterated methylammonium derivatives for both MAPI and nBA-MAPI devices, plotted as a function of the distance of each derivative's peak from the PbI^+ peak ($t = 0$). D_2O penetrates the MAPI film more readily than the nBA-MAPI film resulting in more H/D exchange, as indicated by higher derivative yields at decreased distance from the center of the perovskite layer. The low degree of water penetration through the nBA-MAPI film is further evidence of the material's superior water stability.47

Figure 3.9: a) Possible band schematic for a fresh nBA-MAPI device, shown below, as determined by PL spectroscopy. A thin disordered layer of various low- n species sits atop a mostly $n > 5$ layer near the film surface, closest to the C_{60} , while high concentrations of the lower n phases rest atop the PEDOT:PSS layer; this allows for both hole and electron transport from the perovskite to the device. b) Proposed band schematic and device cross section assuming disproportionation creates conformal low- n layers from the C_{60} interface downward toward the bulk. These layers would inhibit electron transfer to the C_{60} , and therefore is not expected to occur. c) Proposed band schematic and device cross section assuming disproportionation thickens the mixed layer of low- n and MAPI layers at the surface. The presence of the MAPI would allow electrons to be transferred from the bulk nBA-MAPI to the C_{60} , even with the presence of the low- n nBA-MAPI. Some low- n structures may segregate from the film as degradation proceeds.50

Figure 4.1 Crystal structures of Ruddlesden-Popper phase perovskites sharing a chemical formula of $A'_2A_{n-1}B_nX_{3n+1}$, where $n = 2, 3$, and 4. Here, A' is n -butylammonium, A is methylammonium, B is Pb, and X is iodide.58

Figure 4.2 a) Selected regions of the XRD spectrum of an nBA-MAPI film over 72 hours of exposure to 78%RH, showing a shift in the (111) and (202) peaks. b) Low two theta region of the nBA-MAPI film XRD spectrum over 72 hours of humidity exposure, showing the formation of $n = 2$ and 4 phases in the film. c) Radial integrations of the WAXS spectra of an nBA-MAPI film over 72 hours of exposure, showing variations in the peak intensity of the main peak, in addition to the formation of $n = 2$ and 4 peaks (inset).66

Figure 4.3 AFM images of a single area of an nBA-MAPI film in non-contact mode after a) 0, b), 6, c) 12, d) 24, e) 48, and f) 72 hours of exposure to 78%RH. a) shows the film is initially smooth (RMS 5 nm) with only small ridges and valleys at the surface of the film, but upon extended exposure to humidity, cracks (location I) and holes (location II) begin to form, with elongated crystals forming later. Some grain boundaries also experience subsidence (location III) prior to crystal growth, and other areas exhibit crystal growth without apparent damage to the film previously (location IV).68

Figure 4.4 a) PL spectra of the front (solid) and back (dashed) sides of an nBA-MAPI film, before and after 72 hours of exposure to 78%RH. After 72 hours, the intensity of both spectra decreases, and peaks between 575 and 650 nm appear on the front. b) Difference spectra of the normalized PL spectra from the front and back of a film after 72 hours of exposure, showing the formation of low- n and 3D like species and concurrent decrease of the $n > 5$ peak due to disproportionation. c) Graphic representing the proposed n -phase structure of the nBA-MAPI film.73

Figure 4.5 a) CFM image of an nBA-MAPI film exposed to 78%RH for 24 hours, showing localized fluorescence below 740nm from crystal-like structures, such as the circled examples. b) Average background-corrected point fluorescence spectra from low-*n* nBA-MAPI crystals after moisture exposure for 72 hours, showing an increase in the intensity of *n* = 3-5 peaks with increasing exposure to humidity.76

Figure 4.6 Negative ion polarity ToF-SIMS depth profiles for a) a bare nBA-MAPI film and d) a model PV device. PbI_2^- represents the inorganic portion of the perovskite, CN^- represents the organic portion of the perovskite, SnO^- represents FTO, Au_4^- represents the Au contact, C_2N^- represents BCP, C_9^- represents the C_{60} layer, and $^{34}\text{S}^-$ represents the PEDOT:PSS layer. A fresh film (b) and one exposed to 78% RH for 8 hours (c) were sputtered to the dashed line in a) and the surface was imaged by AFM, showing the presence of new crystals (I) and cracks (II) only in interior of the exposed sample. A fresh device (e) and one exposed to humidity for 24 hours (f), likewise showing the formation of crystals (III) inside the film.80

Figure 4.7 Proposed growth mechanism for low- n nBA-MAPI crystallites. a) water diffuses through grain boundaries in the $n > 5$ surface, carrying solvated perovskite components to low- n nuclei buried in the bulk of the film. The nuclei begin to grow in height and length, causing the film above them to split (b) and allowing more water to diffuse into the film. As exposure continues (c), the crystals also begin to exhibit growth in thickness, as well as disproportionation. These processes continue (d), with crystals eventually ceasing vertical growth near the film surface but continuing to lengthen and widen as exposure continues.83

Figure 5.1 Crystal structures of a) $n = 4$ butyl-MAPI and b) $n = 4$ hexyl-MAPI, showing the layered quasi-2D structure of the materials. Dimensionally-confined layers of MAPI material (brown) are separated by a bi-layer of alkylammonium species (A'), either n -butylammonium (A'_1 , red) or n -hexylammonium (A'_2 , blue).94

Figure 5.2 Normalized PCE of butyl- and hexyl-MAPI devices fabricated using both Ag, and Au electrodes, exposed to 78%RH. All devices except for the Au-hexyl devices showed complete degradation within two weeks. The inset shows the rate of PCE loss over the first two days.101

Figure 5.3 XRD spectra of bare films and Ag/Au-perovskite devices for a) butyl-MAPI and b) hexyl-MAPI samples before and after 8 hours of exposure to 78%RH. All materials show similar spectra before exposure, but the butyl-MAPI film and Ag-butyl device both show the formation of low- n phases after exposure.103

Figure 5.4 Normalized PL spectra (a) of bare butyl- and hexyl-MAPI films and Ag/Au devices of each material, before and after exposure to 78%RH for 8 hours. The butyl-MAPI film and Ag-butyl device both show the formation of low- n species below the $n > 5$ peak at 715 nm following exposure, while the Ag/Au-hexyl devices both show an apparent loss of signal in these regions following exposure. ToF-SIMS depth profiles of the C₆₀/perovskite interface of (b) Ag-butyl, (c) Ag-hexyl, (d) Au-butyl, and (e) Au-hexyl devices. The top portion of b-e shows the C₆₀ (C₉⁻) and inorganic portions of the perovskites (PbI₂⁻) before and after 8 hours of exposure, while the bottom portion shows the organic portion (CH₂⁻) of the perovskite. In all cases, expansion of the perovskite is observed in the hydration region of the device (blue box), indicating perovskite degradation.....106

Figure 5.5 a) Yield of Ag/AuI⁻ species from the metal contact and metal/C₆₀ interface for all butyl- and hexyl-MAPI devices, before (solid) and after (solid + dashed) 8 hours of exposure to 78%RH. b) I⁻ depth profiles for Ag-hexyl/butyl devices before and after moisture exposure. The interface I⁻ peak decreases after exposure as more I⁻ migrates into the metal contact. c) I⁻ depth profiles for Au-hexyl/butyl devices before and after moisture exposure. The interface I⁻ peak increases following exposure as more I⁻ diffuses to the Au electrode and accumulates.....114

Figure 5.6 a) UV-Vis spectra of paired $n = 2$ iodo/bromo hexyl-MAPI films held at 100°C for 3 hours. As iodide and bromide species exchange, the $n = 1$ iodo peak at 575 nm decreased. b) Activation energies for halide mobility in $n = 2$ butyl- and hexyl-MAPI perovskite determined by UV-Vis spectroscopy. The dashed line represents the previously reported activation energy of a 3D perovskite. (ref. 23)118

Figure 6.1 Diagram of the possible chemical compositions of metal chalcogenide electrocatalysts post-electrocatalysis. Starting with an unoxidized chalcogenide (red), the material can (1) remain unoxidized, (2) develop an oxidized shell surrounding an oxidized core, or (3) become completely oxidized.127

Figure 7.1. The cubic unit cell of $\text{SrCoO}_{3-\delta}$. The green sphere represents Sr^{2+} , the blue spheres $\text{Co}^{3+,4+}$, and the red spheres represent O^{2-}132

Figure 7.2. a) XRD spectra for iron-doped SCO samples. Increasing levels of iron doping cause the crystal structure to shift from the trigonal polymorph (UnSCO, 1%Fe-SCO) to the orthorhombic (5%Fe-SCO), and finally to the cubic polymorph (10%Fe-SCO). b) XRD spectra for the scandium-doped SCO samples. A similar pattern to the iron-samples is visible, where higher doping levels adopt the cubic crystal structure (5%, 10%Sc-SCO) while the lowest doping level (1%Sc-SCO) exhibits a mixture of trigonal and orthorhombic structure. Peaks marked “*” can be indexed to an impurity Co_3O_4 phase (PDF#00-043-1003).138

Figure 7.3. a) Representation of orthorhombic $\text{SrCoO}_{2.5}$, containing an ordered oxygen vacancy and significantly disordered CoO_6 octahedra in the crystal lattice. The green sphere represents Sr^{2+} , the blue spheres $\text{Co}^{3/4+}$, and the red spheres O^{2-} . b) Representation of cubic SrCoO_3 , containing ordered, corner-sharing CoO_6 octahedra arranged around a central Sr^{2+} . c) Representation of trigonal $\text{Sr}_6\text{Co}_5\text{O}_{15}$, containing face-sharing CoO_6 octahedra arranged in columns surrounded by alternating layers of Sr^{2+} ions arranged in a trigonal pattern. Sufficient loss or gain of oxygen can cause transitions between the cubic and orthorhombic polymorphs, while transitions between the trigonal and cubic phases are related to changes in temperature, with the cubic structure being favored above $\sim 900^\circ\text{C}$140

Figure 7.4. XPS spectra and fitted peaks for the 10%Fe-SCO sample. a) Spectra of the carbon 1s peak. b) Spectra of the strontium 3d 5/2 and 3/2 peaks. c) Spectra of the cobalt 2p 3/2 peak. d) Spectra of the oxygen 1s peak.144

Figure 7.5. HRTEM images (a,d,g) and nanobeam-diffraction (NBED) patterns from the surface (b,e,h) and non-surface (c,f,i) of 5%Fe-SCO (a-c), 10%Fe-SCO (d-f), and 10%Sc-SCO (g-i). Inset FFTs of the images show the orthorhombic (top-left corners) and cubic (bottom-right corners) phases. There was not enough of the cubic phase in the 5% Fe-SCO to get a reliable FFT. The surface NBED patterns are indexed as the SrCoO_3 phase and the bulk NBED patterns are indexed as the orthorhombic $\text{SrCoO}_{2.5}$ phase. The beam directions are all indicated in the lower right corner.151

Figure 7.6. HRTEM images of particle surfaces of (a) UnSCO, (b) 5% Fe-SCO, (c) 10% Fe-SCO, and (d) 10% Sc-SCO showing nanoparticles embedded in an amorphous layer. The particles in the UnSCO, 5% Fe-SCO, and 10% Sc-SCO samples are indexed as orthorhombic SrCO_3 (Pmcn) ⁴⁸ viewed down $[11\bar{2}]$, $[\bar{1}10]$, and $[\bar{1}01]$. Not enough planes are present in the particle from the 10% Fe-SCO sample to reliably determine the phase. The planes present could match (111) SrCO_3 and (211) $\text{SrCoO}_{2.5}$	153
Figure 7.7. Electron dispersive X-ray spectroscopy maps of a) 5%Fe-SCO, b) 10%Fe-SCO, and c) 10%Sc-SCO. Cobalt is blue, strontium is red and the dopant (Fe or Sc) is green. The inset tables show the atomic percents taken for the average spectrum from the indicated area	154
Figure 7.8. a) LSVs of iron-doped SCO samples and b) LSVs of scandium-doped SCO samples measured in 0.1M KOH at 5 mV/s. The dotted line marks the intercept with a current density of 10 mA/cm ² . Data was collected from the third anodic sweep segment.	156
Figure 7.9. Overpotential-vs.-time plots for the a) iron-doped and b) scandium-doped SCO samples over the course of two hours, recorded at a current density of 10 mA/cm ²	159

Figure 8.1: a) XRD spectra of a series of nickel sulfoselenide composite materials. The primary Ni_3S_2 phase is gradually replaced by NiSe as more Se is added to the composite. b) The Ni_3S_2 (010) peak shows a gradual shift to lower two theta with increasing Se-content as more Se is incorporated into the lattice; (c) a similar effect occurs in the NiSe (101) peak, where increasing S-content causes a shift to higher two theta. SEM images of the NiS_{100} (d) and NiSe_{100} (e) shows both composites consist of agglomerated particles between 0.5 and 1 μm in diameter.....175

Figure 8.2: a) Averaged CVs of the NiSSe composites measured in 1M KOH. The addition of 10-25%Se significantly reduces the overpotential when compared to the pure sulfide or selenide, as well as the 50/50 mixture. b) Chronoamperomogram of the NiS_{100} and $\text{NiS}_{90}\text{Se}_{10}$ composites at 10 mA/cm^2 over 10 hours of continuous use, showing the superior stability of the Se-incorporated material. All experiments were performed versus a Pt counter electrode with an Ag/AgCl(sat'd KCl) reference electrode....179

Figure 8.3: a) Ni 2p 3/2 XPS spectra of all NiSSe composites, showing a gradual shift to lower binding energies with increasing Se-content, indicating a more metallic character b) XPS spectra of the S 2s and Se 3s regions for the NiS₁₀₀, NiS₉₀Se₁₀, and NiSe₁₀₀ samples. The addition of Se results in a decreased quantity of oxidized chalcogen at the surface. c) O 1s XPS spectra for the NiS₁₀₀, NiS₉₀Se₁₀, and NiSe₁₀₀ composites, showing the contributions from surface hydroxides (red), oxides (green), and adsorbed water (purple). The addition of Se reduces the quantity of NiO_x species at the surface. d) Se 3d spectra for the NiS₅₀Se₅₀ composite, showing contributions from single and dichalcogenide bonds, as well as oxidized selenium species.....186

Figure 8.4: TEM image of post-OER NiS₁₀₀ (a) with accompanying EDX mapping (b) showing the formation of an oxidized shell approximately 20 nm thick surrounding an un-oxidized interior. HRTEM shows that the oxidized region appears relatively crystalline, and composed of NiO, while the interior is composed of Ni₃S₂. EDX mapping of the NiS₉₀Se₁₀ material (d, scale bar 10 nm) shows a similarly oxidized surface, that is much thinner (10 nm) with HRTEM and FFT (e) likewise corresponding to NiO at the surface and Ni₃S₂ in the bulk. This oxide appears less particulate than then NiS₁₀₀ material, however.....192

Figure A.1 Normalized (a) open-circuit potential, (b) short-circuit current, and (c) fill factor values for MAPI, nBA-MAPI, and 2D/3D MAPI devices exposed to 78% relative humidity over time. For all three metrics, the 2D-containing perovskites show slower degradation.215

Figure A.2 Cyclic voltammograms of characteristic perovskite devices before exposure to humidity showing the performance of the three types of perovskite material. A hysteresis index (HI) at 80% of the maximum V_{oc} for each cell is provided, demonstrating the low degree of hysteresis between the forward and reverse scans.....	216
Figure A.3 Statistical distributions for the a) V_{oc} , b) J_{sc} , c) PCE, and d) FF at $t = 0$ hrs for all cells tested. Two partially shorted devices are responsible for the outlier values in the FF and PCE of the 2D/3D devices, which would otherwise distribution similar to those for MAPI and nBA-MAPI.	217
Figure A.4 Normalized PCE values for MAPI and nBA-MAPI devices exposed to a humid environment as reported by Tsai <i>et al.</i> (ref. 5), compared to similar devices reported in the current work. Within error, the devices presented here show similar degradation kinetics and trends to those reported previously, indicating the degradation process is similar in both.	218
Figure A.5 XRD spectra for (a) MAPI, (b) nBA-MAPI, and (c) 2D/3D MAPI films before and after exposure to 78%RH for 8 hours. Little crystallographic change is observed for any of the films tested.	219
Figure A.6 a) XRD spectra for a fresh nBA-MAPI film, with the 111 and 202 peaks labeled. b) graphic of an nBA-MAPI film with an orientation normal to the FTO substrate, as would be expected from a hot-cast film. Both the 111 and 202 planes have a significant horizontal component. Pole figure measurements for the 111 (c) and 202 (d) peaks, with a sharp central peak demonstrating the good agreement with the orientation of image b).	220

Figure A.7 In-plane (y-axis) and grazing incidence (x-axis) X-ray diffraction spectra from a fresh nBA-MAPI film. The lack of the 202 peak on the y-axis indicates a well-ordered film.	221
Figure A.8 a) Cross-sectional HAADF (left) image of a nBA-MAPI device, with the perovskite in the center of the cross section. Accompanying EDX elemental maps of C (blue) and Pb (orange), showing a gradient in both elements as a function of depth. b) Theoretical C/Pb elemental ratio based on the stoichiometric ratios of both elements in various n -phases of the nBA-MAPI perovskite, showing that the ratio would increase as n decreases.	222
Figure A.9 Normalized fluorescence spectra for the front and back of nominally a) $n = 1$ and b) $n = 2$ films, before and after exposure to 78% relative humidity for 8 hours. c) Normalized difference plot for the front-side spectra for both films. After exposure, the $n = 1$ film shows a slight shift toward lower emission energies, while the $n = 2$ film shows both the loss of $n = 1$ and 3 from the surface, as well as a general peak narrowing for the $n = 2$ peak.	223

Figure A.10 AFM images of an nBA-MAPI film a) before and b) after 8 hours of exposure to a 78%RH environment. For reference, the blue star indicates the same location in each image. New elongated structures are observed to form on the surface of the film, and are likely discrete crystals of low-*n* perovskite. c) Schematic of the cross section of the fresh nBA-MAPI film, showing a disordered surface layer composed of various low-*n* phases atop a bulk of high-*n* nBA-MAPI. d) Schematic of the cross section of the same film following moisture exposure, showing an increase in the thickness of the disordered surface, as well as the formation of the localized structures observed in b). e) Simplified energy diagram for c), showing electron transfer both from the low-*n* phases of the surface to the bulk, and from the bulk to 3D MAPI within the disordered surface (1). f) Simplified energy diagram showing the preferential motion of electrons (2) and holes (3) generated within the type II heterojunction well structure, as well as possible charge transfer from the surface to the bulk (4). Generally, however, photogenerated electrons will be trapped in the interior, unable to escape (5). g) Simplified energy diagram for a type I heterojunction well, with similar electron transfer to the type II well. Here, hole transfer also flows to the higher-*n* interior (6), where radiative recombination could occur.224

Figure A.11 Wide angle x-ray scattering spectra for a) fresh and b) 8 hour-exposed nBA-MAPI films on FTO. Bragg diffraction spots for a well-oriented perovskite lattice have been assigned based on previous reports. Following exposure, two diffraction rings (marked with white arrows) appear, indicative of the formation of randomly-oriented low- <i>n</i> perovskites in the film. c) intensity plot vs two theta generated from the WAXS spectra, clearly showing the formation of the two peaks near 8-9° two theta which can be indexed to <i>n</i> = 2,4 phases. The small feature near 6° is an instrumental artifact, and is independent of the film.....	225
Figure A.12 a) Fluorescence spectra for the front and back of a bare 2D/3D MAPI film, before and after exposure to 78% relative humidity for 8 hours. The primary peak is at 1.65 eV, and a broad shoulder near 1.8 eV indicates the presence of nBA-MAPI phases. b) Normalized difference plot for the front of a 2D/3D MAPI film, showing the loss of the shoulder near 1.8 eV following exposure.	226
Figure A.13 a) cross sectional SEM image of a 200 nm C ₆₀ MAPI device, with the C ₆₀ layer outlined in red. b) Normalized PCE for two batches of our typical 50 nm C ₆₀ MAPI devices (red) and the 200 nm C ₆₀ device (black).	227
Figure A.14 Full negative-mode ToF-SIMS depth profiles for fresh 200 nm C ₆₀ MAPI (top) and nBA-MAPI (bottom) with characteristic species chosen to represent different materials.	228

Figure A.15 Negative-mode ToF-SIMS depth profiles of (a) MAPI, (b), nBA-MAPI, and (c) 2D/3D MAPI devices, before and after exposure to humidity, near the C_{60} /perovskite interface; the blue box represents the hydration region in each device. The top profiles show the changes to the perovskite (PbI_2^-) with exposure; nBA-MAPI and 2D/3D MAPI show little change, while MAPI shows the formation of a new peak in the hydration region and a significant decrease in intensity due to hydration damage. The bottom profiles show changes to the hydrated species (OH^-) before and after exposure to humidity. The FWHM of the OH^- peak after exposure is used to determine the hydration region (blue). nBA-MAPI (b) and 2D/3D MAPI (c) show only a slight increase in OH^- , while MAPI shows a large decrease, indicating loss of hydrated species with exposure.229

Figure A.16 Positive-mode ToF-SIMS depth profiles for the $C_4NH_{12}^+$ species representing *n*-butylammonium in (a) MAPI and (b) 2D/3D MAPI devices. The larger signal and dynamic nature of the signal with humidity in b) indicates that the signal is likely a product of *n*-butylammonium; the peak near 1750 s after exposure agrees with the formation of an nBA-MAPI layer following hydration.230

Figure A.17 a) Positive mode ToF-SIMS depth profiles for $C_4NH_{12}^+$ (representing *n*-butylammonium), PbI^+ (representing 3D MAPI), and SnO^+ (representing FTO) for a bare 2D/3D MAPI film, showing a sharp *n*-butylammonium peak at the surface of the film that tapers off into the film. b) Corresponding cross sectional SEM image of a 2D/3D MAPI film on FTO. The blue lines represent the nBA-MAPI at the film surface and the coating on the grain boundaries of the 3D MAPI crystals (red). c) Depth profile of the first 10 seconds (~13 nm) of the 2D/3D MAPI film, showing a nBA-MAPI film thickness of roughly 2.5 nm. d) Full cross sectional SEM image of the 2D/3D MAPI film.....231

Figure A.18 ToF-SIMS depth profiles of N- and H-containing (C_2N^- and CH_2^- , respectively) organic species in (a) MAPI and (b) nBA-MAPI devices following exposure to D_2O vapor near the C_{60} /Perovskite interface; the blue box represents the hydration region. The MAPI sample shows clear formation of a peak in both species inside the hydration region, in agreement with the formation of degraded hydrated-MAPI species at the interface.....232

Figure A.19 a) Deuterated *n*-butylammonium derivatives ($D = 1-3$, i.e. $D1 = C_4NH_{11}D^+$) and PbI^+ for an nBA-MAPI device exposed to D_2O vapor for 1 hour. The total ion counts, and therefore abundance, of the derivatives decreases as the level of deuteration increases. b) Total integrated yield of the deuterated *n*-butylammonium derivatives as a function of distance of each derivative's peak from the PbI^+ peak ($t = 0$). The relatively large distance from the center of the perovskite layer indicates a low degree of water penetration into the material.233

Figure B.1 XRD spectra of an nBA-MAPI film over 72 hours of moisture exposure at 78%RH.....	237
Figure B.2 WAXS spectra of nBA-MAPI films at a) 0 hours, b) 6 hours, c) 12 hours, d) 24 hours, e) 48 hours, and f) 72 hours of exposure to 78%RH. All samples show well-oriented crystal structures, as indicated by the clear spots for the (0 0 -2), (-1 5 -2), and (-1 1 -1) reflections. Spectra after 48 hours of exposure (e and f) show the formation of rings at low- q (indicated by white arrows), indicating the formation of un-oriented low- n perovskite phases after sufficient exposure.	238
Figure B.3 AFM images of a single area of an nBA-MAPI film acquired <i>in situ</i> over a) 0 hours, b) 6 hours, c) 12 hours, d) 24 hours, e) 48 hours, and f) 72 hours of exposure to 78%RH. Cracks initially form in the surface of the film after just 6 hours of exposure (b), and grow over time. Crystalline structures also appear between b) and c), and likewise continue to grow, covering the surface after 72 hours (f).....	239
Figure B.4 Cross-sectional SEM image of a typical nBA-MAPI film showing an average thickness of roughly 350 nm.	240
Figure B.5 PL spectra taken from the front (a) and back (b) of an nBA-MAPI film over the course of 72 hours of exposure to 78%RH. New peaks in the 575 to 650 nm range, corresponding to $n = 2-5$ phases, appear on the front side (a) after exposure, and the primary peak at 715 nm shifts to 725 nm. Similar, but smaller spectral changes are observed in b). Normalized PL difference plots from the front (c) and back (d) of the same film, showing the formation of low- n species and a 3D-like species concurrent with the loss of the $n > 5$ species with exposure.....	241

Figure B.6 Point fluorescence spectrum from an nBA-MAPI film showing a strong peak near 750 nm.	242
Figure B.7 CFM images of a nBA-MAPI films at a) 0 hours, b) 12 hours, c) 24 hours, d) 48 hours, and e) 72 hours of exposure to 78%RH with a 740 nm short-pass filter. After 12 hours (b) fluorescence from elongated structures on the film is observed, and the size and surface density of these structures increases with exposure. The red crosshairs and numbers are artifacts from the imaging software.	243
Figure B.8 Average normalized point fluorescence spectra from CFM of areas off- (a) and on-crystal (b) taken from nBA-MAPI films exposed to 78%RH over 72 hours. In a) only the shoulder of the large peak at 750 nm can be observed for all samples. In b), there is a clear increase in peaks at 620, 660, and 680 nm with exposure time, corresponding to formation of $n=$ 3, 4, and 5 peaks, respectively.	244
Figure B.9 Point fluorescence spectra taken from three different locations of the same nBA-MAPI crystal using CFM at a) 12 hours and b) 72 hours of exposure to 78%RH, demonstrating differences in crystal homogeneity. The inset image in each provides an example of the locations sampled for each spectrum. Scale bar equal to 1 μm . c) Plot showing the prevalence of different levels of crystal homogeneity in nBA-MAPI crystals over 72 hours of exposure. Over time, the overall homogeneity of the crystals decreases as spectra from different locations of the crystals begin to show varying quantities of different n -phases.	245

Figure B.10 ToF-SIMS depth profile of various species from fresh (solid line) and exposed (dashed line) model PV devices. Exposed devices were left exposed to 78%RH for 24 hours prior to analysis. After exposure, the perovskite layer (PbI_2) shows an increase in width at the C_{60} interface, largely corresponding the hydration layer that has built up here (blue shaded region) and indicating moisture-related changes in the material.	246
Figure C.1 Average (a) V_{oc} , (b) J_{sc} , (c) PCE, and (d) FF of all butyl- and hexyl-MAPI devices with both Ag and Au contacts.....	247
Figure C.2 Cross sectional SEM image of (a) butyl-MAPI and (b) hexyl-MAPI films.	248
Figure C.3 Normalized (a) V_{oc} , (b) J_{sc} , (c) PCE, and (d) FF of butyl- and hexyl-MAPI devices fabricated using Au and Ag contacts exposed to 78%RH.	249
Figure C.4 Full XRD spectra of (a) hexyl-MAPI and (c) butyl-MAPI films exposed to 78%RH over 48 hours. Low-angle XRD spectra of (b) hexyl-MAPI and (d) butyl-MAPI films exposed to humidity. As exposure time progresses, the butyl-MAPI films exhibit the growth of low- n peaks below $2\theta = 12^\circ$, while hexyl-MAPI does not.	250
Figure C.5 Full XRD spectra of (a) Ag-hexyl and (c) Ag-butyl devices exposed to 78%RH over 48 hours. Low-angle XRD spectra of (b) Ag-hexyl and (d) Ag-butyl devices exposed to humidity. As exposure time progresses, the Ag-butyl devices exhibit the growth of low- n peaks below $2\theta = 12^\circ$ and the near complete loss of the original diffraction peaks, while hexyl-MAPI does not. Weak low- n peaks are visible in (b), likely indicating the formation of some low- n species during fabrication.	251

Figure C.6 Full XRD spectra of (a) Au-hexyl and (c) Au-butyl devices exposed to 78%RH over 48 hours. Low-angle XRD spectra of (b) Au-hexyl and (d) Au-butyl devices exposed to humidity. Both hexyl- and butyl-MAPI show low- <i>n</i> peaks below $2\theta = 12^\circ$ formed during fabrication, but these peaks do not grow with exposure time.	252
Figure C.7 Normalized PL spectra of (a) hexyl-MAPI and (b) butyl-MAPI films over 48 hours of exposure to 78% RH. Both the hexyl- and butyl-MAPI films shows a slight (~10 nm) red-shift of the primary peak, but the butyl-MAPI film also shows clear formation of low- <i>n</i> peaks from 700 – 600 nm.	253
Figure C.8 Normalized PL spectra of (a) Ag-hexyl and (b) Ag-butyl devices over 48 hours of exposure to 78% RH. Both the hexyl- and butyl-MAPI devices shows a slight (~10 nm) red-shift of the primary peak, but the butyl-MAPI film also shows clear formation of low- <i>n</i> peaks from 700 – 550 nm up to 12 hours. Afterwards, the film shows only a broad emission below 550 nm. The hexyl-MAPI film showed a decrease in the relative intensity of low- <i>n</i> peaks with exposure with time.	254
Figure C.9 Normalized PL spectra of (a) Au-hexyl and (b) Au-butyl devices over 48 hours of exposure to 78% RH. Both the hexyl- and butyl-MAPI devices shows a slight (~10 nm) red-shift of the primary peak, but the hexyl-MAPI device shows a decrease in the relative intensity of the low- <i>n</i> peaks from 700 – 550 nm. In contrast, the butyl-MAPI device shows almost no change.....	255

Figure C.10 PL spectra of a (a) butyl-MAPI film, (b) hexyl-MAPI film, (c) Ag-butyl device, (d) Ag-hexyl device, (e) Au-butyl device, and (f) Au-hexyl device before and after exposure to 78% RH for 8 hours. The hexyl-MAPI film shows a slight increase in the $n > 5$ peak with exposure, likely due to passivation of the surface, while the butyl-MAPI film shows a decrease in the primary $n > 5$ peak and an increase in the low- n peaks below 700 nm, likely due to disproportionation of the perovskite. All of the devices show an increase in PL intensity with moisture exposure, indicating decreased quenching of carriers by the C₆₀ due to the formation of a low- n passivation layer at the surface of the film. Low- n features are observed prior to degradation in (d) and (f), but do not appear to grow larger following degradation.....256

Figure C.11 Photographs of the backs of (a) Au-butyl, (b) Au-hexyl, (c) Ag-butyl, and (d) Ag-hexyl devices over the course of 12 hours of exposure to 78% RH. Both (a) and (b) show little change to the devices over the time period, while (d) shows the formation of a thin strip of yellow material around the outer edges of the Ag contacts only. (c) shows the formation of a large quantity of yellow material around the outer edges of the contacts, as well as some areas in the interior after just 3 hours. The degradation continues over the next 9 hours, until almost the entire device is yellow. Of interest, the yellow material only forms in areas directly under or adjacent to the Ag electrode. The scale bar indicates 0.5 cm.....257

Figure C.12 OH ⁻ depth profiles of (a) Ag-butyl, (b) Au-butyl, (c) Ag-hexyl, and (d) Au-hexyl devices before and after 8 hours of exposure to 78% RH. The hydration region for each device is defined as the FWHM of the OH ⁻ peak at the C ₆₀ /perovskite interface following exposure.	258
Figure C.13 CH ₂ ⁻ and ³⁴ S ⁻ depth profiles for (a) Ag-butyl, (b) Au-butyl, (c) Ag-hexyl, and (d) Au-hexyl devices before and after moisture exposure. The colored bars on top of each profile show the relative location of the peaks within the larger device. In all cases, there is a CH ₂ ⁻ peak on the bottom (rightward) side of the perovskite layer that corresponds with the organics in the PEDOT (indicated by the ³⁴ S ⁻ species).....	259
Figure C.14 UV-Vis spectra of <i>n</i> = 5 films of butyl-MAPI (red), butyl-MAPBr (blue), and a paired butyl iodo/bromo set (purple). The iodo <i>n</i> = 5 band gap (arrow in inset) is poorly defined in the paired sample, as is the <i>n</i> = 1 feature.	260
Figure C.15 UV-Vis spectra of <i>n</i> = 2 (top) and 1 (bottom) films of (a) butyl-MAPI and (b) hexyl-MAPI. The spectra include single iodo (red) and bromo (blue) materials, as well as a paired set of iodo/bromo films (purple).	261
Figure C.16 a) UV-Vis spectra of <i>n</i> = 2 hexyl-MAPI iodo/bromo pairs held at several temperatures over time. b) Decay in the intensity of the iodo UV-Vis peak near 575 nm in (a) measured over time; each point corresponds to a spectrum in (a). The data is fit to first order decay (line). c) Arrhenius plot derived from decay constants calculated using the data in (b), providing the activation energy of halide migration in the material.....	262

Figure C.17	a) UV-Vis spectra of $n = 2$ butyl-MAPI iodo/bromo pairs held at several temperatures over time. b) Decay in the intensity of the iodo UV-Vis peak near 575 nm in (a) measured over time; each point corresponds to a spectrum in (a). The data is fit to first order decay (line). c) Arrhenius plot derived from decay constants calculated using the data in (b), providing the activation energy of halide migration in the material.....	263
Figure C.18	a) UV-Vis spectra of $n = 1$ hexyl-MAPI iodo/bromo pairs held at several temperatures over time. b) Decay in the intensity of the iodo UV-Vis peak near 510 nm in (a) measured over time; each point corresponds to a spectrum in (a). The data is fit to first order decay (line). c) Arrhenius plot derived from decay constants calculated using the data in (b), providing the activation energy of halide migration in the material.....	264
Figure C.19	a) UV-Vis spectra of $n = 1$ butyl-MAPI iodo/bromo pairs held at several temperatures over time. b) Decay in the intensity of the iodo UV-Vis peak near 510 nm in (a) measured over time; each point corresponds to a spectrum in (a). The data is fit to first order decay (line). c) Arrhenius plot derived from decay constants calculated using the data in (b), providing the activation energy of halide migration in the material.....	265
Figure C.20	Activation energies for halide mobility in $n = 1$ butyl- and hexyl-MAPI perovskite determined by UV-Vis spectroscopy. The dashed line represents the previously reported activation energy of a 3D perovskite....	266
Figure D.1.	XRD spectra of a) SCO precursor annealed for 4.5 hours at 450°C, b) SCO precursor annealed at 850°C for 2 and 8 hours	269

Figure D.2. XPS spectra and fitted peaks for the 1%Fe-SCO sample. a) Spectra of the carbon 1s peak. b) Spectra of the strontium 3d 5/2 and 3/2 peaks. c) Spectra of the cobalt 2p peak. d) Spectra of the oxygen 1s peak.....	270
Figure D.3. XPS spectra and fitted peaks for the 5%Fe-SCO sample. a) Spectra of the carbon 1s peak. b) Spectra of the strontium 3d 5/2 and 3/2 peaks. c) Spectra of the cobalt 2p peak. d) Spectra of the oxygen 1s peak.....	271
Figure D.4. XPS spectra and fitted peaks for the 1%Sc-SCO sample. a) Spectra of the carbon 1s peak. b) Spectra of the strontium 3d 5/2 and 3/2 peaks. c) Spectra of the cobalt 2p peak. d) Spectra of the oxygen 1s peak.....	272
Figure D.5. XPS spectra and fitted peaks for the 5%Sc-SCO sample. a) Spectra of the carbon 1s peak. b) Spectra of the strontium 3d 5/2 and 3/2 peaks. c) Spectra of the cobalt 2p peak. d) Spectra of the oxygen 1s peak.....	273
Figure D.6. XPS spectra and fitted peaks for the 10%Sc-SCO sample. a) Spectra of the carbon 1s peak. b) Spectra of the strontium 3d 5/2 and 3/2 peaks. c) Spectra of the cobalt 2p peak. d) Spectra of the oxygen 1s peak.....	274
Figure D.7. XPS spectra and fitted peaks for the UnSCO sample. a) Spectra of the carbon 1s peak. b) Spectra of the strontium 3d 5/2 and 3/2 peaks. c) Spectra of the cobalt 2p peak. d) Spectra of the oxygen 1s peak.....	275
Figure D.8. XPS spectra and fitted peaks for the Fe 2p 3/2 peaks of the Fe-SCO samples. a) 1%Fe-SCO b) 5%Fe-SCO c) 10%Fe-SCO.....	276
Figure D.9. XPS spectra and fitted peaks for the Sc 2p 3/2 peaks of the Sc-SCO samples. a) 1%Sc-SCO b) 5%Sc-SCO c) 10%Sc-SCO.....	277
Figure D.10. XPS spectra of the Co 3p region in all SCO samples. The dashed line lies on 61.0 eV, the dotted line lies on 62.8 eV	277

Figure D.11. Selected area electron diffraction patterns of a) undoped-SCO, b) 5%Fe-SCO, c) 10%Fe-SCO, and d) 10% Sc-SCO showing the polycrystalline nature of the undoped material. The other diffraction patterns have been indexed as orthorhombic $\text{SrCoO}_{2.5}$	278
Figure D.12. Radial distribution plot of the SAED in Figure D.X1 for undoped-SCO integrated over 360° indexed as trigonal $\text{Sr}_6\text{Co}_5\text{O}_{15}$	279
Figure D.13. Electron dispersive X-ray spectroscopy maps of a) UnSCO, b) 5%Fe-SCO, c) 10%Fe-SCO, and d) 10% Sc-SCO. Cobalt is blue, strontium is red, and the dopant (Fe or Sc) is green	280
Figure D.14. SEM images of a) 10%Fe-SCO and b) undoped SCO microparticle catalyst on conductive FTO substrate. Surface morphology for the c) 10%Fe-SCO and d) undoped SCO microparticles both appear rough, and composed of sintered microparticles.	281
Figure D.15. SEM images of UnSCO Electrode	281
Figure D.16. SEM images of 1%Fe-SCO Electrode.....	282
Figure D.17. SEM images of 5%Fe-SCO Electrode.....	282
Figure D.18. SEM images of 10%Fe-SCO Electrode.....	283
Figure D.19. SEM images of 1%Sc-SCO Electrode.....	283
Figure D.20. SEM images of 5%Sc-SCO Electrode.....	284
Figure D.21. SEM images of 10%Sc-SCO Electrode.....	284
Figure D.22. Plot of measured overpotential at 10 mA/cm^2 versus [Fe] in several Fe-doped SCO electrodes.....	285

Figure E.1: Higher-magnification SEM images of a) NiS ₁₀₀ , b) NiS ₁₀ Se ₁₀ , c) NiS ₇₅ Se ₂₅ , d) NiS ₅₀ Se ₅₀ , and e) NiSe ₁₀₀ NiSSe composite materials. All materials show primarily spherical particle-like morphologies, with particle size tending to increase as Se-content increases, ultimately resulting in roughly 1 micron-diameter microspheres of NiSe material for the NiSe ₁₀₀ composite.....	286
Figure E.2: Lower-magnification SEM images of a) NiS ₁₀₀ , b) NiS ₁₀ Se ₁₀ , c) NiS ₇₅ Se ₂₅ , d) NiS ₅₀ Se ₅₀ , and e) NiSe ₁₀₀ NiSSe composite materials. S-rich composites tend to show larger polydispersity in particle size, frequently forming micron-scale agglomerates from much smaller particles. The Se-rich materials tend to be composed of much more uniform particles.	287
Figure E.3: a) Krypton uptakes at 77K over the classical BET relative pressure range and b) the resulting multi-point BET plot for extraction of surface area from adsorption analysis by linear regression (solid lines), with all samples showing excellent fits ($r > 0.9998$).	288
Figure E.4: Mass activity of NiS _x Se _y composites measured at 300 mV and 400 mV of overpotential. A total catalyst mass of 48 µg was used for all measurements.....	289
Figure E.5: RRDE-derived Faradaic efficiency of NiS ₁₀₀ , NiS ₉₀ Se ₁₀ , and NiSe ₁₀₀ electrocatalysts over a range of applied current densities. All measurements were performed in Ar-sparged 0.1M KOH solution at a rotation rate of 1600 rpm. The Pt ring electrode was held at 0.435V vs. RHE while the glassy carbon disk was held at 1.0, 2.0, and 4.0 mA/cm ² ..	289

Figure E.6: Dissolved Ni and Se content of 1 M KOH electrolyte solution for after 6 hours of OER electrocatalysis at 10 mA/cm^2 using NiS_{100} , $\text{NiS}_{90}\text{Se}_{10}$, and NiSe_{100} . The addition of Se to the composite correlates to reduced Ni dissolution with OER testing.	290
Figure E.7: CVs of the NiSSe composites performed in 1M KOH solution, with OER-derived current normalized by BET surface areas to better determine the intrinsic performance of each material. Here, the $\text{NiS}_{75}\text{Se}_{25}$ composite shows superior performance. All measurements were made vs a Pt counter electrode using an Ag/AgCl(sat'd KCl) reference electrode, using a 20 mV/s sweep rate.	290
Figure E.8: Full (a) and low-Ohm region (b) EIS spectra of NiS_{100} , $\text{NiS}_{90}\text{Se}_{10}$, and NiSe_{100} electrocatalysts before (fresh) and after electrochemical surface oxidation (ox.), recorded from 0.1Hz to 100kHz at 1.52V vs. RHE. Se-containing samples show the lowest R_{CT} prior to oxidation, while the $\text{NiS}_{90}\text{Se}_{10}$ sample shows the lowest R_{CT} after testing at 10 mA/cm^2 for 30 minutes, indicating increased resistance to oxidation compared to pure S and Se materials. Samples were tested in a 1M KOH solution with a Pt wire counter electrode and an Ag/AgCl (sat'd KCl) reference electrode.	291

Figure E.9: a) Relative ratio of S/Se calculated from the fitted peaks in (b) and from EDX measurements made during SEM, indicating generally good agreement between the theoretical quantity of each species and the measured quantity. The $\text{NiS}_{90}\text{Se}_{10}$ S/Se ratio from XPS may be skewed due to preferential oxidation of S at the surface, as indicated by the higher value when measured using EDX. b) S 2s and Se 3s region for all NiSSe composites, showing fitted peaks for Ni-S, Ni-Se, and oxidized chalcogen species. c) O 1s region for all NiSSe composites, showing the surface oxygen species are primarily OH^- , with small quantities of NiO_x present at high Se-contents, as well as several adsorbed water peaks. d) Se 3d spectra for all NiSSe composites, showing peak fits for the monoselenide (green), di-selenide (blue), and oxidized selenium (purple) species.292

Figure E.10: Pourbaix diagrams and Gibbs free energy overlays for a) Ni_3S_2 , b) Ni_3Se_2 , and c) Ni_3Te_2 . The nickel selenide and telluride materials are generally stable across a wider range of pH and potential than the sulfide material, indicative of their superior stability and the empirically observed resistivity to oxidation. Diagrams are produced using the Materials Project (ref. 1-3).....293

Figure E.11: Comparison of the observed overpotential at 10 mA/cm^2 for each composite (red) with the percentage of oxidized S or Se (blue). This shows that as the Se content increases in S-rich materials, the amount of oxidized chalcogen and the overpotential both decrease in a similar fashion.....294

Figure E.12: Chronoamperogram of the NiS ₁₀₀ and NiS ₉₀ Se ₁₀ composites at 10 mA/cm ² until material failure, as indicated by the sharp increase in overpotential, showing the superior stability of the Se-incorporated material. The experiments was performed versus a Pt counter electrode with an Ag/AgCl(sat'd KCl) reference electrode, with N ₂ sparging to remove accumulated bubbles.	294
Figure E.13: TEM images of a) NiS ₁₀₀ and b)NiS90Se10 as-synthesized, showing that both materials appear to be agglomerates composed of smaller nanoparticles.	295
Figure E.14: a) HRTEM image of as-synthesized NiS ₁₀₀ and b) an EDX map of Ni and O from the same region demonstrating the large degree of oxidation natively present at the surface of this material. FFT from the oxidized surface shows d-spacing corresponding to NiO (c), while FFT from the interior of the particle corresponds to NiS and Ni ₃ S ₂ (d,e).	296
Figure E.15: a) HRTEM image of as-synthesized NiS ₉₀ Se ₁₀ and b) an EDX map of Ni and O from the region within the white box, demonstrating a small degree of oxidation is natively present on the surface of the material. FFT from Spot 1 shows d-spacings corresponding to NiSe, NiS, and some NiOOH, while FFT from Spot 2 shows primarily metal chalcogenide character. Lattice fringes from the area inside the black box (c) can be indexed to Ni ₃ S ₂ and NiS, in agreement with the FFT. There appears to be relatively little amorphous oxide/hydroxide on this sample, and the metal chalcogenide lattice extends to the surface of the particle.....	297

Figure E.16: a) HAADF image of the NiS_{100} composite after OER testing, with corresponding EDX maps for b) Ni, c) O, and d) S. There is a roughly 20 nm-thick layer of O-rich material surrounding the NiS_{100} material, and both Ni and S are evenly distributed in the interior.298

Figure E.17: a) HAADF image of the $\text{NiS}_{90}\text{Se}_{10}$ composite after OER testing, with corresponding EDX maps for b) Ni, c) O, d) S, and e) Se. There is a roughly 10 nm-thick layer of O-rich material surrounding the $\text{NiS}_{90}\text{Se}_{10}$ material, and what appears to be multiple planes of material, as evidenced by multiple O-rich edges. Ni, S, and Se appear to be evenly mixed in the particle.....299

Chapter 1: Introduction to Renewable Energy Production and Storage

1.1 OPENING REMARKS AND ORGANOLEAD HALIDE PEROVSKITES

As our world moves further into the 21st century and seeks to wean itself from fossil fuels, it seems inevitable that renewable energy sources will become an increasingly important part of our energy portfolio. In 2019, renewable energy sources accounted for 231 GW of electricity generation in the US, and this is projected to grow to over 600 GW by 2050.¹ Much of this capacity is expected to come in the form of wind and solar power, as both energy sources are widely available across the country. Solar power, in particular, is expected to grow significantly in the next 30 years, a reflection of increased interest and investment in photovoltaic technologies.^{2,3}

Currently, one of the most common means of capturing solar power and converting it into useable electricity is the Si photovoltaic (PV) module, used everywhere from the rooftops of homes to grid-scale solar energy farms. The popularity of Si PVs is due in large part to the high power conversion efficiency (PCE) of the technology,⁴ as well as recent developments in production capabilities in China and other countries. Between 2010 and 2020 the price of manufacturing a Si solar panel decreased significantly, to the extent that most of the cost of deploying Si PV is now due to the cost of installation rather than materials or fabrication.^{2,5} Unfortunately, while the solar panels themselves produce clean energy, our current means of producing them remain relatively dirty. The energy required to produce the raw Si necessary for solar panels in places like China frequently comes from coal, initially offsetting at least some of the benefits of producing electricity using solar power.⁶

While Si is the most common material for PV power generation, a variety of next-generation thin film PV materials are currently under development.^{7,8} Thin film PV

devices rely on photoabsorbing layers that are typically less than 5 μm thick and can frequently be fabricated using solution-based methods, offering the potential for inexpensive wide-scale manufacturing of PV devices. Among the most exciting thin film PV materials are a family of semiconductors broadly known as organolead halide perovskites. Broadly speaking, the term “perovskite” refers to any material with an ABX_3 crystal structure (**Figure 1.1**), where “A” is a monovalent cation (frequently a short-chain alkylammonium species), “B” is a divalent cation (typically Pb or Sn), and “X” is a halide. The most common perovskite material is methylammonium lead triiodide (MAPI), and was first shown to be photoactive in 2009.⁹ Since then, perovskites have gone on to show record efficiencies approaching those of single crystalline Si devices.⁴ In part, this rapid increase in efficiency has been due to the relatively high chemical flexibility of the material, with the substitution of methylammonium for compounds like formamidinium and elements like Cs resulting in improvements to various chemical and optoelectronic properties.⁷

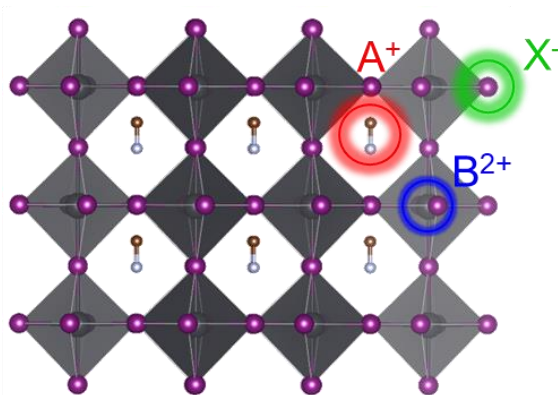


Figure 1.1 Model of the crystal structure of a cubic organolead halide perovskite. The A-site (red) is a monovalent cation which is typically an alkylammonium species, the B-site (blue) is a divalent metal cation such as Pb^{2+} , and the X-site (green) is a halide species.

In addition to the wide range of chemistries possible, perovskite materials are also exciting for the relative ease with which they can be produced. Thin films of the material can readily be created directly from solutions containing dissolved precursors, opening the door for the use of inexpensive printing technologies to create PV devices.¹⁰ Additionally, perovskite thin films have been successfully deposited onto flexible substrates like poly(ethylene terephthalate),¹¹ indicating that roll-to-roll processing of perovskite PV devices may be possible.¹⁰ As a result, organolead halide perovskites could potentially become the material of choice for use in portable, inexpensive solar power for a variety of applications.

An unfortunate commonality in most perovskite materials, however, is their relatively low stability under many environmental conditions. Perovskites have been shown to degrade rapidly in the presence of humidity and under illumination,^{12,13} although the use of protective encapsulation layers can address this instability.¹⁴ Encapsulation does not address the underlying fundamental problems with the material, however, and may introduce other issues. For instance, it is readily apparent that

encapsulation will undoubtedly result in increased rigidity and weight for flexible perovskite PVs, and that the additional encapsulation material and processing will add additional manufacturing costs.⁵ As a result, there is a significant need for a means to chemically stabilize perovskite materials such that minimal encapsulation is necessary in applications such as these.

One viable option is the use of Ruddlesden-Popper phase (RPP) perovskites in place of more traditional materials, as they have been found to be more stable under a variety of common conditions.¹⁵ RPP perovskites are quasi-2D perovskite materials with a chemical formula of $A'_2A_{n-1}B_nX_{3n+1}$, where A' is a typically an amphiphilic alkylammonium species with a long alkyl chain (such as *n*-butylammonium), and A, B, and X are similar species to those found in the previously-described perovskite materials. The A' species are frequently referred to as “spacers”, segregating the ABX_3 components of RPP perovskites into discrete 2D sheets of perovskite material separated from each other by bilayers of A' species (**Figure 1.2**). These sheets are typically labeled by their thickness, best described by *n*, the number of adjacent PbI_6^{4-} octahedra in a given sheet. The quasi-2D nature of these materials leads to exciting physical and chemical properties in these materials, including their increased stability, and we will explore them more deeply in the following chapters.

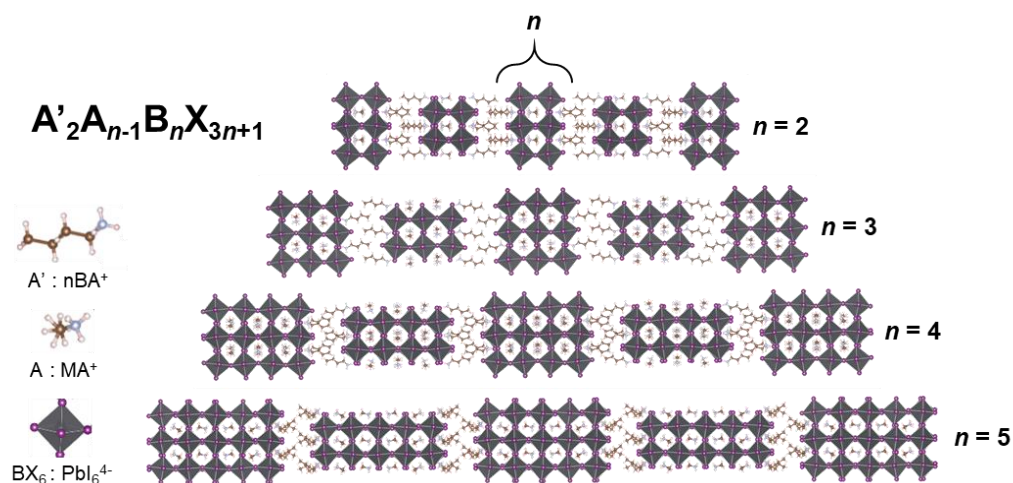


Figure 1.2 Model of the crystal structures of a series of quasi-2D organolead halide perovskites with different n -phases a cubic organolead halide perovskite with the generic formula $A'_2A_{n-1}B_nX_{3n+1}$. Here, the A' -site is a long alkylammonium species, the A -site is a monovalent organic cation, the B -site is a divalent metal cation, and the X -site is a halide species.

1.2 TRANSITION METAL-BASED OXYGEN EVOLUTION REACTION ELECTROCATALYSTS

Solar power, whether harnessed by Si or perovskite PVs unfortunately remains an intermittent energy source as does wind, the other major renewable energy source available today. In the long term, this poses a fundamental hurdle to any efforts to create an economy powered entirely by renewable energy sources, and will require the development and deployment technologies to store renewable energy for use during periods of low solar or wind power. Likewise, such storage will be needed in the short term to stabilize our current electricity grid as we introduce more renewable energy sources alongside more traditional energy sources. To illustrate this, **Figure 1.3** shows the load on the electrical grid of municipality in California over the course of a day, supplied by traditional fossil fuel energy sources.¹⁶ As more solar power generation capability is added to the local electricity grid in the near future, the amount of electricity

fossil fuel-fired plants need to produce to meet demand decreases during daylight hours. Unfortunately, the highest load on the local grid comes around 5 pm, just as the sun is setting and solar electricity generation ceases. As can be seen in **Figure 1.3**, dealing with this additional demand requires power plants to rapidly ramp the generators to supply sufficient electricity. This process is highly inefficient, producing more CO₂ emissions and costing the plant more money than if no renewable capability were present. Further, the problem will become more pronounced as additional solar power generation is added to the grid, further increasing the environmental and economic cost.

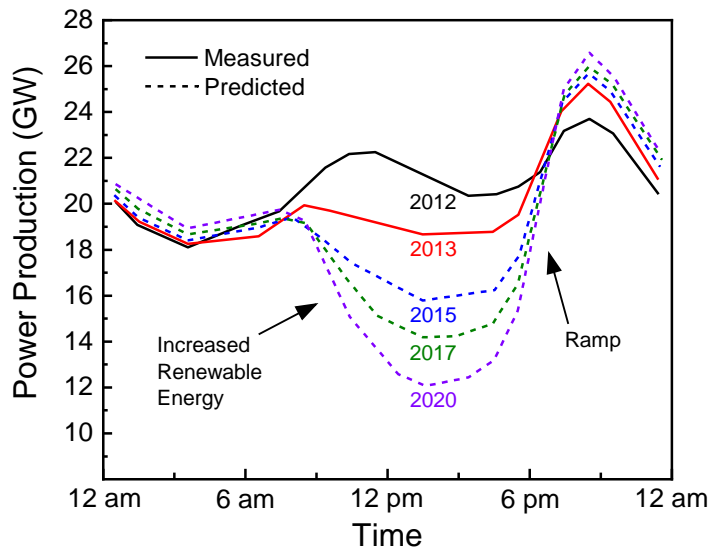


Figure 1.3 Actual and predicted electricity generation by fossil fuel-fired power plants for a municipality in California, showing the impact of adding increasing amounts of renewably-generated electricity to the grid. Because most renewable energy is available during the day rather than night, increased quantities of renewable-derived electricity will require more extreme production ramps (after 3 pm) from fossil fuel-fired plants to meet peak demand (around 8 pm). Image adapted from source 16.

This example clearly demonstrates our need for an efficient means of storing renewable energy and delivering it onto the grid reliably. By storing excess renewable energy produced during the day, it will be possible to flatten the production curve for fossil fuel plants before and after the evening peak, improving the efficiency of the power grid even as additional renewable energy is added to the grid. A number of storage solutions have been proposed, but one of the most exciting is the use of renewable energy to generate H_2 gas that can then be stored and used as a chemical fuel. The simplest way to achieving this is to use electricity to perform water electrolysis, alternatively known as water splitting, which electrochemically splits two molecules of H_2O into one molecule of O_2 and two molecules of H_2 . Since the 1970s, research has shown that semiconducting metal oxides like TiO_2 and $BiVO_4$ can absorb sunlight to directly drive this reaction,¹⁷ but the process remains relatively inefficient. Instead, a more efficient way of performing this reaction is to use electricity from a renewable source to drive a device known as an electrolyzer.¹⁸ Powered directly by electricity, electrolyzers allow H_2 to be generated by any energy source, including wind and solar power, making it more versatile than a purely photon-driven system.

An electrolyzer consists of two electrodes submerged in an electrolyte solution, at which the cathodic hydrogen evolution reaction (HER) and anodic oxygen evolution reaction (OER) occur (**Figure 1.4**). The HER has a standard potential of 0.0 V vs. RHE and the OER has a standard potential of 1.23 V vs RHE, and thus the thermodynamic barrier to water splitting is only 1.23 V. Unfortunately, both reactions also exhibit kinetic barriers that increase the electrochemical potential needed; this extra potential, beyond that which is called for by thermodynamics, is commonly referred to as “overpotential.” Of the two reactions, the 4-electron OER exhibits a greater kinetic barrier that leads to higher overpotentials, and thus the OER is commonly regarded as the rate limiting step in

water electrolysis.¹⁹ As a result, it is here that we have focused our attention in the following chapters.

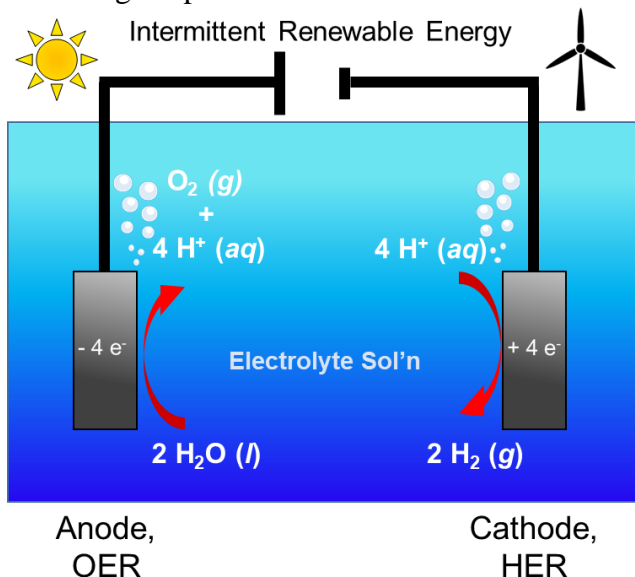


Figure 1.4 Diagram of a typical water electrolyzer system. Electricity, here provided by intermittent renewable sources, powers the oxygen evolution reaction (OER) at the anode and the hydrogen evolution reaction, (HER) at the cathode. Both electrodes are submerged in an aqueous electrolyte solution, typically strongly acidic or basic.

A common means of surmounting this barrier to efficient water splitting is the use of electrocatalysts capable of reducing the kinetic barrier for the OER, thus reducing the overpotential required to drive the reaction forward.²⁰ To date, the most efficient of these materials are precious metals and their oxides, such as Ru, RuO₂, Ir, and IrO₂. Unfortunately, such materials are not abundant in the Earth's crust and as a result are expensive,²⁰ creating an additional hurdle to the widespread use of electrolyzers to produce H₂. As a result, significant effort has been invested toward exploring a variety of more abundant materials as less expensive electrocatalyst alternatives. These materials are typically transition metal oxides and (oxy)hydroxides, with the most exciting and

efficient typically containing Fe, Co, or Ni, or some combination of the three metals.¹⁹ Fe, in particular, is very earth-abundant, making it an ideal material for making inexpensive electrocatalysts. Due to the low electrical conductivity of many Fe compounds, it frequently is added to other Co- and Ni-based materials to improve the electrocatalytic performance of the resulting composite. Such additions reflect the importance of chemical composition on the electrocatalytic performance of many metal oxides for the OER.

Recent work has also begun to explore a series of metal chalcogenides as potential replacements for more expensive precious metals electrocatalysts. Typically composed of one or two transition metals bound to sulfur, selenium, or tellurium, metal chalcogenides show excellent performance as OER electrocatalysts, comparable to more traditional metal oxides.¹⁹ Due in part to their performance, it was initially thought that these chalcogenide materials were themselves active OER catalysts. Recent results, however, have shown that these materials are in fact best thought of as “pre-catalysts” that undergo full or partial surface oxidation to yield truly catalytic metal (oxy)hydroxide materials.²¹ Work is ongoing to determine exactly why metal (oxy)hydroxides created using metal chalcogenide pre-catalysts show superior performance, as are efforts to further improve the electrocatalytic performance of these materials. One exciting new research direction is the synthesis of metal chalcogenides containing more than one chalcogenide species, i.e., both sulfur and selenium. Preliminary reports show that these materials exhibit increased OER performance compared to single chalcogenide materials, but further work is needed to explore the underlying causes more carefully.

1.3 OVERVIEW OF CHAPTERS

In the following chapters, we will seek to shine light on both the increased stability of RPP perovskites for use in organolead halide PV technologies, and on the effect of elemental composition on both metal oxide and metal chalcogenide OER catalysts. Exploration and development of chemistries, materials, and technologies for both the generation of electricity from renewable energy sources and the efficient storage of that energy are vital if renewable energy is to one day seek to replace fossil fuels entirely. Below, we offer a brief outline of the following chapters before they are presented in more detail.

In Chapter 1, we will provide additional information about different types of perovskite thin film PV devices and our motivation for studying these devices. After this introduction, Chapter 2 presents a detailed study of the differences in the degradation mechanisms of both traditional 3D organolead halide perovskites and quasi-2D RPP perovskites. We show that the RPP perovskites undergo a unique disproportionation-based degradation pathway that increases material stability, and that this effect can be leveraged to increase the stability of traditional 3D perovskites. In Chapter 3, we extend this investigation of the RPP perovskites and explore physical changes that occur within the RPP thin film during moisture-driven degradation. We focus primarily on the formation of small crystallites at the film surface, and show that they are composed of low- n phases resulting from perovskite disproportionation. In Chapter 4, we conclude our investigation of RPP perovskites by exploring differences in stability between two closely related perovskites, in regards to both moisture-exposure and choice of metal electrode. We find that even small changes in composition can dramatically impact the manner in which RPP perovskites degrade, and provide data to explain the sources of these differences.

Chapter 6 provides another brief introduction to the need for inexpensive electrocatalysts for water electrolysis and provides additional context for the materials we chose to study. In Chapter 7, we present a study of the interplay between elemental composition, crystal structure, and OER performance in a transition metal oxide electrocatalyst. We find evidence that adding additional metal species to the electrocatalyst does impact the crystal structure of the final material, but that improvements to the electrocatalytic performance of the material are more closely linked to the choice of metal added than to the crystallographic differences. Finally, in Chapter 8 we explore how the addition of a second chalcogenide species to a nickel chalcogenide impacts both oxidation of the material from pre-catalyst to catalyst, and the performance of this final catalyst. Our results show that the mixed-chalcogenide materials exhibit increased stability to oxidation which is linked to increased electrical conductivity, and that these effects in tandem increase the OER performance of the catalyst.

1.4 REFERENCES

- (1) Annual Energy Outlook 2020 with projections to 2050 www.eia.gov/aeo (accessed Apr 2, 2020).
- (2) Woodhouse, M.; Smith, B.; Ramdas, A.; Robert Margolis. *Crystalline Silicon Photovoltaic Module Manufacturing Costs and Sustainable Pricing: 1H 2018 Benchmark and Cost Reduction Roadmap*; 2019.
- (3) International Energy Outlook 2019 with projections to 2050 www.eia.gov/ieo (accessed Apr 2, 2020).
- (4) NREL. Best Research-Cell Efficiencies <https://www.nrel.gov/pv/assets/pdfs/pv-efficiency-chart.20181221.pdf>.
- (5) Horowitz, K. A. W.; Fu, R.; Sun, X.; Silverman, T.; Woodhouse, M.; Alam, M. A.; Horowitz, K. A. W.; Fu, R.; Sun, X.; Silverman, T.; et al. An Analysis of the Cost and Performance of Photovoltaic Systems as a Function of Module Area. *Natl. Renew. Energy Lab.* **2017**, No. April.
- (6) Yue, D.; You, F.; Darling, S. B. Domestic and Overseas Manufacturing Scenarios of Silicon-Based Photovoltaics: Life Cycle Energy and Environmental

- Comparative Analysis. *Sol. Energy* **2014**, *105*, 669–678. <https://doi.org/10.1016/j.solener.2014.04.008>.
- (7) Jena, A. K.; Kulkarni, A.; Miyasaka, T. Halide Perovskite Photovoltaics: Background, Status, and Future Prospects. *Chem. Rev.* **2019**, *119* (5), 3036–3103. <https://doi.org/10.1021/acs.chemrev.8b00539>.
 - (8) Habas, S. E.; Platt, H. A. S.; Van Hest, M. F. A. M.; Ginley, D. S. Low-Cost Inorganic Solar Cells: From Ink to Printed Device. *Chem. Rev.* **2010**, *110* (11), 6571–6594. <https://doi.org/10.1021/cr100191d>.
 - (9) Kojima, A.; Teshima, K.; Shirai, Y.; Miyasaka, T. Organometal Halide Perovskites as Visible-Light Sensitizers for Photovoltaic Cells. *J. Am. Chem. Soc.* **2009**, *131* (17), 6050–6051. <https://doi.org/10.1021/ja809598r>.
 - (10) Dunlap-Shohl, W. A.; Zhou, Y.; Padture, N. P.; Mitzi, D. B. Synthetic Approaches for Halide Perovskite Thin Films. *Chem. Rev.* **2019**, *119* (5), 3193–3295. <https://doi.org/10.1021/acs.chemrev.8b00318>.
 - (11) Yang, D.; Yang, R.; Priya, S.; Liu, S. (Frank). Recent Advances in Flexible Perovskite Solar Cells: Fabrication and Applications. *Angew. Chemie - Int. Ed.* **2019**, *58* (14), 4466–4483. <https://doi.org/10.1002/anie.201809781>.
 - (12) Leguy, A. M. A.; Hu, Y.; Campoy-Quiles, M.; Alonso, M. I.; Weber, O. J.; Azarhoosh, P.; van Schilfgaarde, M.; Weller, M. T.; Bein, T.; Nelson, J.; et al. Reversible Hydration of CH₃NH₃PbI₃ in Films, Single Crystals, and Solar Cells. *Chem. Mater.* **2015**, *27* (9), 3397–3407. <https://doi.org/10.1021/acs.chemmater.5b00660>.
 - (13) Akbulatov, A. F.; Frolova, L. A.; Griffin, M. P.; Gearba, I. R.; Dolocan, A.; Vanden Bout, D. A.; Tsarev, S.; Katz, E. A.; Shestakov, A. F.; Stevenson, K. J.; et al. Effect of Electron-Transport Material on Light-Induced Degradation of Inverted Planar Junction Perovskite Solar Cells. *Adv. Energy Mater.* **2017**, *7* (19), 1700476. <https://doi.org/10.1002/aenm.201700476>.
 - (14) Cheacharoen, R.; Rolston, N.; Harwood, D.; Bush, K. A.; Dauskardt, R. H.; McGehee, M. D. Design and Understanding of Encapsulated Perovskite Solar Cells to Withstand Temperature Cycling. *Energy Environ. Sci.* **2018**, *11* (1), 144–150. <https://doi.org/10.1039/c7ee02564e>.
 - (15) Tsai, H.; Nie, W.; Blancon, J.-C.; Stoumpos, C. C.; Asadpour, R.; Harutyunyan, B.; Neukirch, A. J.; Verduzco, R.; Crochet, J. J.; Tretiak, S.; et al. High-Efficiency Two-Dimensional Ruddlesden–Popper Perovskite Solar Cells. *Nature* **2016**, *536* (7616), 312–316. <https://doi.org/10.1038/nature18306>.
 - (16) Denholm, P.; O’Connell, M.; Brinkman, G.; Jorgenson, J. *Overgeneration from Solar Energy in California: A Field Guide to the Duck Chart* (NREL/TP-6A20-65023); 2015.

- (17) Yao, T.; An, X.; Han, H.; Chen, J. Q.; Li, C. Photoelectrocatalytic Materials for Solar Water Splitting. *Adv. Energy Mater.* **2018**, *8* (21), 1800210. <https://doi.org/10.1002/aenm.201800210>.
- (18) You, B.; Sun, Y. Innovative Strategies for Electrocatalytic Water Splitting. *Acc. Chem. Res.* **2018**, *51* (7), 1571–1580. <https://doi.org/10.1021/acs.accounts.8b00002>.
- (19) Wygant, B. R.; Kawashima, K.; Mullins, C. B. Catalyst or Precatalyst? The Effect of Oxidation on Transition Metal Carbide, Pnictide, and Chalcogenide Oxygen Evolution Catalysts. *ACS Energy Lett.* **2018**, *3* (12), 2956–2966. <https://doi.org/10.1021/acsenergylett.8b01774>.
- (20) McCrory, C. C. L.; Jung, S.; Ferrer, I. M.; Chatman, S. M.; Peters, J. C.; Jaramillo, T. F. Benchmarking Hydrogen Evolving Reaction and Oxygen Evolving Reaction Electrocatalysts for Solar Water Splitting Devices. *J. Am. Chem. Soc.* **2015**, *137* (13), 4347–4357. <https://doi.org/10.1021/ja510442p>.
- (21) Mabayoje, O.; Shoola, A.; Wygant, B. R.; Mullins, C. B. The Role of Anions in Metal Chalcogenide Oxygen Evolution Catalysis: Electrodeposited Thin Films of Nickel Sulfide as “Pre-Catalysts.” *ACS Energy Lett.* **2016**, *1* (1), 195–201. <https://doi.org/10.1021/acsenergylett.6b00084>.

Chapter 2: Introduction to Perovskite Photovoltaics

As discussed briefly in Chapter 1, organolead halide perovskites are among the most promising of the thin film photovoltaic (PV) materials currently studied. Their high absorption coefficients and relatively low band gaps enable films hundreds of nanometers thick to absorb most of the solar spectrum, while their solution-phase processing enables simple deposition of films onto a variety of substrates.¹ The original solid state perovskite devices were fabricated using a modified form of the traditional dye-sensitized solar cell,² but recent years have seen the rise of planar n-i-p perovskite PV devices.³ An example of this type of device is provided in **Figure 2.1a**, and the notation refers to the relative orientation of the electron transport material (ETM) and hole transport material (HTM) relative to the perovskite and the transparent conductive metal oxide (TCO) contact in the device. The ETM is an n-type (n) semiconductor responsible for selectively conducting electrons out of the intrinsic (i) perovskite photoabsorber, while the HTM is a p-type (p) semiconductor which selectively transmits holes from the perovskite layer. In an n-i-p device, the ETM is first deposited on top of the TCO, followed by the perovskite and HTM layer, and finally a metal electrode (typically Au) is deposited on top of the HTM layer. The ETM and HTM help to separate the photogenerated electron-hole pairs in the perovskite, and inhibit recombination of the carriers before they are shuttled out of the device.

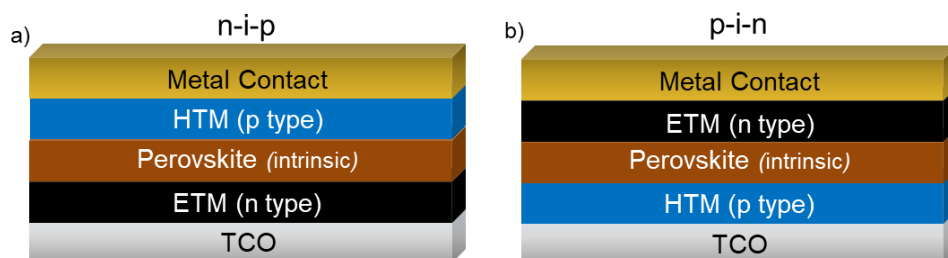


Figure 2.1 The architectures of typical (a) n-i-p and (b) p-i-n organolead halide perovskite devices. Both devices contain an intrinsic perovskite photoabsorbing layer, an n-type electron-selective electron transport material (ETM), and a p-type hole-selective hole transport material (HTM).

In addition to the more typical n-i-p device, many researchers also fabricate and study inverted p-i-n perovskite PV devices (**Figure 2.1b**).³ These devices also rely on hole- and electron-selective materials to function, but the order of deposition is opposite relative to the n-i-p devices. Because the HTM is deposited first, this architecture allows materials such as PEDOT:PSS and NiO to be used in place of more complex materials like Spiro-OMeTAD (2,2',7,7'-tetrakis[N,N-di(4-methoxyphenyl)amino]-9,9'-spirobifluorene).² Cast from a water-based solution, PEDOT:PSS cannot be used in traditional n-i-p architectures as they would damage the underlying perovskite layer during deposition; the p-i-n architecture allows for this problem to be circumvented, however. Following deposition and drying of the HTM layer, the perovskite can be safely deposited on top of the water-free material, followed by thermal evaporation of the ETM layer that is typically composed of C₆₀ or a derivative to complete the p-i-n device.⁴

While both n-i-p and p-i-n perovskite devices have shown promising performance, we have chosen to study the stability of p-i-n devices due to their suitability for fabrication on polymer substrates which could enable flexible PV devices. The use of minimal protective encapsulation will likely be necessary to maximize the flexibility and minimize the weight of such devices, and as such, increasing the intrinsic stability of the

perovskite material will be of paramount importance. The high stability of quasi-2D perovskites when exposed to moisture thus makes them an ideal candidate for use in flexible devices, but a better understanding of how they degrade in humid conditions will be key to further stabilizing these materials prior to commercialization. In the following chapters we will present the results of our research in this area, focusing on detailed studies of how an *n*-butylammonium-derived quasi-2D perovskite degrades in comparison to a more typical 3D perovskite (Chapters 3-4), before investigating how devices containing *n*-butylammonium perovskite differ from those fabricated using *n*-hexylammonium (Chapter 5).

REFERENCES

- (1) Dunlap-Shohl, W. A.; Zhou, Y.; Padture, N. P.; Mitzi, D. B. Synthetic Approaches for Halide Perovskite Thin Films. *Chem. Rev.* **2019**, *119* (5), 3193–3295. <https://doi.org/10.1021/acs.chemrev.8b00318>.
- (2) Kim, H.-S.; Lee, C.-R.; Im, J.-H.; Lee, K.-B.; Moehl, T.; Marchioro, A.; Moon, S.-J.; Humphry-Baker, R.; Yum, J.-H.; Moser, J. E.; et al. Lead Iodide Perovskite Sensitized All-Solid-State Submicron Thin Film Mesoscopic Solar Cell with Efficiency Exceeding 9%. *Sci. Rep.* **2012**, *2*, 1–7. <https://doi.org/10.1038/srep00591>.
- (3) Jena, A. K.; Kulkarni, A.; Miyasaka, T. Halide Perovskite Photovoltaics: Background, Status, and Future Prospects. *Chem. Rev.* **2019**, *119* (5), 3036–3103. <https://doi.org/10.1021/acs.chemrev.8b00539>.
- (4) Tsai, H.; Nie, W.; Blancon, J.-C.; Stoumpos, C. C.; Asadpour, R.; Harutyunyan, B.; Neukirch, A. J.; Verduzco, R.; Crochet, J. J.; Tretiak, S.; et al. High-Efficiency Two-Dimensional Ruddlesden–Popper Perovskite Solar Cells. *Nature* **2016**, *536* (7616), 312–316. <https://doi.org/10.1038/nature18306>.

Chapter 3: Probing the Degradation Chemistry and Enhanced Stability of 2D Organolead Halide Perovskites¹

3.1 INTRODUCTION

Organolead halide perovskites are among the most promising materials for next-generation thin film solar devices, as first demonstrated by solid state methylammonium lead iodide (MAPI) devices.¹ In recent years, the power conversion efficiency (PCE) of lab-scale perovskite devices has increased at a remarkable rate to levels that are comparable with more traditional Si and CdTe solar cells.² While the future for perovskite solar cells is bright, most members of the organolead halide perovskite family suffer from severe sensitivity to both moisture and light.³⁻⁵ Additionally, these materials demonstrate significant electrochemical reactivity, both toward common solvents and electrolytes,^{6,7} as well as toward solid state redox reactions within the material itself and with the metal contacts present in full solar devices.^{8,9} While this instability toward external forces can be somewhat mitigated by the use of encapsulation similar to that used in commercial Si photovoltaic panels,¹⁰ such techniques would prove challenging to implement for perovskite devices on flexible substrates and may do little to address the electrochemical reactivity of perovskites, leading researchers to probe alternative methods of improving stability.¹¹ Ultimately, the fundamental chemical instability of these materials must be addressed in order to maximize their viability as a photovoltaic material.

Recent work within the field has focused on Ruddlesden-Popper (RP) phase quasi-2D perovskites, based on well-known oxide perovskites of a similar crystal

¹ This work was previously published: Wygant, B.R., Ye, A.Z., Dolocan, A., Vu, Q., Abbot, D.M., Mullins, C.B. Probing the Degradation Chemistry and Enhanced Stability of 2D Organolead Halide Perovskites, *J. Am. Chem. Soc.*, **2019**, *141*, 18170-18181. The author of the dissertation was responsible for the design, execution, and interpretation of all experiments.

structure.¹² These materials possess a variety of interesting photophysical properties, and have been explored for use in both photovoltaics^{12,13} and light emitting diodes.^{14,15} Organolead halide RP perovskites possess an $A'_2(A_{n-1}B_nX_{3n+1})$ stoichiometry, with quasi-2D layers of an ABX_3 perovskite separated by a double layer of an amphiphilic A' cation (**Figure 3.1a**). Here, n represents the number of adjacent PbI_6^{4-} in each sheet of perovskite material, thus RP perovskite phases of different thickness can be labeled using their n -phase. Quantum confinement in the layers leads to an inverse proportionality between n and the corresponding electronic bandgap, ranging from 2.35 eV for $n = 1$ and 1.91 eV for $n = 4$ to the band gap of 1.5 eV observed in MAPI, making them robust optoelectronically-tunable systems.¹⁶

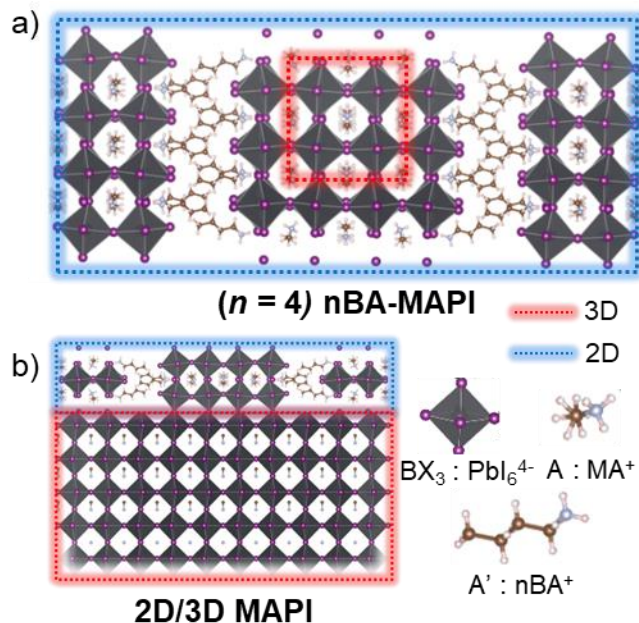


Figure 3.1: a) Crystal structure of an $n = 4$ nBA-MAPI perovskite (blue), with sheets composed of 3D MAPI perovskite (red) separated by A' n -butylammonium ions. b) Graphical representation of proposed 2D/3D MAPI structure, where a thin layer of nBA-MAPI is coated on the surface of the 3D MAPI.

More interestingly, a member of this class of materials, *n*-butylammonium methylammonium lead iodide (nBA-MAPI), has been shown to be considerably more stable than traditional MAPI under exposure to both light and humidity, even when unencapsulated.¹⁷ Similarly superior stability has since been further observed, and while a variety of explanations for the superior stability of these materials have been proposed,^{18–}²¹ the exact mechanism responsible for the stability of these unique materials has not been well-identified. This uncertainty is due, in part, to the general research on bare perovskite films aimed at developing the proposed mechanisms; while such films present much simpler, more idealized samples, compatible with analytic techniques such as x-ray diffraction, and contact angle goniometry,²² full perovskite devices are significantly more complicated systems. Important chemical degradation processes could occur at any of the layers or interfaces within the device, buried beyond the reach of many analytical techniques.

To bridge the gap between films and devices, we use time-of-flight secondary ion mass spectrometry (ToF-SIMS) depth profiling to identify, locate, and quantify relative amounts of various chemical species of interest, providing an unprecedented window into how such perovskite devices degrade.^{23–28} In combination with photoluminescence spectroscopy (PL), X-ray diffraction spectroscopy (XRD), and cyclic voltammetry we study the mechanism responsible for the improved moisture resistance of nBA-MAPI devices compared to traditional MAPI devices. Spectroscopic evidence suggests that nBA-MAPI undergoes disproportionation when exposed to humidity, resulting in the formation of new, more thermodynamically-stable nBA-MAPI phases at the film's surface, slowing further degradation; this is further confirmed by ToF-SIMS depth profiling of full device stacks exposed to both H₂O and D₂O, showing the minimal interaction between the 2D perovskite and the hydration layer we find at the

C₆₀/perovskite interface in full devices. Based upon our observations of surface-driven passivation in nBA-MAPI, we created and tested a 2D/3D hybrid perovskite device (**Figure 3.1b**) to show that even a thin layer of the nBA-MAPI on the surface is sufficient to significantly slow the reaction of MAPI films with the water in the hydration layer. Together, our results show that the disproportionation-driven degradation of nBA-MAPI is responsible for the superior stability of these materials in humid environments, and demonstrate that this feature of 2D organolead halide perovskites can be leveraged to improve the stability of existing 3D MAPI devices.

3.2 EXPERIMENTAL

3.2.1 Device and Film Fabrication

MAPI and nBA-MAPI solar devices were constructed using the following protocols. 2x2 cm FTO substrates (TEC15, Hartford Glass) were first etched using a 2M HCl solution (Fisher Scientific, ACS Grade) and zinc powder (Alfa Aesar, 99.9%) to create a 3 mm wide area of glass along one edge. They were then washed in a 1% (m/m) Contrex AP solution using sonication for 15 minutes, before being lightly scrubbed and rinsed to remove grease and other debris. This was followed by 5 minutes of sonication in acetone, followed by 5 minutes of sonication in ethanol, and a final drying with compressed air. Once dry, the substrates were treated in UV/O₃ (BioForce Nanosciences) for 25 minutes to create a hydrophilic surface.

Following ozone treatment, the substrates were coated with PEDOT:PSS (Heraeus). A 1:2 dilution of the polymer in methanol (Fisher Scientific, ACS Grade) was used for spin coating. Two drops of the PEDOT:PSS solution were filtered through a 0.2 micrometer PTFE filter onto the center of the substrate, which was then spun at 4000 rpm

for 40 s, using a 3 second ramp and deceleration. Following coating, the substrates were annealed at 150 °C for 10 minutes before being immediately brought into a glovebox.

All perovskite thin film fabrication was performed in a N₂ glovebox (VAC Atmospheres, O₂/H₂O <5 ppm), and all perovskite solution concentrations are listed versus total lead content. For MAPI, a 0.75M solution composed of PbI₂ (TCI, 99.99%) and methylammonium iodide (GreatCell Solar) in a 3:1 solution of dimethylformamide (DMF, Acros Organics, Extra Dry) and dimethylsulfoxide (DMSO, Acros Organics, Extra Dry) was spin coated onto the prepared substrates using a common antisolvent method. The solution was prepared at least 30 minutes prior to film preparation, and stirred until all components were dissolved. Two drops of the solution were filtered through a 0.2 micrometer PTFE filter onto the substrate and carefully spread to evenly coat the surface. The substrate was then spun at 1000 rpm for 3 seconds, followed by 6000 rpm for 30 seconds with immediate ramps between. At 9 seconds from the start of the process, 100 µL of chlorobenzene (Acros Organics, Extra Dry) was dispensed in one swift motion onto the center of the substrate to remove the primary solvent. Following spin coating, the substrate was heated at 80°C for approximately 30 seconds, before being heated at 110°C for 5 minutes.

For $n=1, 2$, and 4 nBA-MAPI, a 0.5M solution of PbI₂, methylammonium iodide, and n -butylammonium iodide (GreatCell Solar) in a solution of pure DMF was prepared at least 30 minutes prior to fabrication. An aliquot (typically <1 mL) was filtered through a 0.2 µm PTFE filter into a 2 mL glass vial, and placed on an 80°C hotplate for at least 5 minutes. At the same time, the prepared substrates were placed on a 110°C hotplate to heat. After both the solution and the substrate were heated, the substrate was quickly placed onto the spincoater and 80 µL of the hot solution was dispensed onto the center of the substrate. The substrate was immediately accelerated to 5000 rpm for 20 seconds, and

within 5 seconds the substrate turned a dark brown color as the solvent evaporated and the perovskite crystallized. The finished film was then removed from the spincoater and allowed to continue cooling.

To create the 2D/3D MAPI substrates, after spending 5 minutes on the 110 °C hotplate, a MAPI substrate was moved directly to the spin coater chuck and rotated at 6000 rpm for 35 seconds. Immediately upon reaching 6000 rpm (< 2 s), 50 μ L of a filtered 5 mM solution of *n*-butylammonium iodide (nBAI) in dry isopropanol (99%, Acros Organics) was dropped onto the substrate. After the substrate stopped spinning, it was then annealed at 110 °C for a further 10 minutes before being allowed to cool.

Films with thicknesses of 40 nm of C₆₀ (MER Corp., 99.9%) and 7 nm of bathocuproine (BCP, Sigma-Aldrich, 99.9%) were thermally evaporated using an AMOD thermal evaporator at a base pressure of approximately 8×10^{-7} torr. The first 10 nm of C₆₀ were deposited at a rate of 0.2 Å/s, while the remaining 30 nm were deposited at 1 Å/s; the 7 nm BCP film was deposited at 0.2 Å/s. Following deposition, the BCP/C₆₀/Perovskite/PEDOT:PSS stack was scratched away with a razor blade from two sides of the device to expose the FTO beneath. A film with a thickness of 125 nm of gold was then deposited through a shadow mask via electron beam evaporation using a Cooke Evaporation System to create the top contacts (0.2 cm²), as well as gold contacts for the FTO bottom contact to reduce unnecessary series resistance. Similarly to the C₆₀, the first 10 nm were deposited at 0.2 Å/s and the remaining 115 nm were deposited at 1 Å/s. The finished devices were then stored in an Ar-filled MBraun glovebox (O₂/H₂O < 0.1 ppm) until testing.

3.2.2 Electrochemical Testing

Device testing was performed using a xenon solar simulator (Oriel) with a 1.5AM-G filter and a CHI 660D potentiostat, and power density was normalized to 1 sun using an optical power meter (Newport 1916-C) equipped with a thermopile sensor (Newport, 818P-020-12). Cyclic voltammograms were measured from 0.2 to -1.2 V at a sweep rate of 150 mV/s, under ambient air at room temperature. A 0.08 cm² mask was used to specify the active surface area of each device. For stability testing, devices were stored in the dark in a sealed container under ambient air holding a saturated solution of KCl with a relative humidity of approximately 78%. For stability measurements, 14 individual devices for each type of perovskite were tested, and the results at each time point averaged.

3.2.3 Physical Characterization

Devices analyzed via ToF-SIMS (ION-TOF) for H₂O exposure were prepared as above, but were not tested to prevent exposure to the intense light. Instead, for each type of perovskite tested, a typical two-cell device was broken in half, and one half of each device was left inside the glovebox while the other half was exposed to the water for the requisite amount of time. After exposure was completed, the device was then brought into the glovebox and loaded with the unexposed half into an inert atmosphere transfer vessel to prevent exposure to the atmosphere while transferring to the ToF-SIMS instrument. The devices were then placed in high vacuum ($\sim 1 \times 10^{-9}$ torr) for 2 weeks to remove any lightly adsorbed water inside the devices. For devices exposed to D₂O, the devices were loaded into the antechamber of the ToF-SIMS instrument through the atmosphere as quickly as possible (<30 seconds of actual air exposure), then pumped down to high vacuum ($< 1 \times 10^{-6}$ torr), transferred to the TOF-SIMS main chamber and

analyzed. After analysis, the devices were placed back in the antechamber and brought to low vacuum (1×10^{-3} torr) before being exposed to pure D₂O vapor at a pressure of approximately 15 torr for 1 hour. Following this hour, the devices were pumped down again to high vacuum ($<1 \times 10^{-7}$ torr) for 2 weeks to remove any remaining lightly adsorbed D₂O.

ToF-SIMS depth profiling in negative polarity was performed using a Bi₃⁺ (30 keV ion energy, 0.8 pA measured sample current) analysis beam to raster scan a 100x100 μm^2 area located within the boundaries of a larger crater (300x300 μm^2) created using a Cs⁺ sputtering beam (500 eV ion energy, ~40 nA measured sample current). Similarly, positive ion mode analysis was conducted using an O₂⁺ sputtering beam (1 keV ion energy, ~41 nA measured sample current), instead of Cs⁺, while maintaining all other sputtering conditions. The pressure inside the analysis chamber was typically below 1.5×10^{-9} torr during analysis.

Photoluminescence was performed on a Horiba Jobin Yvon Fluorolog3 spectrophotometer, using an excitation wavelength of 450 nm and a typical 90° detector geometry, with the film held at 45°. Excitation was performed on both the front (shining directly on the perovskite film) and the back (shining through the glass) of the films. X-ray diffraction was performed on a Rigaku Ultima IV diffractometer in a thin film configuration using a Cu K α X-ray source. Wide angle x-ray scattering was performed on a Xenocs Ganesha small angle scattering instrument fitted with a moveable Dectris 300k detector was used to record wide angle scattering data. The instrument is fitted with a microfocus Cu k-alpha source operated at 50kV and 0.6mA. A manufacturer supplied utility, SAXSGUI, was used to make the corrections and reduced the 2D detector data into intensity vs. scattering angle data. Data was collected from a 0.7 x 12 mm area, using a 1° tilt of the substrate. Scanning electron microscopy (SEM) was performed with an FEI

Quanta 650 ESEM, using an accelerating voltage of 15 kV at a vacuum of approximately 5×10^{-6} torr. TEM cross sections (80 nm thick) were prepared on a FEI Scios DualBeam focused ion beam (FIB) SEM, and imaged on a FEI Talos F200X TEM at 200 kV accelerating voltage. Atomic force microscopy (AFM) was conducted on a Park NX10 atomic force microscope in noncontact mode. The microscope is enclosed in a climate-controlled box allowing a constant 78% RH to be maintained during analysis.

3.3 RESULTS AND DISCUSSION

To investigate what leads to the improved stability of nBA-MAPI devices we first fabricated a batch of planar perovskite devices, using either MAPI or nBA-MAPI, and tested their power conversion efficiency (PCE) using cyclic voltammetry over the course of 2 days under exposure to 78% relative humidity (RH). A detailed description of the devices is available in Appendix A, including average/champion device performance, normalized solar cell metrics, statistical distributions for important metrics, and typical JV plots including a hysteresis index value.²⁹ (**Table A1, Figure A.1-3**). A p-i-n architecture using PEDOT:PSS as the hole transport material and C₆₀ as the electron transport material was chosen due to its applicability toward devices fabricated on flexible substrates, which would be ideal platforms for solar cells fabricated using minimal encapsulation. In **Figure 3.2**, we present the normalized PCE of the devices as a function of exposure time; it is immediately apparent that the nBA-MAPI devices are more stable over the first 48 hours than the MAPI devices. This is in good agreement with previous reports on the relative stability of the two perovskite materials,¹⁹ and indeed, comparison between the devices in the present work and those of Tsai *et al.* shows that the degradation kinetics are very similar in both works and shows that similar reactions are likely taking place (**Figure A.4**). Our nBA-MAPI devices show less than

20% reduction in PCE over an 8-hour period while the MAPI devices show a roughly 80% loss of efficiency over the same time period, demonstrating just how rapidly degradation typically sets in for unprotected perovskite devices. In light of this, we chose to compare devices after 8 hours (dashed line) in a humid environment, allowing us to examine working, but degraded, devices at the same level of exposure.

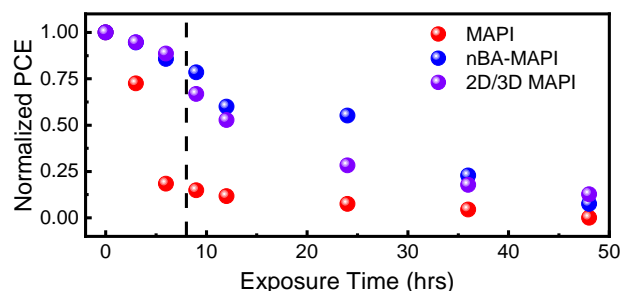


Figure 3.2: Normalized power conversion efficiency (PCE) of MAPI, nBA-MAPI, and 2D/3D MAPI devices following exposure to 78% RH over the course of 48 hours, showing the decrease in PCE for all devices as they degrade.

3.3.1 X-ray Diffraction Spectroscopy

To investigate any structural changes within the bulk of both perovskites after moisture damage, we performed XRD analysis on films of both materials before and after 8 hours of humidity exposure. Out-of-plane XRD spectra of the MAPI and nBA-MAPI films in **Figure A.5** show little change over the course of the experiment, with both materials showing peaks characteristic of either 3D or 2D perovskite, respectively.¹⁹ Further characterization of the orientation of the nBA-MAPI sheets relative to the FTO substrate has also been included in Appendix A, and confirms that the 202 plane on nBA-MAPI is parallel to the substrate (**Figure A.6-A7**). The out-of-plane XRD showed that despite the large differences in electrochemical stability, both materials appear to exhibit similar bulk crystallographic stability at 8 hours of exposure. This discrepancy made it clear that more sensitive analytical techniques than XRD were required to identify the

subtle physical changes the materials undergo during water exposure, and which might be correlated to the electrochemical evolution we observed.

3.3.2 Photoluminescence Spectroscopy

One such technique is PL spectroscopy, which has recently been used to identify the different n -phases present in nBA-MAPI films.^{30,31} Because of its relative surface sensitivity, PL allowed us to see any small changes at the top and bottom surfaces of our films corresponding to material degradation. Our results are presented in **Figure 3.3**, and show that even before they are exposed to humidity, MAPI and nBA-MAPI films exhibit distinct emission spectra. The MAPI film shows a single peak at 1.64 eV on both sides of the film, while the front and back of the nBA-MAPI film have dramatically distinct spectra. On the front, the nBA-MAPI film exhibits a single peak at 1.74 eV with a broad shoulder at higher energies; this slight blue-shift from the pure 3D perovskite is a result of the presence of a “bulk” $n > 5$ that predominates at the surface. Rather than a single peak, the back of the film shows a broad emission with peaks at 2.04, 1.94, and 1.89 eV (identified as the $n = 3, 4$, and 5 peaks of nBA-MAPI, respectively.)^{31–33}

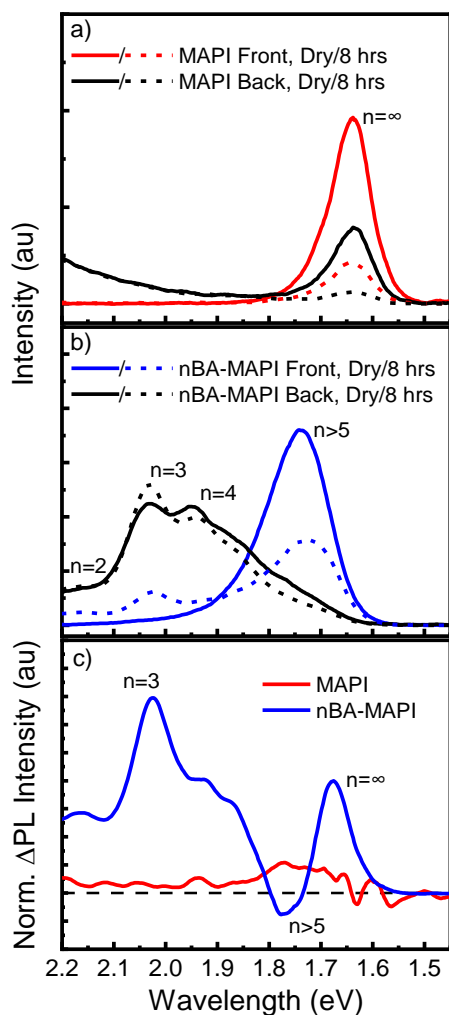
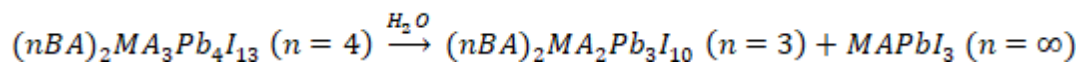


Figure 3.3: Fluorescence spectra for the front and back of a) MAPI and b) nBA-MAPI films, before and after exposure to 78% relative humidity for 8 hours. c) Normalized difference plot for the front-side spectra for both films. nBA-MAPI shows the growth of $n = 3$ and ∞ peaks, as well as the loss of the $n > 5$ peak, while little change visible in the MAPI spectra.

This distribution of different n -phases with film depth in the nBA-MAPI sample was further corroborated using EDX mapping of C and Pb in a cross section of the device (**Figure A.8a**). Moving from the C_{60} interface at the top of the film toward the

PEDOT:PSS, there is an increase in the number of C counts and a concurrent decrease in the Pb counts, which qualitatively agrees with the stoichiometric differences between low- and high- n RP perovskites (**Figure A.8b**) and is similar to previous reports on similar RP perovskite films.¹⁵ While the EDX map is not sufficiently quantitative to definitively correlate a particular C/Pb count ratio to a particular stoichiometry, the overall trend in relative EDX intensity for both elements is suggestive of a layered perovskite structure. Thus, together, both the PL and EDX data confirm that, as-synthesized, our nBA-MAPI films exhibit a layered structure in which low- n phases are found near the FTO while a “bulk” 2D phase is predominant near the surface of the film. We next used PL to study how this unique structure responded to moisture, and how this response differed from MAPI.

Upon exposure to high humidity, both nBA-MAPI and MAPI films exhibit a significant decrease in front-side PL intensity, indicative of crystallographic damage (a decrease of in-plane long range order) from hydration. More interesting, however, is the growth of peaks in the front-side nBA-MAPI spectrum at energies above 1.75 eV, easily visible in the difference plot in **Figure 3.3c**. These peaks correspond with the $n = 2-4$ RP phases initially present on the back of the film, and their appearance in our films after moisture exposure is in agreement with a stabilizing disproportionation mechanism previously observed in oxide RP perovskites following high-temperature synthesis.³⁴ Adapting this mechanism to organolead halide perovskites, a nominally $n = (x)$ nBA-MAPI phase would degrade into one equivalent each of an $n = (x-1)$ nBA-MAPI and a 3D MAPI phase (**Equation 3.1**).



Equation 3.1

Such a mechanism has previously been hypothesized by Stoumpos *et al.*, to explain the appearance of an $n = 3$ nBA-MAPI phase in the synchrotron powder diffraction spectrum of an nBA-MAPI sample,³² but our results provide much clearer evidence of this process. Not only do we observe the growth of the $n = 3$ phase in the PL, the difference plot of nBA-MAPI also clearly shows growth near the $n = \infty$ MAPI peak at 1.64 eV (**Figure 3.3c**), accounting for both disproportionation products. Based on the spectrum collected from the back of the nBA-MAPI film, the minimal change to the $n = 3$ -5 peaks suggests that if disproportionation does occur, such low- n phases may be uniquely resistant to interaction with water. Supporting this observation, PL degradation experiments performed on nominally $n = 1$ and 2 nBA-MAPI films likewise showed considerable stability for these low- n phases (**Figure A.9**). While the $n = 1$ films showed no significant spectral changes, as would be expected for the end product of disproportionation, an $n = 3$ impurity peak on the surface of the $n = 2$ film was observed to decrease in relative intensity following exposure, similar to the way that the high- n peaks decreased in the $n = 4$ nBA-MAPI film shown above. While disproportionation is not the only possible reason for these changes, as differences in the stability of the individual phases could result in the selective degradation of one phase over another, this behavior is strongly suggestive of the process when considered in combination with recent theoretical calculations and other observations described below.

The relative increase and decrease of PL signal from various n -phases in the films, and by extension the disproportionation mechanism, is supported by theoretical calculations performed on a similar perovskite, which substituted phenylethylammonium for n -butylammonium (PEA-MAPI). Quan *et al.* performed density functional theory calculations on a series of n -phases for this PEA-MAPI perovskite, and showed that as the value of n for a RP perovskite decreases, the formation energy of the phase increases,

indicating a more thermodynamically-stable material.²¹ Applied to our nBA-MAPI material, it is clear that the rate of perovskite degradation will slow as the surface begins to disproportionate and forms increasingly stable low- n phases. Potentially aiding this process, the new phases will be more stoichiometrically-rich in hydrophobic nBA, which has been shown to increase the hydrophobicity of the film and reduce interaction of the perovskite with water.¹⁸ The exact extent of this effect will be dependent upon the orientation of the crystals, however, and would be difficult to completely disentangle from the improved thermodynamic stability of these phases. A more thorough discussion of this effect is included in the SI. Through both enhanced thermodynamic stability, and possibly hydrophobicity, these phases will resist further hydration and limit additional damage to the nBA-MAPI film. In contrast, MAPI will not produce these protective layers, and will continue to degrade.

AFM images of the nBA-MAPI film surface before and after degradation further support this disproportionation mechanism by showing that the changes occur on the microscopic scale in addition to the atomic scale (**Figure A.10**). As seen in **Figure A.10a,b**, following exposure to humidity the bare nBA-MAPI film appears to grow 0.1 – 1 micron long, and roughly 100 nm thick, structures at the surface of the otherwise smooth film. These structures appear similar in morphology to previously-reported low- n quasi-2D perovskites crystallites grown on a PbI₂ film from an nBA/MA solution.³³ Here, the authors' showed that the films exhibited a front-side spectrum that was enriched in low- n nBA-MAPI species, and confocal fluorescence microscopy conducted by Li *et al.* further correlated the structures to more intense areas of higher energy fluorescence.

To further bolster the assignment of low- n phases to these new structures on the surface, we also conducted wide-angle X-ray scattering (WAXS) analysis of nBA-MAPI films before and after 8 hours of moisture exposure. The fresh film (**Figure A.11a**) shows

a Bragg diffraction spot pattern indicative of a well-ordered, perpendicularly-oriented nBA-MAPI, in excellent agreement with previously published results, and the spots have been indexed accordingly.^{19,35} Following exposure, the diffraction spot pattern remains, but an additional set of rings appear near $q_y = 0.6 \text{ \AA}^{-1}$, indicating the formation of disordered crystalline phases in the film (**Figure A.11b**); a 1D intensity plot vs two theta (**Figure A.11c**) shows the location of the rings more clearly. Comparing the peak positions to previously published powder diffraction results,¹⁶ we can index these peaks to the $n = 4$ (060) and $n = 2$ (020) reflections for the lower- and higher-two theta peaks, respectively. This result is in agreement with the appearance of both n -phases in the PL spectra in **Figure 3.3a,c**, and further supports these peak assignments. Given the clear formation of small, randomly-oriented platelet-like structures in the AFM image following exposure, we conclude that the ring patterns observed in **Figure A.11b** are the result of these new structures at the surface.

Taken together with our PL and AFM data, the WAXS data appears to show that as the nBA-MAPI undergoes disproportionation, some of the low- n phases produced are segregated into small surface structures, while the rest likely thicken an already disordered layer of such phases on the surface of the film (**Figure A.10c,d**). It is reasonable that such structures could arise as new, crystallographically-distinct low- n phases are segregated from the higher- n phases still remaining in the film in order to minimize entropy in the system. More importantly, such structures would act like quantum wells for photogenerated charge carriers. Electrons produced in the low- n phases near the crystal surfaces would be prevented from undergoing the predicted charge transfer to the bulk $n > 5$ nBA-MAPI film below (**Figure A.10e-g**), a process which normally makes such phases spectrally invisible at steady state PL conditions.^{14,36} A more detailed discussion on these structures is presented in the SI, but it is clear these

structures preserve the evidence for low- n perovskite generation at the surface via disproportionation, further strengthening the case for such a mechanism.

Motivated by this evidence, as well as several reports of interface engineering in organolead halide perovskites,^{18,33,37,38} we also investigated the performance of a MAPI perovskite treated with a dilute nBAI solution to produce an artificial skin of nBA-MAPI on the surface. Such a skin might function in a similar manner to the low- n phases naturally produced by disproportionation, protecting the underlying bulk perovskite. In order to mitigate the effects of the poor carrier transport in low- n RP perovskites²¹ while preserving the protective qualities of the RP phase, we optimized our treatment to create an extremely thin layer (approximately 2.5 nm, see section 3.5) of the 2D perovskite on the surface of the bulk MAPI, which will henceforth be labeled as 2D/3D MAPI.

We used both XRD and PL spectroscopy to study the as-synthesized and degraded 2D/3D MAPI films and prove that we successfully created only a thin layer of nBA-MAPI. XRD (**Figure A.5**) shows no significant changes to the characteristic MAPI spectrum, with only a PbI₂ impurity peak previously observed in $n = 1$ RP perovskite films, indicating the film has been treated.³⁸ Likewise, the PL spectra of the treated films in **Figure A.12a** appear almost identical to those of a pure MAPI film (**Figure 3.3a**) showing a single MAPI PL peak. The only indication of the nBAI treatment is the presence of a weak, broad shoulder extending from the primary peak to roughly 2.1 eV, confirming the presence of a very thin film of $n > 3$ nBA-MAPI on the surface of the treated perovskite. The PL spectrum shows that the shoulder largely disappears after 8 hours (**Figure A.12b**) potentially due to transformation of the nBA-MAPI into thin layers of $n = 1, 2$, and 3 perovskite whose PL is silenced by energy transfer to the underlying 3D MAPI.¹⁴ Simultaneously, the PL intensity of the MAPI peak increases after degradation, possibly due to the production of the bulk MAPI as a product of surface

layer disproportionation, or due to improvements in the crystallinity of the underlying MAPI via passivation of defects.³⁹ Electrochemically, the long-term stability of the 2D/3D MAPI devices is almost identical to that of the nBA-MAPI devices (**Figure 3**), demonstrating the ability of even a thin layer of RP perovskite to improve resistance to humidity.

3.3.3 ToF-SIMS Device Profiling

The improved electrochemical stability of the 2D/3D MAPI devices shows that even small changes to the materials and interfaces in a full device can have dramatic effects on device performance. While it is relatively easy to probe the effects of such modifications in a bare film using bulk-sensitive techniques like XRD, studying these changes in a full device is complicated by the additional layers that compose a full perovskite solar cell. When using a surface sensitive technique such as PL, for example, the addition of hole- or electron-transport layers to the perovskite can substantially reduce PL intensity, dramatically affecting the measurement.⁴⁰ Worse still, examining the chemical changes associated with degradation using a technique like X-ray photoelectron spectroscopy (XPS) is completely impossible in a full stack, a direct result of depth of the buried interfaces where this damage occurs. XPS has a shallow intrinsic depth of information (~10 nm),^{27,28} which is too small to reach the buried interfaces from the surface yet large enough to miss most of these interfaces when combined with depth profiling, making these interfaces effectively invisible. If depth profiling is used with XPS, it frequently results in the breakdown of molecules within the sample following sputtering with the ion beam, breaking chemical bonds and reducing XPS analysis to the detection of single elements rather than compounds. Thus, while chemical changes in the device caused by the hydration of the perovskite layer undoubtedly play a significant role

in how the electrochemical performance of the devices evolves with time, the nature of the device stack locks this valuable information away. Furthermore, as previously discussed, the fundamental differences between film and device samples make comparison and correlation of the two sample types difficult at best, and dubious at worst. In an effort to circumvent these limitations, and explore the chemistry of degradation in more detail, we employ a highly surface, depth, and elemental sensitive technique, TOF-SIMS, to study the chemical composition of our MAPI and nBA-MAPI devices as a function of depth, both in a pristine state and following moisture exposure.

To begin our analysis, we first sputtered through our device stacks and generated full depth profiles of pristine MAPI, nBA-MAPI, and 2D/3D MAPI devices, all acquired in negative polarity (**Figure 34**). Specific secondary ion fragments of interest were selected to represent the device layers, such as Au_4^- for Au in green, and $^{34}\text{S}^-$ for PEDOT:PSS in blue; these fragments were normalized to the maximum signal of each species, allowing us to build a full cross-sectional chemical profile of the device. For comparison, **Figure 3.4a** shows a cross-sectional TEM image of a full nBA-MAPI device stack with the various layers marked in the same colors as those used in the SIMS depth profiles in **Figure 3.4b**, demonstrating the ability of the ToF-SIMS to build an accurate picture of the various materials present.

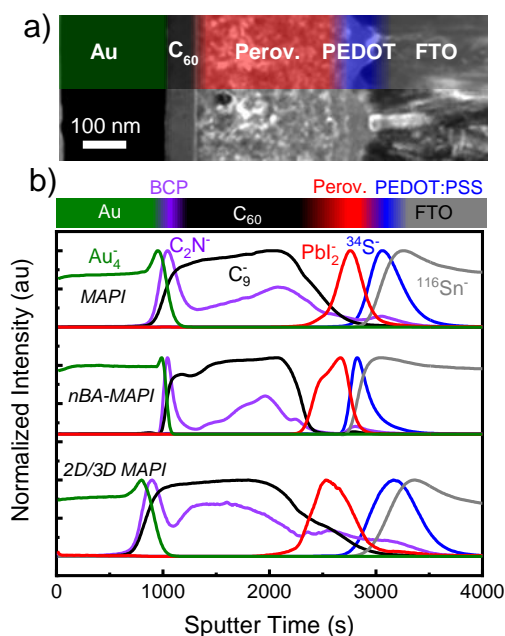


Figure 3.4: a) Cross sectional TEM image of a typical nBA-MAPI device with layers labeled. b) Full negative-mode ToF-SIMS depth profiles for fresh MAPI (top), nBA-MAPI (middle) and 2D/3D MAPI (bottom) devices with characteristic species chosen to represent different layers and color-coded to the bar at top.

The full depth profiles for the different perovskite devices show good agreement for all species, including a broad C_2N^- feature, buried deeper than the narrow peak representing BCP at the Au/ C_{60} interface, which extends through the bulk of the C_{60} layer in all three devices. This feature is likely due to various native contaminant species within the C_{60} layer, but near the C_{60} /perovskite interface it could also contain smaller C_2N^- peaks indicative of perovskite degradation products resulting from the breakdown or reaction of the methylammonium ion, methylamine gas, or other species released as perovskite degrades.⁵ In an attempt to mitigate the broadness of this feature and resolve any hidden peaks within it, we fabricated MAPI and nBA-MAPI devices with a much thicker, 200 nm-thick, C_{60} layer (**Figure A.13**). This thicker layer successfully resolved

the broad C_2N^- feature into three separate C_2N^- peaks, including one near the C_{60} /perovskite interface that could be important for understanding device damage (**Figure A.14**), but did not significantly affect the rate of device degradation under humid environments (**Figure A.13b**). Therefore, we used these thicker- C_{60} devices to study the degradation chemistry of the nBA-MAPI and MAPI devices in greater detail, and then used what we learned to interpret the chemical results from the 50 nm C_{60} 2D/3D MAPI devices.

3.3.4 C_{60} /Perovskite Interface Studies

Based on the changes visible in the surface PL spectra and AFM images of the nBA-MAPI films, and the beneficial effects of the nBAI treatment on the 2D/3D MAPI devices, we focused primarily on the C_{60} /perovskite interface in the depth profiles as opposed to the lower perovskite PEDOT:PSS interface. A brief discussion in the SI provides additional commentary on this point. At the surface interface, we examined secondary ions that were Pb-based, or which contained N- and H-containing moieties, all of which could be indicative of the products of MAPI hydrolysis.⁵ Of equal importance, we also studied the OH^- depth profiles to determine if hydration occurs at this interface in full device stacks, and how this hydration changes with humidity exposure. Because the high vacuum conditions of the ToF-SIMS measurement should remove any adsorbed water species prior to analysis, without causing damage to the perovskite itself,⁴¹ we expect that all OH^- observed in the films should be produced only by hydrated species in the film where water is chemically bound, such as MAPI hydrates.⁵ **Figure 3.5a** clearly shows the presence of an OH^- peak near the MAPI interface, both before and after exposure to elevated humidity. This peak is present in all three perovskites studied (**Figure A.15**), leading us to conclude that this feature represents a hydration layer

(defined as the FWHM of the OH^- peak at the C_{60} /perovskite interface after exposure and demarcated in blue) common to all perovskite devices with broad implications in device degradation.

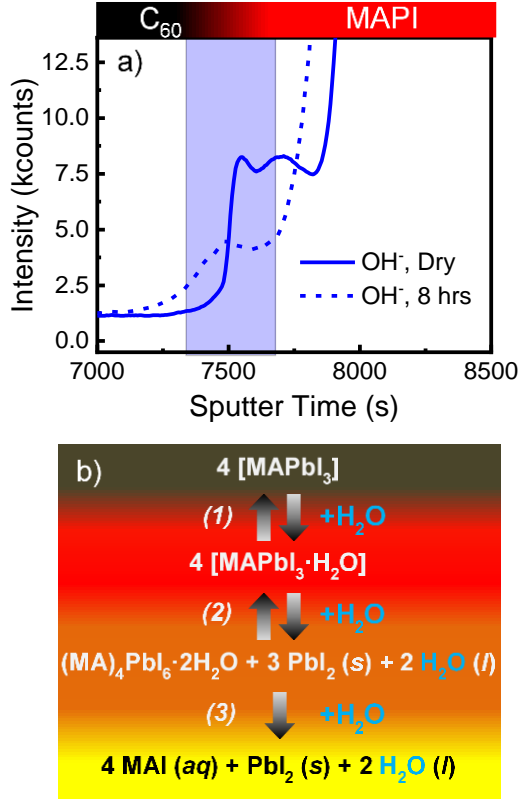


Figure 3.5: a) ToF-SIMS depth profile of OH^- before and after exposure to humidity. The peak at the hydration region in blue shifts slightly and decreases in intensity, indicating a loss of hydrated water b) proposed degradation scheme for MAPI with three separate hydration steps. Steps 2 and 3 produce liquid water, which could then be removed via vacuum, producing the decrease observed in a).

To account for the formation of this hydration layer, we propose that, upon exposure, water from the environment migrates through the relatively porous C_{60} layer of a generic MAPI device until it reaches the less-permeable perovskite layer. The water

then collects at the interface and begins to interact with the perovskite, inducing degradation at the surface and creating the hydration layer we observe in the depth profiles. Given this proposed mechanism, one would expect that the area or intensity of the OH^- peak would increase with exposure time as more hydrated species form in the region. Such an increase is observed in the nBA-MAPI and 2D/3D MAPI samples, but examination of the MAPI profile shows an anomalous decrease in peak intensity following exposure. This discrepancy can be explained by looking to the work of Leguy *et al.*, who studied the hydration of MAPI and found it proceeds *via* a two-step process in which the first step is easily reversible while the second step is not.⁵ We summarize this process in **Figure 3.5b**, and note that the final degradation steps produce liquid water as a product. Under normal conditions, this water would be free to interact with the film and continue the hydration process, but under the high vacuum conditions of the ToF-SIMS analysis chamber this water would be removed as water vapor. This removal would appear as a decrease in the total quantity of MAPI hydrate present at the interface, in agreement with **Figure 3.5a**. Additionally, if the OH^- peaks at the interface represent distinct hydrated species, then such a process could also explain the transformation of the double peak we observe prior to hydration to a single peak after 8 hours. Prior to exposure, the two peaks likely represent two discrete hydrate phases, while following exposure, it is reasonable that the di-hydrate perovskite would be more abundant, thus we observe only a single peak.

3.3.5 Inorganic Profile Analysis

With the identification of the hydration region in our perovskite devices, we were able to focus our interest at the interface more tightly and probe the inorganic and organic perovskite components in the area in more detail. Looking at the area around the

hydration regions in Figure 2.6a-c, we observe that the C₉⁻ (C₆₀) profile does not change significantly following exposure for any of the devices, as would be expected given the chemically-inert nature of C₆₀. On the other hand, the PbI₂⁻ profile, representative of the perovskite, does change at least slightly in all devices following moisture exposure, and this change is most apparent in the MAPI device profile.

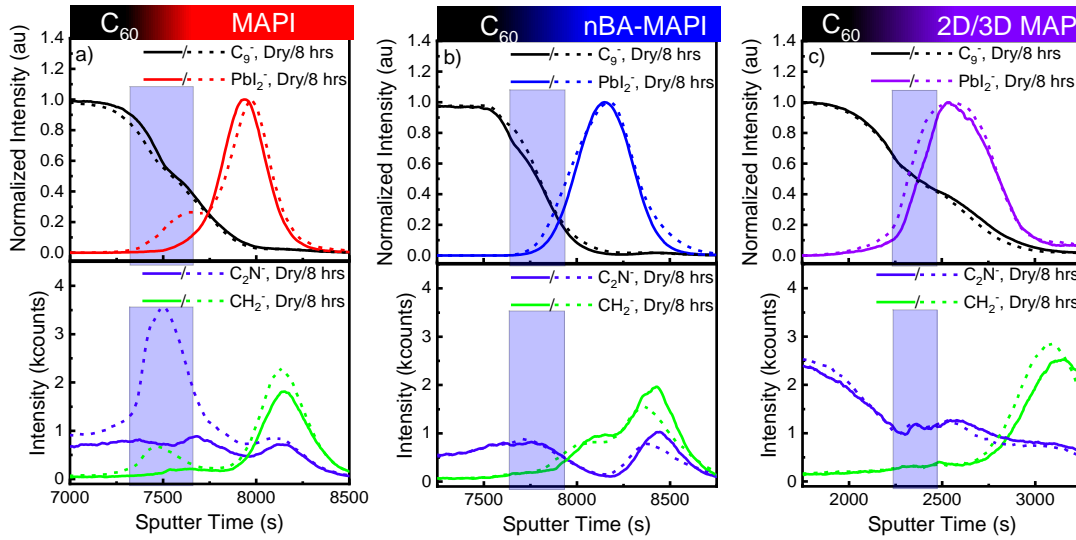


Figure 3.6: Negative-mode ToF-SIMS depth profiles of (a) MAPI, (b) nBA-MAPI, and (c) 2D/3D MAPI devices, before and after exposure to humidity, near the C₆₀/perovskite interface; the blue box represents the hydration region in each device. The top profiles show the changes to the C₆₀ (C₉⁻) and perovskite (PbI₂⁻) with exposure; nBA-MAPI and 2D/3D MAPI show little change, while MAPI shows the formation of a new peak in the hydration region. The bottom profiles show changes to N- and H-containing organic species (C₂N⁻ and CH₂⁻, respectively). A clear peak in both ions is visible at 7500 s, within the hydration region in (a), while neither nBA-MAPI nor 2D/3D MAPI show any increase in these species. Such species are indicative of the formation of degraded hydrated MAPI species.

Immediately evident in **Figure 3.6a** is the growth of a PbI₂⁻ shoulder in the hydration region, which may be the product of perovskite degradation into a hydrated

form or non-perovskite PbI_2 , as previously explored in work by Kamat and others.^{5,22,42} Additionally, the un-normalized PbI_2^- profile (**Figure A.15a**) shows that the overall intensity of the peak decreases dramatically with exposure, further indicating significant damage to the perovskite with hydration. In contrast, neither the nBA-MAPI nor the 2D/3D MAPI show the formation of a shoulder in the hydration region (**Figure 3.6b,c**), or a significant loss of peak intensity (**Figure A.15b,c**). Both devices do exhibit a slight increase in FWHM, which could be attributed to the formation of the low- n phases with degradation, and indeed, both materials display nearly the same degree of change in FWHM at the C_{60} interface. For the nBA-MAPI device, some of this broadening may be due to the formation of the small crystallites visible in the AFM of the bare film, but there is currently no evidence which can confirm or deny the existence of these structures in a full device. Regardless, these results lead us to conclude that the presence of the thin nBA-MAPI phases on the surface, whether natural or artificial, govern the rate of perovskite degradation in these materials.

We previously confirmed the presence of these layers at the surface in both nBA-MAPI and 2D/3D MAPI using PL, but ToF-SIMS can help further confirm this for the 2D/3D MAPI. The analysis of positive secondary ion fragments from full devices (**Figure A.16**) shows that there is more than 4 times the $\text{C}_4\text{NH}_{12}^+$ present in the 2D/3D MAPI material than is present in the MAPI. Furthermore, the profile of this $\text{C}_4\text{NH}_{12}^+$ peak is asymmetric toward the C_{60} /perovskite interface (**Figure A.16b**), in agreement with a top-down treatment of the film to produce the layer, and this asymmetry grows with exposure, indicating the formation of an nBA-rich phase at the interface over time. Finally, ToF-SIMS analysis of a bare 2D/3D MAPI film shows that there is a sharp peak in the $\text{C}_4\text{NH}_{12}^+$ species at the very surface of the film, and comparison to a cross sectional SEM image allows us to calculate that the 2D surface layer is roughly 2.5 nm thick, with

some penetration of the nBA^+ into the bulk of the film (**Figure A.17**). This penetration likely occurs along grain boundaries in the film, as has been previously reported.³⁸ Taken together with the PL spectroscopy, this provides clear evidence for a surface-specific layer of nBA-MAPI in the 2D/3D MAPI which behaves chemically similar to pure nBA-MAPI.

3.3.6 Organic Profile Analysis

From the degradation mechanism provided in **Figure 3.5b**, it is clear that perovskite hydration should also yield a variety of organic species with H- and N-containing moieties resulting from the methylammonium iodide produced. Examining the ToF-SIMS depth profiles near the hydration region of our devices, we do in fact see such species are present in the exposed MAPI device. Using C_2N^- (N-containing) and CH_2^- (H-containing) as representative examples for these moieties, **Figure 3.6a** shows a sharp peak in both species following degradation that corresponds directly to the location of the hydration layer in this device; this strongly suggests a direct relationship between hydration and the liberation of these organic species. Further strengthening this relationship is the location of the peak above that of the PbI_2^- shoulder also produced by moisture exposure. The solvated organics should be more mobile than the insoluble inorganics, and would therefore migrate more readily to the C_{60} interface. Thus, as the hydration process proceeds, the C_{60} /perovskite interface slowly degrades and device performance is lost through some combination of structural reorganization and increased charge transfer resistance, with the latter due to the formation of less conductive hydrated MAPI and PbI_2 species.⁵ The end result is the eventual death of the solar device when the degradation layer becomes too thick, even though the bulk of the film may appear relatively undamaged using bulk techniques like XRD. In contrast, neither the nBA-

MAPI nor the 2D/3D MAPI show any significant change to N- or H-containing species in the hydration region following exposure, indicating that neither perovskite interacted significantly with the moisture in the hydration layer. Given their electrochemical stability at the same exposure level, this is strong evidence of the direct correlation between chemical and electrochemical perovskite stability in these devices.

3.3.7 Isotope Studies

To further confirm that the disproportionation observed in the PL spectrum of the films and the minimal changes in the hydration region of the full devices do correspond to the decreased interaction between the nBA-MAPI and water, we performed isotopic studies with D₂O vapor, using the ToF-SIMS to track the extent of water damage in the device. As described in the Experimental section, MAPI and nBA-MAPI devices were exposed to an environment nearly saturated with D₂O vapor at room temperature for 1 hour to simulate a longer exposure in a more moderately-humid environment. Then, without removing the devices from the ToF-SIMS instrument, they were analyzed using both positive and negative polarity ToF-SIMS depth profiling to better understand how water infiltrates these devices.

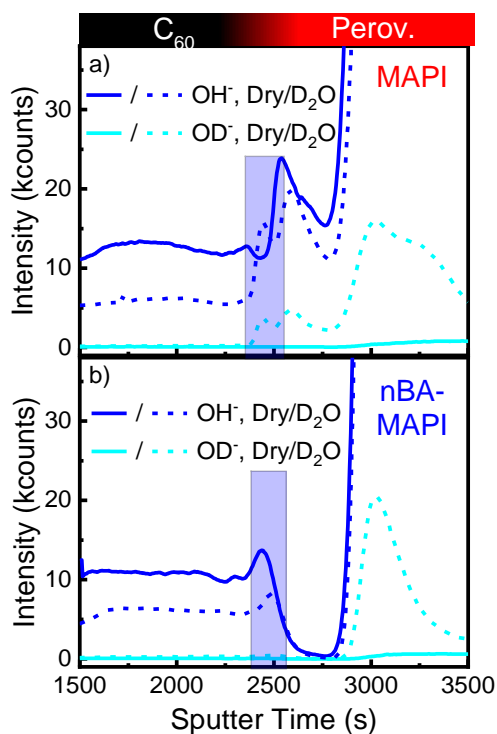


Figure 3.7: ToF-SIMS depth profiles of OH^- and OD^- before and after exposure to D_2O vapor in (a) MAPI and (b) nBA-MAPI devices near the C_{60} /Perovskite interface. MAPI (a) exhibits the formation of an OD^- hydration feature (blue box) after exposure, while nBA-MAPI (b) does not. The OD^- peak in (a) is due to the formation of hydrated species at the perovskite surface which have formed during reaction with the D_2O vapor, remaining stable under vacuum.

Similar to the devices exposed to normal humidity, these D_2O -exposed devices show a clear hydration region at the C_{60} /perovskite interface. Importantly, isotopic analysis of the depth profiles for OD^- (the deuterated analogue of OH^-) shows a peak concomitant with the OH^- peak which confirms that the hydration layer is the result of water diffusion to the perovskite interface from the environment, rather than some intracellular source. In **Figure 3.7a**, there is a clear increase in both OH^- and OD^- in the

hydration region of the MAPI device, making it clear that not only has D₂O diffused through the MAPI device to this interface, but that a significant portion of it has reacted with the perovskite during the exposure to form a deuterated-hydration layer. Because of the shorter exposure time, we do not expect to see the same water-loss from this region as in the devices exposed to normal humidity. We can also confirm that hydration has occurred by observing the growth of organic fragments in the hydration region, as were previously observed in H₂O-exposed devices (**Figure A.18a**). While neither the OD⁻ hydration layer nor the organic fragments are found in the nBA-MAPI device (**Figure 3.7b, A.18b**), further evidence of its low reactivity, the organic components in the perovskite do offer another way to study how water interacts with the material.

Amine groups, such as those present in both methylammonium and *n*-butylammonium, can undergo proton exchange with water, producing deuterated-derivatives of the molecules if exchanged with D₂O. During this process, as shown by Zare and coworkers, the rate of H/D exchange slows considerably as the number of D in the amine group increases.⁴³ Therefore, one can conclude that in order to observe heavily-deuterated amine moieties, the material must be exposed to a deuterium source for an extended period of time, allowing the slower exchange reactions to occur. This means that more highly deuterated methylammonium species (CNH₄D₂⁺ and CNH₃D₃⁺) will be formed from methylammonium which has been exposed to D₂O vapor for longer, and so finding these species deeper in the film would indicate that D₂O vapor penetrated the film more readily and had sufficient time to undergo H/D exchange. Organic species like these derivatives can be easily identified and tracked by switching the ToF-SIMS to positive polarity, and this allows us to study the extent of water interaction as a function of depth in both perovskites with high sensitivity.

To do so, we studied the depth profiles of a series of deuterated-methylammonium derivatives, $\text{CNH}_{6-x}\text{D}_x^+$ ($x \leq 3$), for both the MAPI and the nBA-MAPI devices (**Figure 3.8a,b**). As expected, the total intensity of each derivative decreases as the degree of deuteration increases due to slower reaction rates (**Figure 3.8c**), and the triply-deuterated methylammonium (D3) is the least prevalent derivative in both devices. It is also possible for *n*-butylammonium to undergo this exchange, and similar results are observed for this species as well (**Figure A.19**). Then, taking the peak of the PbI^+ in both perovskites as the center of the film, we plotted the total yield of each derivative as a function of the distance of its peak center from that of the perovskite layer (**Figure 3.8d**). Doing so allows us to both quantify the extent of reaction in terms of both chemical interaction and total penetration.

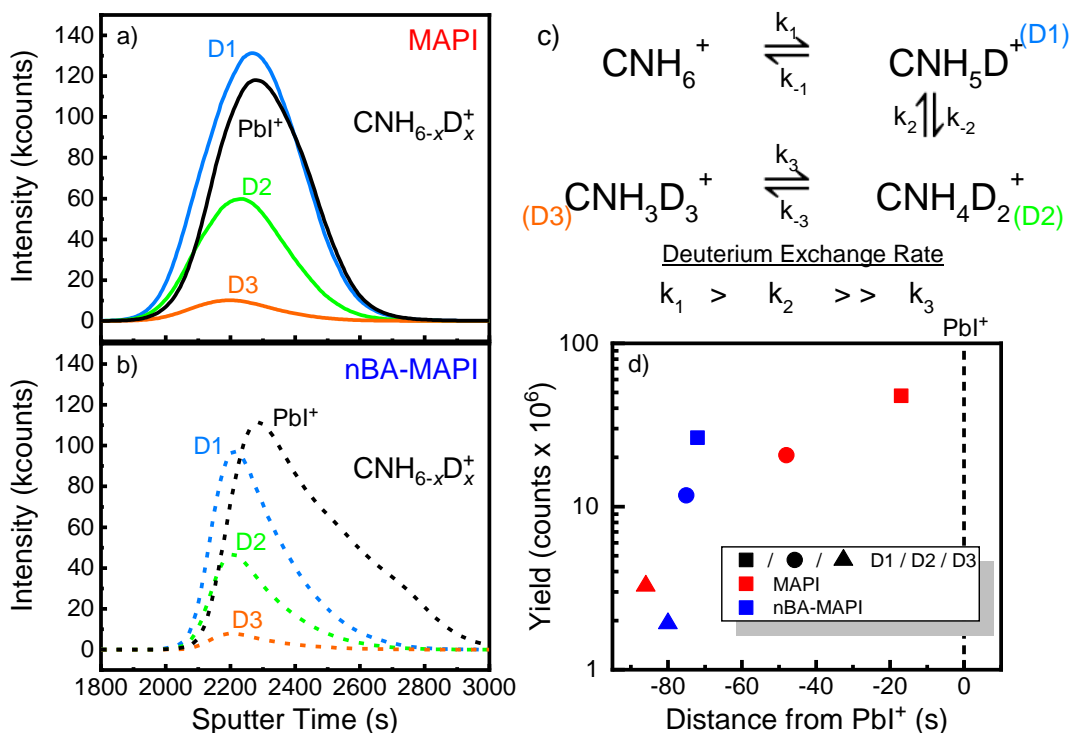


Figure 3.8: Deuterated methylammonium derivatives (D = 1-3, i.e. D1 = CNH₅D⁺) and PbI⁺ for (a) MAPI and (b) nBA-MAPI devices exposed to D₂O vapor for 1 hour. The total ion counts, and therefore abundance, of the derivatives decreases as the level of deuteration increases. c) Simple exchange pathway for the deuteration of methylammonium species; the rate of the H/D exchange reaction slows with the extent of deuteration, therefore high concentrations of D2 and D3 require longer exposure times. d) Total integrated yield of the deuterated methylammonium derivatives for both MAPI and nBA-MAPI devices, plotted as a function of the distance of each derivative's peak from the PbI⁺ peak (t = 0). D₂O penetrates the MAPI film more readily than the nBA-MAPI film resulting in more H/D exchange, as indicated by higher derivative yields at decreased distance from the center of the perovskite layer. The low degree of water penetration through the nBA-MAPI film is further evidence of the material's superior water stability.

It is immediately apparent from **Figure 3.8d** that the surfaces of both perovskites are interacting with the hydration layer we identified in our devices. Importantly, all three deuterated-derivatives show higher yields in MAPI than in nBA-MAPI, clear evidence of the higher water reactivity of the 3D perovskite, and both the D1 and D2 species are found significantly closer (4 and 1.5 times, respectively) to the center of the perovskite in the MAPI device than the nBA-MAPI device. While the D3 species in nBA-MAPI is located slightly closer to the film center than in MAPI, this is likely due to the methylammonium diffusion previously observed in **Figure 3.6a** creating a broader interface in the MAPI device than in the nBA-MAPI device. Taken together, the low degree of water penetration and decreased water reactivity provide further evidence of increased water resistance for quasi-2D perovskites, in good agreement with the disproportionation-based stabilization mechanism suggested previously.

3.3.8 Mechanism of nBA-MAPI Degradation

Together our electrochemical, spectroscopic, and ToF-SIMS results show that MAPI and nBA-MAPI do not share the same degradation pathway, but instead interact with humidity via two distinct mechanisms: a hydration-driven mechanism for MAPI and a disproportionation-driven mechanism for nBA-MAPI. It is this difference in the degradation mechanism that explains the improved stability of nBA-MAPI devices towards humidity. Previous reports indicate that the penetration of water into the MAPI film we observe would result in hydration damage and loss of conductivity within the perovskite layer itself, while the PbI_2 or MAPI hydrates visible at the C_{60} /perovskite interface would inhibit charge transfer to the C_{60} layer.^{5,22} Minimization of both effects due to nBA-MAPI disproportionation is therefore likely responsible for the improved stability of these devices. But, it is important to remember that the nBA-MAPI perovskite

is not static and that the disproportionation which stabilizes it can also explain its eventual failure.

Based on the PL spectrum of our nBA-MAPI film, it is possible to create a simplified cross sectional cartoon of the nBA-MAPI device, as seen in **Figure 3.9a**, with a corresponding band structure based on previous reports.¹² If disproportionation were to create perfectly conformal $(n - 1)$ layers from the initial disordered surface, it would be expected that an upward shift in the conduction band of the lower- n phases at the surface of the film would quickly prevent electron transfer from the bulk to the C₆₀ (**Figure 3.9b**). This does not happen, however, and we hypothesize that this is due to the simultaneous production of one equivalent of MAPI with each $(n - 1)$ phase. MAPI has a significantly lower conduction band position than the low- n nBA-MAPI phases, and would act as an intermediate through which photogenerated electrons could be transferred from the bulk perovskite to the C₆₀. Given that this disproportionation process would likely proceed along grain boundaries, similar to water diffusion in MAPI,⁵ we would expect a mixed nBA-MAPI/MAPI layer at the film's surface that would place the MAPI in contact with the bulk perovskite as well as the C₆₀ (**Figure 3.9c**); a similar mechanism would likely occur in the 2D/3D MAPI cells. In any nBA-MAPI device, the degraded layer would gradually increase in thickness, eventually straining the ability of the MAPI to transfer charge from the bulk, reducing photon absorption, and resulting in the observed loss of cell performance. Additionally, the small crystals visible in the AFM image of the bare film will likely also form inside the device, embedded in the growing degradation layer but in most areas not significantly impacting charge transfer to the C₆₀ at the surface until they grow much larger.

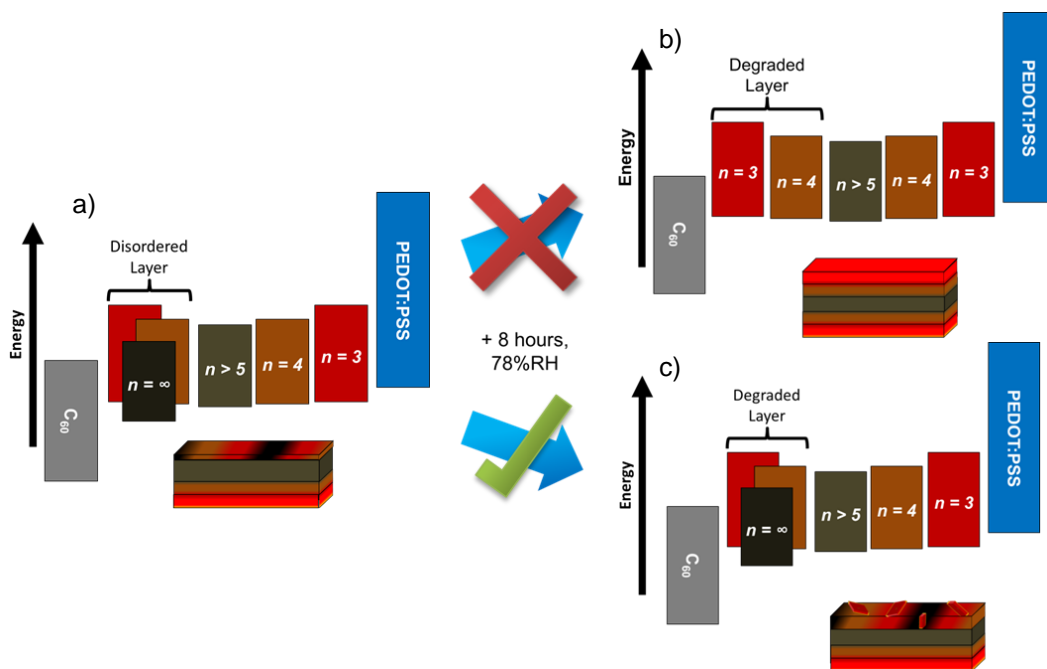


Figure 3.9: a) Possible band schematic for a fresh nBA-MAPI device, shown below, as determined by PL spectroscopy. A thin disordered layer of various low- n species sits atop a mostly $n > 5$ layer near the film surface, closest to the C_{60} , while high concentrations of the lower n phases rest atop the PEDOT:PSS layer; this allows for both hole and electron transport from the perovskite to the device. b) Proposed band schematic and device cross section assuming disproportionation creates conformal low- n layers from the C_{60} interface downward toward the bulk. These layers would inhibit electron transfer to the C_{60} , and therefore is not expected to occur. c) Proposed band schematic and device cross section assuming disproportionation thickens the mixed layer of low- n and MAPI layers at the surface. The presence of the MAPI would allow electrons to be transferred from the bulk nBA-MAPI to the C_{60} , even with the presence of the low- n nBA-MAPI. Some low- n structures may segregate from the film as degradation proceeds.

Normalized V_{oc} plots for both nBA-MAPI and 2D/3D MAPI in **Figure A.1a** support the proposed growth of a low- n degradation layer at the surface of these perovskites. Devices made using both materials show a 25% V_{oc} increase after exposure to moisture, which can be explained by the accumulation of carriers in the various n -

phases in **Figure 3.9c** prior to transfer to the interstitial MAPI. Low carrier mobility has previously been observed in low- n perovskites, and accounts for the increased open circuit voltage of the devices following exposure.²¹ Additionally, inhomogeneous disproportionation of the perovskite surface into a mixture of n -phases would allow the device to function even if some areas underwent more extensive degradation.¹⁴ Further high resolution studies of the degraded surfaces will be necessary to determine the spatial and chemical distribution of different n -phases in this surface interface layer, and to explore the growth of segregated low- n crystals there.

3.4 CONCLUSIONS

Using a combination of electrochemistry, fluorescence spectroscopy, and secondary ion mass spectrometry we have carefully probed the stability and chemistry of traditional MAPI, quasi-2D nBA-MAPI, and composite 2D/3D MAPI perovskite solar devices. After just 8 hours of exposure to a high humidity environment, we found that the performance of the pure MAPI devices decreased significantly, while both the nBA-MAPI and the 2D/3D MAPI devices exhibited stable performance over a much longer period of time. By analyzing both bare films and full devices, we discovered that the improved stability of the nBA-MAPI devices is a result of a unique disproportionation mechanism that produces a protective layer of quasi-2D nBA-MAPI at the surface of the film. This layer reduces the interaction of the bulk perovskite film with a newly-identified hydration layer located at the C_{60} /perovskite interface of full perovskite devices, slowing the damaging hydration process and therefore extending device lifetime. Furthermore, the 2D/3D MAPI devices confirmed that even a thin layer of nBA-MAPI on the surface of a perovskite will grant this protection to bulk 3D perovskites with minimal modifications.

In total, it is clear that the unique properties possessed by these quasi-2D materials make them an exciting material for use in stabilizing perovskite solar cells.

3.5 REFERENCES

- (1) Kim, H.-S.; Lee, C.-R.; Im, J.-H.; Lee, K.-B.; Moehl, T.; Marchioro, A.; Moon, S.-J.; Humphry-Baker, R.; Yum, J.-H.; Moser, J. E.; et al. Lead Iodide Perovskite Sensitized All-Solid-State Submicron Thin Film Mesoscopic Solar Cell with Efficiency Exceeding 9%. *Sci. Rep.* **2012**, *2*, 1–7. <https://doi.org/10.1038/srep00591>.
- (2) NREL. Best Research-Cell Efficiencies <https://www.nrel.gov/pv/assets/pdfs/pv-efficiency-chart.20181221.pdf>.
- (3) Bryant, D.; Aristidou, N.; Pont, S.; Sanchez-molina, I.; Chotchunangatchaval, T.; Wheeler, S.; Durrant, R.; Haque, S. A. Environmental Science Light and Oxygen Induced Degradation Limits the Operational Stability of Methylammonium Lead Triiodide Perovskite Solar Cells †. *Energy Environ. Sci.* **2016**, *9*, 1655–1660. <https://doi.org/10.1039/C6EE00409A>.
- (4) Shirayama, M.; Kato, M.; Miyadera, T.; Sugita, T.; Fujiseki, T.; Hara, S.; Kadowaki, H.; Murata, D.; Chikamatsu, M.; Fujiwara, H. Degradation Mechanism of CH₃NH₃PbI₃ Perovskite Materials upon Exposure to Humid Air. *J. Appl. Phys.* **2016**, *119* (11), 115501. <https://doi.org/10.1063/1.4943638>.
- (5) Leguy, A. M. A.; Hu, Y.; Campoy-Quiles, M.; Alonso, M. I.; Weber, O. J.; Azarhoosh, P.; van Schilfgaarde, M.; Weller, M. T.; Bein, T.; Nelson, J.; et al. Reversible Hydration of CH₃NH₃PbI₃ in Films, Single Crystals, and Solar Cells. *Chem. Mater.* **2015**, *27* (9), 3397–3407. <https://doi.org/10.1021/acs.chemmater.5b00660>.
- (6) Samu, G. F.; Scheidt, R. A.; Kamat, P. V.; Janáky, C. Electrochemistry and Spectroelectrochemistry of Lead Halide Perovskite Films: Materials Science Aspects and Boundary Conditions. *Chem. Mater.* **2018**, *30* (3), 561–569. <https://doi.org/10.1021/acs.chemmater.7b04321>.
- (7) Hsu, H. Y.; Ji, L.; Ahn, H. S.; Zhao, J.; Yu, E. T.; Bard, A. J. A Liquid Junction Photoelectrochemical Solar Cell Based on P-Type MeNH₃PbI₃ Perovskite with 1.05 v Open-Circuit Photovoltage. *J. Am. Chem. Soc.* **2015**, *137* (46), 14758–14764. <https://doi.org/10.1021/jacs.5b09758>.
- (8) Zohar, A.; Kedem, N.; Levine, I.; Zohar, D.; Vilan, A.; Ehre, D.; Hodes, G.; Cahen, D. Impedance Spectroscopic Indication for Solid State Electrochemical Reaction in (CH₃NH₃)PbI₃ Films. *J. Phys. Chem. Lett.* **2016**, *7* (1), 191–197. <https://doi.org/10.1021/acs.jpcllett.5b02618>.

- (9) Zhao, L.; Kerner, R. A.; Xiao, Z.; Lin, Y. L.; Lee, K. M.; Schwartz, J.; Rand, B. P. Redox Chemistry Dominates the Degradation and Decomposition of Metal Halide Perovskite Optoelectronic Devices. *ACS Energy Lett.* **2016**, *1* (3), 595–602. <https://doi.org/10.1021/acsenenergylett.6b00320>.
- (10) Bush, K. A.; Palmstrom, A. F.; Yu, Z. J.; Boccard, M.; Cheacharoen, R.; Mailoa, J. P.; McMeekin, D. P.; Hoyer, R. L. Z.; Bailie, C. D.; Leijtens, T.; et al. 23.6%-Efficient Monolithic Perovskite/Silicon Tandem Solar Cells with Improved Stability. *Nat. Energy* **2017**, *2* (4), 17009. <https://doi.org/10.1038/nenergy.2017.9>.
- (11) Kaltenbrunner, M.; Adam, G.; Glowacki, E. D.; Drack, M.; Schwödiauer, R.; Leonat, L.; Apaydin, D. H.; Groiss, H.; Scharber, M. C.; White, M. S.; et al. Flexible High Power-per-Weight Perovskite Solar Cells with Chromium Oxide–Metal Contacts for Improved Stability in Air. *Nat. Mater.* **2015**, *14* (10), 1032–1039. <https://doi.org/10.1038/nmat4388>.
- (12) Cao, D. H.; Stoumpos, C. C.; Farha, O. K.; Hupp, J. T.; Kanatzidis, M. G. 2D Homologous Perovskites as Light-Absorbing Materials for Solar Cell Applications. *J. Am. Chem. Soc.* **2015**, *137* (24), 7843–7850. <https://doi.org/10.1021/jacs.5b03796>.
- (13) Grancini, G.; Roldán-Carmona, C.; Zimmermann, I.; Mosconi, E.; Lee, X.; Martineau, D.; Nabey, S.; Oswald, F.; De Angelis, F.; Graetzel, M.; et al. One-Year Stable Perovskite Solar Cells by 2D/3D Interface Engineering. *Nat. Commun.* **2017**, *8*, 15684. <https://doi.org/10.1038/ncomms15684>.
- (14) Yuan, M.; Quan, L. N.; Comin, R.; Walters, G.; Sabatini, R.; Voznyy, O.; Hoogland, S.; Zhao, Y.; Beauregard, E. M.; Kanjanaboos, P.; et al. Perovskite Energy Funnels for Efficient Light-Emitting Diodes. *Nat. Nanotechnol.* **2016**, *11* (10), 872–877. <https://doi.org/10.1038/nnano.2016.110>.
- (15) Wang, N.; Cheng, L.; Ge, R.; Zhang, S.; Miao, Y.; Zou, W.; Yi, C.; Sun, Y.; Cao, Y.; Yang, R.; et al. Perovskite Light-Emitting Diodes Based on Solution-Processed Self-Organized Multiple Quantum Wells. *Nat. Photonics* **2016**, *10* (11), 699–704. <https://doi.org/10.1038/nphoton.2016.185>.
- (16) Stoumpos, C. C.; Cao, D. H.; Clark, D. J.; Young, J.; Rondinelli, J. M.; Jang, J. I.; Hupp, J. T.; Kanatzidis, M. G. Ruddlesden-Popper Hybrid Lead Iodide Perovskite 2D Homologous Semiconductors. *Chem. Mater.* **2016**, *28* (8), 2852–2867. <https://doi.org/10.1021/acs.chemmater.6b00847>.
- (17) Tsai, H.; Nie, W.; Blancon, J.-C.; Stoumpos, C. C.; Asadpour, R.; Harutyunyan, B.; Neukirch, A. J.; Verduzco, R.; Crochet, J. J.; Tretiak, S.; et al. High-Efficiency Two-Dimensional Ruddlesden–Popper Perovskite Solar Cells. *Nature* **2016**, *536* (7616), 312–316. <https://doi.org/10.1038/nature18306>.
- (18) Koh, T. M.; Shanmugam, V.; Guo, X.; Lim, S. S.; Filonik, O.; Herzig, E. M.; Müller-Buschbaum, P.; Swamy, V.; Chien, S. T.; Mhaisalkar, S. G.; et al.

- Enhancing Moisture Tolerance in Efficient Hybrid 3D/2D Perovskite Photovoltaics. *J. Mater. Chem. A* **2018**, 2122–2128. <https://doi.org/10.1039/C7TA09657G>.
- (19) Tsai, H.; Nie, W.; Blancon, J.-C.; Stoumpos, C. C.; Asadpour, R.; Harutyunyan, B.; Neukirch, A. J.; Verduzco, R.; Crochet, J. J.; Tretiak, S.; et al. High-Efficiency Two-Dimensional Ruddlesden–Popper Perovskite Solar Cells. *Nature* **2016**, 536 (7616), 312–316. <https://doi.org/10.1038/nature18306>.
 - (20) Stoumpos, C. C.; Soe, C. M. M.; Tsai, H.; Nie, W.; Blancon, J. C.; Cao, D. H.; Liu, F.; Traoré, B.; Katan, C.; Even, J.; et al. High Members of the 2D Ruddlesden–Popper Halide Perovskites: Synthesis, Optical Properties, and Solar Cells of (CH₃(CH₂)₃NH₃)₂(CH₃NH₃)₄Pb₅I₁₆. *Chem* **2017**, 2 (3), 427–440. <https://doi.org/10.1016/j.chempr.2017.02.004>.
 - (21) Quan, L. N.; Yuan, M.; Comin, R.; Voznyy, O.; Beauregard, E. M.; Hoogland, S.; Buin, A.; Kirmani, A. R.; Zhao, K.; Amassian, A.; et al. Ligand-Stabilized Reduced-Dimensionality Perovskites. *J. Am. Chem. Soc.* **2016**, 138 (8), 2649–2655. <https://doi.org/10.1021/jacs.5b11740>.
 - (22) Christians, J. A.; Miranda Herrera, P. A.; Kamat, P. V. Transformation of the Excited State and Photovoltaic Efficiency of CH₃NH₃PbI₃ Perovskite upon Controlled Exposure to Humidified Air. *J. Am. Chem. Soc.* **2015**, 137 (4), 1530–1538. <https://doi.org/10.1021/ja511132a>.
 - (23) Lin, W. C.; Chang, H. Y.; Abbasi, K.; Shyue, J. J.; Burda, C. 3D In Situ ToF-SIMS Imaging of Perovskite Films under Controlled Humidity Environmental Conditions. *Adv. Mater. Interfaces* **2017**, 4 (2), 1–9. <https://doi.org/10.1002/admi.201600673>.
 - (24) Zhang, T.; Meng, X.; Bai, Y.; Xiao, S.; Hu, C.; Yang, Y.; Chen, H.; Yang, S. Profiling the Organic Cation-Dependent Degradation of Organolead Halide Perovskite Solar Cells. *J. Mater. Chem. A* **2017**, 5 (3), 1103–1111. <https://doi.org/10.1039/C6TA09687E>.
 - (25) Harvey, S. P.; Li, Z.; Christians, J. A.; Zhu, K.; Luther, J. M.; Berry, J. J. Probing Perovskite Inhomogeneity beyond the Surface: TOF-SIMS Analysis of Halide Perovskite Photovoltaic Devices. *ACS Appl. Mater. Interfaces* **2018**, 10 (34), 28541–28552. <https://doi.org/10.1021/acsami.8b07937>.
 - (26) Akbulatov, A. F.; Frolova, L. A.; Griffin, M. P.; Gearba, I. R.; Dolocan, A.; Vanden Bout, D. A.; Tsarev, S.; Katz, E. A.; Shestakov, A. F.; Stevenson, K. J.; et al. Effect of Electron-Transport Material on Light-Induced Degradation of Inverted Planar Junction Perovskite Solar Cells. *Adv. Energy Mater.* **2017**, 7 (19), 1700476. <https://doi.org/10.1002/aenm.201700476>.

- (27) Chou, H.; Ismach, A.; Ghosh, R.; Ruoff, R. S.; Dolocan, A. Heterostructures at the Atomic Level. *Nat. Commun.* **2015**, *6* (May), 1–7. <https://doi.org/10.1038/ncomms8482>.
- (28) Griffin, M. P.; Gearba, R.; Stevenson, K. J.; Vanden Bout, D. A.; Dolocan, A. Revealing the Chemistry and Morphology of Buried Donor/Acceptor Interfaces in Organic Photovoltaics. *J. Phys. Chem. Lett.* **2017**, *8* (13), 2764–2773. <https://doi.org/10.1021/acs.jpcllett.7b00911>.
- (29) Chen, J.; Lee, D.; Park, N. G. Stabilizing the Ag Electrode and Reducing J-V Hysteresis through Suppression of Iodide Migration in Perovskite Solar Cells. *ACS Appl. Mater. Interfaces* **2017**, *9* (41), 36338–36349. <https://doi.org/10.1021/acsami.7b07595>.
- (30) Liu, J.; Leng, J.; Wu, K.; Zhang, J.; Jin, S. Observation of Internal Photoinduced Electron and Hole Separation in Hybrid Two-Dimensional Perovskite Films. *J. Am. Chem. Soc.* **2017**, *139* (4), 1432–1435. <https://doi.org/10.1021/jacs.6b12581>.
- (31) Zhou, N.; Shen, Y.; Li, L.; Tan, S.; Liu, N.; Zheng, G.; Chen, Q.; Zhou, H. Exploration of Crystallization Kinetics in Quasi Two-Dimensional Perovskite and High Performance Solar Cells. *J. Am. Chem. Soc.* **2018**, *140* (1), 459–465. <https://doi.org/10.1021/jacs.7b11157>.
- (32) Stoumpos, C. C.; Soe, C. M. M.; Tsai, H.; Nie, W.; Blancon, J.-C.; Cao, D. H.; Liu, F.; Traoré, B.; Katan, C.; Even, J.; et al. High Members of the 2D Ruddlesden-Popper Halide Perovskites: Synthesis, Optical Properties, and Solar Cells of $(\text{CH}_3(\text{CH}_2)_3\text{NH}_2)_2(\text{CH}_3\text{NH}_3)_4\text{Pb}_5\text{I}_{16}$. *Chem* **2017**, *2* (3), 427–440. <https://doi.org/10.1016/j.chempr.2017.02.004>.
- (33) Li, L.; Zhou, N.; Chen, Q.; Shang, Q.; Zhang, Q.; Wang, X.; Zhou, H. Unraveling the Growth of Hierarchical Quasi-2D/3D Perovskite and Carrier Dynamics. *J. Phys. Chem. Lett.* **2018**, *9* (5), 1124–1132. <https://doi.org/10.1021/acs.jpcllett.7b03294>.
- (34) Yan, L.; Niu, H. J.; Duong, G. V.; Suchomel, M. R.; Bacsá, J.; Chalker, P. R.; Hadermann, J.; van Tendeloo, G.; Rosseinsky, M. J. Cation Ordering within the Perovskite Block of a Six-Layer Ruddlesden-Popper Oxide from Layer-by-Layer Growth – Artificial Interfaces in Complex Unit Cells. *Chem. Sci.* **2011**, *2* (2), 261–272. <https://doi.org/10.1039/C0SC00482K>.
- (35) Feng, J.; Gong, C.; Gao, H.; Wen, W.; Gong, Y.; Jiang, X.; Zhang, B.; Wu, Y.; Wu, Y.; Fu, H.; et al. Single-Crystalline Layered Metal-Halide Perovskite Nanowires for Ultrasensitive Photodetectors. *Nat. Electron.* **2018**, *1* (7), 404–410. <https://doi.org/10.1038/s41928-018-0101-5>.
- (36) Proppe, A. H.; Quintero-Bermudez, R.; Tan, H.; Voznyy, O.; Kelley, S. O.; Sargent, E. H. Synthetic Control over Quantum Well Width Distribution and

- Carrier Migration in Low-Dimensional Perovskite Photovoltaics. *J. Am. Chem. Soc.* **2018**, *140* (8), 2890–2896. <https://doi.org/10.1021/jacs.7b12551>.
- (37) Wang, J.; Leng, J.; Liu, J.; He, S.; Wang, Y.; Wu, K.; Jin, S. Engineered Directional Charge Flow in Mixed Two-Dimensional Perovskites Enabled by Facile Cation-Exchange. *J. Phys. Chem. C* **2017**, *121* (39), 21281–21289. <https://doi.org/10.1021/acs.jpcc.7b08535>.
- (38) Lin, Y.; Bai, Y.; Fang, Y.; Chen, Z.; Yang, S.; Zheng, X.; Tang, S.; Liu, Y.; Zhao, J.; Huang, J. Enhanced Thermal Stability in Perovskite Solar Cells by Assembling 2D/3D Stacking Structures. *J. Phys. Chem. Lett.* **2018**, *9* (3), 654–658. <https://doi.org/10.1021/acs.jpclett.7b02679>.
- (39) Li, Z.; Chen, Z.; Yang, Y.; Xue, Q.; Yip, H. L.; Cao, Y. Modulation of Recombination Zone Position for Quasi-Two-Dimensional Blue Perovskite Light-Emitting Diodes with Efficiency Exceeding 5%. *Nat. Commun.* **2019**, *10* (1), 1–10. <https://doi.org/10.1038/s41467-019-09011-5>.
- (40) Wei, J.; Li, H.; Zhao, Y.; Zhou, W.; Fu, R.; Leprince-Wang, Y.; Yu, D.; Zhao, Q. Suppressed Hysteresis and Improved Stability in Perovskite Solar Cells with Conductive Organic Network. *Nano Energy* **2016**, *26*, 139–147. <https://doi.org/10.1016/j.nanoen.2016.05.023>.
- (41) Yang, B.; Dyck, O.; Ming, W.; Du, M.; Das, S.; Rouleau, C. M.; Duscher, G.; Geohegan, D. B.; Xiao, K. Observation of Nanoscale Morphological and Structural Degradation in Perovskite Solar Cells by in Situ TEM. *ACS Appl. Mater. Interfaces* **2016**, *8* (47), 32333–32340. <https://doi.org/10.1021/acsami.6b11341>.
- (42) Mosconi, E.; Azpiroz, J. M.; De Angelis, F. Ab Initio Molecular Dynamics Simulations of Methylammonium Lead Iodide Perovskite Degradation by Water. *Chem. Mater.* **2015**, *27* (13), 4885–4892. <https://doi.org/10.1021/acs.chemmater.5b01991>.
- (43) Jansson, E. T.; Lai, Y.; Santiago, J. G.; Zare, R. N. Rapid Hydrogen – Deuterium Exchange in Liquid Droplets. *J. Am. Chem. Soc.* **2017**, *139* (20), 6851–6854. <https://doi.org/10.1021/jacs.7b03541>.

Chapter 4: Moisture-Driven Formation and Growth of Quasi-2D Organolead Halide Perovskite Crystallites

4.1 INTRODUCTION

In recent years, researchers have made a concerted effort to explore novel thin film photovoltaic (PV) materials to augment solar energy production. Of the materials studied, organolead halide perovskites have been among the most promising to date, currently showing lab-scale device efficiencies that are near that of polycrystalline Si devices.¹ The term perovskite is generally used to refer to any crystalline material with a stoichiometric composition of ABX_3 , where A is typically an organic 1+ cation, B is a metallic 2+ cation, and X is a halide. Perovskites demonstrate a remarkable tolerance toward crystalline disorder and chemical impurities, and can be synthesized using a variety of different precursors.² Methylammonium lead triiodide (MAPI) is generally regarded as the archetypical perovskite material, but the most efficient devices to date are typically composed of complex mixtures of different organic and inorganic A-site cations including formamidinium,³ cesium,⁴ guanidinium,⁵ and rubidium,⁶ as well as mixtures of iodide and bromide.⁷ This flexibility allows for careful tuning and optimization of electronic properties like the band gap and the conductivity of the material.³

A relatively recent innovation in the field has been the introduction of Ruddlesden-Popper phase organolead halide perovskites, with a generic stoichiometry of $A'_2A_{n-1}B_nX_{3n+1}$. Here, the A' species is typically an amphiphilic alkylammonium species, such as *n*-butylammonium (nBA), that causes the ABX_3 crystal lattice to segregate into distinct quasi-2D sheets.⁸ These sheets are composed of PbI_6^{4-} octahedra and an A-site cation (**Figure 4.1**), and can range from sheets one octahedron thick to potentially over 7.⁹ Below, we will be using the term *n*-phase to refer to a material containing sheets of

perovskite composed of n adjacent octahedra. While the thin sheets of perovskite cause quantum confinement effects which lead to wider band gaps and less light absorption than more common 3D perovskites,¹⁰ researchers have shown that these materials are considerably more stable when exposed to humidity than the related 3D materials.^{11–14} Thus, these quasi-2D perovskites represent an interesting path to creating perovskite devices that are more resistant to the effects of moisture.

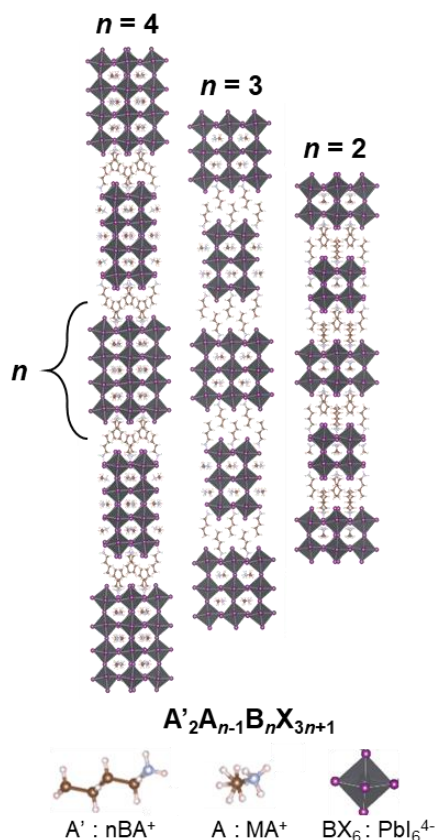


Figure 4.1 Crystal structures of Ruddlesden-Popper phase perovskites sharing a chemical formula of $A'_2A_{n-1}B_nX_{3n+1}$, where $n = 2, 3$, and 4 . Here, A' is n -butylammonium, A is methylammonium, B is Pb, and X is iodide.

Work from our group and others has shown that this moisture resistance stems from a unique disproportionation-based degradation mechanism that helps to create a

passivating layer of low- n ($n=1-3$) species at the surface of a higher- n ($n=4+$) material, inhibiting further degradation.^{11,15} Interestingly, we also observed the previously unreported formation of small crystallites at or near the surface of n -butylammonium methylammonium lead iodide (nBA-MAPI) films, which indirect measurements using wide-angle X-ray scattering (WAXS) suggested were composed of low- n perovskite.¹⁵ While a thin, continuous, and conformal layer of such low- n perovskite is useful as a passivation layer to protect the perovskite from further damage,¹⁶ these crystals are relatively thick, discrete, and oriented perpendicular to the plane of the film. As such they may in fact be deleterious, inducing damage and strain in the surrounding film as they grow and cause undesired changes to the band structure of the perovskite film. Given that these crystals arose simply from the exposure of an nBA-MAPI film to a humid environment, and that such exposure may occur naturally during typical use of perovskite devices, it is important to definitively identify and carefully study these crystals so that we can develop techniques to inhibit their formation.

To that end, we have used a suite of characterization techniques including X-ray diffraction spectroscopy (XRD), WAXS, atomic force microscopy (AFM), photoluminescence spectroscopy (PL), confocal fluorescence microscopy (CFM), and time-of-flight secondary ion mass spectrometry (ToF-SIMS) to study the formation and growth of these crystallites on the surface of an nBA-MAPI film. XRD and WAXS measurements confirm that the fresh films exhibit excellent crystallinity and orientation relative to the substrate, while also showing that a low- n polycrystalline material forms in these films after 48 hours of exposure to 78% relative humidity (RH). This corresponds to a similar increase in low- n and 3D-like species in the PL spectra, and a concurrent decrease in the $n > 5$ phase native to the film surface; together this is evidence of degradation by disproportionation. Likewise, AFM images of an nBA-MAPI film

exposed to humidity over 72 hours show the appearance and growth of platelet-like structures at the surface of the film, which CFM spectra confirm to be composed of low- n phases. Finally, we used a combination of ToF-SIMS and AFM to study the topography of the interiors of both bare nBA-MAPI films and model PV devices exposed to moisture, and discover evidence of these crystallites forming deep within the nBA-MAPI layer of each. Based on these results, we propose a mechanism to describe the crystal growth and perovskite disproportionation which occurs in these films. Altogether, we provide a holistic view of the composition and formation of these crystals that will serve as a foundation for future attempts to mitigate, or even encourage, similar growth in new perovskite materials.

4.2 EXPERIMENTAL

4.2.1 Film Fabrication and Moisture Exposure

The nBA-MAPI films were fabricated using a hot casting method manner similar to our previous procedure.¹⁵ Briefly, solutions of *n*-butylammonium iodide (nBAI, GreatCell Solar), methylammonium iodide (MAI, GreatCell Solar), and PbI₂ (99.99%, Alfa Aesar) in *N,N*-dimethylformamide (DMF, 99% ultra-dry, Acros Organics) were prepared in a N₂-filled glovebox (VAC Atmospheres, H₂O, O₂ < 5 ppm) by stirring for at least 24 hours prior to film fabrication. The solutions were 0.5 M with respect to Pb²⁺ in solution, with a solution stoichiometry of (nBA)₂(MA)₃Pb₄I₁₃. Clean 2x2 cm² F:SnO₂ (FTO) coated glass substrates (TEC15, Harford Glass) were washed in 1% (m/m) Contrex AP solution through sonication for 15 minutes, and then lightly scrubbed and rinsed to remove any grease or debris. This was followed by 5 minutes of sonication in acetone and then 5 minutes more in isopropanol, before being dried with compressed air. After drying, the substrates were brought into the glovebox.

Prior to film deposition, an aliquot (typically 300-800 μL) was filtered through a 0.2 μm PTFE filter into a 2 mL glass vial and heated on a 75°C hotplate for at least 20 minutes. Likewise, FTO substrates were allowed to heat on a 110°C hotplate for at least 20 minutes to ensure thorough heating as part of the hot casting procedure. Following heating, the substrate was rapidly moved to the chuck of a spin coater, where 80 μL of the preheated solution was pipetted onto the center of the film. The substrate was then immediately ramped to 5000 rpm and held for 20 seconds. Within 5 seconds, the substrate turned a dark brown color as the perovskite film crystallized. After spin coating, the film was removed from the chuck and allowed to continue cooling. Films were typically prepared as close to the time of experimentation as possible, and stored out of direct light to inhibit photodegradation. To controllably degrade the films under humid conditions, they were placed in a sealed container containing a saturated solution of KCl in water, which kept the atmosphere inside the container at a relative humidity of 78%, for a pre-determined period of time. After degradation, the films were removed from the container and analyzed as quickly as possible.

Model PV devices for ToF-SIMS/AFM analysis were prepared similarly to above, with several additions. After drying, the FTO substrates were treated with UV/O₃ (BioForce Nanosciences) for 25 minutes to create a hydrophilic surface, then a PEDOT:PSS (Heraeus) film was applied to the surface. A 1:2 dilution of the polymer in methanol (Fisher Scientific, ACS Grade) was used for spin coating. Two drops of the PEDOT:PSS solution were filtered through a 0.2 micrometer PTFE filter onto the center of the substrate, which was then spun at 4000 rpm for 40 s, using a 3 second ramp and deceleration. Following coating, the substrates were annealed at 150 °C for 10 minutes before being immediately brought into the glovebox. Perovskite film deposition onto these substrates was accomplished in a manner identical to the procedure listed above.

To complete the model devices, 40 nm of C₆₀ (MER Corp., 99.9%) and 7 nm of bathocuproine (BCP, Sigma-Aldrich, 99.9%) were thermally evaporated using an AMOD thermal evaporator at a base pressure of approximately 8×10^{-7} torr. The first 10 nm of C₆₀ were deposited at a rate of 0.2 Å/s, while the remaining 30 nm were deposited at 1 Å/s; the 7 nm BCP film was deposited at 0.2 Å/s. Following deposition, thin strips of the BCP/C₆₀/Perovskite/PEDOT:PSS stack was scratched away with a razor blade from two sides of the device to expose the FTO beneath. 125 nm of gold were then deposited through a shadow mask via electron beam evaporation using a Cooke Evaporation System to create the top contacts (0.2 cm²), as well as gold contacts for the FTO bottom contact to reduce unnecessary series resistance. Similar to C₆₀, the first 10 nm of Au were deposited at 0.2 Å/s and the remaining 115 nm were deposited at 1 Å/s. The finished devices were then stored in an Ar-filled MBraun glovebox (O₂/H₂O < 0.1 ppm) until testing.

4.2.2 Instrumental Characterization

X-ray diffraction (XRD) was performed on a Rigaku Ultima IV diffractometer in a thin film configuration using a Cu K α X-ray source. Atomic force microscopy (AFM) was conducted on a Park NX10 atomic force microscope in noncontact mode. This microscope is enclosed in a climate-controlled box allowing a constant RH to be maintained during analysis. The box was purged with ultra-high purity N₂ gas for 1 hour prior to sample loading to reduce the humidity to <15% before the fresh films were analyzed, then the humidity was increased to 78% for film exposure. For the ToF-SIMS/AFM measurements the AFM box was purged continuously with ultra-high purity N₂ gas, which kept the RH level very low in order to minimize the reaction between residual water and the Cs-sputtered spots. Photoluminescence spectroscopy (PL) was

performed on a Horiba Jobin Yvon Fluorolog3 spectrophotometer, using an excitation wavelength of 450 nm and a typical 90° detector geometry, with the film held at 45°. Excitation was performed on both the front (shining directly on the perovskite film) and the back (shining through the glass) of the films. Wide angle x-ray scattering (WAXS) was performed on a Xenocs Ganesha small angle scattering instrument fitted with a moveable Dectris 300k detector to record wide angle scattering data. The instrument is fitted with a microfocus Cu K α source operated at 50kV and 0.6mA. A manufacturer supplied utility, SAXSGUI, was used to reduce 2D scattering intensity images into intensity vs. scattering angle plots. Data was collected from a 0.7 x 12 mm area, using a 1° tilt of the substrate. Scanning electron microscopy (SEM) was performed with an FEI Quanta 650 ESEM, using an accelerating voltage of 15 kV at a vacuum of approximately 5×10^{-6} torr.

In preparation for confocal fluorescence microscopy (CFM) studies, the perovskite films were placed face-up on fresh piranha solution cleaned coverslips in a custom-machined sample holder that held them together with a secure contact. The fluorescence microscopy was performed with a custom built microscope in a confocal scheme with 488 nm excitation and a 100x oil objective (Zeiss) in a Zeiss Axiovert 200 inverted microscope. Due to the highly emissive nature of the samples and the sensitivity of the detectors, the excitation power was too low to be measured. The piezo stage was controlled through a home-written Labview program (National Instruments). The emitted light was filtered through a 496 nm long pass filter and a 721 nm short pass filter and was directed onto either an APD (Perkin Elmer) or a spectrograph (Princeton Instruments, Acton SP-150) that was coupled with a liquid N₂ cooled CCD detector for imaging and spectroscopy respectively. Each crystallite had spectra taken at three positions, once on each end and once in the middle. Each spot on a given crystal had

three consecutive spectra taken with 25 s integration times. These three spectra were then averaged to increase the signal-to-noise ratio.

Time-of-flight secondary ion mass spectrometry (ToF-SIMS) depth profiling in negative polarity was performed using a Bi_3^+ (30 keV ion energy, 0.8 pA measured sample current) analysis beam to raster scan a $100 \times 100 \text{ }\mu\text{m}^2$ area located within the boundaries of a larger crater ($300 \times 300 \text{ }\mu\text{m}^2$) created using a Cs^+ sputtering beam (500 eV ion energy, $\sim 40 \text{ nA}$ measured sample current). The pressure inside the analysis chamber was typically below 1.5×10^{-9} torr during analysis. Both films and devices analyzed using ToF-SIMS were split in half inside the glovebox prior to analysis, with one half left inside the glovebox as a control and the other half exposed to humidity. After exposure, the device or film was brought back into the glovebox and loaded with the control into an inert atmosphere transfer vessel to limit exposure to the environment while transferring the devices to and from the ToF-SIMS instrument. Following sputtering, the samples were loaded back into the vessel and transferred back to a glovebox to prepare them for AFM analysis. The samples were transferred under inert atmosphere into the AFM box ($<15\% \text{ RH}$) and analyzed quickly to prevent any physical and chemical interactions of water or oxygen with residual Cs in the sputtered areas.

4.3 RESULTS AND DISCUSSION

4.3.1 XRD Analysis

We used nBA-MAPI films with a nominal $n=4$ stoichiometry similar to those previously reported in literature^{13,15} to more closely investigate film degradation and crystal growth in humid environments, fabricated using a hot casting method previously shown to produce well-oriented nBA-MAPI films.¹³ Proper crystallographic orientation of the quasi-2D perovskite is important in devices made using these materials, as it

allows for charge conduction within the planes of the perovskite and thus improves device efficiency.¹⁷ The XRD spectrum of a freshly fabricated film (**Figure B.1**) shows only two sharp peaks near $2\theta = 14.2^\circ$ and 28.5° (**Figure 4.2a**), in agreement with previous reports on nominally $n=4$ nBA-MAPI films. Frequently, polycrystalline 2D organolead halide perovskite powders and un-oriented films show peaks in the region below $2\theta = 10^\circ$,¹⁸ but our unexposed film shows no peaks here (**Figure 4.2b**), indicating a well-oriented film. WAXS measurements of the film prior to exposure (**Figure B.2a**) further confirm this, with the WAXS spectra exhibiting distinct Bragg diffraction spots which correspond to the primary crystallographic planes of an nBA-MAPI material oriented perpendicular to the substrate.^{13,14}

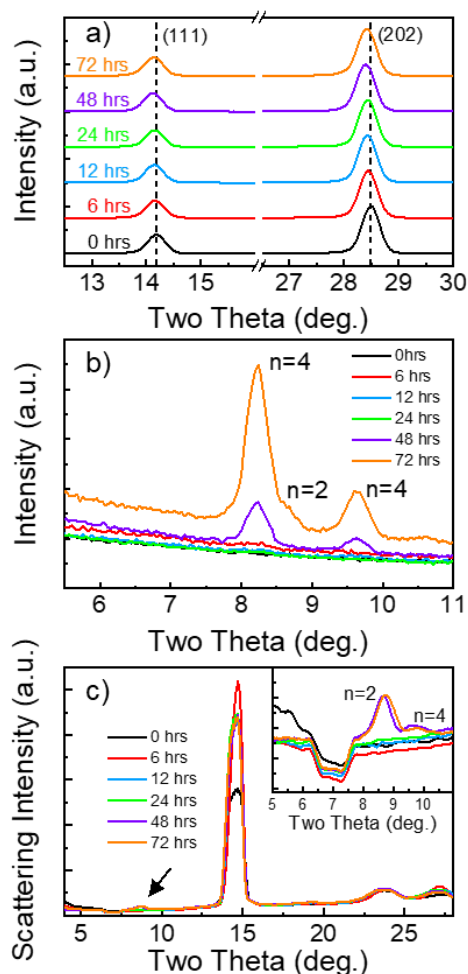


Figure 4.2 a) Selected regions of the XRD spectrum of an nBA-MAPI film over 72 hours of exposure to 78%RH, showing a shift in the (111) and (202) peaks. b) Low two theta region of the nBA-MAPI film XRD spectrum over 72 hours of humidity exposure, showing the formation of $n = 2$ and 4 phases in the film. c) Radial integrations of the WAXS spectra of an nBA-MAPI film over 72 hours of exposure, showing variations in the peak intensity of the main peak, in addition to the formation of $n= 2$ and 4 peaks (inset).

After confirming the crystallographic uniformity and orientation of the films, we repeated both the XRD and WAXS measurements after 6, 12, 24, 48, and 72 hours of exposure to a 78% RH environment to study what changes occur. Full XRD spectra of the films did not show significant changes to the relative intensity of the two primary

peaks (**Figure B.1**), only a slight 0.1 to 0.3° shift of the major peaks following exposure (**Figure 4.2a**). Such a shift could be due to an expansion of the perovskite unit cell due to humidity-induced hydration, but we believe it is more likely the result of a slight increase in the relative quantity of lower- n perovskite species, which exhibit (111) and (202) peaks at slightly smaller 2θ than our initial material.¹⁸ More interestingly, after 48 hours of exposure we observe the appearance of two peaks at $2\theta = 8.2^\circ$ and 9.7° and index these to the $n = 4$ phase; the two peaks grow stronger after 72 hours, and are joined by an additional $n = 2$ peak at $2\theta = 8.65^\circ$.¹⁸ Likewise, the WAXS spectra for films exposed for 48 and 72 hours shows the formation of two Debye-Scherrer diffraction rings at low q values (indicated by white arrows in **Figure B.2e,f**), and radial integration of the spectra confirms that these peaks correspond to the $2\theta = 8.65^\circ$ and 9.7° peaks visible in the XRD spectra (**Figure B.2c**).¹⁸ Such rings are typically indicative of un-oriented crystals in the film,¹⁹ and their appearance is suggestive of the formation of low- n crystals in the film as a result of moisture-driven disproportionation.¹⁵

4.3.2 AFM Analysis of Film Surface

To better study morphology and growth of the crystals indicated by the ring patterns in the WAXS spectra, we conducted AFM analysis of the nBA-MAPI film surface during different stages of moisture exposure. Using a microscope inside of a sealed container, we monitored the degradation of a film *in situ* over the course of 3 days. Initial AFM images of the surface show that the initial film surface is very smooth, with a root mean squared (RMS) roughness of only 5 nm (**Figure 4.3a B.3a**). However, after 6 hours (**Figure 4.3b**) of exposure the film begins to show the formation of extended micron-long cracks (location I) and small pits (location II) which extend into the bulk of the film, as well as several nodules extending above the surface. AFM shows the cracks

extend roughly 10-40 nm into the film surface, but the sharp edges of the cracks and their relatively narrow width may prevent the AFM tip from accurately reading their true depth.

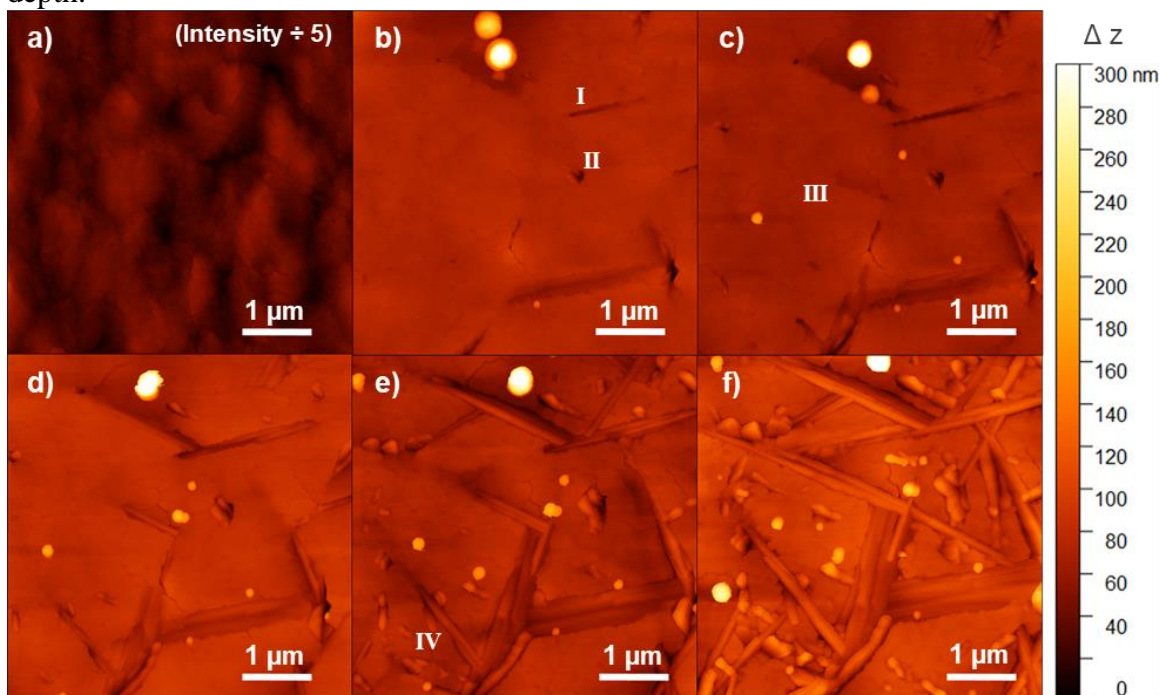


Figure 4.3 AFM images of a single area of an nBA-MAPI film in non-contact mode after a) 0, b), 6, c) 12, d) 24, e) 48, and f) 72 hours of exposure to 78%RH. a) shows the film is initially smooth (RMS 5 nm) with only small ridges and valleys at the surface of the film, but upon extended exposure to humidity, cracks (location I) and holes (location II) begin to form, with elongated crystals forming later. Some grain boundaries also experience subsidence (location III) prior to crystal growth, and other areas exhibit crystal growth without apparent damage to the film previously (location IV).

Time-lapse images of a single area of the film (**Figures 4.3** and **B.3**) show that the density of the cracks at the surface continues to increase with exposure to moisture. Notably, between 12-24 hours we observe the formation of thin, elongated crystallites within the cracks themselves (**Figure 4.3c**, location I). On average, these crystallites appear to be roughly 2-3 μm long and approximately 100 nm wide. The crystallites

exhibit flat faces perpendicular to their narrow edges, indicating the crystallites may be quasi-2D platelets which extend into the film rather than 1D rods laying within the cracks themselves. Similar micro-scale crystallites have previously been reported on perovskite films treated to create an artificial 2D perovskite layer, as well as in 2D films exposed to humidity for extended periods of time.^{15,20} Given their random orientation in the film, and that Ruddlesden-Popper phase organolead halide perovskites are well-known to adopt similar stacked platelet structures upon crystallization in solution,²¹ these crystallites seem to correspond to the low-*n* perovskite previously evidenced by the XRD and WAXS spectra.

These crystallites continue to grow over the course of 72 hours of observation as new gaps and crystals also emerge, resulting in a rough surface covered in both features. (**Figure 4.3f.**) Because the measurements were made *in situ*, we can more closely study the process by which the crystals appear to grow and relate these observations to previous work in solution-based systems. As previously noted, the crystals appear to grow out of cracks in the perovskite that formed as the film was exposed to humidity. Interestingly most, if not all, of these cracks appear to form at the grain boundaries between the individual nBA-MAPI grains which compose the film. Over time, the crystals grow in thickness and appear to force these cracks wider, separating previously adjacent crystal grains on the surface (location I). Given that these boundaries are likely the weakest points in the film and where it is most permeable to humidity these are unsurprising but important observations.

We also observe evidence of apparent subsidence along grain boundaries in the film, most notably near the very center of **Figure 4.3b,c** (location III). Between 6 and 12 hours, several grains on one side of a grain boundary dropped sharply downward into the film, and after 24 hours **Figure 4.3d** shows that a crystal formed at this location. This

appears to be evidence of some form of dynamic process deeper in the film which directly impacts the stability of the surface and which is related to the appearance and growth of the crystals. In addition to the formation of the long, thin cracks, we also observed holes that appeared to be more or less round, with several examples visible in **Figures 4.3** and **B.3b**. Crystals emerge from these holes after continued exposure to moisture, similar in appearance to those growing from the cracks but generally smaller and shorter overall (**Figure 4.3d**, location II). Similar short crystals appear to be able to form without the initial hole, as is visible in the bottom left corner of **Figure 4.3f** (location IV), suggesting that there may be at least two distinct crystal growth pathways available in these films.

After first appearance, the crystals grew primarily in length rather than in thickness, likely along the plane of the quasi-2D sheets. This growth appears to be limited primarily by the presence of other crystals in the path of growth, based on observations of the crystals in **Figure 4.3d**. Almost all of the crystals also appear to increase in thickness and height with time, although at a much slower rate than that of growth along the long axis. Most of the crystals appear to initially measure approximately 90 nm wide, but grow to an average thickness of 150 nm after 72 hours. Additionally, many of the crystals appeared to grow and develop into two distinct, adjacent platelets as exposure continues, giving them a layered appearance that is not dissimilar to macroscopic images of 2D perovskites.¹¹ From the images, it is not clear if the two crystals grow and develop separately, or if the second grows as part of the development of the first. Finally, with regard to vertical growth, we observe that the crystals initially appeared to be recessed into the film, and slowly grew toward the surface until they were either level with, or very slightly above, the average level of the film; this may indicate that their growth is limited by the availability of material from the bulk film surrounding them. Taken

together, these AFM results provide a detailed look at how the films physically change with exposure to moisture, as well as the types of structural evolutions that the nBA-MAPI crystals undergo during formation and growth. Unfortunately, the AFM results are unable to differentiate between the different n -phases indicated in the XRD and WAXS results, preventing a definitive assignment of which n -phases compose these crystals.

4.3.3 Bulk Photoluminescence Spectroscopy

To further study which low- n phases form during moisture exposure and crystals growth, we also conducted PL analysis of the nBA-MAPI films during degradation. Previous reports using this technique have reported the presence of multiple n -phases from a nominally $n = 4$ film, the result of an inherent gradient in the n -phases comprising the film as a function of depth.^{22,23} Due to an increase in the thermodynamic stability of nBA-MAPI phases as n decreases, the hot cast nBA-MAPI solutions tend to form films that feature low- n phases at the FTO-interface and very high- n phases, similar to 3D MAPI, near the surface.²³ Recently, Liu *et al.* provided a much clearer n -phase depth map of hot cast nBA-MAPI films and showed that for relatively thick ($\sim 1\ \mu\text{m}$) films, there are three distinct regions of n -phase composition within the film.²⁴ The top third of their film is almost completely composed of a high- n ($n > 5$) species, while the bottom third is dominated by $n = 3$ and 4 species, with shoulders corresponding to $n = 2$ and 5. The middle portion appears to be a transition zone where the high- and low- n species are both present in various quantities.

While we are unable to probe the center of our film directly, PL spectra taken from the front and back of our films (**Figure 4.4a**) show a similar peak distribution to those previously reported.^{15,24} The front-side spectrum shows a broad peak centered near 715 nm with an asymmetric shoulder toward shorter wavelengths, and we note that the

peak is shifted to shorter wavelengths than the peak reported by Liu *et al.* We suggest that this may be due to the relative thinness of our films (~350 nm, **Figure B.4**) inhibiting the formation of a large nBA⁺ concentration gradient during fabrication, and thus creating a less 3D-like surface.²³ The back-side spectra of our film shows a broad distribution of peaks ranging from 575 to 715 nm, previously identified as the $n=2-5$ peaks of nBA-MAPI.¹⁸

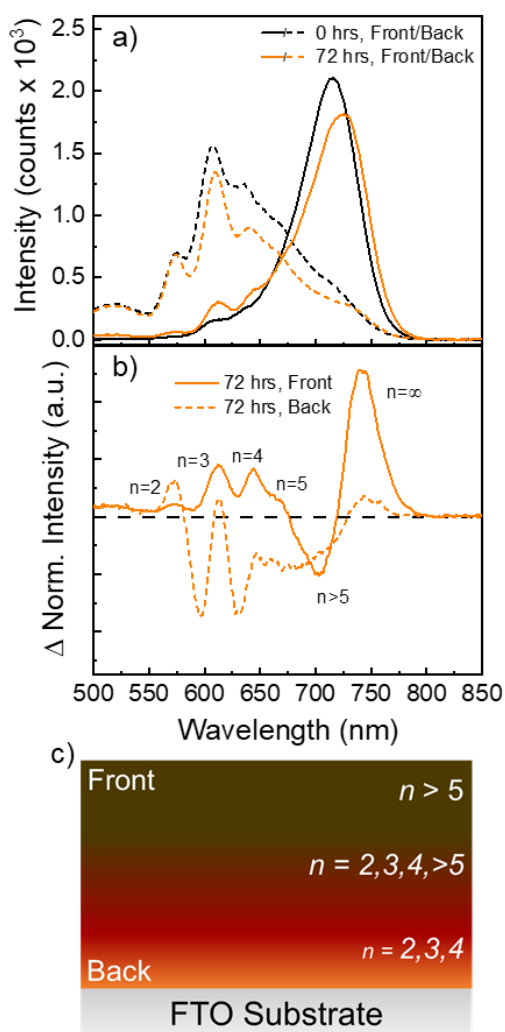


Figure 4.4 a) PL spectra of the front (solid) and back (dashed) sides of an nBA-MAPI film, before and after 72 hours of exposure to 78%RH. After 72 hours, the intensity of both spectra decreases, and peaks between 575 and 650 nm appear on the front. b) Difference spectra of the normalized PL spectra from the front and back of a film after 72 hours of exposure, showing the formation of low- n and 3D like species and concurrent decrease of the $n > 5$ peak due to disproportionation. c) Graphic representing the proposed n -phase structure of the nBA-MAPI film.

After confirming the composition of the unexposed nBA-MAPI films, we exposed the material to a 78% RH environment over 72 hours in a similar manner to the film analyzed by XRD, and recorded PL spectra from both the front- and back-sides at various time points. Similar to our previous report,¹⁵ we observe the formation of low- n peaks at the surface of the film after just 6 hours of exposure, which become more distinct as additional time passes (**Figure B.5a**). Small changes are observed in the back-side spectra (**Figure B.5b**), including a slight shift in the $n=3$ peak to longer wavelength, indicating crystallographic changes as the perovskite interacts with moisture. Likewise, the primary front-side peak shifts by 10 nm to 725 nm after 72 hours of exposure, a result of the formation of higher- n species during degradation and disproportionation of the perovskite under humid conditions. This is clearly evidenced by the difference plot of the front- and back-side spectra after 72 hours (**Figure 4.4b**) where, in addition to the aforementioned growth of the $n=2-5$ species, the front-side spectrum also shows clear growth of a peak near 740 nm assigned to a 3D-like perovskite in previous reports.²⁴ This peak is visible in both front- and back-side spectra recorded at all exposure times (**Figure B.5c,d**), and is accompanied by a loss of the $n > 5$ peak. Taken together, the growth of low- and high- n species at the expense of the original nBA-MAPI material during exposure to moisture indicates the films are likely undergoing disproportionation as they degrade in humid environments.

These observations agree well with similar changes in the XRD and WAXS spectra, and based on the polycrystalline nature of these newly-formed phases as determined by the ring patterns in the WAXS spectra, further confirm the crystals we observe growing in the AFM images are composed of these low- n phases. Like the film in which they are imbedded, the surfaces of these crystals are also likely to undergo disproportionation into progressively lower- n phases, resulting in a surface of $n = 1-3$

surrounding a core of $n = 4$ and larger phases.^{10,25} The local quantum well-like band structure resulting from this n -phase arrangement is expected to trap electrons photogenerated within the crystallites at the crystallite surfaces. This will prevent charge transfer from the crystallites to the $n > 5$ film surrounding them, and allow the $n = 1-5$ phases in the crystallites to be visible in the PL spectra; a more detailed explanation is presented in our previous work.¹⁵ This hypothesis is supported by recent work showing similar low- n 2D surface features in Pb-Sn perovskite films visible with hyperspectral PL mapping.²⁶ Unfortunately, while the strong correlation between the XRD, WAXS, AFM, and PL data allows us to infer the n -phases contained in the crystals, none of these techniques allow for direct identification, and a more precise technique is thus required to do so.

4.3.4 Fluorescence Microscopy Analysis

Confocal fluorescence microscopy (CFM) is one such technique, and offers both the spatial and spectral resolution necessary to accurately probe and confirm the n -phase composition of the small crystallites in these films. CFM is regularly used to measure the fluorescence of both single molecules and molecular aggregates,^{27–29} and using this technique we can generate both total fluorescence images of the film surface and point fluorescence spectra from single diffraction-limited spots on the film. Together, these capabilities make it ideal for both imaging the crystals visible by AFM and identifying their composition. A point spectrum from an unexposed nBA-MAPI film shows a single intense fluorescence peak near 740 nm (**Figure B.6**), which is significantly red shifted from the primary peak in the bulk PL spectrum (**Figure 4.4a**). Similar in PL wavelength to the species observed by Liu *et al.*, it is evidence of a thin surface layer of 3D-like perovskite.²⁴ Due to the intensity of the peak, we used a 721 nm short pass filter for

further imaging and spectroscopy which allowed us to focus more closely on the region of the PL spectra occupied by low- n perovskite phases.

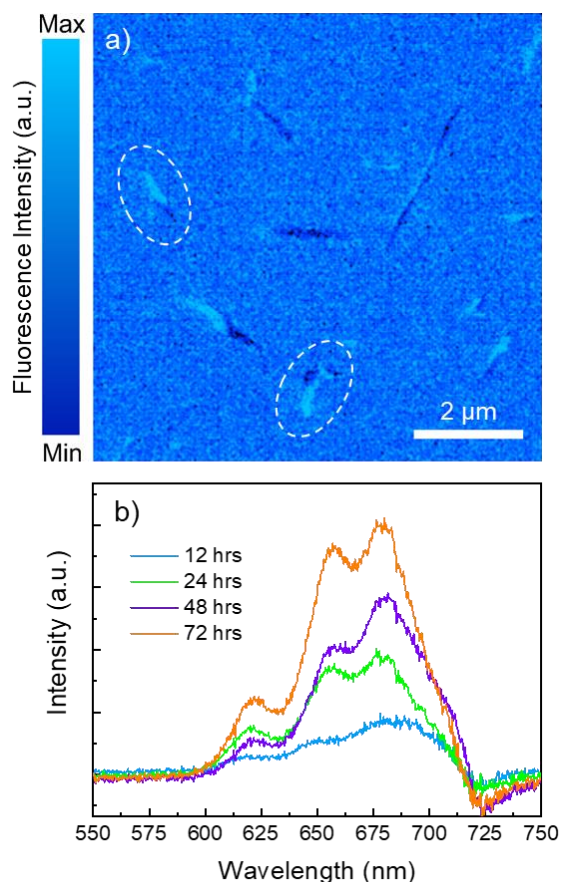


Figure 4.5 a) CFM image of an nBA-MAPI film exposed to 78%RH for 24 hours, showing localized fluorescence below 740nm from crystal-like structures, such as the circled examples. b) Average background-corrected point fluorescence spectra from low- n nBA-MAPI crystals after moisture exposure for 72 hours, showing an increase in the intensity of $n = 3-5$ peaks with increasing exposure to humidity.

Prior to moisture exposure, CFM images of the nBA-MAPI films with the short pass filter in place show no evidence of crystals at the surface (**Figure B.7a**), in agreement with AFM images. Following 12 hours of exposure, however, we begin to

observe elongated regions of fluorescence in the CFM images that increase in intensity and surface density over the course of 72 hours of exposure (**Figure B.7b-e**). Additionally, high resolution CFM imaging of a film exposed for 24 hours (**Figure 4.5a**) shows that the regions (such as the example circled in white) are roughly 1 μm long and 100 nm wide, as well as dark areas that appear identical to the surface cracks visible in the AFM images. Taken together, the CFM images are strong evidence that these regions correspond to the crystals previously observed using AFM.

After using CFM imaging to locate the low- n crystals, we used point spectra taken from the crystals and films at each exposure condition to study how the n -phase composition of the crystals changed with time. To do so, we measured point spectra from both off- and on-crystal sites and generated average spectra of each type of site (**Figure B.8**). This allowed us to create background-subtracted on-crystal spectra at each time point between 12 and 72 hours (**Figure 4.5b**). These spectra show that as exposure continues, the crystals exhibit progressively stronger signal for peaks corresponding to $n = 3$ -5 phases, indicating an increase in the abundance of these phases as the crystals grow. We note that these CFM peaks exhibit a 10 nm red shift when compared to the bulk PL spectra (i.e., $n = 3$ at 610 nm in PL but 620 nm in CFM), which is evidence of crystal compression due to the surrounding film.³⁰ In all, the phases and changes we observe in the CFM agree with the bulk PL measurements, and confirm that the low- n features we observe in the bulk spectra come from these smaller crystallites.

In addition to measuring average spectra from multiple crystals, we also analyzed point spectra taken from three separate points on individual crystals (the middle and both ends) and compared them to determine the relative compositional homogeneity of individual crystals as a function of exposure time. Examples are provided in **Figure B.9**, and we find that the homogeneity of the crystals decreases significantly over time

(**Figure B.9c**), a reflection of the rough and uneven surface observed with AFM. As a result of this roughness, and the resolution of the microscope (~200 nm) due to the incident laser when compared to the crystal width, we are currently unable to provide a more quantitative analysis of the spatial composition of the crystallites. Despite this, our CFM images and spectra not only confirm that the crystals visible via AFM are composed of $n = 3-5$ nBA-MAPI phases, but also that no significant phase changes occur on the rest of the film surface during film degradation. This does not preclude the presence of other phases at the surface, either as a result of an initially disordered material²⁵ or as a function of disproportionation,¹⁵ but it does indicate that if they exist they are likely transferring charge to other, higher- n phases and would not be expected to negatively impact charge conduction in a full device.

4.3.5 ToF-SIMS/AFM

As mentioned above, Liu *et al.* recently showed that the surface 3D-like perovskite phase in a hot cast nBA-MAPI thin film extended roughly a third of the way into the film before gradually giving way to low- n phases. Given that AFM images during moisture exposure appear to show cracks into the film forming prior to crystal growth, we used a combination of time-of-flight secondary ion mass spectrometry (ToF-SIMS) and AFM to study the topography of the interior of our films before and after degradation, and determine if the crystals might form within the film rather than at the surface. Similar to previous reports on both 2D materials³¹ and organic solar cells,³² ToF-SIMS allowed us to controllably sputter to the interior of the film before imaging and analyzing the topography of the freshly uncovered surface using AFM.

Figure 4.6a shows the full depth profile of an nBA-MAPI film acquired in negative ion polarity, with PbI_2^- representing the inorganic portion of the perovskite and

SnO⁻ representing the FTO substrate. We next sputtered approximately 50% of the way through the film (approximately 175 nm), as indicated by the dashed line in **Figure 4.6a**, using the ToF-SIMS before removing the film from the instrument and subsequently analyzing the surface using AFM. The uniform ion sputtering from the ToF-SIMS preserves the ridge and valley pattern previously visible on the surface in **Figure 4.3a**, as well as some of the grain boundaries between individual nBA-MAPI crystallites (**Figure 4.6b**). In addition, the exposed surface is uniformly covered in small nodules that are likely artifacts of ion sputtering. **Figure 4.6c** shows that after sputtering through a film exposed to moisture for 8 hours, several 1-2 μm -long cracks are visible in the newly-exposed surface of the film (location II); these are similar in appearance to those visible in **Figure 4.3c** and indicate the cracks at the surface extend deeply into the film. Additionally, a few linear structures, likely the bases of the crystals seen at the surface of the film, were also visible near some of the cracks (location I). Their presence in the center of the film shows that the crystals visible at the surface also extend into the interior of the film, and may even originate there, while their proximity to the cracks further suggests a link between the two features.

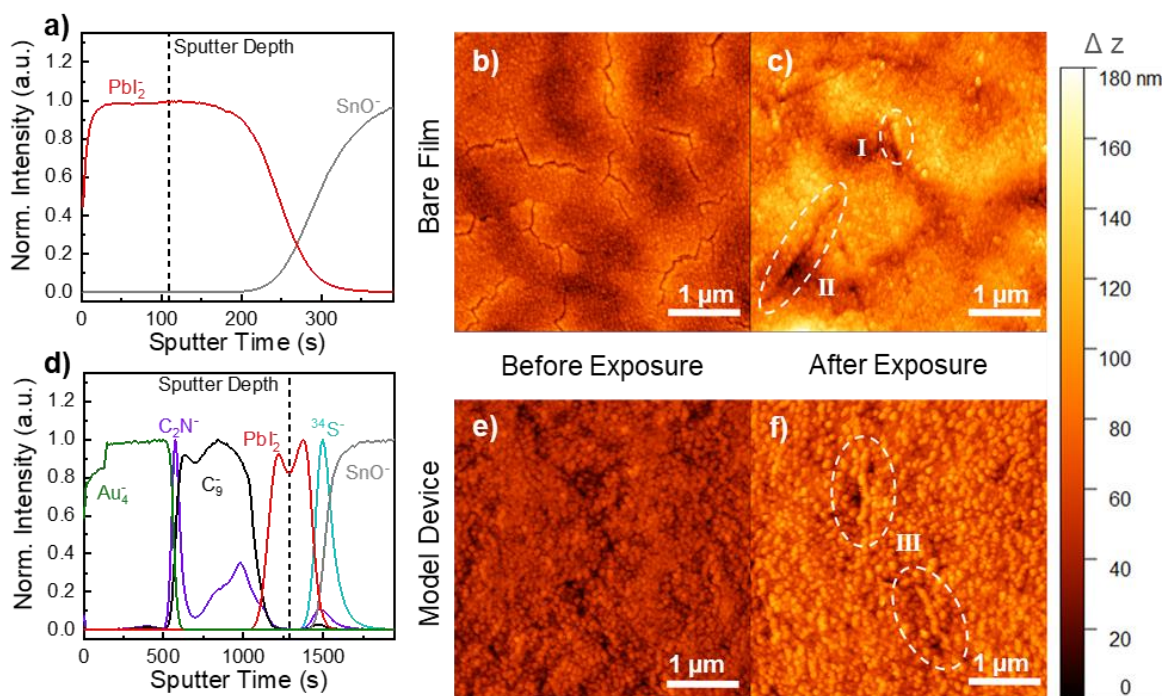


Figure 4.6 Negative ion polarity ToF-SIMS depth profiles for a) a bare nBA-MAPI film and d) a model PV device. PbI_2^- represents the inorganic portion of the perovskite, CN^- represents the organic portion of the perovskite, SnO^- represents FTO, Au_4^- represents the Au contact, C_2N^- represents BCP, C_9^- represents the C_{60} layer, and $^{34}\text{S}^-$ represents the PEDOT:PSS layer. A fresh film (b) and one exposed to 78% RH for 8 hours (c) were sputtered to the dashed line in a) and the surface was imaged by AFM, showing the presence of new crystals (I) and cracks (II) only in interior of the exposed sample. A fresh device (e) and one exposed to humidity for 24 hours (f), likewise showing the formation of crystals (III) inside the film.

In light of these observations, as well as the importance of perovskite stability in photovoltaic devices, we next fabricated model device stacks and analyzed them using a similar ToF-SIMS/AFM experiment to investigate how the presence of C_{60} and Au overlayers might affect the formation of these crystallites. Selected ionic species in the ToF-SIMS depth profile of the device (**Figure 4.6d**) show the presence of the various components of the device: Au_4^- for the Au contact, C_2N^- for the bathocuproine, C_9^- for the

C₆₀ electron transport material, PbI₂ for the nBA-MAPI, ³⁴S⁻ for the PEDOT:PSS hole transport material, and SnO⁻ for the FTO substrate. After sputtering to the center of the nBA-MAPI layer of a fresh device, also indicated by the dashed line in the depth profile, we observe a similar interior morphology to that of the fresh bare film (**Figure 4.6e**). Once again, the surface is relatively featureless and covered with small nodules, with no other extended structures visible. This is to be expected given the pristine nature of the device, and indicates that there are few differences that arise in the AFM image of the interior of the nBA-MAPI as a result of sputtering through the Au and C₆₀ overlayers.

Next, based on previous reports of 2D device stability,^{13,15} we exposed our devices to 24 hours of humidity exposure to induce a moderate degree of damage to the device before once again sputtering to the center of the nBA-MAPI layer and imaging it with AFM. **Figure 4.6f** shows a mostly level surface largely dominated by the small sputtering-induced nodules. Unlike the fresh sample, however, the interior of the degraded device does appear to show additional features. Near the center of **Figure 4.6f** (location III) is a roughly 1 μ m-long, 100 nm-wide structure, with a second similar structure slightly below it. These distinct structures are similar in appearance to those observed in the interior of the degraded film (**Figure 4.6c**, location I), as well as the low-*n* crystals visible at the surface in **Figure 4.3**. The surface density of these structures is much lower than was observed in even the 6-hour film in **Figure 4.3b**, likely a result of decreased water diffusion through the overlayers. Additionally, no clear cracks in the film are visible near them, which may be the result of increased film rigidity due to the presence of the C₆₀ layer above.

The increased strength and moisture protection offered by the overlayers seems to inhibit the growth of the low-*n* crystallites we observe in the bare films, but **Figure 4.6f** suggests that it does not halt the process completely. Indeed, identical devices have

shown a relatively gradual decrease in their power conversion efficiency (PCE) during the same time period, before exhibiting significant performance loss only 12 hours later. We hypothesize that this relatively rapid loss of PCE could be due to the delayed growth of low- n crystals within the nBA-MAPI layer causing chemical and structural damage like that observed at earlier times in bare films. Further work is necessary to fully explore this proposal, but the evidence of crystal growth within full devices we present here suggests quasi-2D crystal growth should be taken into account when developing devices based on Ruddlesden-Popper phase perovskites.

4.3.6 Proposed Crystal Growth Mechanism

Drawing upon the data presented above, we have developed a proposed process by which the crystallographic and morphologic changes we observe in our nBA-MAPI films occur (**Figure 4.7**). To begin, while the presence of Bragg spots in our WAXS data indicates that our films are well-oriented and crystalline, the breadth of the peaks, particularly the $(-1\ 1\ -1)$ peak, indicates a moderate degree of disorder in the films. Qiu *et al.* have reported similarly broad peaks in grazing-incidence WAXS (GIWAXS) spectra of Sn-based nBA-containing perovskites, which they attribute to formation of intermediate low- n 2D phases during film fabrication.³³ While they are able to suppress the formation of these phases through addition of a second spacer species (phenylethylammonium), without this addition, the films show increased disorder in the orientation of the predominant perovskite phases. This has also been seen in some Pb-based 2D perovskites.¹⁴ In addition to this crystallographic disorder, our films also contain a gradient n -phase composition from top to bottom, with n increasing with film thickness. Combined with the moisture-driven disproportionation, we believe these features explain the crystal formation and growth we observe.

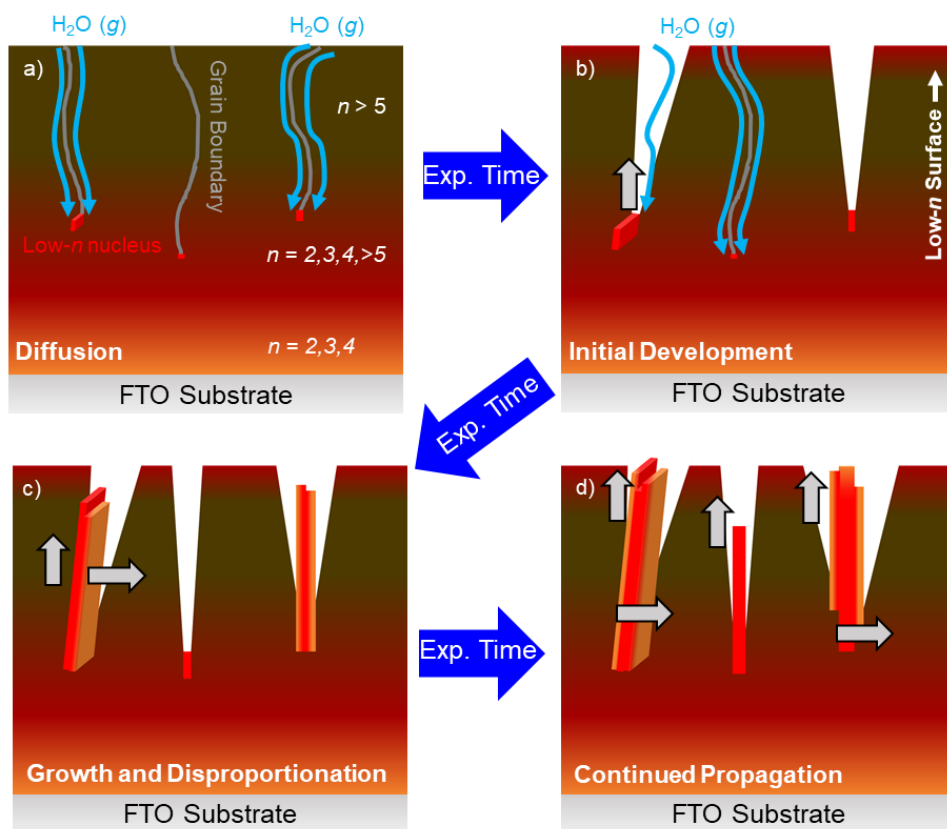


Figure 4.7 Proposed growth mechanism for low- n nBA-MAPI crystallites. a) water diffuses through grain boundaries in the $n > 5$ surface, carrying solvated perovskite components to low- n nuclei buried in the bulk of the film. The nuclei begin to grow in height and length, causing the film above them to split (b) and allowing more water to diffuse into the film. As exposure continues (c), the crystals also begin to exhibit growth in thickness, as well as disproportionation. These processes continue (d), with crystals eventually ceasing vertical growth near the film surface but continuing to lengthen and widen as exposure continues.

As water diffuses through the more permeable grain boundaries at the film surface, likely slowed by the hydrophobic nBA⁺ tails,¹⁶ it eventually penetrates through the high- n surface layer and into the mixed phase region below (**Figure 4.7a**). Based on the native disorder in the films, we propose the mixed region contains segregated areas of $n = 3$ -5, either in the form of small discontinuities in the crystal lattice or as small grains

of low- n material within the bulk. Evidence of similar segregated phases has been observed in related systems,³⁴ supporting this hypothesis. These crystallites would act as local low- n nucleation sites within the bulk of the film, where solvated perovskite compounds dissolved as the water diffused through the high- n layer above could recrystallize. DFT calculations have shown that the low- n phases are more stable, providing a thermodynamic driving force for this dissolution and recrystallization.³⁵ Further, given that the alkylammonium components are more likely to be solvated than the Pb-I lattice, this process may also explain the disproportionation observed previously, simultaneously creating new low- n species in the bulk and higher- n species at the surface, evidenced by the peak shift observed in **Figure B.5a**. Some of the solvated species may also recrystallize at the film surface, resulting in the passivation layer previously hypothesized to exist there.^{11,15} The lack of clear polycrystallinity in the WAXS is evidence that these nuclei are oriented such that the 2D sheets are perpendicular to the substrate. Thus, the crystals would exhibit preferential edge-on growth along the edge of the quasi-2D sheets,³⁶ resulting in characteristic platelet-like crystals of Ruddlesden-Popper materials.²¹ As they grow, the grain boundaries above will split open (**Figure 4.7b**), creating the cracks we observe in AFM images (**Figure 4.3**).

With cracks opening in the surface, the film becomes more permeable to moisture, accelerating vertical growth of nascent crystals at the bottom of the cracks. This growth would further split the cracks, exposing new high- n nBA-MAPI along the walls to moisture and inducing strain on the film. This strain may allow diffusion through previously unfavorable grain boundaries, allowing new nuclei to grow and opening more cracks (**Figure 4.7c**). The crystals would grow vertically until water is no longer able to efficiently diffuse solvated species to the leading crystal growth edge, explaining the limited vertical growth observed by AFM. In turn, this would encourage additional

growth on the flat faces and edges of the platelets, widening and lengthening the crystals and the cracks. Compression of the crystals' lattices due to the surrounding film could cause a decrease in the perovskite band gap, explaining the red-shifted spectra in **Figure B.8b**. CFM spectra of the crystals themselves show they contain $n = 3-5$ phases. Higher $n = 4$ and 5 phases would be expected to disproportionate into lower- n phases with time as well, potentially indicated by the increased crystal point spectra heterogeneity indicated in **Figure B.9c**.

This process of water diffusion to buried nuclei, followed by crystal growth and disproportionation would continue as long as the film was exposed to humidity (**Figure 4.7d**), resulting in the dynamic surface covered in cracks and crystals we observe in our bare films. Such films represent a “best-case” scenario for degradation, however, as it allows for minimal protection of the films as they are exposed to water. Even still, the AFM image in **Figure 4.6f** indicates that despite the protective overlayers, the nBA-MAPI layers of full devices appear to undergo a similar process, albeit more slowly. This slower rate may be due in part to the surface disproportionation previously described by our group in full devices,¹⁵ as the formation of a lower- n surface at the C₆₀/nBA-MAPI interface would likely stabilize the surface and inhibit the diffusion of soluble nuclei in the bulk. Formation of this lower- n surface is evidenced by a widening of the PbI₂⁻ peak in ToF-SIMS experiments after moisture exposure (**Figure B.10**), as it occurred primarily in the hydration region present at the C₆₀/nBA-MAPI interface. A similar perovskite widening was previously observed in films that had suffered moisture damage.

In light of this, the plateau in the loss of power conversion efficiency previously observed in nBA-MAPI devices may be the result of a two-step degradation process. In the first step, surface disproportionation occurs at the C₆₀/nBA-MAPI interface, resulting in negligible loss of performance as a protective low- n layer forms that protects the bulk

of the film. Gradually, sufficient water diffuses through the film to induce nucleation of crystals within the bulk, causing both physical and chemical damage to the device. This culminates in a second, more severe loss of performance. Given that this process is proposed to be dependent upon the presence of nuclei within the bulk of the film, techniques which increase the homogeneity of similar films throughout their depth may be an effective way to prevent or inhibit the crystal growth. Recently, careful control of the substrate temperature during film fabrication²⁴ and the addition of a second linker species³³ have been shown to have some control over the distribution of phases in the film, making them promising avenues for future work. Experiments are currently underway to investigate this further, including the use of FIB milling to generate cross sections of devices at different levels of exposure, which can then be analyzed using TEM and other high-resolution techniques.

4.4 CONCLUSIONS

In the present work, we have used a series of spectroscopic and microscopy techniques to explore the composition, morphology, and growth of previously un-studied crystals forming in the surface of nBA-MAPI films. XRD and WAXS spectra of fresh samples confirm that the films are oriented largely perpendicular to the underlying substrate and are highly crystalline. After exposure to humidity, the films exhibit the growth of polycrystalline low- n phases over time, confirmed by AFM to be platelet-like structures buried in the film, roughly 2-3 μm in length and 100 nm in width. PL spectra taken at identical exposure times likewise show increases in low- n species, as well as the growth of 3D-like peaks in difference spectra; this is concurrent with a decrease in $n > 5$ 2D species and indicative of perovskite disproportionation. CFM images and spectra confirm crystals visible in AFM images are composed of these newly-formed, low- n

phases, consistent with WAXS spectra. Using ToF-SIMS/AFM, we have shown crystal features visible at the film surface extend deep into the bulk, and that similar crystallites are also visible in AFM images taken from the interior of model nBA-MAPI perovskite devices. This suggests that a similar process of degradation also occurs in the active layers of full 2D organolead halide solar devices. Using our combined data, we propose a mechanism to explain the crystal growth during water exposure, which accounts for the developments we observe. Together, our results suggest future research should pursue thin film fabrication methods that limit heterogeneity within quasi-2D perovskite films. We expect this to prevent creation of the low- n nuclei in the bulk that allow for crystal growth and thus film damage, which in turn should lead to improved device lifetimes.

4.5 REFERENCES

- (1) NREL. Best Research-Cell Efficiencies <https://www.nrel.gov/pv/assets/pdfs/pv-efficiency-chart.20181221.pdf>.
- (2) Kim, H. S.; Hagfeldt, A.; Park, N. G. Morphological and Compositional Progress in Halide Perovskite Solar Cells. *Chem. Commun.* **2019**, 55 (9), 1192–1200. <https://doi.org/10.1039/c8cc08653b>.
- (3) Prochowicz, D.; Runjhun, R.; Tavakoli, M. M.; Yadav, P.; Saski, M.; Alanazi, A. Q.; Kubicki, D. J.; Kaszkur, Z.; Zakeeruddin, S. M.; Lewiński, J.; et al. Engineering of Perovskite Materials Based on Formamidinium and Cesium Hybridization for High-Efficiency Solar Cells. *Chem. Mater.* **2019**, 31 (5), 1620–1627. <https://doi.org/10.1021/acs.chemmater.8b04871>.
- (4) Wang, H.; Bian, H.; Jin, Z.; Zhang, H.; Liang, L.; Wen, J.; Wang, Q.; Ding, L.; Liu, S. F. Cesium Lead Mixed-Halide Perovskites for Low-Energy Loss Solar Cells with Efficiency beyond 17%. *Chem. Mater.* **2019**, 31 (16), 6231–6238. <https://doi.org/10.1021/acs.chemmater.9b02248>.
- (5) Zhang, W.; Xiong, J.; Li, J.; Daoud, W. A. Guanidinium Induced Phase Separated Perovskite Layer for Efficient and Highly Stable Solar Cells. *J. Mater. Chem. A* **2019**, 7 (16), 9486–9496. <https://doi.org/10.1039/c9ta01893j>.
- (6) Turren-Cruz, S. H.; Saliba, M.; Mayer, M. T.; Juárez-Santiesteban, H.; Mathew, X.; Nienhaus, L.; Tress, W.; Erodici, M. P.; Sher, M. J.; Bawendi, M. G.; et al. Enhanced Charge Carrier Mobility and Lifetime Suppress Hysteresis and Improve

- Efficiency in Planar Perovskite Solar Cells. *Energy Environ. Sci.* **2018**, *11* (1), 78–86. <https://doi.org/10.1039/c7ee02901b>.
- (7) Gil-Escrig, L.; Momblona, C.; La-Placa, M. G.; Boix, P. P.; Sessolo, M.; Bolink, H. J. Vacuum Deposited Triple-Cation Mixed-Halide Perovskite Solar Cells. *Adv. Energy Mater.* **2018**, *8* (14), 1–6. <https://doi.org/10.1002/aenm.201703506>.
 - (8) Cao, D. H.; Stoumpos, C. C.; Farha, O. K.; Hupp, J. T.; Kanatzidis, M. G. Two-Dimensional Homologous Perovskites as Light Absorbing Materials for Solar Cell Applications. *J. Am. Chem. Soc.* **2015**, *137* (24), 7843–7850. <https://doi.org/10.1021/jacs.5b03796>.
 - (9) Myae Soe, C. M.; Nagabhushana, G. P.; Shivaramaiah, R.; Tsai, H.; Nie, W.; Blancon, J. C.; Melkonyan, F.; Cao, D. H.; Traoré, B.; Pedesseau, L.; et al. Structural and Thermodynamic Limits of Layer Thickness in 2D Halide Perovskites. *Proc. Natl. Acad. Sci. U. S. A.* **2019**, *116* (1), 58–66. <https://doi.org/10.1073/pnas.1811006115>.
 - (10) Silver, S.; Dai, Q.; Li, H.; Brédas, J. L.; Kahn, A. Quantum Well Energetics of an $n = 2$ Ruddlesden–Popper Phase Perovskite. *Adv. Energy Mater.* **2019**, *1901005*, 1–7. <https://doi.org/10.1002/aenm.201901005>.
 - (11) Stoumpos, C. C.; Soe, C. M. M.; Tsai, H.; Nie, W.; Blancon, J. C.; Cao, D. H.; Liu, F.; Traoré, B.; Katan, C.; Even, J.; et al. High Members of the 2D Ruddlesden–Popper Halide Perovskites: Synthesis, Optical Properties, and Solar Cells of $(\text{CH}_3(\text{CH}_2)_3\text{NH}_3)_2(\text{CH}_3\text{NH}_3)_4\text{Pb}_5\text{I}_{16}$. *Chem* **2017**, *2* (3), 427–440. <https://doi.org/10.1016/j.chempr.2017.02.004>.
 - (12) Grancini, G.; Roldán-Carmona, C.; Zimmermann, I.; Mosconi, E.; Lee, X.; Martineau, D.; Nabey, S.; Oswald, F.; De Angelis, F.; Graetzel, M.; et al. One-Year Stable Perovskite Solar Cells by 2D/3D Interface Engineering. *Nat. Commun.* **2017**, *8*, 15684. <https://doi.org/10.1038/ncomms15684>.
 - (13) Tsai, H.; Nie, W.; Blancon, J.-C.; Stoumpos, C. C.; Asadpour, R.; Harutyunyan, B.; Neukirch, A. J.; Verduzco, R.; Crochet, J. J.; Tretiak, S.; et al. High-Efficiency Two-Dimensional Ruddlesden–Popper Perovskite Solar Cells. *Nature* **2016**, *536* (7616), 312–316. <https://doi.org/10.1038/nature18306>.
 - (14) Wang, Z.; Lin, Q.; Chmiel, F. P.; Sakai, N.; Herz, L. M.; Snaith, H. J. Efficient Ambient-Air-Stable Solar Cells with 2D-3D Heterostructured Butylammonium-Caesium-Formamidinium Lead Halide Perovskites. *Nat. Energy* **2017**, *2* (9), 1–10. <https://doi.org/10.1038/nenergy.2017.135>.
 - (15) Wygant, B. R.; Ye, A. Z.; Dolocan, A.; Vu, Q.; Abbot, D. M.; Mullins, C. B. Probing the Degradation Chemistry and Enhanced Stability of 2D Organolead Halide Perovskites. *J. Am. Chem. Soc.* **2019**, *141*, 18170–18181. <https://doi.org/10.1021/jacs.9b08895>.

- (16) Koh, T. M.; Shanmugam, V.; Guo, X.; Lim, S. S.; Filonik, O.; Herzig, E. M.; Müller-Buschbaum, P.; Swamy, V.; Chien, S. T.; Mhaisalkar, S. G.; et al. Enhancing Moisture Tolerance in Efficient Hybrid 3D/2D Perovskite Photovoltaics. *J. Mater. Chem. A* **2018**, 2122–2128. <https://doi.org/10.1039/C7TA09657G>.
- (17) Chen, A. Z.; Shiu, M.; Ma, J. H.; Alpert, M. R.; Zhang, D.; Foley, B. J.; Smilgies, D. M.; Lee, S. H.; Choi, J. J. Origin of Vertical Orientation in Two-Dimensional Metal Halide Perovskites and Its Effect on Photovoltaic Performance. *Nat. Commun.* **2018**, 9 (1), 1–7. <https://doi.org/10.1038/s41467-018-03757-0>.
- (18) Stoumpos, C. C.; Cao, D. H.; Clark, D. J.; Young, J.; Rondinelli, J. M.; Jang, J. I.; Hupp, J. T.; Kanatzidis, M. G. Ruddlesden-Popper Hybrid Lead Iodide Perovskite 2D Homologous Semiconductors. *Chem. Mater.* **2016**, 28 (8), 2852–2867. <https://doi.org/10.1021/acs.chemmater.6b00847>.
- (19) Soe, C. M. M.; Nie, W.; Stoumpos, C. C.; Tsai, H.; Blancon, J. C.; Liu, F.; Even, J.; Marks, T. J.; Mohite, A. D.; Kanatzidis, M. G. Understanding Film Formation Morphology and Orientation in High Member 2D Ruddlesden–Popper Perovskites for High-Efficiency Solar Cells. *Adv. Energy Mater.* **2018**, 8 (1), 2–11. <https://doi.org/10.1002/aenm.201700979>.
- (20) Li, L.; Zhou, N.; Chen, Q.; Shang, Q.; Zhang, Q.; Wang, X.; Zhou, H. Unraveling the Growth of Hierarchical Quasi-2D/3D Perovskite and Carrier Dynamics. *J. Phys. Chem. Lett.* **2018**, 9 (5), 1124–1132. <https://doi.org/10.1021/acs.jpcllett.7b03294>.
- (21) Wang, K.; Wu, C.; Yang, D.; Jiang, Y.; Priya, S. Quasi-Two-Dimensional Halide Perovskite Single Crystal Photodetector. *ACS Nano* **2018**, 12 (5), 4919–4929. <https://doi.org/10.1021/acsnano.8b01999>.
- (22) Liu, J.; Leng, J.; Wu, K.; Zhang, J.; Jin, S. Observation of Internal Photoinduced Electron and Hole Separation in Hybrid Two-Dimensional Perovskite Films. *J. Am. Chem. Soc.* **2017**, 139 (4), 1432–1435. <https://doi.org/10.1021/jacs.6b12581>.
- (23) Quintero-Bermudez, R.; Gold-Parker, A.; Proppe, A. H.; Munir, R.; Yang, Z.; Kelley, S. O.; Amassian, A.; Toney, M. F.; Sargent, E. H. Compositional and Orientational Control in Metal Halide Perovskites of Reduced Dimensionality. *Nat. Mater.* **2018**, 17 (10), 900–907. <https://doi.org/10.1038/s41563-018-0154-x>.
- (24) Liu, N.; Liu, P.; Ren, H.; Xie, H.; Zhou, N.; Gao, Y.; Li, Y.; Zhou, H.; Bai, Y.; Chen, Q. Probing Phase Distribution in 2D Perovskites for Efficient Device Design. *ACS Appl. Mater. Interfaces* **2020**, 12 (2), 3127–3133. <https://doi.org/10.1021/acsami.9b17047>.
- (25) Yuan, M.; Quan, L. N.; Comin, R.; Walters, G.; Sabatini, R.; Voznyy, O.; Hoogland, S.; Zhao, Y.; Beauregard, E. M.; Kanjanaboos, P.; et al. Perovskite

- Energy Funnels for Efficient Light-Emitting Diodes. *Nat. Nanotechnol.* **2016**, *11* (10), 872–877. <https://doi.org/10.1038/nnano.2016.110>.
- (26) Ruggeri, E.; Anaya, M.; Gałkowski, K.; Delport, G.; Kosasih, F. U.; Abfalterer, A.; Mackowski, S.; Ducati, C.; Stranks, S. D. Controlling the Growth Kinetics and Optoelectronic Properties of 2D/3D Lead–Tin Perovskite Heterojunctions. *Adv. Mater.* **2019**, *1905247*, 1–9. <https://doi.org/10.1002/adma.201905247>.
 - (27) Eisele, D. M.; Knoester, J.; Kirstein, S.; Rabe, J. P.; Vanden Bout, D. A. Uniform Exciton Fluorescence from Individual Molecular Nanotubes Immobilized on Solid Substrates. *Nat. Nanotechnol.* **2009**, *4* (10), 658–663. <https://doi.org/10.1038/nnano.2009.227>.
 - (28) Elacqua, E.; Geberth, G. T.; Vanden Bout, D. A.; Weck, M. Synthesis and Folding Behaviour of Poly(p-Phenylene Vinylene)-Based β -Sheet Polychromophores. *Chem. Sci.* **2019**, *10* (7), 2144–2152. <https://doi.org/10.1039/c8sc05111a>.
 - (29) Hu, Z.; Shao, B.; Geberth, G. T.; Vanden Bout, D. A. Effects of Molecular Architecture on Morphology and Photophysics in Conjugated Polymers: From Single Molecules to Bulk. *Chem. Sci.* **2018**, *9* (5), 1101–1111. <https://doi.org/10.1039/c7sc03465b>.
 - (30) Postorino, P.; Malavasi, L. Pressure-Induced Effects in Organic-Inorganic Hybrid Perovskites. *J. Phys. Chem. Lett.* **2017**, *8* (12), 2613–2622. <https://doi.org/10.1021/acs.jpcllett.7b00347>.
 - (31) Chou, H.; Ismach, A.; Ghosh, R.; Ruoff, R. S.; Dolocan, A. Heterostructures at the Atomic Level. *Nat. Commun.* **2015**, *6* (May), 1–7. <https://doi.org/10.1038/ncomms8482>.
 - (32) Griffin, M. P.; Gearba, R.; Stevenson, K. J.; Vanden Bout, D. A.; Dolocan, A. Revealing the Chemistry and Morphology of Buried Donor/Acceptor Interfaces in Organic Photovoltaics. *J. Phys. Chem. Lett.* **2017**, *8* (13), 2764–2773. <https://doi.org/10.1021/acs.jpcllett.7b00911>.
 - (33) Qiu, J.; Xia, Y.; Zheng, Y.; Hui, W.; Gu, H.; Yuan, W.; Yu, H.; Chao, L.; Niu, T.; Yang, Y.; et al. 2D Intermediate Suppression for Efficient Ruddlesden-Popper (RP) Phase Lead-Free Perovskite Solar Cells. *ACS Energy Lett.* **2019**, *4* (7), 1513–1520. <https://doi.org/10.1021/acsenergylett.9b00954>.
 - (34) Lin, Y.; Fang, Y.; Zhao, J.; Shao, Y.; Stuard, S. J.; Nahid, M. M.; Ade, H.; Wang, Q.; Shield, J. E.; Zhou, N.; et al. Unveiling the Operation Mechanism of Layered Perovskite Solar Cells. *Nat. Commun.* **2019**, *10* (1), 1–11. <https://doi.org/10.1038/s41467-019-08958-9>.
 - (35) Quan, L. N.; Yuan, M.; Comin, R.; Voznyy, O.; Beauregard, E. M.; Hoogland, S.; Buin, A.; Kirmani, A. R.; Zhao, K.; Amassian, A.; et al. Ligand-Stabilized

- Reduced-Dimensionality Perovskites. *J. Am. Chem. Soc.* **2016**, *138* (8), 2649–2655. <https://doi.org/10.1021/jacs.5b11740>.
- (36) Riedinger, A.; Ott, F. D.; Mule, A.; Mazzotti, S.; Knüsel, P. N.; Kress, S. J. P.; Prins, F.; Erwin, S. C.; Norris, D. J. An Intrinsic Growth Instability in Isotropic Materials Leads to Quasi-Two-Dimensional Nanoplatelets. *Nat. Mater.* **2017**, *16* (7), 743–748. <https://doi.org/10.1038/nmat4889>.

Chapter 5: The Effects of Alkylammonium Choice on the Stability and Performance of Quasi-2D Organolead Halide Perovskites

5.1 INTRODUCTION

In the years following the publication of the first reports of high efficiency organolead halide perovskite photovoltaic (PV) devices,¹ the field has seen significant advances in performance and stability.^{2,3} Most devices are based on the archetypal 3D perovskite methylammonium lead triiodide (MAPI),⁴ and the chemical flexibility of the material has been leveraged to introduce a range of small components and influence various physical parameters of the resulting perovskite.⁵⁻⁷ The chemical flexibility of the material can be stretched further, however, and bulky alkylammonium molecules have also been introduced into the material to yield a series of layered quasi-2D materials. The most commonly reported of these materials are the Ruddlesden-Popper phase (RPP) perovskites, and they have shown a variety of interesting chemical and optoelectronic properties linked to their unique quasi-2D structure.⁸⁻¹³

RPP perovskites are composed of quasi-2D layers of organolead halide perovskite material separated by layers of alkylammonium “spacer” molecules, and possess a generic stoichiometry of $A'_2A_{n-1}B_nX_{3n+1}$ (A' = alkylammonium spacer, A = monovalent cation such as methylammonium, B = divalent metal cation such as Pb^{2+} , and X = halide). The thickness of the perovskite sheets is frequently referred to as the n -phase of the material, where n indicates the number of adjacent PbI_6^{4-} octahedra in a given sheet. **Figure 5.1** provides example structures of $n = 4$ RPP perovskites composed of n -butylammonium and n -hexylammonium MAPI (butyl-MAPI and hexyl-MAPI, respectively).^{14,15} A common property among many of the RPP perovskites reported to

date is a higher degree of chemical stability compared to similar 3D perovskites, showing increased stability toward heat,¹⁶ humidity,^{10,17} and light.^{3,15,17} Because of this stability, these materials are at the forefront of research in efforts to improve the long term stability of perovskite devices in future commercial applications.¹⁸ However, more work remains before this goal can be realized. For example, relatively little has been done to understand the effect of the linker molecule on the physical and chemical properties of RPP perovskites in solar devices. Studies have reported that both bulky spacers like phenylethylammonium or octylammonium and smaller spacers like *n*-butylammonium can improve the moisture stability of the RPP perovskite^{10,19}; yet there are only few comparisons between molecules of more similar length. Those that do have noted differences arising from slight increases in alkylammonium chain length, thus demanding further investigation.¹⁵ Additionally, it has been suggested that RPP perovskites may be more compatible with Ag electrodes than typical 3D perovskites, but as with the effects of chain length, few studies have explored this topic.²⁰ The use of less expensive Ag electrodes in place of commonly used Au electrodes would be an important step in reducing module costs of future commercial perovskite solar cells. As such, this increased resistance to Ag electrode damage is another interesting topic for study.

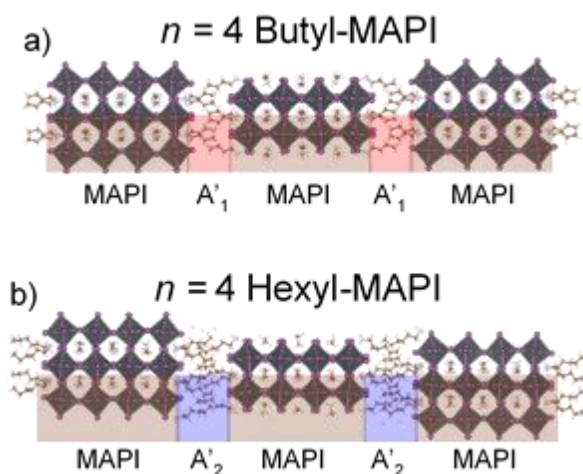


Figure 5.1 Crystal structures of a) $n = 4$ butyl-MAPI and b) $n = 4$ hexyl-MAPI, showing the layered quasi-2D structure of the materials. Dimensionally-confined layers of MAPI material (brown) are separated by a bi-layer of alkylammonium species (A'), either n -butylammonium (A'_1 , red) or n -hexylammonium (A'_2 , blue).

Here, we study the relative stability and performance of nominally $n = 5$ butyl- and hexyl-MAPI RPP perovskites under humid conditions, and directly compare the impact of Ag and Au electrodes on device performance. We refer to the composition as nominal due to previous work that has shown that RPP perovskite films frequently possess a n -phase gradient across the thickness of the film.²¹ Device performance testing shows that devices with Ag electrodes initially out-perform the Au devices, but that their performance decays much faster when the devices are exposed to 78% RH. In all cases, however, the hexyl-MAPI devices show improved performance and stability when compared to the butyl-MAPI devices, despite the mere two-carbon difference in the length of the alkylammonium chain. Using X-ray diffraction (XRD) and photoluminescence (PL) spectroscopy, we study how the two perovskites change during moisture exposure, and find that both exhibit disproportionation of the initial n -phases into lower- n materials, stabilizing the material and resulting in a lower rate of degradation

than 3D materials.²² Time-of-flight secondary ion mass spectrometry (ToF-SIMS) depth profiling provides chemical evidence of this passivation layer at the surface of the buried perovskite layer in full devices, and also indicate that hexyl-MAPI exhibits a lower degree of iodine leaching than butyl-MAPI; this may explain why hexyl-MAPI devices made using Ag electrodes out-perform similar butyl-MAPI devices. We explore this effect more closely using UV-Vis spectroscopy to measure the activation energy of halide mobility in $n = 1$ and 2 films of both butyl- and hexyl-MAPI material, and find that $n = 2$ hexyl-MAPI shows a higher barrier to solid state halide migration than $n = 2$ butyl-MAPI. The $n = 2$ phase of both materials is visible in the XRD and PL spectroscopy of $n = 5$ films, suggesting that this difference in halide mobility may partially explain the stability trends of the Ag devices. Importantly, both RPP perovskites show a higher barrier to halide mobility than previously reported 3D perovskites,²³ indicating that the relative halide mobility of an organolead halide perovskite may have a significant impact on its stability when used in concert with an Ag electrode.

5.2 EXPERIMENTAL

5.2.1 Film Fabrication

Perovskite precursor solutions were prepared by dissolving PbI_2 (99.99%, TCI), methylammonium iodide (MAI, GreatCell Solar), n -butylammonium iodide (nBAI, GreatCell Solar), and n -hexylammonium iodide (nHAI) in N,N -dimethylformamide (DMF, Ultra Dry, Acros Organics) with stirring. The total Pb^{2+} concentration of each solution was 0.5M and the other salts were added in the appropriate stoichiometric ratios to create $n = 1, 2$, and 5 solutions with a nominal composition of $(\text{nXA})_2\text{MA}_{n-1}\text{Pb}_n\text{I}_{3n+1}$ ($X = \text{H}$ or B). 2x2 cm TEC15 FTO substrates (Hartford Glass) were washed by sonication in a 1% (m/m) Contrex AP solution for 15 minutes before being scrubbed lightly and rinsed

thoroughly with ultra-pure (18 M Ω) water. Following rinsing, the substrates were then sonicated for 5 minutes each in acetone and ethanol before being dried using compressed air.

All perovskite film synthesis was performed in a glovebox (N₂ atmosphere, H₂O/O₂ < 5 ppm, VAC Atmospheres). Prior to film fabrication, an aliquot of precursor solution (typically <1 mL) was filtered using a 0.2 μ m PTFE syringe filter and transferred to a 2 mL bottle before being placed on a 75°C hot plate to heat for at least 15 minutes. Likewise, FTO substrates were placed on a calibrated 110°C hot plate prior to film fabrication. After heating, a substrate was quickly placed on the chuck of a spin coater, and an 80 μ L aliquot of the perovskite precursor solution was quickly deposited on the surface. Immediately after adding the solution, the substrate was accelerated to 5000 rpm and held at this speed for 20 seconds. Within several seconds, the film turned a dark brown color as the DMF evaporated and the perovskite thin film formed. After spinning ceased, the substrate was removed from the spin coater and allowed to finish cooling.

5.2.2 Device Fabrication

To fabricate photovoltaic devices, a 3 mm strip of FTO was etched from each substrate using 2M HCl (ACS Grade, Fisher Scientific) and Zn powder (99.9%, Alfa Aesar) using a piece of tape as a mask. The substrate was then cleaned as described above, and following drying it was treated for 25 minutes under UV/O₃ (BioForce Nanosciences) to create a hydrophilic surface. Following substrate cleaning, a 1:2 solution of PEDOT:PSS (Heraeus) in methanol was prepared by sonication. Each substrate was then placed on the chuck of a spin coater in air, and 2 drops of the PEDOT:PSS solution was added to the surface after being passed through a 0.2 μ m PTFE syringe filter. The substrate was then ramped up to 4000 rpm in 3 seconds and held there

for 40 seconds before being ramped down in 3 seconds. The substrate was then placed on a calibrated 150°C hotplate for 10 minutes before being brought into the glovebox. The perovskite layer was then deposited using the above method. An AMOD thermal evaporator (base pressure 8×10^{-7} torr) was used to create sequential films of C₆₀ (30 nm) and (bathocuproine (BCP, 99.9%, SigmaAldrich) on the surface of the perovskite layer. The first 10 nm of the C₆₀ layer was deposited at a rate of 0.2 Å/s to ensure even coverage, while the next 20 nm were deposited at a rate of 1 Å/s; the BCP was deposited at a constant rate of 0.2 Å/s. 1.5x1.5 cm shadow masks were used to control the deposition onto the surface. Following deposition, roughly 2 mm x 1 cm strips of BCP/C₆₀/perovskite/PEDOT:PSS were removed from the sides perpendicular to the etched side to expose the FTO beneath. Following this, 125 nm of Ag or Au (99.99%, Kurt J. Lesker) were then deposited on the devices through a patterned shadow mask. Ag was deposited using the AMOD thermal evaporator, while Au was deposited via electron beam evaporation using a Cooke Evaporation System. Similar to the C₆₀ film, the first 10 nm of both metals were deposited at 0.2 Å/s and the last 110 nm were deposited at 1 Å/s. The finished devices were stored in an Ar-filled glovebox (H₂O/O₂ < 0.1 ppm, MBraun) until testing. To create devices for spectroscopic analysis, the original 1.5x1.5 cm shadow mask was used.

5.2.3 Device Testing

Device testing was performed using a xenon solar simulator (Oriel) with a 1.5AM-G filter and a CHI 660D potentiostat, and power density was normalized to 1 sun using an optical power meter (Newport 1916-C) equipped with a thermopile sensor (Newport, 818P-020-12). Cyclic voltammograms were measured from 0.2 to -1.2 V at a sweep rate of 150 mV/s, under ambient air at room temperature. A 0.08 cm² mask was

used to specify the active surface area of each device. For stability testing, devices were stored in the dark in a sealed container under ambient air holding a saturated solution of KCl with a relative humidity of approximately 78%. For stability measurements, 14 individual devices for each type of perovskite were tested, and the results at each time point averaged. An identical moisture exposure procedure was used for devices analyzed spectroscopically, but no electrochemical testing was used. After moisture exposure and before spectroscopic analysis, the Ag or Au electrode was removed using a piece of tape.

Devices analyzed via ToF-SIMS (ION-TOF) for H₂O exposure were prepared as above, but were not electrochemically tested to prevent exposure to the intense light. Instead, for each type of perovskite tested, a typical two-cell device was broken in half, and one half of each device was left inside the glovebox while the other half was exposed to the water for the requisite amount of time. After exposure was completed, the device was then brought into the glovebox and loaded with the unexposed half into an inert atmosphere transfer vessel to prevent exposure to the atmosphere while transferring to the ToF-SIMS instrument. The devices were then placed in high vacuum ($\sim 1 \times 10^{-9}$ torr) for 2 weeks to remove any lightly adsorbed water inside the devices.

ToF-SIMS depth profiling in negative polarity was performed using a Bi₃⁺ (30 keV ion energy, 0.8 pA measured sample current) analysis beam raster scanning a 100x100 μm^2 area located within the boundaries of a larger crater (300x300 μm^2) created using a Cs⁺ sputtering beam (500 eV ion energy, ~ 40 nA measured sample current). The pressure inside the analysis chamber was typically below 1.5×10^{-9} torr during analysis. Photoluminescence was performed on a Horiba Jobin Yvon Fluorolog3 spectrophotometer, using an excitation wavelength of 450 nm and a typical 90° detector geometry, with the film held at 45°. Excitation was performed on both the front (shining directly on the perovskite film) and the back (shining through the glass) of the films. X-

ray diffraction was performed on a Rigaku Ultima IV diffractometer in a thin film configuration using a Cu K α X-ray source. Scanning electron microscopy (SEM) was performed with an FEI Quanta 650 ESEM, using an accelerating voltage of 15 kV at a vacuum of approximately 5×10^{-6} torr.

A UV-Vis spectrometer (Hewlett-Packard 8453A) was used to monitor halide migration between bromide and iodide films. Films of $n = 1$ and 2 nXA-MAPI and nXA-MAPBr ($X = \text{B}$ or H) were placed face-to-face inside the N₂ glovebox and held together using small binder clips on two sides; $n = 1$ films were placed together and $n = 2$ films were placed together, exclusively. The paired films were then brought into the open air and a UV-Vis spectra recorded through the stack, with the light passing through the Br-film first. After a baseline spectrum was recorded, each pair of films was placed I-film down on a calibrated hot plate to induce halide migration. Temperatures of 60, 76.2, 90.1, 109.5, and 123.8 °C were measured using a thermocouple. With the exception of the first data points at 2 and 10 minutes of heating, the films were typically allowed to heat for at least 10 minutes between spectra acquisition.

5.3 RESULTS AND DISCUSSION

5.3.1 Electrochemical Testing and Stability

To determine the effect of perovskite composition on the initial performance and long-term stability of photovoltaic devices made using both butyl- and hexyl-MAPI, we performed cyclic voltametric analysis of planar p-i-n devices fabricated with both Ag and Au electrodes. For brevity, we will frequently refer to the devices using a “metal-spacer” nomenclature, such that an Au-butyl device refers to an $n = 5$ butyl-MAPI device with an Au electrode. We find that, initially, the Ag devices generally perform better than the Au devices while the hexyl-MAPI devices out-perform the butyl-MAPI (**Figure C.1**); this

yielded an average PCE order of Ag-hexyl > Au-hexyl > Ag-butyl > Au-butyl. In general, the bulk of the difference in the PCEs of the devices appears to come from differences in devices J_{sc} (**Figure C.1b**). As the butyl-MAPI and hexyl-MAPI films are both of similar thickness (**Figure C.2**), these differences are likely due to increased carrier recombination in the butyl-MAPI devices.

After measuring the initial performance, we exposed the devices to 78% RH at room temperature without additional encapsulation to better study how moisture affected the performance of the two RPP materials. **Figure 5.2** shows that the PCE of all of the devices normalized to maximum performance begins to degrade within the first 3 hours of exposure, but that the decay is more marked in both the Ag- and Au-butyl devices. Indeed, the Ag-butyl devices fail completely by 12 hours of exposure and the Au-butyl devices show a roughly 50% decrease in performance; the latter case appears to be faster than the degradation observed in similar $n = 4$ materials^{17,22} and may indicate that a nominal $n = 5$ film composition is less intrinsically stable. The relative lack of device stability in the Ag-butyl samples is expected, based on previous reports of the incompatibility of Ag contacts and perovskite absorber layers.^{20,24,25} Normalized solar cell metrics (**Figure C.3**) show that much of the early decay is due primarily to losses of V_{oc} , with a gradual decrease in fill factor (FF) playing an increasingly large role as the experiment progresses. The Au-butyl devices eventually show complete loss of performance after 6 days, and in the days preceding this a clear decrease in J_{sc} is also observed. In contrast to the butyl-MAPI devices, both of the hexyl-MAPI devices possess at least 70% of their initial performance after 12 hours of exposure (**Figure 5.2**). The Ag-hexyl cells show continued degradation, and eventually failed completely after about 6 days. In contrast, the Au-hexyl devices demonstrate remarkable stability and maintained approximately 40% of their initial PCE from over the course of 40 days. During this time,

both the V_{oc} and FF gradually decreased while the J_{sc} appeared to improve slightly (**Figure C.3**). We tentatively attribute this increase to the passivation of defects within the material through RPP perovskite disproportionation, improving carrier extraction from the bulk of the film.

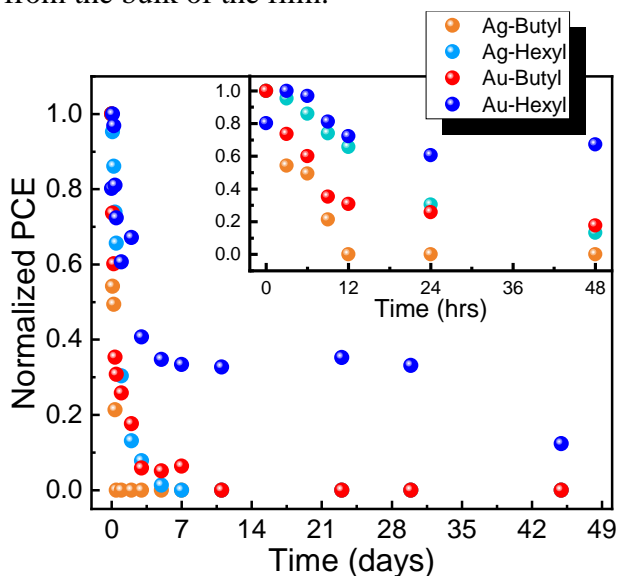


Figure 5.2 Normalized PCE of butyl- and hexyl-MAPI devices fabricated using both Ag, and Au electrodes, exposed to 78%RH. All devices except for the Au-hexyl devices showed complete degradation within two weeks. The inset shows the rate of PCE loss over the first two days.

Previous work on a range of RPP perovskites has shown that they possess greater stability in humid environments than typical 3D perovskites, both chemically and electrochemically.^{7,10,17,22,26} This increased stability has been attributed to the hydrophobicity of the alkylammonium spacer molecules, suggested to inhibit moisture ingress,¹⁰ as well as increased thermodynamic stability of the RPP phase, which arises from the presence of the hydrophobic chains in the crystal structure.¹⁹ The latter property has also been shown to lead to a disproportionation-based degradation mechanism in *n*-butylammonium perovskites exposed to humidity, leading to the formation of a

passivating low- n surface layer which slows the rate of degradation.^{22,26} Such a process may explain the increased longevity of the Au devices studied here, providing both a means of passivation and reduction in the number of recombination centers.⁷ It is reasonable to predict that hexyl-MAPI materials may behave similarly to butyl-MAPI under humid conditions, and indeed Spanopoulos *et al.* have shown the RPP perovskites made with closely related spacers possess similar stability under dark, humid conditions.¹⁵ However, these observations provide little explanation for the relative differences in stability for hexyl- and butyl-MAPI when using Ag contacts; therefore, additional crystallographic, spectroscopic, and chemical characterization is needed to explore this difference more closely.

5.3.2 XRD Analysis

To better understand how the crystallography of the various perovskites changes in response to moisture exposure and in the presence of Ag and Au contacts, we analyzed the XRD spectra of bare films and Ag/Au devices exposed to 78%RH for 48 hours (**Figures C.4-6**). Due to the relatively high degree of decay evidenced by both the Au- and Ag-butyl devices at 8 hours of exposure, we chose to use this time point throughout the remaining work to highlight the differences in our various samples; data from later time points is available in the Supporting Information. As seen in **Figure 5.3**, all of the as-synthesized perovskites showed two strong XRD peaks at approximately 14.2 and 24.8°, corresponding to the (111) and (202) planes of the material, respectively.^{15,17} After 8 hours, there were no visible changes to the spectra of any hexyl-MAPI samples, while the bare butyl-MAPI film and Ag-butyl device both showed the formation of peaks below 11° which can be attributed to low- n phases of the RPP perovskites (**Figure 5.2a**). The

presence of low- n peaks prior to moisture exposure may be due to the crystallization of a range of n -phase materials during film fabrication, as explored in previous works.^{8,27}

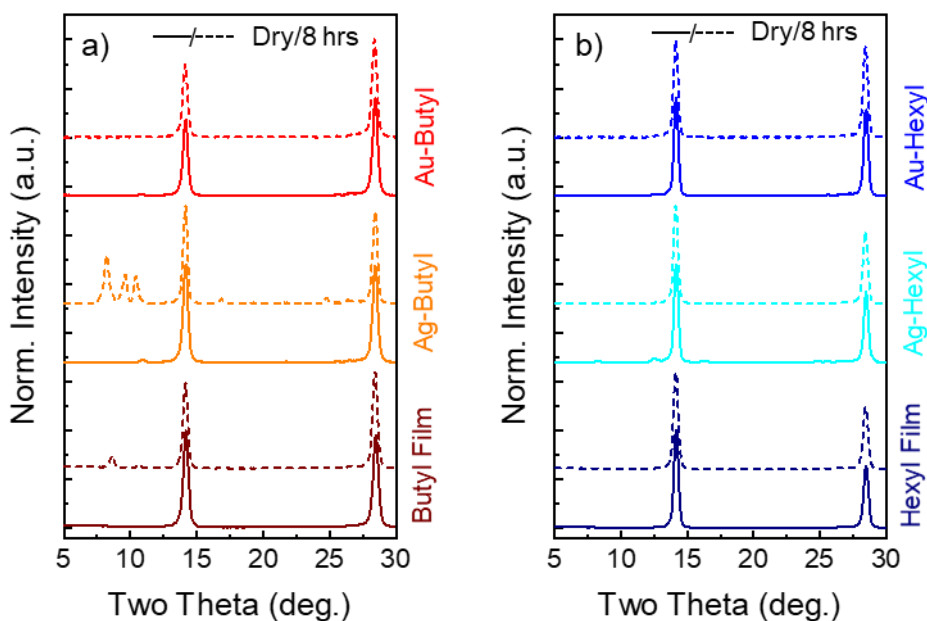


Figure 5.3 XRD spectra of bare films and Ag/Au-perovskite devices for a) butyl-MAPI and b) hexyl-MAPI samples before and after 8 hours of exposure to 78%RH. All materials show similar spectra before exposure, but the butyl-MAPI film and Ag-butyl device both show the formation of low- n phases after exposure.

Closer inspection of the region below $2\theta = 12^\circ$ shows that both the bare as-synthesized hexyl- and butyl-MAPI films exhibited low- n peaks (**Figure C.4b,d**), while both the Au and Ag devices showed very weak peaks in this region (**Figures C.5,6**). These peaks correspond to $n = 2-4$ phases in both materials,¹⁴ and did not change over 48 hours of exposure in the Au devices. In contrast, we observed the growth of these peaks in both the bare butyl-MAPI film and in the Ag-Butyl device over the course of the experiment (**Figures C.4d and C.5d**), coinciding with a significant decrease in the

intensity of the primary (111) and (202) peaks. While the low- n phases formed in both processes are almost identical based on peak position, the rate of degradation appears much higher in the case of the Ag-butyl devices than the bare film. Of note, no crystalline PbI_2 was observed to form in any case, as frequently occurs in 3D MAPI, showing that the addition of the alkylammonium spacers does fundamentally affect the degradation mechanism of the RPP materials.

The apparent relationship between the enhanced degradation rate of the Ag-butyl device and the Ag contact is expected, as Ag electrodes are well-known to be generally incompatible with perovskite PV devices. Under even ambient conditions, diffusion of iodine throughout the cell results in the formation of resistive AgI species near the electrode.²⁴ The formation of this material leads to chemical damage to both the perovskite layer and the Ag contact of the device, and increases the resistivity of the device.^{20,24} To explain our XRD results, we postulate that as I^- diffuses through the C_{60} layer of the device it reacts at the Ag electrode to form amorphous AgI and decreases the local concentration of I^- . This process results in an I^- concentration gradient across the C_{60} layer, increasing the rate of I^- leaching from the butyl-MAPI and speeding the degradation process relative to the bare film. Within this framework, it appears that the hexyl-MAPI material must be less likely to leach I^- , either due to a lack of perovskite disproportionation/degradation or a higher intrinsic stability; both effects may be due to the extra length of the n -hexylammonium spacer. Previous work from Chen *et al.* showed that RPP perovskites made with phenylethylammonium, a larger alkylammonium species, also showed a significant increased resistance to decomposition in the presence of an Ag electrode.²⁰ Their work was performed using an $n = 1$ species, however, and may not be directly applicable to our larger- n materials. Thus, to explore what effect n -

phase composition may have on degradation, we used a more phase-sensitive technique than XRD to study the composition of our materials.

5.3.3 PL Analysis

One promising technique for identifying and studying which n -phases are present in our films is PL spectroscopy, which can be used in both bare films and perovskite devices. Due to the effects of quantum confinement of electrons within the individual RPP sheets, the band gap of each n -phase becomes wider as n decreases, resulting in a red shift of the PL emission.¹² As a result, each n -phase has a distinct PL emission peak that can be identified and studied by measuring the PL spectrum of a given RPP film. Additionally, by monitoring each spectrum over 48 hours of exposure, we can explore how the composition of the film changes as degradation occurs, and attempt to compare this to the XRD results above. **Figure 5.4a** shows the normalized PL spectra of our films and devices before and after 8 hours of exposure; spectra from 0 hours to 48 hours are presented in **Figures C.7-9**.

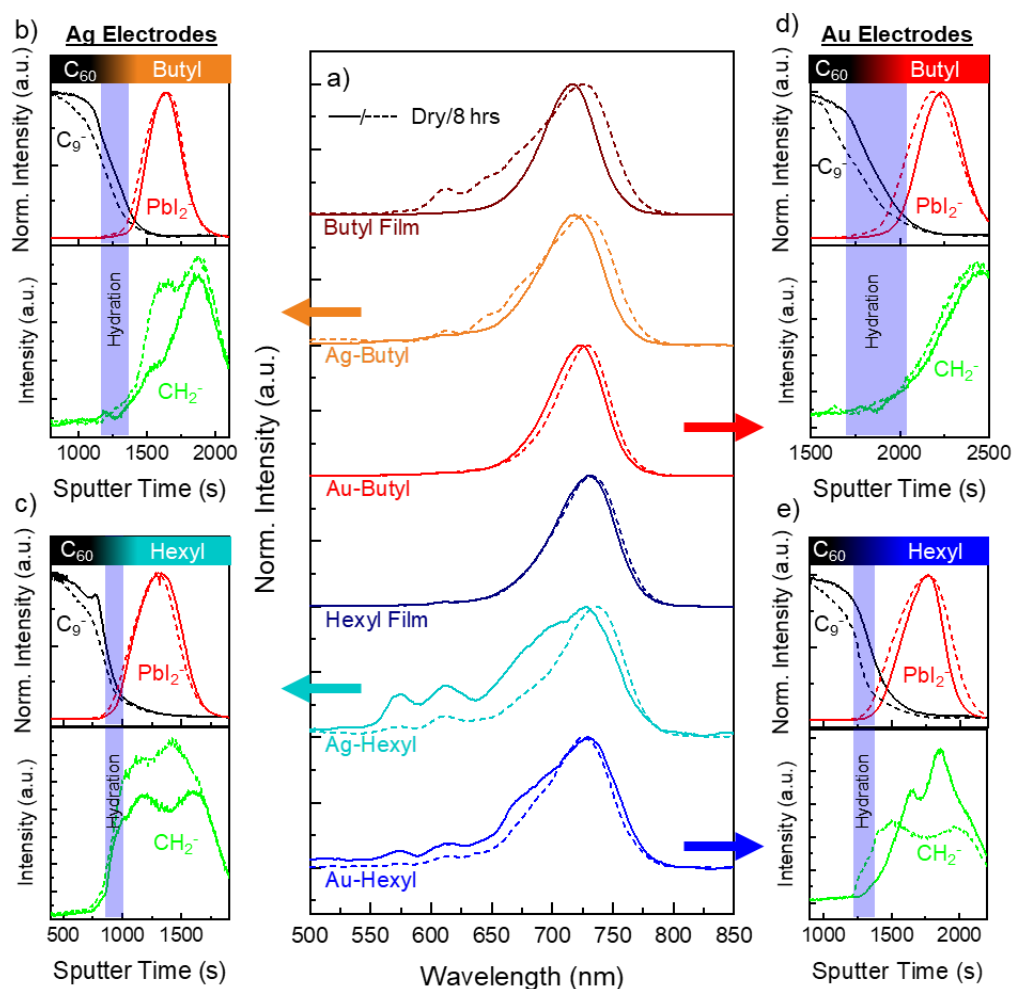


Figure 5.4 Normalized PL spectra (a) of bare butyl- and hexyl-MAPI films and Ag/Au devices of each material, before and after exposure to 78%RH for 8 hours. The butyl-MAPI film and Ag-butyl device both show the formation of low- n species below the $n > 5$ peak at 715 nm following exposure, while the Ag/Au-hexyl devices both show an apparent loss of signal in these regions following exposure. ToF-SIMS depth profiles of the C_{60} /perovskite interface of (b) Ag-butyl, (c) Ag-hexyl, (d) Au-butyl, and (e) Au-hexyl devices. The top portion of b-e shows the C_{60} (C_9^-) and inorganic portions of the perovskites (PbI_2^-) before and after 8 hours of exposure, while the bottom portion shows the organic portion (CH_2^-) of the perovskite. In all cases, expansion of the perovskite is observed in the hydration region of the device (blue box), indicating perovskite degradation.

In general, the spectra of the as-synthesized butyl-MAPI films were dominated by a single peak near 715 nm, while the predominant peak of the hexyl-MAPI samples appeared at 730 nm. Both values are larger than would be expected for a $n = 5$ film, and thus we assign the peak to an $n > 5$ phase distinct from a typical 3D perovskite. This unique phase is the result of a built-in n -phase gradient in the films formed during fabrication.²⁸ As a result, while the nominal composition of each film should be $n = 5$, the upper third of the film is instead likely composed of this $n > 5$ phase and the lower two thirds composed of mixtures of lower- n phases.²¹ However, the 15 nm difference between the emission of the two materials indicates that the hexyl-MAPI material has a narrower band gap than the butyl-MAPI material, likely resulting in increased photon absorption and at least a portion of the improved PV performance of the material. After 8 hours of exposure to humidity there was no change in the hexyl-MAPI spectra, in good agreement with the previous XRD results. We did, however, observe an increase in the peaks corresponding to $n = 2, 3, 4$, and 5 phases in the butyl-MAPI film, and a red shift in the primary PL peak to 725 nm. This agrees with the previously-reported disproportionation-driven degradation mechanism observed in these materials, as well as the formation of low- n species in the XRD at similar exposure levels (**Figure 5.3a**).^{22,26} Over the course of 48 hours, the relative intensity of the low- n peaks in the butyl-MAPI film continued to increase, but no further spectral changes were observed in the hexyl-MAPI film (**Figure C.7**). This again shows the increased stability of the hexyl-MAPI material toward water-driven degradation.

Prior to exposure, all of the butyl-MAPI devices showed the same primary peaks as the bare films and showed no distinct low- n peaks before exposure to humidity (**Figure 5.4a**, top). After 8 hours, both Ag- and Au-butyl devices showed a red-shift of the $n > 5$ peak like that observed in the bare film. In the Ag-butyl film this shift is

accompanied by the appearance of low- n species, while in the Au-butyl film no low- n peak formation is observed. These results appear to match with the PCE and XRD results that showed the increased stability of Au-butyl over Ag-butyl. In contrast to the small changes observed in the butyl-MAPI devices, the as-synthesized Ag-hexyl and Au-hexyl devices both showed what appeared to be significant $n = 2-5$ peaks prior to exposure (**Figure 5.4a**). After 8 hours, these peaks decreased significantly relative to the $n > 5$ peak, which narrowed relative to the fresh device. (**Figure C.8,9**).

Closer inspection of the un-normalized spectra, however, (**Figure C.10**) showed that these changes were artifacts of normalization, rather than true changes to the phases present in the material. Due to the presence of the C₆₀ overlayer on top of the perovskite film, we observed significant quenching of the PL emission due to charge transfer from the perovskite to the C₆₀ in the dry devices.²⁹ After moisture exposure, the intensity of the primary $n > 5$ peak of both hexyl-MAPI devices increased significantly due to less quenching via charge transfer, while the low- n peaks did not change. This resulted in the apparent disparity between the normalized spectra in **Figure 5.4a**. Instead of a decrease in low- n material with exposure, the hexyl-MAPI spectra in **Figure C.10** show that the intensity of the $n = 2-5$ phases is similar in all dry films, in agreement with the presence of low- n peaks in the XRD spectra of the films prior to exposure (**Figures C.5,6**). Based on previous reports, we hypothesize that the increase in the $n > 5$ peaks is due to the formation of a low- n passivation layer at the surface of the hexyl-MAPI films inhibited quenching of the PL signal by the C₆₀. Similar increases in PL intensity are also observed in the Ag/Au-butyl devices (**Figure C.10**), the result of similar processes occurring at the surface of these films as well. While such a passivation layer obviously inhibits charge transfer within the device, it may also act to inhibit further moisture-driven damage of the

film, and thus likely plays a significant role in the improved stability of the RPP perovskites.

This stability was borne out by PL spectra over 48 hours of degradation (**Figures C.7-9**), which generally showed changes similar to those observed in the XRD spectra over the same time period (**Figures C.4-6**). One exception was the Ag-butyl sample, which appeared to show only a slight increase in low- n phases in the PL up to 12 hours, despite significant formation of low- n species observed in the XRD. This deviation in the results from the two techniques is likely due to the inhomogeneous degradation of the material under the Ag electrode, which results in extensive damage to some areas of the film and relatively little damage to others (**Figure C.11**). We also note that damage only occurs to the butyl-MAPI perovskite under the Ag electrode, directly implicating the metal contact in the degradation process. After 12 hours of exposure, the Ag-butyl device showed a complete loss of PL emission from 600-800 nm, and showed only a single broad peak centered near 515 nm (**Figure C.8b**). This peak represents the $n = 1$ phase²² and indicates that this n -phase is likely the final product of butyl-MAPI degradation. In contrast, the Ag-hexyl and both Au devices showed almost no change in PL over the same time period, in good agreement with our previous results on the relative stability of these materials.

From PL analysis of the films, we were able to determine that surface passivation of both the hexyl- and butyl-MAPI films occurs with moisture exposure, likely due to the formation of a low- n surface layer following disproportionation of the initial $n > 5$ material into lower- n species. In the butyl-MAPI samples this manifested itself as the clear formation of higher intensity low- n peaks, which may be due in part to the formation of discrete crystallites of low- n material within the film with degradation.²² The hexyl-MAPI films did not appear to show a similar increase in the intensity of these

peaks, possibly precluding similar growth in this material. Instead, the presence of low- n peaks in the as-synthesized spectra likely indicates that some quantity of these low- n phases already exists near the surface of the freshly-cast films, and by extension, the presence of an already-formed passivation layer following synthesis. Recent work from Kanatzidis and coworkers has shown that the n -hexylammonium-based RPP perovskites possess valence and conduction band energies capable of enabling the transfer of photogenerated electrons from low- n phases to higher- n phases.¹⁵ In the absence of low- n crystallites like those found in butyl-MAPI which could act as local quantum wells and increase the signal of low- n species, the surface passivation layer of a hexyl-MAPI film would be expected to discharge photogenerated carriers into the $n > 5$ phase, reducing PL from the low- n species formed. Unfortunately, this process prevents us from using PL to determine if the hexyl-MAPI materials are degrading into lower- n phases during moisture exposure, limiting our ability to compare them to the butyl-MAPI devices. To circumvent this problem, we turned to a more direct chemical analysis of the devices to study how degradation differs between them.

5.3.4 ToF-SIMS Analysis

As the contact metal used to fabricate the device clearly impacted stability, it was important to study full device stacks as opposed to bare films; this required a chemical analysis technique which could access the perovskite through the metal and C₆₀ layers above it. The depth of the buried perovskite films (~150 nm) compared to the penetration depth of X-ray photoelectron spectroscopy precluded the use of XPS to study the chemical changes occurring with moisture exposure in our devices. Instead, we used time-of-flight secondary ion mass spectrometry (ToF-SIMS) depth profiling to both access and study the perovskite layer before and after 8 hours of exposure to 78% RH.

This technique has been shown to be both chemically and spatially sensitive enough to accurately study the chemistry of buried interfaces in devices and materials such as these.³⁰

Figures 5.4b-e show the C_{60} /perovskite interface of our various devices before and after the devices were subjected to 8 hours of exposure to 78%RH, the same level of degradation experienced by the cells studied by PL in **Figure 5.4a**. A blue bar in each graph represents the hydration layer which forms as water from the atmosphere diffuses to the relatively impermeable perovskite layer and becomes trapped at the interface with the C_{60} , as determined using the OH^- depth profiles of exposed devices (**Figure C.12**); it is in this region previous work has shown chemical changes typically occur in perovskite devices.²² Studying the C_{60} and inorganic portion of the perovskite (represented by the C_9^- and PbI_2^- secondary ions, respectively) for each device we find that the C_{60} /perovskite interface region appeared to expand after exposure to humidity, as indicated by the leftward shift of both the C_9^- and PbI_2^- species after 8 hours. We attribute this shift to a slight expansion of the perovskite layer with the formation of the low- n surface layer, and appears to be most pronounced in the Au devices.

In addition to the inorganic species which compose the perovskite, we also studied organic ions that are likely more diagnostic for changes in the relative n -phase. Here, we have used the CH_2^- secondary ion as a proxy for the MA, nBA, and nHA species in the perovskite. Based on the stoichiometry of the RPP phases ($A'_2A_{n-1}B_nX_{3n+1}$) we expect that a decrease in n will result in an increase in the intensity of this ion, indicative of a higher number of organic species per inorganic component in the perovskite. As seen in the bottom halves of **Figures 5.4b-e** many of the perovskite devices do show changes in the CH_2^- profile after humidity exposure, and we use the Ag-butyl device (**Figure 5.4b**) as a clear example. Prior to exposure, we observed two peaks

in the profile. The smaller peak near 1500 s is from alkylammonium species in the perovskite while the larger peak to the right is largely from the organic PEDOT:PSS layer (**Figure C.13**). After 8 hours of exposure to 78%RH, we observed a clear shift of the CH_2^- profile toward the hydration region and a concurrent increase in the total intensity of the left alkylammonium peak; this is consistent with the similar leftward shift in the PbI_2^- profile. Together, this indicates the expansion of the perovskite and the formation of low- n species at the C_{60} /perovskite interface, consistent with the surface passivation and low- n formation evidenced in the 8 hour PL spectrum of the Ag-butyl device in **Figure 5.4a**. The Ag-hexyl and Au-hexyl CH_2^- profiles show similar changes, reinforcing our hypothesis that this low- n formation is a conserved degradation mechanism between different types of perovskite within the larger RPP family.

The Au-butyl device did not show a significant increase in the CH_2^- after exposure, but due to the relatively high PL signal of the fresh device (**Figure C.10e**) compared to the PL from the fresh Ag-butyl device, we believe that this may indicate that some degree of low- n growth has already occurred due to sample heating during Au deposition. Previous reports have shown that both 3D and RPP perovskites are susceptible to thermal damage,¹⁶ and we observed a similar increase in the PL signal of the dry Au-hexyl when compared to the Ag-hexyl (**Figure C.10d,f**). This may indicate that a similar thermal decomposition process is at work in both materials, but the clear change in the CH_2^- profile and small degree of increased PL intensity shows that hexyl-MAPI is more resistant to this heating than butyl-MAPI. This thermal degradation may also explain why the Ag devices tended to show better initial performance than the Au devices (**Figure C.1**), a result of increased recombination at the C_{60} /perovskite interface and decreased J_{sc} .

Building on this analysis, we next explored how I^- migration to the Au or Ag electrode differed between devices with humidity exposure. We began by studying the quantity of AgI^- and AuI^- , which are the most likely ionic species to represent AgI and AuI, present in the devices. While differences in ionization probability between the two MI^- ($M = Au$ or Ag) species prevented direct comparison, the relative yield of each species before and after water exposure could be compared between similar devices to act as a proxy for total species abundance in each device. The total yield of MI^- , measured from the surface of the metal contact to the metal/BCP/ C_{60} interface, was collected for all four device types, before and after 8 hours of moisture exposure, and reported in **Figure 5.5a**. The butyl-MAPI devices consistently showed higher MI^- yields than hexyl-MAPI devices, and thus we conclude that a higher abundance of the species are present in the butyl-MAPI devices. Given that the amount of Au or Ag in the electrode is expected to be identical in each device, regardless of perovskite type, our results show that the butyl-MAPI films exhibit a higher degree of I^- leaching than similar hexyl-MAPI films before and after moisture exposure.

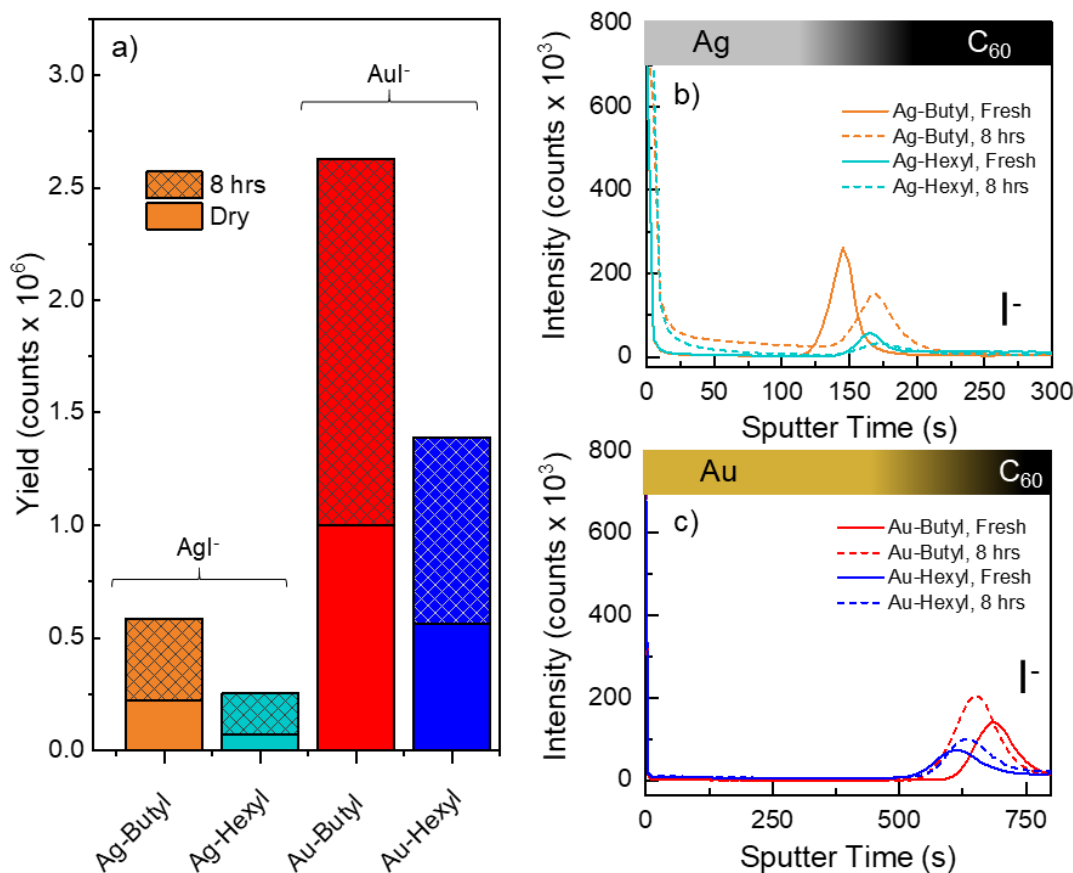


Figure 5.5 a) Yield of Ag/AuI⁻ species from the metal contact and metal/C₆₀ interface for all butyl- and hexyl-MAPI devices, before (solid) and after (solid + dashed) 8 hours of exposure to 78%RH. b) I⁻ depth profiles for Ag-hexyl/butyl devices before and after moisture exposure. The interface I⁻ peak decreases after exposure as more I⁻ migrates into the metal contact. c) I⁻ depth profiles for Au-hexyl/butyl devices before and after moisture exposure. The interface I⁻ peak increases following exposure as more I⁻ diffuses to the Au electrode and accumulates.

This is further supported by I⁻ depth profiles for all devices measured in the same region of the devices (**Figure 5.5b,c**). All of the Ag-perovskite device profiles showed a clear peak at the metal/C₆₀ interface due to a build-up of iodine prior to moisture exposure, and this peak decreased in intensity in both devices following exposure. Taken

with a concurrent increase in I^- signal within the Ag electrode itself, these changes indicated the diffusion of I^- into the Ag contact and the subsequent formation of AgI within the electrode itself. The consumption of iodide to form AgI likely created an I^- gradient across the C_{60} layer, driving further iodide leaching from the perovskite in accordance with Le Chatelier's principle, and indicated by pictures of the damage which occurred to the Ag-butyl device during exposure (**Figure C.11**). In contrast, a similar I^- peak in the Au devices (**Figure 5.5c**) increased following exposure, evidence of I^- migration to the electrode but a low rate of reaction between the iodide and the metallic gold. This low rate of reaction at the Au/ C_{60} interface decreased the driving force for iodide migration through the C_{60} , and therefore decreased the driving force for iodide leaching from the perovskite relative to Ag devices; this, in addition to the previously reported detrimental effects of AgI formation,²⁴ may partially explain the increased stability of the Au perovskite devices. Importantly, and similar to the MI^- results, the intensity of the I^- signal was always higher in butyl-MAPI devices than in hexyl-MAPI devices. Given that we would expect similar rates of AgI or AuI formation in both butyl- and hexyl-MAPI devices, and thus similar driving forces for I^- migration across the C_{60} layer, the lower I^- signal in the M/C_{60} interfaces of the hexyl-MAPI devices suggests the perovskite leaches I^- less readily than butyl-MAPI and is more chemically stable.

Together with the ToF-SIMS depth profiles at the C_{60} /perovskite interface, these results indicate that while both of the RPP perovskites studied here undergo a surface transformation in the presence of moisture, the hexyl-MAPI appears to be more chemically stable and less likely to leach iodide during the process. Based on our present results and previous work on perovskite solar cells, this stability has clear benefits for devices fabricated using Ag electrodes, and is clearly important in Au devices as well. Importantly, and regardless of metal choice, if one considers that I^- leaching is a likely

indicator of perovskite damage,²⁰ it follows that a low rate of I^- loss from the perovskite is a sign of increased environmental stability. As a result, studying halide movement within butyl- and hexyl-MAPI may provide additional insight into their relative stability. While the ToF-SIMS experiments reported here are well-controlled and expected to give accurate results for the relative differences in I^- leaching from hexyl- and butyl-MAPI films, it is difficult to make more precise quantitative measurements using the technique.

5.3.5 UV-Vis Halide Mobility Analysis

Work by Kamat and coworkers on MAPI and MAPBr thin films showed that it is possible to monitor solid state I^- and Br^- diffusion between and within perovskite thin films using UV-Vis spectroscopy, and calculated an activation energy for halide ion movement within the material.²³ By binding a pure MAPbI (iodo) film and a pure MAPBr (bromo) film together face-to-face and heating the resulting iodo/bromo pair, they were able to induce halide migration between the films, ultimately resulting in two films with a 1:1 I/Br composition. Inspired by this, we performed similar measurements on hexyl- and butyl-MAPI materials to study the relative ease of I^- mobility in each material. Due to the lack of a clearly trackable peak from the $n = 5$ phase of the butyl-MAPI material (**Figure C.14**), we chose to conduct measurements on $n = 1$ and 2 phases of the two RPP perovskites. The UV-Vis spectra of both iodo and bromo $n = 1$ and 2 RPP perovskites materials showed clear excitonic features for each phase, regardless of the spacer molecule (**Figure C.15**). For $n = 1$ films we monitored the absorbance of the iodo peak near 510 nm, while for the $n = 2$ films we monitored the iodo peak near 575 nm.

Figure 5.6a shows the UV-Vis spectra for a hexyl-iodo/bromo pair held at 100°C over the course of 3 hours. Over time, the peak signal decreased as the I/Br composition of the film changed. By tracking the rate at which the absorbance of the pure iodo peak decreased, we were able to determine a rate constant for halide migration by fitting the data to a first order exponential decay.²³ **Figures C.16-19a,b** show the raw spectral data for the $n = 1$ and 2 iodo/bromo pairs and the resulting fitted decay curves. We then used rate constants from the fitted curves to generate Arrhenius plots for each RPP material and determine the activation energy for ion mobility in the $n = 1$ and 2 hexyl- and butyl-MAPI RPP perovskites. For the $n = 2$ phase, we found that hexyl-MAPI showed a 14 kJ/mol larger activation energy for halide mobility than butyl-MAPI (**Figure 5.6b**), and thus a lower ion mobility within the material. Given that a lower barrier to ion mobility within a material increases the rate at which the ion leaches from the material,²⁰ the difference in these values agrees with the differences in the MI ion yields and I^- peak intensities measured using ToF-SIMS.

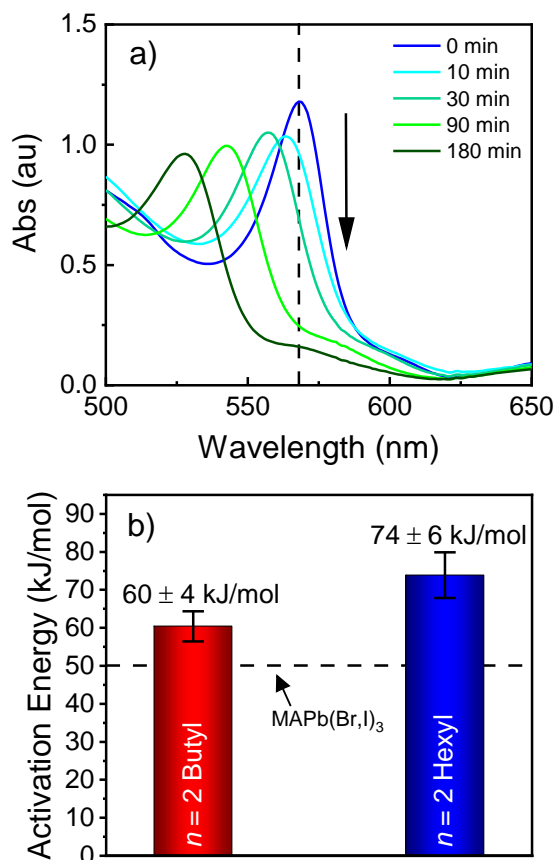


Figure 5.6 a) UV-Vis spectra of paired $n = 2$ iodo/bromo hexyl-MAPI films held at 100°C for 3 hours. As iodide and bromide species exchange, the $n = 1$ iodo peak at 575 nm decreased. b) Activation energies for halide mobility in $n = 2$ butyl- and hexyl-MAPI perovskite determined by UV-Vis spectroscopy. The dashed line represents the previously reported activation energy of a 3D perovskite. (ref. 23)

Interestingly, the $n = 1$ butyl-MAPI showed a much larger activation energy than the comparable hexyl-MAPI film (**Figure C.20**), indicative of much slower ion migration within the butyl-MAPI material. We propose that this change from the $n = 2$ phase results may be due to differences in crystal packing of the hexyl- and butyl-MAPI materials,³¹ but more detailed crystallographic study will be needed to determine the exact cause. The $n = 1$ phase was previously shown to be the final product of butyl-MAPI degradation

(**Figure C.8**), and thus the larger activation energy for this phase of the perovskite is reasonable. However, given the rapid onset of degradation we observe it appears that the formation of the $n = 1$ phase may not be contributing to the stabilization of the film as a whole. As a result, we propose that the degradation of the $n = 2$ phase may play a more significant role in determining the rate of degradation, and consider the $n = 2$ results to be of more importance to the current work.

Regardless of phase, all of the RPP materials showed a larger activation energy than that measured by Kamat and coworkers for a more typical 3D perovskite material (50.68 kJ/mol, dashed line in **Figure 5.6b**).²³ A similar difference in halide mobility between 3D and quasi-2D perovskites was also reported by Chen *et al.* in phenylethylammonium-based RPP perovskites, which theoretical calculations showed was the result of an increased barrier to iodide diffusion along the plane of an $n = 1$ sheet and a preferential sequestration of iodine vacancies at the apical position of the PbI_6^{4-} octahedra.²⁰ Our results indicate that $n = 1$ and 2 n -hexylammonium and n -butylammonium RPP perovskites may exhibit similar barriers to halide mobility, evidence that these barriers to halide diffusion are conserved between different RPP compositions and n -phases. As a result, these materials may be useful in creating non-equilibrium chemical gradients in perovskite devices³² in addition to increasing the performance and stability of single composition materials. More broadly, our results and those of Chen *et al.* suggest that control of halide mobility and the reduction of halide leaching in perovskite devices are important factors to consider when designing stable perovskite devices, whether they be 2D or 3D, and that RPP perovskite materials may provide a means to mitigate the detrimental effects of both factors while providing other benefits.

5.4 CONCLUSIONS

Through the use of a variety of analytical techniques we have been able to explore the differences in device performance and stability between *n*-butylammonium and *n*-hexylammonium RPP perovskites, and show that both are affected by the choice of Ag or Au as an electrode material. Device performance measurements show that the average PCE of Ag devices is initially superior to those of Au devices, but rapidly degrades under exposure to 78% RH. Au-butyl devices retain a small degree of functionality over the course of a week, while the Au-hexyl devices maintain just under 50% of their initial performance for over a month. Both XRD and PL spectra recorded over 48 hours of humidity exposure show that the butyl-MAPI materials tend to form $n = 2-4$ phases as they degrade and that this formation is influenced by the metal electrode in full device stacks. In contrast, the PL spectra of the hexyl-MAPI devices have peaks indicating the presence of low- n phases prior to degradation, but these peaks change little with exposure (**Figure C.10**). Despite the apparent stability of the hexyl-MAPI devices, all RPP perovskite devices showed an increase in the $n > 5$ PL signal at 8 hours of exposure, attributable to the formation of a low- n passivation layer. ToF-SIMS profiles of the C₆₀/perovskite interface in these devices supports this interpretation, and provides chemical evidence of changes to the perovskite layer under humidity, including iodide migration. Halide mobility activation energies calculated for the $n = 2$ phases of both materials using UV-Vis spectroscopy indicate that butyl-MAPI has a lower barrier to iodide mobility within the material, corresponding to the higher degree of I⁻ leaching in ToF-SIMS measurements. Importantly, the activation energies of all RPP perovskites studied were higher than that previously measured for 3D perovskites, in agreement with previous work. Given that halide diffusion within, and subsequent leaching from, perovskites has been found to be linked to poor device stability, the high activation

barrier to such diffusion observed in RPP perovskites indicates that they may be more resistant to such processes and able to improve device stability. Together, our results show that (i) choice of alkylammonium spacer can have a significant impact on the performance and stability of a perovskite device, (ii) suggest that RPP perovskites may one day enable the use of more inexpensive contacts like Ag or Cu for perovskite solar devices, and (iii) provide a means for controlling halide mobility in perovskite materials.

5.5 REFERENCES

- (1) Kim, H.-S.; Lee, C.-R.; Im, J.-H.; Lee, K.-B.; Moehl, T.; Marchioro, A.; Moon, S.-J.; Humphry-Baker, R.; Yum, J.-H.; Moser, J. E.; et al. Lead Iodide Perovskite Sensitized All-Solid-State Submicron Thin Film Mesoscopic Solar Cell with Efficiency Exceeding 9%. *Sci. Rep.* **2012**, *2*, 1–7. <https://doi.org/10.1038/srep00591>.
- (2) NREL. Best Research-Cell Efficiencies <https://www.nrel.gov/pv/assets/pdfs/pv-efficiency-chart.20181221.pdf>.
- (3) Grancini, G.; Roldán-Carmona, C.; Zimmermann, I.; Mosconi, E.; Lee, X.; Martineau, D.; Nabey, S.; Oswald, F.; De Angelis, F.; Graetzel, M.; et al. One-Year Stable Perovskite Solar Cells by 2D/3D Interface Engineering. *Nat. Commun.* **2017**, *8*, 15684. <https://doi.org/10.1038/ncomms15684>.
- (4) Kojima, A.; Teshima, K.; Shirai, Y.; Miyasaka, T. Organometal Halide Perovskites as Visible-Light Sensitizers for Photovoltaic Cells. *J. Am. Chem. Soc.* **2009**, *131* (17), 6050–6051. <https://doi.org/10.1021/ja809598r>.
- (5) Belisle, R. A.; Bush, K. A.; Bertoluzzi, L.; Gold-Parker, A.; Toney, M. F.; McGehee, M. D. Impact of Surfaces on Photoinduced Halide Segregation in Mixed-Halide Perovskites. *ACS Energy Lett.* **2018**, *3* (11), 2694–2700. <https://doi.org/10.1021/acsenenergylett.8b01562>.
- (6) Beal, R. E.; Slotcavage, D. J.; Leijtens, T.; Bowring, A. R.; Belisle, R. A.; Nguyen, W. H.; Burkhard, G. F.; Hoke, E. T.; McGehee, M. D. Cesium Lead Halide Perovskites with Improved Stability for Tandem Solar Cells. *J. Phys. Chem. Lett.* **2016**, *7* (5), 746–751. <https://doi.org/10.1021/acs.jpcllett.6b00002>.
- (7) Wang, Z.; Lin, Q.; Chmiel, F. P.; Sakai, N.; Herz, L. M.; Snaith, H. J. Efficient Ambient-Air-Stable Solar Cells with 2D-3D Heterostructured Butylammonium-Caesium-Formamidinium Lead Halide Perovskites. *Nat. Energy* **2017**, *2* (9), 1–10. <https://doi.org/10.1038/nenergy.2017.135>.

- (8) Chen, A. Z.; Shiu, M.; Ma, J. H.; Alpert, M. R.; Zhang, D.; Foley, B. J.; Smilgies, D. M.; Lee, S. H.; Choi, J. J. Origin of Vertical Orientation in Two-Dimensional Metal Halide Perovskites and Its Effect on Photovoltaic Performance. *Nat. Commun.* **2018**, *9* (1), 1–7. <https://doi.org/10.1038/s41467-018-03757-0>.
- (9) Paritmongkol, W.; Dahod, N. S.; Stollmann, A.; Mao, N.; Settens, C.; Zheng, S. L.; Tisdale, W. A. Synthetic Variation and Structural Trends in Layered Two-Dimensional Alkylammonium Lead Halide Perovskites. *Chem. Mater.* **2019**, *31* (15), 5592–5607. <https://doi.org/10.1021/acs.chemmater.9b01318>.
- (10) Koh, T. M.; Shanmugam, V.; Guo, X.; Lim, S. S.; Filonik, O.; Herzig, E. M.; Müller-Buschbaum, P.; Swamy, V.; Chien, S. T.; Mhaisalkar, S. G.; et al. Enhancing Moisture Tolerance in Efficient Hybrid 3D/2D Perovskite Photovoltaics. *J. Mater. Chem. A* **2018**, 2122–2128. <https://doi.org/10.1039/C7TA09657G>.
- (11) Silver, S.; Yin, J.; Li, H.; Brédas, J. L.; Kahn, A. Characterization of the Valence and Conduction Band Levels of $n = 1$ 2D Perovskites: A Combined Experimental and Theoretical Investigation. *Adv. Energy Mater.* **2018**, *8* (16), 1–7. <https://doi.org/10.1002/aenm.201703468>.
- (12) Cao, D. H.; Stoumpos, C. C.; Farha, O. K.; Hupp, J. T.; Kanatzidis, M. G. Two-Dimensional Homologous Perovskites as Light Absorbing Materials for Solar Cell Applications. *J. Am. Chem. Soc.* **2015**, *137* (24), 7843–7850. <https://doi.org/10.1021/jacs.5b03796>.
- (13) Xing, J.; Yan, F.; Zhao, Y.; Chen, S.; Yu, H.; Zhang, Q.; Zeng, R.; Demir, H. V.; Sun, X.; Huan, A.; et al. High-Efficiency Light-Emitting Diodes of Organometal Halide Perovskite Amorphous Nanoparticles. *ACS Nano* **2016**, *10* (7), 6623–6630. <https://doi.org/10.1021/acs.nano.6b01540>.
- (14) Stoumpos, C. C.; Cao, D. H.; Clark, D. J.; Young, J.; Rondinelli, J. M.; Jang, J. I.; Hupp, J. T.; Kanatzidis, M. G. Ruddlesden-Popper Hybrid Lead Iodide Perovskite 2D Homologous Semiconductors. *Chem. Mater.* **2016**, *28* (8), 2852–2867. <https://doi.org/10.1021/acs.chemmater.6b00847>.
- (15) Spanopoulos, I.; Hadar, I.; Ke, W.; Tu, Q.; Chen, M.; Tsai, H.; He, Y.; Shekhawat, G.; Dravid, V. P.; Wasielewski, M. R.; et al. Uniaxial Expansion of the 2D Ruddlesden-Popper Perovskite Family for Improved Environmental Stability. *J. Am. Chem. Soc.* **2019**, *141* (13), 5518–5534. <https://doi.org/10.1021/jacs.9b01327>.
- (16) Lin, Y.; Bai, Y.; Fang, Y.; Chen, Z.; Yang, S.; Zheng, X.; Tang, S.; Liu, Y.; Zhao, J.; Huang, J. Enhanced Thermal Stability in Perovskite Solar Cells by Assembling 2D/3D Stacking Structures. *J. Phys. Chem. Lett.* **2018**, *9* (3), 654–658. <https://doi.org/10.1021/acs.jpcllett.7b02679>.

- (17) Tsai, H.; Nie, W.; Blancon, J.-C.; Stoumpos, C. C.; Asadpour, R.; Harutyunyan, B.; Neukirch, A. J.; Verduzco, R.; Crochet, J. J.; Tretiak, S.; et al. High-Efficiency Two-Dimensional Ruddlesden–Popper Perovskite Solar Cells. *Nature* **2016**, 536 (7616), 312–316. <https://doi.org/10.1038/nature18306>.
- (18) Rong, Y.; Hu, Y.; Mei, A.; Tan, H.; Saidaminov, M. I.; Seok, S. Il; McGehee, M. D.; Sargent, E. H.; Han, H. Challenges for Commercializing Perovskite Solar Cells. *Science* (80-.). **2018**, 361 (6408). <https://doi.org/10.1126/science.aat8235>.
- (19) Quan, L. N.; Yuan, M.; Comin, R.; Voznyy, O.; Beauregard, E. M.; Hoogland, S.; Buin, A.; Kirmani, A. R.; Zhao, K.; Amassian, A.; et al. Ligand-Stabilized Reduced-Dimensionality Perovskites. *J. Am. Chem. Soc.* **2016**, 138 (8), 2649–2655. <https://doi.org/10.1021/jacs.5b11740>.
- (20) Chen, J.; Lee, D.; Park, N. G. Stabilizing the Ag Electrode and Reducing J-V Hysteresis through Suppression of Iodide Migration in Perovskite Solar Cells. *ACS Appl. Mater. Interfaces* **2017**, 9 (41), 36338–36349. <https://doi.org/10.1021/acsami.7b07595>.
- (21) Liu, N.; Liu, P.; Ren, H.; Xie, H.; Zhou, N.; Gao, Y.; Li, Y.; Zhou, H.; Bai, Y.; Chen, Q. Probing Phase Distribution in 2D Perovskites for Efficient Device Design. *ACS Appl. Mater. Interfaces* **2020**, 12 (2), 3127–3133. <https://doi.org/10.1021/acsami.9b17047>.
- (22) Wygant, B. R.; Ye, A. Z.; Dolocan, A.; Vu, Q.; Abbot, D. M.; Mullins, C. B. Probing the Degradation Chemistry and Enhanced Stability of 2D Organolead Halide Perovskites. *J. Am. Chem. Soc.* **2019**, 141, 18170–18181. <https://doi.org/10.1021/jacs.9b08895>.
- (23) Elmelund, T.; Scheidt, R. A.; Seger, B.; Kamat, P. V. Bidirectional Halide Ion Exchange in Paired Lead Halide Perovskite Films with Thermal Activation. *ACS Energy Lett.* **2019**, 4 (8), 1961–1969. <https://doi.org/10.1021/acsenergylett.9b01280>.
- (24) Kato, Y.; Ono, L. K.; Lee, M. V.; Wang, S.; Raga, S. R.; Qi, Y. Silver Iodide Formation in Methyl Ammonium Lead Iodide Perovskite Solar Cells with Silver Top Electrodes. *Adv. Mater. Interfaces* **2015**, 2 (13), 2–7. <https://doi.org/10.1002/admi.201500195>.
- (25) Li, J.; Dong, Q.; Li, N.; Wang, L. Direct Evidence of Ion Diffusion for the Silver-Electrode-Induced Thermal Degradation of Inverted Perovskite Solar Cells. *Adv. Energy Mater.* **2017**, 7 (14), 1–8. <https://doi.org/10.1002/aenm.201602922>.
- (26) Stoumpos, C. C.; Soe, C. M. M.; Tsai, H.; Nie, W.; Blancon, J. C.; Cao, D. H.; Liu, F.; Traoré, B.; Katan, C.; Even, J.; et al. High Members of the 2D Ruddlesden–Popper Halide Perovskites: Synthesis, Optical Properties, and Solar Cells of (CH₃(CH₂)₃NH₃)₂(CH₃NH₃)₄Pb₅I₁₆. *Chem* **2017**, 2 (3), 427–440. <https://doi.org/10.1016/j.chempr.2017.02.004>.

- (27) Quintero-Bermudez, R.; Gold-Parker, A.; Proppe, A. H.; Munir, R.; Yang, Z.; Kelley, S. O.; Amassian, A.; Toney, M. F.; Sargent, E. H. Compositional and Orientational Control in Metal Halide Perovskites of Reduced Dimensionality. *Nat. Mater.* **2018**, *17* (10), 900–907. <https://doi.org/10.1038/s41563-018-0154-x>.
- (28) Liu, J.; Leng, J.; Wu, K.; Zhang, J.; Jin, S. Observation of Internal Photoinduced Electron and Hole Separation in Hybrid Two-Dimensional Perovskite Films. *J. Am. Chem. Soc.* **2017**, *139* (4), 1432–1435. <https://doi.org/10.1021/jacs.6b12581>.
- (29) Eperon, G. E.; Stranks, S. D.; Menelaou, C.; Johnston, M. B.; Herz, L. M.; Snaith, H. J. Formamidinium Lead Trihalide: A Broadly Tunable Perovskite for Efficient Planar Heterojunction Solar Cells. *Energy Environ. Sci.* **2014**, *7* (3), 982. <https://doi.org/10.1039/c3ee43822h>.
- (30) Chou, H.; Ismach, A.; Ghosh, R.; Ruoff, R. S.; Dolocan, A. Revealing the Planar Chemistry of Two-Dimensional Heterostructures at the Atomic Level. *Nat. Commun.* **2015**, *6* (May), 7482. <https://doi.org/10.1038/ncomms8482>.
- (31) Billing, D. G.; Lemmerer, A. Synthesis, Characterization and Phase Transitions in the Inorganic-Organic Layered Perovskite-Type Hybrids [(C_n H_{2n} + 1NH₃)₂PbI₄], n = 4, 5 and 6. *Acta Crystallogr. Sect. B Struct. Sci.* **2007**, *63* (5), 735–747. <https://doi.org/10.1107/S0108768107031758>.
- (32) Draguta, S.; Sharia, O.; Yoon, S. J.; Brennan, M. C.; Morozov, Y. V.; Manser, J. M.; Kamat, P. V.; Schneider, W. F.; Kuno, M. Rationalizing the Light-Induced Phase Separation of Mixed Halide Organic-Inorganic Perovskites. *Nat. Commun.* **2017**, *8* (1). <https://doi.org/10.1038/s41467-017-00284-2>.

Chapter 6: Introduction to Transition Metal-based Oxygen Evolution Reaction Electrocatalysts

While photovoltaic technologies like perovskite solar cells represent a promising means of producing electricity from the sun, the intermittent nature of sunlight means that efficient energy storage will also be necessary if it is to replace electricity produced from fossil fuels. As introduced in Chapter 1, one of the most exciting ways of storing intermittent renewable energy is in the form of H_2 generated by the electrolysis of water.¹ H_2 can be produced using electrolyzers powered by solar power and stored for later use and providing an energy source when solar power is less abundant or unavailable. Currently, one of the largest hurdles to the wide-scale development of water splitting technologies is the cost of the materials needed to create the efficient electrocatalysts required to overcome kinetic barriers in both the hydrogen evolution reaction (HER) and the oxygen evolution reaction (OER).² For example, while a cell voltage of only 1.23 V should be needed to drive the OER, the kinetic barrier to reaction means that overpotentials of hundreds more millivolts are typically required to achieve reasonable rates of reaction. By reducing the kinetic barriers to the reactions, electrocatalysts reduce the amount of overpotential required and thus make the overall process more efficient. Unfortunately, many of the benchmark electrocatalyst materials for the HER and the OER are precious metals like Pt, Ir, and Ru, as well as their oxides.³ This has spurred significant research in alternative electrocatalyst materials made using more earth-abundant metals for both reactions,^{4,5} but special attention has been paid to the more kinetically-challenging 4-electron OER, which represents the rate-limiting step in total water splitting.

In recent years, the premier OER electrocatalyst materials have been metal oxides and (oxy)hydroxides containing some combination of Fe, Co, and Ni.^{4,6,7} NiFe (oxy)hydroxides frequently show overpotentials as low as 200 mV, and operate for relatively long times.⁴ Researchers have also shown that metal oxides such as the oxide perovskite (BaSr)CoFeO₃ have also shown excellent performance for the OER,⁷ and as oxides are very stable under common alkaline electrolytes. More recently, researchers have begun to investigate a new family of metal chalcogenide materials, composed of transition metals and sulfur, selenium, and tellurium, which have shown excellent performance as OER electrocatalysts.^{8,9} Although the chalcogenide materials are sometime considered to be the active electrocatalytic species,⁹ recent research suggests that under reaction conditions the materials are themselves oxidized to produce a metal (oxy)hydroxide species which is the true electrocatalyst.¹⁰ This indicates that the chalcogenides may be best thought of as “pre-catalysts”, which oxidize *in situ* to yield the truly catalytic species.⁸ Ambiguity remains, however, as to how extensive the oxidation is (**Figure 6.1**) and what role, if any, the composition of the chalcogenide pre-catalyst plays in the final performance of the true catalyst.

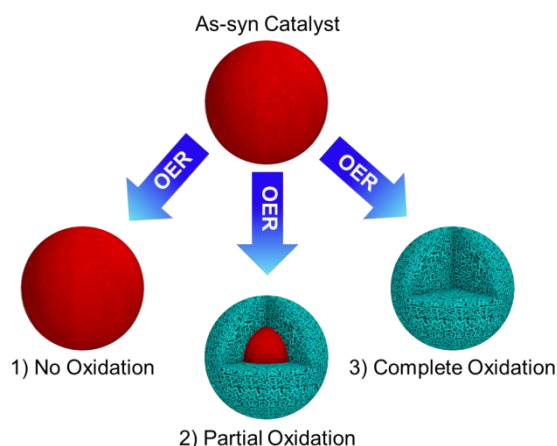


Figure 6.1 Diagram of the possible chemical compositions of metal chalcogenide electrocatalysts post-electrocatalysis. Starting with an unoxidized chalcogenide (red), the material can (1) remain unoxidized, (2) develop an oxidized shell surrounding an oxidized core, or (3) become completely oxidized.

In the following chapters, we will seek to better understand the relationship between the elemental composition of OER electrocatalyst materials, the various material properties of the resulting electrocatalysts (including crystal structure, morphology, and stability), and the electrocatalytic performance of both metal oxide and chalcogenide electrocatalysts. Compositional changes can range from the selection of metals used to create a metal oxide electrocatalyst to the relative ratio of two chalcogenide elements in a metal chalcogenide, but both can have significant impacts on the electrocatalytic performance. To better understand the effects of composition on both metal oxide electrocatalysts, we first present a study of the impact of Fe- and Sc-incorporation in a common metal oxide OER catalyst, and show that metal choice rather than crystal structure has a more significant impact on electrocatalytic performance (Chapter 7). We then show that, with regards to metal chalcogenide electrocatalysts, the relative quantity of Se incorporated into a nickel sulfide material directly impacts both the conductivity of

the resulting electrocatalyst and the overpotential required to drive the OER (Chapter 8). Together, these studies demonstrate the importance of chemical composition when developing and optimizing materials for use as OER electrocatalysts.

REFERENCES

- (1) Zou, X.; Zhang, Y. Noble Metal-Free Hydrogen Evolution Catalysts for Water Splitting. *Chem. Soc. Rev.* **2015**, *44* (15), 5148–5180. <https://doi.org/10.1039/c4cs00448e>.
- (2) You, B.; Sun, Y. Innovative Strategies for Electrocatalytic Water Splitting. *Acc. Chem. Res.* **2018**, *51* (7), 1571–1580. <https://doi.org/10.1021/acs.accounts.8b00002>.
- (3) Gorlin, Y.; Jaramillo, T. F. A Bifunctional Nonprecious Metal Catalyst for Oxygen Reduction and Water Oxidation. *J. Am. Chem. Soc.* **2010**, *132* (39), 13612–13614. <https://doi.org/10.1021/ja104587v>.
- (4) Gong, M.; Li, Y.; Wang, H.; Liang, Y.; Wu, J. Z.; Zhou, J.; Wang, J.; Regier, T.; Wei, F.; Dai, H. An Advanced Ni-Fe Layered Double Hydroxide Electrocatalyst for Water Oxidation. *J. Am. Chem. Soc.* **2013**, *135* (23), 8452–8455. <https://doi.org/10.1021/ja4027715>.
- (5) Benck, J. D.; Hellstern, T. R.; Kibsgaard, J.; Chakthranont, P.; Jaramillo, T. F. Catalyzing the Hydrogen Evolution Reaction (HER) with Molybdenum Sulfide Nanomaterials. *ACS Catal.* **2014**, *4* (11), 3957–3971. <https://doi.org/10.1021/cs500923c>.
- (6) Wang, H.; Lee, H.-W.; Deng, Y.; Lu, Z.; Hsu, P.-C.; Liu, Y.; Lin, D.; Cui, Y. Bifunctional Non-Noble Metal Oxide Nanoparticle Electrocatalysts through Lithium-Induced Conversion for Overall Water Splitting. *Nat. Commun.* **2015**, *6* (1), 7261. <https://doi.org/10.1038/ncomms8261>.
- (7) Suntivich, J.; May, K. J.; Gasteiger, H. a; Goodenough, J. B.; Shao-Horn, Y. A Perovskite Oxide Optimized for Oxygen Evolution Catalysis from Molecular Orbital Principles. *Science* (80-.). **2011**, *334* (6061), 1383–1385. <https://doi.org/10.1126/science.1212858>.
- (8) Mabayoje, O.; Shoola, A.; Wygant, B. R.; Mullins, C. B. The Role of Anions in Metal Chalcogenide Oxygen Evolution Catalysis: Electrodeposited Thin Films of Nickel Sulfide as “Pre-Catalysts.” *ACS Energy Lett.* **2016**, *1* (1), 195–201. <https://doi.org/10.1021/acsenergylett.6b00084>.
- (9) De Silva, U.; Masud, J.; Zhang, N.; Hong, Y.; Liyanage, W. P. R.; Asle Zaeem, M.; Nath, M. Nickel Telluride as a Bifunctional Electrocatalyst for Efficient

- Water Splitting in Alkaline Medium. *J. Mater. Chem. A* **2018**, No. March. <https://doi.org/10.1039/C8TA01760C>.
- (10) Wygant, B. R.; Kawashima, K.; Mullins, C. B. Catalyst or Precatalyst? The Effect of Oxidation on Transition Metal Carbide, Pnictide, and Chalcogenide Oxygen Evolution Catalysts. *ACS Energy Lett.* **2018**, *3* (12), 2956–2966. <https://doi.org/10.1021/acsenergylett.8b01774>.

Chapter 7: Structural and Catalytic Effects of Iron- and Scandium-Doping on a Strontium Cobalt Oxide Electrocatalyst for Water Oxidation²

7.1 INTRODUCTION

The generation of hydrogen gas through the electrocatalytic splitting of water ($2\text{H}_2\text{O} \rightarrow 2\text{H}_2 + \text{O}_2$) is an attractive means of storing electricity generated from intermittent power sources, such as solar and wind energy, in the form of a chemical fuel. Electrocatalytic water splitting is composed of two half-reactions: the hydrogen evolution reaction (HER), $2\text{H}^+ + 2\text{e}^- \rightarrow \text{H}_2$, and the oxygen evolution reaction (OER), $4\text{OH}^- \rightarrow \text{O}_2 + 2\text{H}_2\text{O} + 4\text{e}^-$. Of these two reactions the OER, which is a four-electron transfer reaction, is the rate limiting step in the overall scheme and requires much higher overpotentials to drive the reaction to completion. As a result, considerable research has been conducted on synthesizing catalyst materials to perform the reaction at minimal overpotentials in an effort to increase the total efficiency of the water splitting reaction.¹⁻⁸

Currently, the best-performing catalysts for the OER are noble metal nanoparticles and oxides, including iridium and ruthenium.^{1,3,8-10} Unfortunately, these noble metals are expensive and found in relatively low abundance in the earth's crust, making their widespread adoption for electrocatalysis unfeasible. As a result, many research groups have instead focused on developing catalysts composed of the much more abundant transition metals of the first row (Mn, Fe, Co, etc.) as alternatives to the classical noble metal catalysts, including but not limited to: amorphous metal-anion films

² This work was previously published: Wygant, B.R., Jarvis, K., Chemelewski, W., Mabayoje, O., Celio, H., Mullins, C.B. Structural and Catalytic Effects of Iron- and Scandium-Doping on a Strontium Cobalt Oxide Electrocatalyst for Water Oxidation, *ACS Catal.*, **2016**, 6, 1122-1133. The author of the dissertation was responsible for the development, execution, and interpretation of XRD, XPS, SEM, and electrochemical experiments.

such as CoP_i and CoB_i ,^{4,11–13} metal (oxy)hydroxide films such as Ni-OOH and Fe-OOH ,^{5,14–16} and various metal oxide nanoparticles such as Co_3O_4 and NiCo_2O_4 .^{6,17–19}

Theoretical calculations have proven to be invaluable to the discovery, design, and analysis of catalytic systems in recent years. In 2011, Man *et al.* published a theoretical and experimental study of a class of metal oxides known as perovskites.²⁰ This family of metal oxide has the chemical formula ABO_3 , where the A-site is typically a divalent (2+) alkaline earth metal cation, and the B-site is a tetravalent (4+) transition metal cation (**Figure 7.1**). Perovskites have long been known to be effective electrocatalysts for the OER,^{21,22} and in their work Man *et al.* provided theoretical evidence that a perovskite's OER performance is related to the Gibbs free energy of O^* and OH^* binding to the surface of the oxide. Applying their calculations to a wide range of perovskite compositions, the researchers found that the perovskite $\text{SrCoO}_{3-\delta}$ (SCO) was predicted to be among the most active catalysts in the family studied.

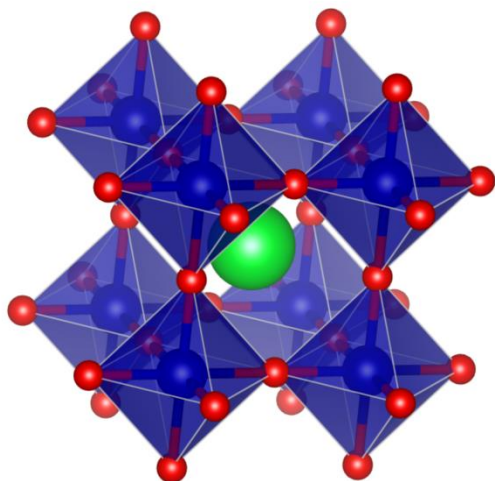


Figure 7.1. The cubic unit cell of $\text{SrCoO}_{3-\delta}$. The green sphere represents Sr^{2+} , the blue spheres $\text{Co}^{3,4+}$, and the red spheres represent O^{2-} .

Sintered pellets of SCO have been previously explored as OER catalysts,²³ and in recent years lanthanum-doped SCO has shown promise as a membrane for solid oxide fuel cells²⁴ (SOFCs) and oxygen reduction reaction (ORR) catalysts.²⁵ As an OER catalyst, however, the experimental results from testing failed to match those that theory predicted. Man *et al.* attribute this discrepancy to difficulties in obtaining a SCO sample with classical cubic perovskite-type structure. When synthesized, SCO tends to form as trigonal $\text{Sr}_6\text{Co}_5\text{O}_{15}$, but can also be synthesized as orthorhombic $\text{SrCoO}_{2.5}$.^{26,27} All three polymorphs tend to be oxygen deficient, as indicated by the $3-\delta$ in the chemical formula, where δ represents the degree of oxygen non-stoichiometry. This nonstoichiometry is related to the relatively large ionization energy required to create Co(IV) in the lattice, resulting in a preference for Co(III) atoms which are charge balanced by disordered oxygen vacancies.²⁸

In the SOFC field, several B-site dopants, including iron and scandium, have been shown to stabilize cubic SCO materials while also improving the oxygen permeability

and performance of the material.^{25–27,29,30} Similarly, the doping of SCO with barium and iron has yielded a $\text{Ba}_{0.5}\text{Sr}_{0.5}\text{Co}_{0.8}\text{Fe}_{0.2}\text{O}_3$ catalyst that shows excellent OER performance.⁷ In both cases, doping the base SCO with additional metals produces a more cubic material with improved performance, but it is unclear as to what degree both the dopant and the structure play in the observed improvements. In this study, we hope to clarify the relationship between dopant metal, crystal structure, and OER performance in cubic, iron- and scandium-doped SCO electrocatalysts.

7.2 EXPERIMENTAL

7.2.1 Materials

All materials were of the indicated grade, and were used without further purification. Cobalt nitrate hexahydrate ($\text{Co}(\text{NO}_3)_2 \cdot 6 \text{H}_2\text{O}$, 98%) was purchased from Acros Organics. Strontium nitrate ($\text{Sr}(\text{NO}_3)_2$, 99%) and scandium nitrate hydrate ($\text{Sc}(\text{NO}_3)_3 \cdot x \text{H}_2\text{O}$, 99.999%) were purchased from Alfa Aesar. Iron nitrate nonohydrate ($\text{Fe}(\text{NO}_3)_3$, 99.9%) and citric acid monohydrate ($\text{C}_6\text{H}_8\text{O}_7 \cdot \text{H}_2\text{O}$, 98%) were purchased from Sigma Aldrich. Ethylene glycol ($\text{C}_2\text{H}_6\text{O}_2$, certified) and potassium hydroxide (KOH, certified ACS pellets) were purchased from Fisher Scientific. All water was purified by an 18 M Ω water filtration system.

7.2.2 Materials Synthesis

SCO catalyst powders were synthesized using a polymerized complex reaction of metal nitrates, citric acid, and ethylene glycol.^{31,32} In a typical synthesis, 2.5 mmol $\text{Sr}(\text{NO}_3)_2$ and 2.5 mmol $\text{Co}(\text{NO}_3)_2 \cdot 6 \text{H}_2\text{O}$ were dissolved in 20 mL of DI water with stirring before adding 15 mmol citric acid to the solution. For doped SCO samples, the doping concentration was taken as the mole percent of cobalt nitrate, e.g. 10%Fe would

require 0.25 mmol $\text{Fe}(\text{NO}_3)_2 \cdot 9 \text{H}_2\text{O}$ and 2.25 mmol $\text{Co}(\text{NO}_3)_2 \cdot 6 \text{H}_2\text{O}$. After the addition of the citric acid, the resulting solution was allowed to stir magnetically for 30 minutes in a 70°C water bath to encourage the complexation of the metal ions by citric acid. Following complexation, 13.4 mmol of ethylene glycol was added and the resulting solution was left in the 70°C water bath to stir for an additional 1.5 hours. During this time, the citric acid and ethylene glycol underwent a polyesterification reaction and formed a thick resin.

After 1.5 hours, the solution was removed from the water bath, placed in a muffle furnace and heated to 90°C for 2 hours (2°C/min), followed by 200°C for 2 hours (2°C/min). The product, a light foam-like substance, was removed from the reaction vessel and ground in a porcelain mortar and pestle until a homogenous light brown powder was obtained. This powder was subsequently annealed at 450°C for 4.5 hours (5°C/min) in a porcelain crucible to yield a black powder composed of Co_3O_4 , SrCO_3 , and unreacted carbon (**Figure D.1**), which was then ground until smooth (approximately 5 minutes) using a small agate mortar and pestle. Once ground, the precursor was then annealed once more at 800°C for 10 hours (5°C/min) and allowed to cool naturally. The product of this annealing is a lightly sintered black pellet which crumbles easily under pressure, and was once more ground until smooth using an agate mortar and pestle (approximately 20 minutes). This fine black powder was annealed for the final time at 1000°C for 12 hours and allowed to cool naturally. After cooling, a lightly sintered pellet, ranging in color from grey to black, was collected and ground until smooth (approximately 30 minutes) to produce the final SCO catalyst powder.

7.2.3 Electrode Preparation

A thin dispersion of the SCO catalyst on fluorine-doped tin oxide (FTO) coated-glass served as the working electrode in all electrochemical experiments. To deposit the catalyst, a 1 mg-per-mL suspension of SCO catalyst in a solution of 75% ethylene glycol and 25% ethanol was prepared via sonication for 30 minutes prior to casting. 1.5 x 1.5 cm squares of FTO-coated glass were used as the substrate, and were prepared by sonicating in an ethanol/detergent mixture to remove any oils and other materials on the surface. After rinsing with ethanol and drying, a thin film of nitrocellulose and ethyl acetate (approximately 3x4 mm) was applied to one corner as a mask to ensure clear electrical contact with the electrode.

To cast the dispersion, 100 μL of the sonicated catalyst ink was dispensed via autopipette onto a prepared FTO substrate which had been allowed to heat for 10 minutes on a hot plate at 300°C. After the solvent in this aliquot evaporated, four more 100 μL aliquots were added in a similar manner. Following the fifth addition, the substrate was removed from the hotplate and allowed to cool to room temperature. Once cool, the mask was removed using acetone, and a piece of 3M 470 electroplating tape was used to mask off a 0.2 cm² working area along one edge of the substrate.

7.2.4 Material Characterization

Powder x-ray diffraction (XRD) patterns were acquired using a Spider (Rigaku) diffractometer with a Cu K α radiation source. Scanning electron microscopy (SEM) images were collected using a FEI Quanta 650 SEM using a 15 kV accelerating voltage. X-ray photoelectron spectroscopy (XPS) spectra were collected with a Kratos Axis Ultra photoelectron spectrometer using a non-monochromated Mg K α excitation source for the doped SCO samples, and a monochromated Al K α excitation source for undoped

samples. The use of the non-monochromated Mg source was required to shift the position of the Co LMM Auger peak away from the region associated with the iron 2p peaks. This resulted in total full width, half max (FWHM) broadening of approximately 1.0 eV for all recorded spectra. High resolution transmission electron microscopy (HRTEM), selected-area electron diffraction (SAED), nanobeam-electron diffraction (NBED), and energy dispersive X-ray spectroscopy (EDXS) were all done on a JEOL 2010F with a ultra-high resolution pole piece. The EDXS was done on an Oxford X-MaxN 80TLE solid state detector.

7.2.5 Electrochemical Characterization

All electrochemical characterization experiments were performed using a CHI660D potentiostat. All OER activity and stability experiments were performed in approximately 40 mL of 0.1M KOH using a 50 mL beaker. A platinum wire was used as the counter electrode and Ag/AgCl in 1M KCl was used as the reference electrode.

In a typical OER activity experiment, three successive cyclic voltammograms (CV) of a SCO catalyst were recorded from 0.2 to 0.9 V vs Ag/AgCl at a scan rate of 5 mV/s. During testing, the solution was magnetically stirred at 300 rpm to prevent accumulation of bubbles on the surface, and the working area of the electrode was gently purged of bubbles using a pipette following each experiment. Prior to the experiment, the IR drop from the solution was measured using the potentiostat software.³³ The CV was then recorded without correction, and the final anodic sweep segment was manually corrected for 100% of the measured resistance following the experiment to give a single linear sweep voltammogram (LSV).

In a typical stability experiment, a current density of 10 mA/cm² was applied to a SCO catalyst. The potential of the cell was then monitored over the course of 2 hours.

The electrolyte was stirred to prevent accumulation of oxygen bubbles on the electrode surface.

7.3. RESULTS AND DISCUSSION

7.3.1 XRD Analysis

Study of the various doped materials using XRD shows a clear change in the oxide crystal structure, induced by the introduction of iron and scandium into the pure strontium cobalt oxide. The spectra of the undoped SCO (UnSCO), as seen in **Figure 7.2**, can be indexed to the trigonal perovskite polymorph $\text{Sr}_6\text{Co}_5\text{O}_{15}$. Several peaks are also indicative of a Co_3O_4 impurity phase, which has previously been observed to accompany this crystal structure.²⁶ In the iron-doped SCO samples, incorporation of 1% iron was insufficient to induce a change from the trigonal polymorph. Upon incorporation of 5% iron, however, the SCO adopted an orthorhombic crystal structure, which can be most clearly seen in the loss of the peak at approximately two theta equal 28 degrees. Finally, after incorporation of 10% iron, the SCO adopts the typical cubic structure associated with perovskite materials. We note, however, the presence of a peak near 23 degrees two theta in the 10%Fe-SCO that is indexed to the orthorhombic phase. This may indicate that while primarily cubic, the sample does retain a small amount of orthorhombic structure.

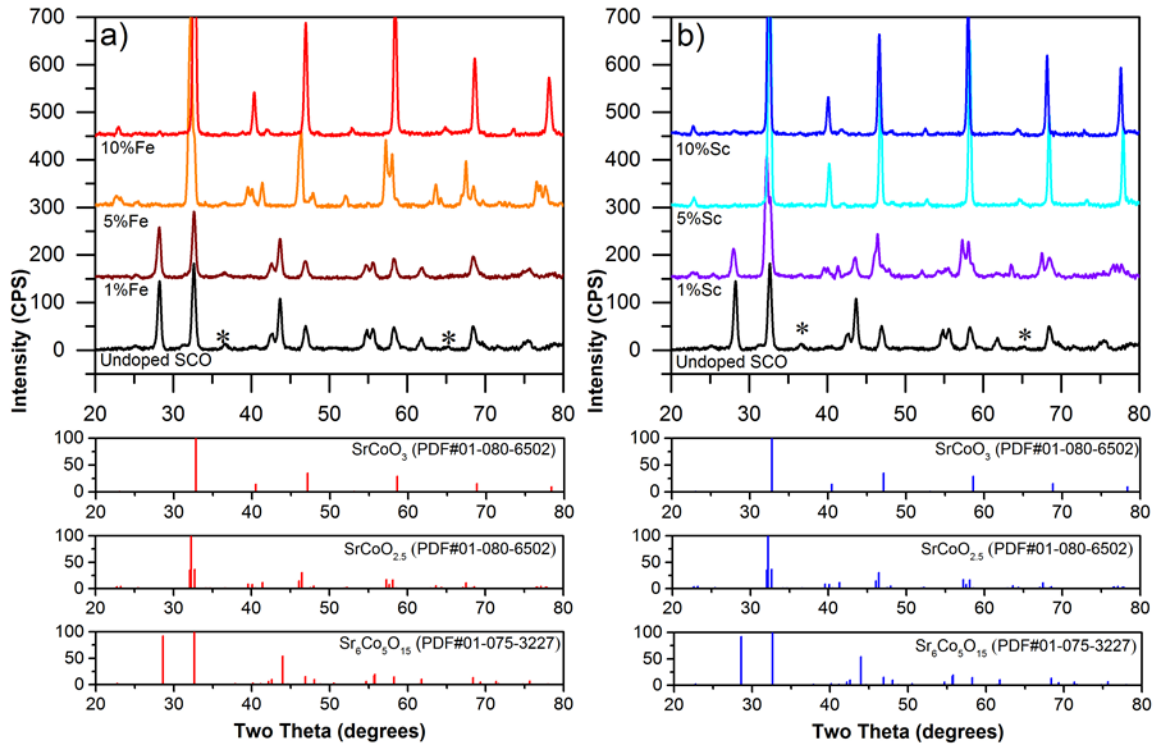


Figure 7.2. a) XRD spectra for iron-doped SCO samples. Increasing levels of iron doping cause the crystal structure to shift from the trigonal polymorph (UnSCO, 1%Fe-SCO) to the orthorhombic (5%Fe-SCO), and finally to the cubic polymorph (10%Fe-SCO). b) XRD spectra for the scandium-doped SCO samples. A similar pattern to the iron-samples is visible, where higher doping levels adopt the cubic crystal structure (5%, 10%Sc-SCO) while the lowest doping level (1%Sc-SCO) exhibits a mixture of trigonal and orthorhombic structure. Peaks marked “*” can be indexed to an impurity Co₃O₄ phase (PDF#00-043-1003).

In the case of the scandium-doped SCO, 1% scandium incorporation was sufficient only to induce a partial change to the crystal structure, and both the trigonal and orthorhombic polymorphs are clearly visible in the spectrum seen in **Figure 7.2b**. The doping of the SCO with 5% and 10% scandium results in the formation of the classical cubic perovskite phase. Of note is a slight upward shift in the location of the peak near two theta equal 32 degrees in the 10% scandium material versus the 5% scandium

material. As a result, the 10%Sc-SCO can be most closely indexed to a severely oxygen-deficient reference $\text{SrCoO}_{2.29}$ (PDF#00-039-1083). It is also important to note that there are no clear peaks assignable to either Fe_2O_3 or Sc_2O_3 in the XRD spectra for any sample. We can therefore conclude that all dopants have been fully integrated into the SCO lattice rather than segregating out to form a separate oxide phase.

Most clearly exemplified in the iron-doped SCO, but seen also in the scandium-doped samples, there is a clear progression from the trigonal to the orthorhombic to the cubic polymorph as the amount of dopant in the crystal lattice increases. This trend is dependent upon the final 1000°C annealing to form the final perovskite, however.

As seen in **Figure D.1b**, even at 10% iron concentration, the cubic perovskite will not form unless the sample has been annealed above 850°C. Prior to this, the sample will remain in the trigonal or orthorhombic polymorphs. A previous study using a similar lanthanum-doped SCO for solid oxide fuel cells (SOFCs) showed that when annealed to high temperature, the trigonal SCO will adopt the cubic structure upon cooling, if doped.²⁹ Furthermore, a separate study showed that depending upon the identity of the dopant used, this cubic structure may not be stable when the oxide is subjected to elevated temperatures below 900°C and can revert back to the trigonal phase if left for extended periods of time.³⁰ Images of the various SCO crystal structures are shown in **Figure 7.3**.

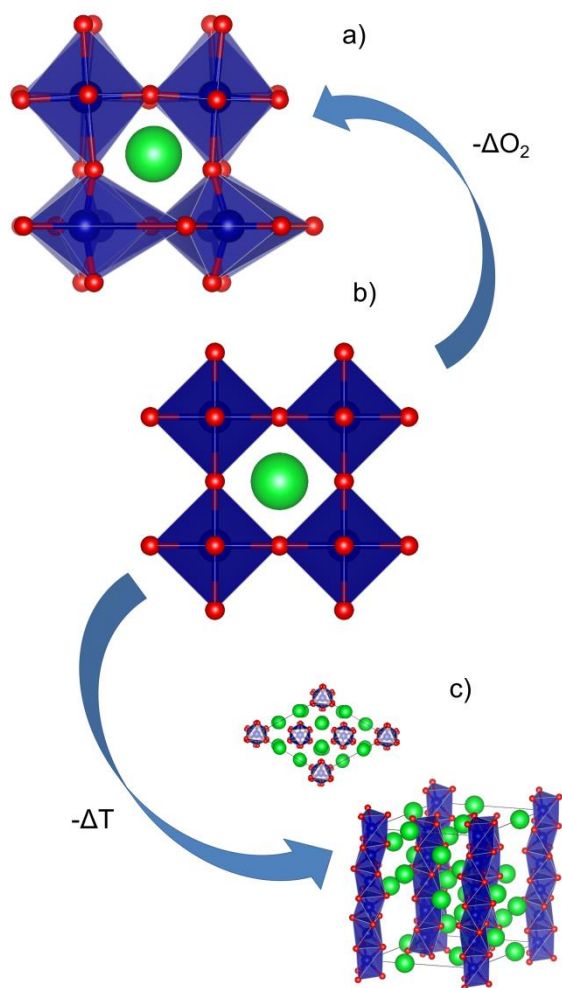


Figure 7.3. a) Representation of orthorhombic $\text{SrCoO}_{2.5}$, containing an ordered oxygen vacancy and significantly disordered CoO_6 octahedra in the crystal lattice. The green sphere represents Sr^{2+} , the blue spheres $\text{Co}^{3/4+}$, and the red spheres O^{2-} . b) Representation of cubic SrCoO_3 , containing ordered, corner-sharing CoO_6 octahedra arranged around a central Sr^{2+} . c) Representation of trigonal $\text{Sr}_6\text{Co}_5\text{O}_{15}$, containing face-sharing CoO_6 octahedra arranged in columns surrounded by alternating layers of Sr^{2+} ions arranged in a trigonal pattern. Sufficient loss or gain of oxygen can cause transitions between the cubic and orthorhombic polymorphs, while transitions between the trigonal and cubic phases are related to changes in temperature, with the cubic structure being favored above $\sim 900^\circ\text{C}$.

Given this information, there appears to be a critical temperature around 900°C, above which the cubic structure is thermodynamically stable and below which the trigonal polymorph is favored instead. Through doping, it is possible to stabilize the high-temperature lattice such that the cubic crystal structure remains once the oxide has cooled to room temperature. Therefore, the dopant must induce a distortion in the lattice that is capable of providing this stabilization. One possible source of this distortion could be alterations to the ionic radii of the component atoms, resulting in an alteration of the material's tolerance factor.

First formulated by Goldschmidt,³⁴ the tolerance factor provides a metric to describe the geometrical structure of a perovskite based upon the relative sizes of its components. It can be calculated using **Equation 7.1**, in which t is the tolerance factor, R_{Sr} is the ionic radius of strontium, R_O is the ionic radius of oxygen, R_B is the average ionic radius of the B-site cation (Co/Fe/Sc).

$$\text{Equation 7.1. } t = \frac{R_{Sr} + R_O}{\sqrt{2}(R_{Co} + R_O)}$$

Typically cited values of t are as follows: $t < 0.9$ for orthorhombic materials, $t = 0.9$ -1.0 for cubic materials, and $t > 1.0$ for trigonal materials. This value varies with differences in sizes between the A- and B-site cations, and breaks from unity when there is too great a discrepancy between the two. In the case of scandium doping, the larger ionic radius of the Sc(III) (0.745 Å vs. 0.61 Å for Co(III)³⁵) is able to increase the average B-site radius sufficiently to cause a decrease in the tolerance factor, as seen in **Table D.1** of Appendix D. This correlation between scandium and the decreasing tolerance factor suggests that it is the larger ionic radius of scandium over cobalt that leads to stabilization of the cubic SCO, with 5% marking the minimum value for

substitution. Iron follows a similar trend, ending at $t=1.0$ for the 10% composition. Despite the ionic radius of Fe(IV) being only slightly greater than that of Co(III), it appears the radius is sufficiently large to stabilize the cubic structure.

Additionally, the 1%Sc-SCO and 5%Fe-SCO samples, which appear to have similar crystal lattices by XRD, also share a tolerance factor of $t=1.001$. While orthorhombic polymorphs are typically found to have tolerance factors below 0.9, it is possible that oxygen non-stoichiometry in the lattice could stabilize the crystal phase, as previous studies have shown that oxygenation of $\text{SrCoO}_{2.5}$ to SrCoO_3 results in a shift between the orthorhombic and cubic phases.²⁷ The tolerance factors shown in the **Table D.1** are calculated using the most common oxidation states and ionic radius associated with the component elements.³⁵ The true crystal lattice is assumed to be much more nuanced than the simple averages we show here, with partial oxidation states and oxygen vacancies expected to be common. Therefore the numbers calculated from the tolerance factor are to be taken as a qualitative guide to changes in crystal structure, rather than as definitive proof.

An alternative explanation for the iron-doped material involves the relative increase in electrostatic repulsion between Co(III) and Fe(IV). As noted previously,^{30,36} B-site cations in the trigonal polymorph create columns of face-sharing octahedra, where the cations themselves are only separated by 2.41 Å. Shielding by the triad of oxygen atoms separating them, as well as an increased covalency in the Co-O bond may account for a stabilizing effect that ordinarily allows the Co(III) to remain in close proximity. It is possible that moderate doping of Fe(IV) may lead to enough repulsive force between the two cations to overcome the stabilizing influences and form the more sterically stable cubic polymorph.

7.3.2 XPS Analysis

Analysis by XPS provides the doping levels of pristine SCO powder samples prior to electrochemical testing, as well as valuable information about the oxidation states and chemical environments of the various components of the oxide at the surface. As can be seen in **Table D.2**, doping of the SCO with iron and scandium was successfully achieved, and the measured values differed only slightly from the intended doping concentrations. The iron spectra **Figure D.8** are too weak for extensive peak fitting, but the location of the primary peak at approximately 712 eV is higher than typical for iron (III), and indicates that some or most of the iron is in the 4+ oxidation state.³⁷ This is supported by previous work on a similar perovskite.²⁸ The spectra for scandium **Figure D.9** were equally weak, but agree well with literature values for Sc(III),³⁸ indicating that scandium remains in the 3+ oxidation state, as would be expected given its chemical nature.

Representative samples of the strontium, cobalt, oxygen, and carbon peaks are presented in **Figure 7.4** for the 10%Fe-SCO samples, and full spectra for the other samples are available in Appendix D. The cobalt 2p 3/2 peak in **Figure 7.4c** shows the primary peak at approximately 781 eV, and is in good agreement with the literature for Co(III).³⁹ This is further corroborated by the lack of satellite peaks that would indicate a Co(II) oxidation state. We were able to fit the Co 2p peak using a minimum of 3 peaks, as seen in **Figure 7.4c**. However, given the complicated deconvolutions of the 2p XPS peaks of transition metals such as cobalt and iron, we were unable to assign distinct chemical states to these peaks, or definitively show the existence of the Co(IV) that might be expected in a stoichiometric perovskite. The presence of shake-up peaks in the region broadens the signal, making definitive assignment of oxidation states dubious.⁴⁰ To provide additional evidence of potential Co(III) and Co(IV) without the complications of

these peaks, we also studied the Co 3p region (**Figure D.9**). The undoped sample shows a peak near 61 eV, which agrees well with previous literature for Co(II).⁴¹ As both Fe- and Sc-doping increase, the binding energy of the Co 3p peak gradually increases to approximately 62.8 eV. This is inconsistent with literature values for Co₃O₄,⁴² and therefore we interpret this to indicate significant quantities of Co(III) and potentially Co(IV) in these SCO samples.

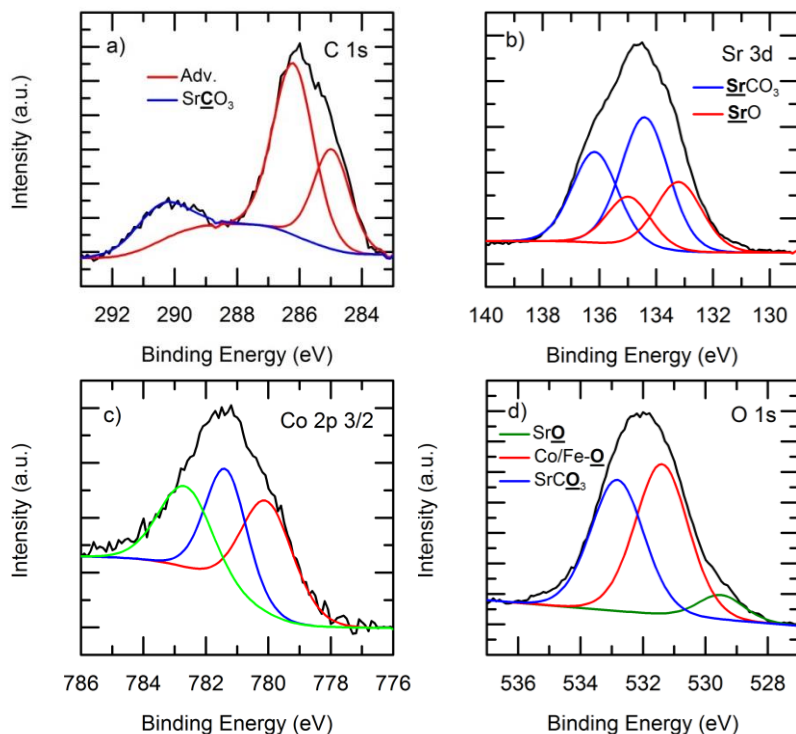


Figure 7.4. XPS spectra and fitted peaks for the 10%Fe-SCO sample. a) Spectra of the carbon 1s peak. b) Spectra of the strontium 3d 5/2 and 3/2 peaks. c) Spectra of the cobalt 2p 3/2 peak. d) Spectra of the oxygen 1s peak.

The strontium 3d peak in **Figure 7.4b** can be de-convoluted into two pairs of peaks relating to the 5/2 and 3/2 peaks for two distinct strontium species; we will reference the binding energy of the 5/2 peak for species identification. The peak at approximately 133.3 eV can be assigned to a layer of SrO on the surface of the particles,

while the peaks near 134 eV are assignable to SrCO_3 adsorbed to the surface.⁴³ This SrCO_3 impurity layer on the surface is confirmed by additional carbonate peaks in both the carbon and oxygen spectra in **Figure 7.4a** and **7.4d**, and has been previously observed on the surface of strontium and strontium-containing oxides.^{44,45} The impurity is common to alkaline earth metal-containing compounds due to their high reactivity with CO_2 and H_2O in the air.⁴⁴ The relative intensities of these two species are linked, and we note that as the signal for the SrCO_3 increases, that of the SrO decreases. This would seem to indicate an increase in the thickness of the carbonate impurity, masking the oxide signal.

We also observe that as the doping level increases, the ratio of strontium-to-cobalt of the surface of the samples increases significantly. Given a stoichiometrically balanced SCO sample, the ratio of strontium to cobalt at the surface should be approximately 1:1. By comparing the relative areas under the XPS peaks for the two species, we were able to calculate the average atomic percent of each element at the sample surface. These results have been tabulated in **Table 7.1**. The undoped SCO sample shows an approximately 2:1 ratio of strontium to cobalt on the surface, ~80% more strontium than would be expected based upon stoichiometry alone, even if the trigonal $\text{Sr}_6\text{Co}_5\text{O}_{15}$ polymorph is taken into account. This discrepancy is further magnified with increased doping, culminating in a ratio of roughly 3 strontium atoms for every one B-site cation (cobalt, iron, or scandium) on the sample surface.

Sample	Ratio Sr:Co(FeSc)
UnSCO	2.15
1%Fe-SCO	2.31
5%Fe-SCO	2.82
10%Fe-SCO	2.91
1%Sc-SCO	2.46
5%Sc-SCO	2.73
10%Sc-SCO	3.13

Table 7.1: The ratio of the atomic percent of Sr and B-site cation (Co, Fe, Sc) present on the SCO surface.

Previous studies have observed similar segregation in related Sr-containing perovskites,^{24,45–47} and have largely assigned this increase to the formation of SrO in interstitial layers and on the surface of the oxide. This process is driven by a mixture of kinetic and mechanical stressors within the lattice that cause the strontium to segregate out of the lattice and onto the surface. A study on a related Fe-doped SrTiO₃ also found that higher iron doping led to more segregation, and attributed this to lattice strain caused by size mismatch with the iron.⁴⁷ As larger B-site ions insert into the lattice, they cause the lattice to distort and apply stress on the lattice components. The large strontium atom is forced out of the cubic lattice to the surface in order to accommodate the strain. Both iron and scandium dopants would likely cause similar strains on the SCO lattice, and therefore we conclude that a similar effect is driving the strontium segregation in our own

samples, resulting in a Sr-rich layer near the surface of the oxide particles, composed of a carbonate layer which lies atop the segregated SrO.

The O 1s spectra of the SCO samples **Figure 7.4d** appears as a broad, asymmetric peak, which differs considerably from the typically sharp peaks seen in other metal oxides. Fitting yields three peaks at 529.5, 531.3, and 532.8 eV, which we assign, based on a previous study,⁴³ to SrO, (Co,Fe,Sc)-O, and SrCO₃, respectively. The average areas of the SrO and carbonate peaks correlate well with peaks for the same species in the Sr 3d spectra, supporting these assignments. Previously, van der Heide had tentatively assigned the peak near 531 eV to a B-site cation bound to an oxygen species at the surface.⁴³ Given similar binding energies for Co hydroxides and oxyhydroxides,³⁹ we likewise make this assignment. While we note that there is a near 1:1 ratio between the hydroxide and carbonate O 1s peaks for the doped samples, the lack of electrochemical variation despite differences in the spectra of the Sc-doped samples (**Figures D.2-D.7**) leads us to conclude this does not play a significant role in catalysis.

The carbon peak in **Figure 7.4a** shows two species of carbon on the surface of the SCO samples. The first, designated 285 and 286.2 eV, correspond to adventitious carbon on the oxide surface.⁴³ The second peak near 290 eV belongs to the SrCO₃ on the surface. We note that there is a trend for the carbonate binding energy of the more highly doped samples to shift towards greater energies. This trend is conserved across carbonate peaks for the Sr 3d and O 1s peaks, as well, and correlates to increased binding energies of the Co 3p peaks of these samples. We speculate that electrostatic interactions occurring at the interface of the bulk particle and the carbonate impurity results in a transfer of electron density from the carbonate to the higher oxidation state Co, resulting in the observed binding energy shifts. As these trends are conserved across several samples, we conclude

that if the presence or chemical environment of the carbonate does impact catalytic performance, it should be conserved across both Fe- and Sc-doped samples.

7.3.3 SEM Analysis

Scanning electron microscopy of the SCO catalyst dispersions provides important information about the morphology of the SCO catalyst powder and the microstructure of the working electrodes. **Figure D.11** shows representative samples of SEM images for the UnSCO and 10%Fe-SCO catalysts. Similar images for the additional five doping levels can be found in Appendix D. The active electrodes are composed of dispersed microparticles of SCO distributed atop the conductive FTO surface. These particles range from 0.5 to 20 μm in size, with the average size approximately 5 μm . They are relatively evenly distributed on the FTO surface, with larger particles located 20 μm away from others of similar sizes. As seen in **Figure D.11c-d**, the larger particles tend to have rough surfaces with smaller particles adhered to the surface. The particles appear to lack any visible mesoporosity that could be indicative of high surface area. Attempts at Brunauer-Emmet-Teller (BET) determination of surface area through nitrogen physisorption experiments failed due to the low surface area (below 5 m^2/g) exhibited by these SCO powders (data not included).

Closer examination of the microparticles reveals that they appear to be composed of a collection of sintered nanoparticles. These nanoparticles are similar to those observed during the original synthesis,³¹ and the sintering is a result of the prolonged annealing of the powders at high temperatures. The result is a catalyst powder with a much lower surface area than would be expected to be produced by the original synthetic technique. A reduction in annealing time or temperature would likely reduce the degree of sintering observed, but would also prevent formation of the cubic polymorph in the

doped samples. In order to maintain consistency across all doping levels, annealing conditions were standardized to allow all materials to come to full completion of reaction for accurate comparison. Qualitatively, all dispersions appear to be of similar topography, with similar distributions of particles sizes, morphologies, and spacing (**Figures D.12-D.18**). Therefore we conclude that any differences in catalytic performance should not be directly related to the morphology of the catalysts, but is instead related to the composition and crystal structure of the different SCO samples.

7.3.4 TEM Analysis

Further investigation of untested SCO powder samples using transmission electron microscopy provides a more detailed view of the crystal structures near the surface of the catalyst. **Figure D.11** shows representative samples of selected area electron diffraction (SAED) patterns from, UnSCO, 5%Fe-SCO, 10%Fe-SCO and 10%Sc-SCO catalysts, chosen to investigate each of the crystal patterns identified via XRD. The patterns indicate that the undoped sample is much more polycrystalline in nature than the doped samples, likely an artifact of the initial synthesis conditions. From this, we gather the trigonal phase is may be more resistive to sintering than the cubic perovskite material. The SAED rings for the undoped sample can be indexed to the trigonal $\text{Sr}_6\text{Co}_5\text{O}_{15}$ (**Figure D.12**), while all of the doped samples show the orthorhombic $\text{SrCoO}_{2.5}$ phase. However, due to the large area collected for SAED ($> 10 \mu\text{m}$), HRTEM and nanobeam-electron diffraction (NBED) are needed to determine the phases present on the nanoscale near the catalytic surface.

HRTEM images show that there are two phases present in all of the doped SCO, an orthorhombic phase and a cubic phase (**Figure 7.5**). While the cubic phase is found at the surface of the crystalline area for all of the compositions, it is restricted to a thin layer

on the surface of the 5%Fe-SCO sample. Given that this would indicate the extent of cubic structure on the surface is related to doping concentration, and that no evidence of the phase is visible in the SAED, we conclude there is likely little to no cubic perovskite present in the undoped sample. Contrast variations, due to thickness changes in the sample, prohibit the determination of structure by the HRTEM imaging alone, however. Furthermore, the SrCoO_3 phase and the $\text{SrCoO}_{2.5}$ phase both look similar when viewed down the $[100]$ direction, as seen for 5%Fe-SCO, and can only be differentiated by a decrease from a 90° angle between the $\langle 001 \rangle$ planes of the cubic phase, to an approximately 88° angle between the $[011]$ and $[01\bar{1}]$ planes of the orthorhombic phase. Therefore, to support and confirm the HRTEM data, we also collected nanobeam-electron diffraction (NBED) patterns, which, due to symmetry, should show different patterns for SrCoO_3 and the $\text{SrCoO}_{2.5}$ even when viewed down the $[100]$ direction.

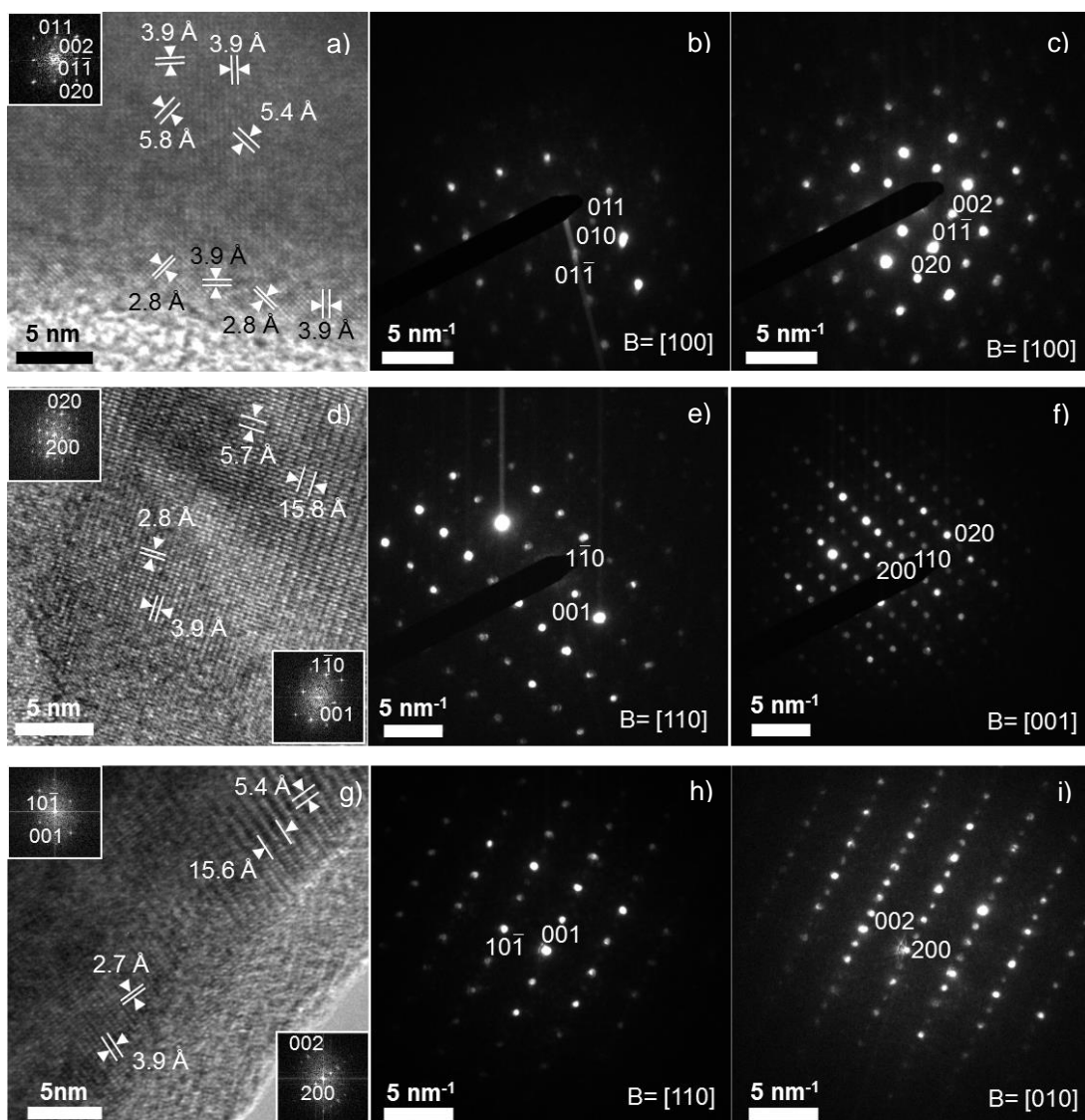


Figure 7.5. HRTEM images (a,d,g) and nanobeam-diffraction (NBED) patterns from the surface (b,e,h) and non-surface (c,f,i) of 5%Fe-SCO (a-c), 10%Fe-SCO (d-f), and 10%Sc-SCO (g-i). Inset FFTs of the images show the orthorhombic (top-left corners) and cubic (bottom-right corners) phases. There was not enough of the cubic phase in the 5% Fe-SCO to get a reliable FFT. The surface NBED patterns are indexed as the SrCoO_3 phase and the bulk NBED patterns are indexed as the orthorhombic $\text{SrCoO}_{2.5}$ phase. The beam directions are all indicated in the lower right corner.

Using NBED, all three doped compositions have the cubic phases at the surface, confirming the HRTEM results. Again, there is a much smaller amount present in 5%Fe-SCO, as indicated by the weak spots (**Figure 7.6**). Although the XRD spectra indicated a larger percentage of the cubic phase present in both the 10%Fe-SCO and 10%Sc-SCO, the orthorhombic phase also appears in these compositions, as indicated by NBED. This confirms our observations of orthorhombic peaks in XRD spectra of these samples. While we cannot determine the percentage of each phase due to the overlap of the cubic spots with orthorhombic spots in electron diffraction, we can say that the surface is cubic and at least some of the bulk is orthorhombic. In all samples, there is an amorphous layer surrounding the particle, about 5 – 20 nm thick (**Figure 7.6**), containing small crystals. In all but the 10%Fe-SCO, the lattice spacings were unique enough to identify these crystals as SrCO_3 .⁴⁸ While the particles in the 10%Fe-SCO sample may be SrCO_3 , the lattice spacings could also match the SrCoO_3 phase or the $\text{SrCoO}_{2.5}$ phase. Therefore, we cannot conclude if the amorphous layer for 10%Fe-SCO contains the SrCO_3 phase via HRTEM alone.

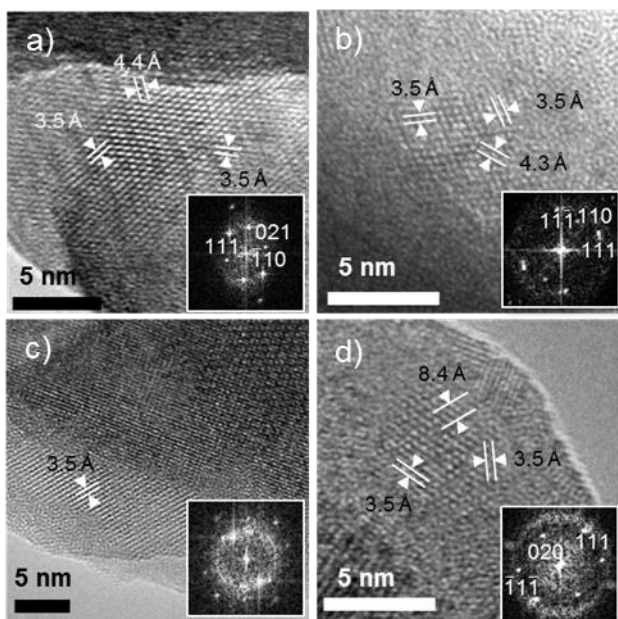


Figure 7.6. HRTEM images of particle surfaces of (a) UnSCO, (b) 5% Fe-SCO, (c) 10% Fe-SCO, and (d) 10% Sc-SCO showing nanoparticles embedded in an amorphous layer. The particles in the UnSCO, 5% Fe-SCO, and 10% Sc-SCO samples are indexed as orthorhombic SrCO_3 (Pmcn)⁴⁸ viewed down $[112]$, $[\bar{1}10]$, and $[\bar{1}01]$. Not enough planes are present in the particle from the 10% Fe-SCO sample to reliably determine the phase. The planes present could match (111) SrCO_3 and (211) $\text{SrCoO}_{2.5}$

Coupled with the previously discussed XPS results, however, we are confident that the SrCO_3 impurity layer seen via XPS correlates to the amorphous layer imaged here. Energy dispersive X-ray spectroscopy (EDXS) indicates that the undoped and 5%Fe-SCO are relatively Co-rich on the surface, while the 10%Fe-SCO and 10%Sc-SCO possess both Co-rich areas and Sr-rich areas on the surface (**Figure D.13**). Upon zooming in, however, we see that even the Co-rich surface actually has a 0.5-20 nm thick Sr-rich region (**Figure 7.7**), which is the same thickness as the amorphous layer with small crystallites. This roughly correlates to thickness of the XPS measurements, and corroborates the Sr-segregation we observe in the spectra.

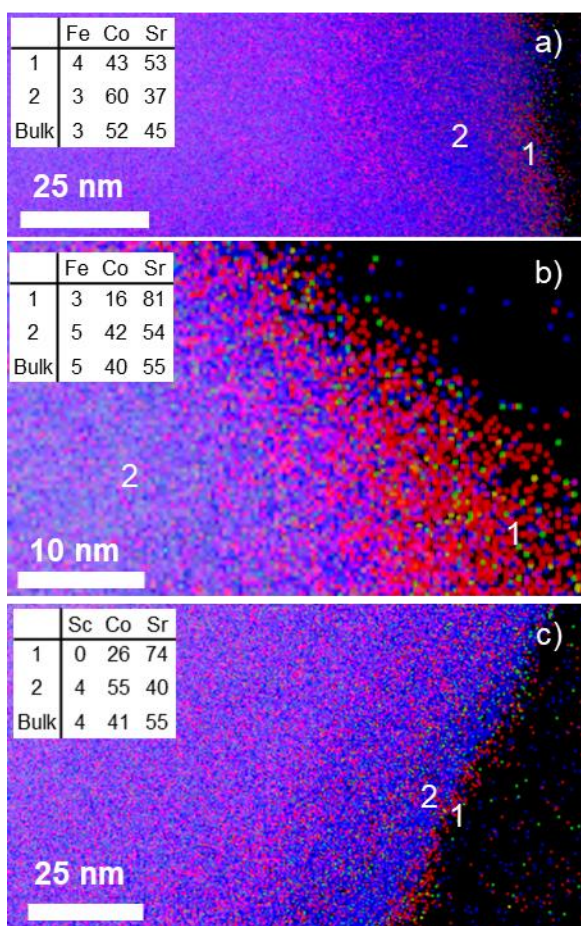


Figure 7.7. Electron dispersive X-ray spectroscopy maps of a) 5%Fe-SCO, b) 10%Fe-SCO, and c) 10%Sc-SCO. Cobalt is blue, strontium is red and the dopant (Fe or Sc) is green. The inset tables show the atomic percents taken for the average spectrum from the indicated area

While the amorphous layer appears to cover the majority of the particles, the EDXS and XPS measurements show that there are areas where the underlying perovskite is near, or at, the surface, and that at least some cobalt does persist in the top nanometers of the catalyst. This amorphous layer may partially explain the deviation between previous theoretical and experimental OER results for this material. If this layer does prevent 100% of the catalyst surface area from being OER-active, it is very likely that theoretical calculations would outstrip experimental results. Further work to remove this

layer prior to OER testing will be needed to fully characterize the performance of SCO without complication from the amorphous layer. Our data suggests, however, that the degree of particle coverage by the amorphous layer is similar across the samples in this study (Figure D.13), and that as a result, the trends we observe are independent of the amorphous layer. We conclude that there are likely still areas of active perovskite catalyst accessible on each particle, displaying the cubic structure. It is in these areas we believe that OER catalysis occurs.

7.3.5 Cyclic Voltammetric Testing

Cyclic voltammetry of the seven SCO samples provided quantitative analysis of OER performance for each doping level; the results can be seen in **Figure 7.8**. The intercept of the LSVs with the dotted line marks the value of η_{10} , the overpotential required to reach a current density of 10 mA/cm². With an η_{10} value of 450 mV for the UnSCO and 410 mV for the 10%Fe-SCO sample, the iron-doped SCO catalysts show a clear decrease in overpotential with increasing iron, up to 10% iron (**Figure D.18**). In contrast, the scandium-doped SCO catalysts show no significant change in overpotential with relation to the doping concentration. Both dopant metals, however, are shown to have considerable impact upon the crystal structure of the oxide depending upon the dopant concentration, ultimately resulting in the formation of a cubic layer at the surface of the doped particles. From this data, we conclude that it is the dopant species and not the crystal structure of the SCO that is responsible for the observed improvement in OER performance, as the 10%Sc-SCO and undoped samples possess different surface phases, yet possess the same OER activity.

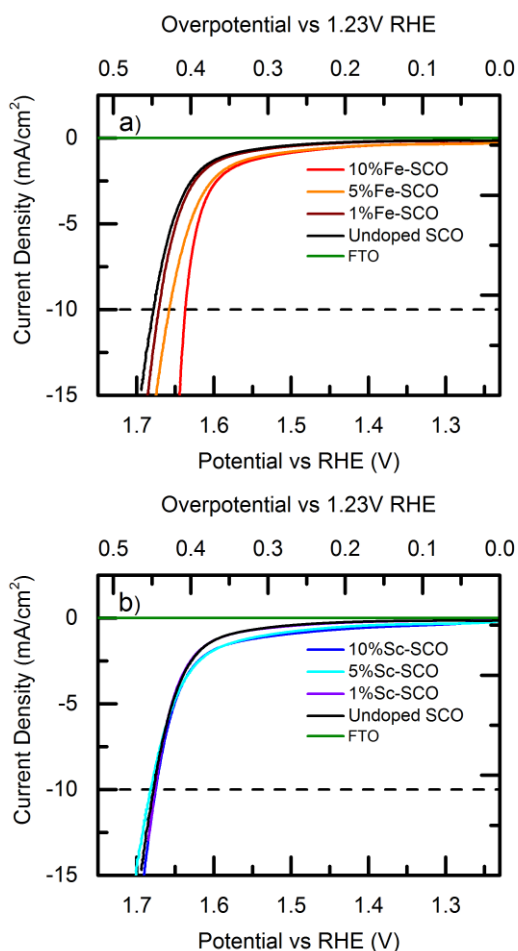


Figure 7.8. a) LSVs of iron-doped SCO samples and b) LSVs of scandium-doped SCO samples measured in 0.1M KOH at 5 mV/s. The dotted line marks the intercept with a current density of 10 mA/cm². Data was collected from the third anodic sweep segment.

This is in contrast to the assessment by Man *et al.*, who hypothesized that the difference between the theoretically predicted performance and the experimental observations lies in the inability to create a SrCoO_{3-δ} with a “perovskite-type structure.”²⁰ Were structure the primary cause of this discrepancy, one would expect to see the η_{10} of both the 10%Fe-SCO and 10%Sc-SCO samples significantly differ from the undoped case due to their cubic perovskite structures. We do concede that our samples likely have

a considerable degree of oxygen non-stoichiometry, but are confident that our arguments concerning the crystal structure are separate from those related to the degree of oxygen vacancy. In fact, previous research on a manganese-based perovskite showed that reductive annealing in hydrogen resulted in a significant improvement in OER performance.⁴⁹ The authors concluded that removal of an oxygen from the octahedron resulted in both molecular-level porosity and improved OH⁻ binding to the oxide, both of which led to a decreased overpotential for the OER. Therefore, we do not believe that that these oxygen vacancies would have a detrimental effect on our SCO samples. Our results indicate that the presence, or lack, of a cubic crystal structure is not the single factor which determines OER performance in SCO electrocatalysts.

We also note that our SCO catalysts possess much lower mass activities than similar perovskites that have been studied in recent years.⁵⁰ In their study, Hardin *et al.*⁵⁰ synthesized nanoparticulate perovskite catalysts which were then supported on a N-doped carbon support. Because of the drop casting technique used to create our electrodes, we were unable to likewise support our SCO catalysts on conductive carbon to improve conductivity. Attempts to add carbon to the catalyst ink resulted in poorly adhered films which detached from the FTO substrate during testing, and carbon supports were not further studied. As seen in **Table D.4**, our SCO catalyst possess OER mass activities an order of magnitude lower than those of similar catalysts (~6.5 mA/g at 1.56 V vs RHE). We attribute this reduction in activity to the smaller surface areas of our catalyst particles as compared to those of the more active catalysts due to their nanostructuring and carbon support. Support for this conclusion can be found in a comparison of our microparticle catalysts with sintered pellet catalysts from Bockris *et al*, possessing considerably lower surface area than the catalysts we report here.²² The current density of the most active catalyst from this study (LaNiO₃) is an order of magnitude lower than those of our

UnSCO catalyst at 0.3V vs. RHE, and four orders of magnitude lower than those of our 10%Fe-SCO catalyst. Therefore, an improved synthesis method that allows for the preservation of the initial SCO nanoparticles after annealing would likely further improve our SCO catalysts, as well as selection of a suitable conductive support.

The highly redox-active nature of iron may be the cause of the improvement seen in our doped samples. Iron is vitally important in many enzymes and proteins for oxygen binding and electron transfer, due to the ease with which it can change oxidation state, a necessary component of electrocatalysis. Even small amounts of iron, such as that found at the impurity level in KOH have been found to have beneficial effects on the OER performance of metal oxide OER catalysts.⁵¹ It would not be surprising, then, for the presence of iron in the SCO to synergistically improve its catalytic ability beyond that of the undoped material, as this has been observed to improve cobalt-based systems in amorphous cobalt (oxy)hydroxide thin films used as cocatalysts in photoelectrochemical (PEC) water splitting cells.⁵² This explanation would also help explain why the scandium does not appear to improve the SCO OER catalysis. Scandium typically remains in a static 3+ oxidation state, giving it a stable noble gas electron configuration. It is therefore extremely unlikely for scandium to lose an electron to adopt the 4+ state, and would also be unlikely to accept an electron. This leads to a highly redox-inactive metal ion which would be unlikely to take part in the chemistry of the OER. From the XRD, TEM, and cyclic voltammetry results, we can conclude that while both scandium and iron possess an ionic radius sufficiently large to stabilize the cubic SCO crystal structure at the surface, the electronic flexibility of the iron atoms in the crystal lattice allows for improved catalytic performance over the static scandium-doped materials.

7.3.6 Stability Testing

In order to determine the stability of the SCO samples under oxidative conditions, a current density of 10 mA/cm^2 was applied to each film for a total of two hours while monitoring the overpotential required to perform the OER. The results of this experiment can be seen in **Figure 7.9**. We further characterize catalyst stability by using the percent difference between the final recorded overpotential and the overpotential at 10 minutes as a measure. This allows sufficient time for the samples to reach a steady state current after a break-in period.

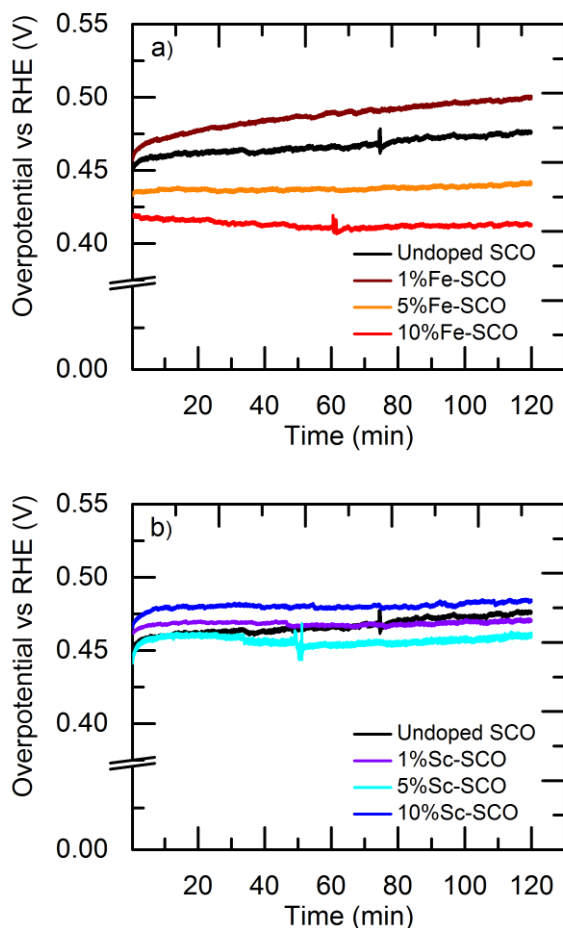


Figure 7.9. Overpotential-vs.-time plots for the a) iron-doped and b) scandium-doped SCO samples over the course of two hours, recorded at a current density of 10 mA/cm^2 .

The iron-doped materials show a considerable decrease in percent difference as the doping level increases, culminating in the 10%Fe-SCO sample which shows a small degree of improvement after 2 hours. Higher doping levels also result in a more abrupt onset of steady state current, as can be seen by the steeper onset slopes in the UnSCO and 1%Fe-SCO samples in **Figure 7.9a**. In addition, the 1%Fe-SCO sample appears to be considerably less stable than the undoped sample. This would appear to indicate that the presence of dopant in a trigonal SCO lattice results in less chemical stability, even as it helps improve OER performance. As observed in the cyclic voltammetry experiments, the scandium samples exhibit a much narrower range of overpotentials over the course of two hours, as well as much broader and slower onset curves than the iron-doped materials. In contrast to the iron-containing samples, there appears to not be as strong a correlation between dopant levels and stability for the scandium-substituted SCO. While doping with scandium does result in a roughly 50% reduced percent difference between the initial and final currents for all samples, there is not a strong correlation between the doping levels and the observed stability. All of the scandium-doped samples show a roughly 2.5% decrease in performance over two hours, regardless of doping concentration.

From the observed differences between the two sample sets, it appears that while OER performance is dependent upon the choice of metal dopant, the stability of the material under oxidative conditions is dependent upon the crystal structure. The cubic perovskites (10% iron, 5 and 10% scandium) show similar improvements in stability over the trigonal undoped base material, as do the orthorhombic perovskites (5% iron, 1% scandium). The thin layer of cubic SCO at the surface of each particle may help to prevent degradation during testing. This trend is most clearly seen in the iron-doped materials, where the marked improvement is clearly visible due to the wider range of

overpotentials. Thus, while the cubic crystal structure is not necessary for the improvement of OER performance in SCO, it is important for the synthesis of a catalyst capable of remaining stable over extended periods of time.

7.4. Conclusions

In this work, we demonstrate the effects of iron and scandium doping on the crystal structure and catalytic performance of SCO electrocatalysts for water oxidation. As the amount of either dopant in the SCO increases, the material experiences a shift from a trigonal polymorph to the classical cubic perovskite structure. OER testing shows that despite similar changes to the crystal structures of both doped catalysts, only the iron-doped SCO shows improvement with increasing dopant levels. Therefore, we conclude that the crystal structure of cobalt-based perovskite polymorphs has little impact on the OER performance of the catalyst. Rather, it is the choice of an appropriate catalytically-active metal such as iron that improves electrocatalytic water oxidation in SCO. Crystal structure does, however, appear to impact catalytic stability, as observed in the increased stability of cubic versus trigonal SCO under oxidative conditions. In conclusion, the incorporation of moderate amounts of iron into the SCO lattice results in the formation of an active, stable cubic perovskite OER catalyst with an η_{10} value of 410 mV and moderate stability over extended periods of operation in alkaline media.

7.5 REFERENCES

- (1) Mills, A.; Russell, T. Comparative Study of New and Established Heterogeneous Oxygen Catalysts. *J. Chem. Soc. Faraday Trans.* **1991**, 87 (8), 1245. <https://doi.org/10.1039/ft9918701245>.
- (2) Lee, Y.; Suntivich, J.; May, K. J.; Perry, E. E.; Shao-Horn, Y. Synthesis and Activities of Rutile IrO₂ and RuO₂ Nanoparticles for Oxygen Evolution in Acid and Alkaline Solutions. *Journal of Physical Chemistry Letters*. **2012**, pp 399–404. <https://doi.org/10.1021/jz2016507>.

- (3) Osterloh, F. E. Inorganic Nanostructures for Photoelectrochemical and Photocatalytic Water Splitting. *Chem. Soc. Rev.* **2013**, 42 (6), 2294–2320. <https://doi.org/10.1039/C2CS35266D>.
- (4) Kanan, M. W.; Nocera, D. G. In Situ Formation of an Oxygen-Evolving Catalyst in Neutral Water Containing Phosphate and Co^{2+} . *Science* **2008**, 321 (5892), 1072–1075. <https://doi.org/10.1126/science.1162018>.
- (5) Gao, M.; Sheng, W.; Zhuang, Z.; Fang, Q.; Gu, S.; Jiang, J.; Yan, Y. Efficient Water Oxidation Using Nanostructured γ -Nickel-Hydroxide as an Electrocatalyst. *J. Am. Chem. Soc.* **2014**, 136 (19), 7077–7084. <https://doi.org/10.1021/ja502128j>.
- (6) Lee, D. U.; Kim, B. J.; Chen, Z. One-Pot Synthesis of a Mesoporous NiCo_2O_4 Nanoplatelet and Graphene Hybrid and Its Oxygen Reduction and Evolution Activities as an Efficient Bi-Functional Electrocatalyst. *J. Mater. Chem. A* **2013**, 1 (15), 4754. <https://doi.org/10.1039/c3ta01402a>.
- (7) Suntivich, J.; May, K. J.; Gasteiger, H. A.; Goodenough, J. B.; Shao-Horn, Y. A Perovskite Oxide Optimized for Oxygen Evolution Catalysis from Molecular Orbital Principles. *Science*. **2011**, pp 1383–1385. <https://doi.org/10.1126/science.1212858>.
- (8) Reier, T.; Oezaslan, M.; Strasser, P. Electrocatalytic Oxygen Evolution Reaction (OER) on Ru, Ir, and Pt Catalysts: A Comparative Study of Nanoparticles and Bulk Materials. *ACS Catal.* **2012**, 2 (8), 1765–1772. <https://doi.org/10.1021/cs3003098>.
- (9) Nakagawa, T.; Beasley, C. a.; Murray, R. W. Efficient Electro-Oxidation of Water near Its Reversible Potential by a Mesoporous IrO_x Nanoparticle Film. *J. Phys. Chem. C* **2009**, 113 (30), 12958–12961. <https://doi.org/10.1021/jp9060076>.
- (10) Suntivich, J.; Gasteiger, H. a.; Yabuuchi, N.; Shao-Horn, Y. Electrocatalytic Measurement Methodology of Oxide Catalysts Using a Thin-Film Rotating Disk Electrode. *J. Electrochem. Soc.* **2010**, 157 (8), B1263. <https://doi.org/10.1149/1.3456630>.
- (11) Esswein, A. J.; Surendranath, Y.; Reece, S. Y.; Nocera, D. G. Highly Active Cobalt Phosphate and Borate Based Oxygen Evolving Catalysts Operating in Neutral and Natural Waters. *Energy Environ. Sci.* **2011**, 4 (2), 499. <https://doi.org/10.1039/c0ee00518e>.
- (12) Jeon, T. H.; Choi, W.; Park, H. Cobalt–Phosphate Complexes Catalyze the Photoelectrochemical Water Oxidation of BiVO_4 Electrodes. *Physical Chemistry Chemical Physics*. **2011**, p 21392. <https://doi.org/10.1039/c1cp23135a>.
- (13) Surendranath, Y.; Dincă, M.; Nocera, D. G. Electrolyte-Dependent Electrosynthesis and Activity of Cobalt-Based Water Oxidation Catalysts. *J. Am. Chem. Soc.* **2009**, 131 (7), 2615–2620. <https://doi.org/10.1021/ja807769r>.

- (14) Chemelewski, W. D.; Lee, H. C.; Lin, J. F.; Bard, A. J.; Mullins, C. B. Amorphous FeOOH Oxygen Evolution Reaction Catalyst for Photoelectrochemical Water Splitting. *J. Am. Chem. Soc.* **2014**, *136* (7), 2843–2850. <https://doi.org/10.1021/ja411835a>.
- (15) Smith, R. D. L.; Prévot, M. S.; Fagan, R. D.; Trudel, S.; Berlinguette, C. P. Water Oxidation Catalysis: Electrocatalytic Response to Metal Stoichiometry in Amorphous Metal Oxide Films Containing Iron, Cobalt, and Nickel. *J. Am. Chem. Soc.* **2013**, *135* (31), 11580–11586. <https://doi.org/10.1021/ja403102j>.
- (16) Seabold, J. A.; Choi, K. S. Efficient and Stable Photo-Oxidation of Water by a Bismuth Vanadate Photoanode Coupled with an Iron Oxyhydroxide Oxygen Evolution Catalyst. *J. Am. Chem. Soc.* **2012**, *134* (4), 2186–2192. <https://doi.org/10.1021/ja209001d>.
- (17) De Koninck, M.; Poirier, S.; Marsan, B. Cu[Sub x]Co[Sub 3–x]O[Sub 4] Used as Bifunctional Electrocatalyst. *Journal of The Electrochemical Society*. **2007**, p A381. <https://doi.org/10.1149/1.2454366>.
- (18) Zhang, M.; de Respinis, M.; Frei, H. Time-Resolved Observations of Water Oxidation Intermediates on a Cobalt Oxide Nanoparticle Catalyst. *Nat. Chem.* **2014**, *6* (4), 362–367. <https://doi.org/10.1038/nchem.1874>.
- (19) Chen, S.; Qiao, S. Z. Hierarchically Porous Nitrogen-Doped Graphene-NiCo₂O₄ Hybrid Paper as an Advanced Electrocatalytic Water-Splitting Material. *ACS Nano* **2013**, *7* (11), 10190–10196. <https://doi.org/10.1021/nn404444r>.
- (20) Man, I. C.; Su, H. Y.; Calle-Vallejo, F.; Hansen, H. a.; Martínez, J. I.; Inoglu, N. G.; Kitchin, J.; Jaramillo, T. F.; Nørskov, J. K.; Rossmeisl, J. Universality in Oxygen Evolution Electrocatalysis on Oxide Surfaces. *ChemCatChem* **2011**, *3* (7), 1159–1165. <https://doi.org/10.1002/cctc.201000397>.
- (21) Matsumoto, Y.; Yamada, S.; Nishida, T.; Sato, E. Oxygen Evolution on La(1-x)SrxFe(1-y)Co_yO₃ Series Oxides. *J. Electrochem. Soc.* **1980**, *127* (11), 2360–2364.
- (22) Bockris, J. O. The Electrocatalysis of Oxygen Evolution on Perovskites. *Journal of The Electrochemical Society*. **1984**, p 290. <https://doi.org/10.1149/1.2115565>.
- (23) Takeda, Y.; Kanno, R.; Kondo, T.; Yamamoto, O.; Taguchi, H.; Shimada, M.; Koizumi, M. Properties Of SrMO_{3-?} (M=Fe, Co) as Oxygen Electrodes in Alkaline Solution. *Journal of Applied Electrochemistry*. **1982**, pp 275–280. <https://doi.org/10.1007/BF00615092>.
- (24) Mutoro, E.; Crumlin, E. J.; Biegalski, M. D.; Christen, H. M.; Shao-Horn, Y. Enhanced Oxygen Reduction Activity on Surface-Decorated Perovskite Thin Films for Solid Oxide Fuel Cells. *Energy Environ. Sci.* **2011**, *4* (9), 3689. <https://doi.org/10.1039/c1ee01245b>.

- (25) Chen, D.; Chen, C.; Zhang, Z.; Baiyee, Z. M.; Ciucci, F.; Shao, Z. Compositional Engineering of Perovskite Oxides for Highly Efficient Oxygen Reduction Reactions. *ACS Appl. Mater. Interfaces* **2015**, 7 (16), 8562–8571. <https://doi.org/10.1021/acsami.5b00358>.
- (26) Harrison, W. T. a.; Hegwood, S. L.; Jacobson, A. J. A Powder Neutron Diffraction Determination of the Structure of Sr₆Co₅O₁₅, Formerly Described as the Low-Temperature Hexagonal Form of SrCoO₃?X . *J. Chem. Soc. Chem. Commun.* **1995**, No. 19, 1953. <https://doi.org/10.1039/c39950001953>.
- (27) Le Toquin, R.; Paulus, W.; Cousson, A.; Prestipino, C.; Lamberti, C. Time-Resolved in Situ Studies of Oxygen Intercalation into SrCoO 2.5, Performed by Neutron Diffraction and X-Ray Absorption Spectroscopy. *J. Am. Chem. Soc.* **2006**, 128 (40), 13161–13174. <https://doi.org/10.1021/ja063207m>.
- (28) Stølen, S.; Bakken, E.; Mohn, C. E. Oxygen-Deficient Perovskites: Linking Structure, Energetics and Ion Transport. *Phys. Chem. Chem. Phys.* **2006**, 8 (4), 429–447. <https://doi.org/10.1039/b512271f>.
- (29) Zeng, P.; Ran, R.; Chen, Z.; Zhou, W.; Gu, H.; Shao, Z.; Liu, S. Efficient Stabilization of Cubic Perovskite SrCoO₃-δ by B-Site Low Concentration Scandium Doping Combined with Sol-Gel Synthesis. *J. Alloys Compd.* **2008**, 455 (1–2), 465–470. <https://doi.org/10.1016/j.jallcom.2007.01.144>.
- (30) Nagai, T.; Ito, W.; Sakon, T. Relationship between Cation Substitution and Stability of Perovskite Structure in SrCoO₃-??-Based Mixed Conductors. *Solid State Ionics* **2007**, 177 (39–40), 3433–3444. <https://doi.org/10.1016/j.ssi.2006.10.022>.
- (31) Gaoke, Z.; Ying, L.; Xia, Y.; Yanping, W.; Shixi, O.; Hangxing, L. Comparison of Synthesis Methods, Crystal Structure and Characterization of Strontium Cobaltite Powders. *Mater. Chem. Phys.* **2006**, 99 (1), 88–95. <https://doi.org/10.1016/j.matchemphys.2005.09.078>.
- (32) May, K. J.; Carlton, C. E.; Stoerzinger, K. a.; Risch, M.; Suntivich, J.; Lee, Y. L.; Grimaud, A.; Shao-Horn, Y. Influence of Oxygen Evolution during Water Oxidation on the Surface of Perovskite Oxide Catalysts. *J. Phys. Chem. Lett.* **2012**, 3 (22), 3264–3270. <https://doi.org/10.1021/jz301414z>.
- (33) He, P.; Faulkner, L. R. Intelligent, Automatic Compensation of Solution Resistance. *Anal. Chem.* **1986**, 58 (3), 517–523. <https://doi.org/10.1021/ac00294a004>.
- (34) Goldschmidt, V. M. *Die Gesetze Der Krystallochemie. Naturwissenschaften* **1926**, 14 (21), 477–485. <https://doi.org/10.1007/BF01507527>.
- (35) Shannon, R. D. Revised Effective Ionic Radii and Systematic Studies of Interatomic Distances in Halides and Chalcogenides. *Acta Crystallographica Section A*. **1976**, pp 751–767. <https://doi.org/10.1107/S0567739476001551>.

- (36) Takeda, Y.; Kanamura, F.; Shimada, M.; Koizumi, M. The Crystal Structure of BaNiO₃. *Acta Crystallogr. Sect. B Struct. Crystallogr. Cryst. Chem.* **1976**, 32 (8), 2464–2466. <https://doi.org/10.1107/S056774087600798X>.
- (37) Grosvenor, a. P.; Kobe, B. a.; Biesinger, M. C.; McIntyre, N. S. Investigation of Multiplet Splitting of Fe 2p XPS Spectra and Bonding in Iron Compounds. *Surf. Interface Anal.* **2004**, 36 (12), 1564–1574. <https://doi.org/10.1002/sia.1984>.
- (38) Biesinger, M. C.; Lau, L. W. M.; Gerson, A. R.; Smart, R. S. C. Resolving Surface Chemical States in XPS Analysis of First Row Transition Metals, Oxides and Hydroxides: Sc, Ti, V, Cu and Zn. *Appl. Surf. Sci.* **2010**, 257 (7), 887–898. <https://doi.org/10.1016/j.apsusc.2010.07.086>.
- (39) Biesinger, M. C.; Payne, B. P.; Grosvenor, A. P.; Lau, L. W. M.; Gerson, A. R.; Smart, R. S. C. Resolving Surface Chemical States in XPS Analysis of First Row Transition Metals, Oxides and Hydroxides: Cr, Mn, Fe, Co and Ni. *Appl. Surf. Sci.* **2011**, 257 (7), 2717–2730. <https://doi.org/10.1016/j.apsusc.2010.10.051>.
- (40) Singh, P.; Shiva, K.; Celio, H.; Goodenough, J. B. Eldfellite, NaFe(SO₄)₂: An Intercalation Cathode Host for Low-Cost Na-Ion Batteries. *Energy Environ. Sci.* **2015**, 8 (10), 3000–3005. <https://doi.org/10.1039/C5EE02274F>.
- (41) Kim, K. X-Ray-Photoelectron Spectroscopic Studies of the Electronic Structure of CoO. *Phys. Rev. B* **1975**, 11 (15), 2177–2185.
- (42) Strydom, C. A.; Strydom, H. J. X-Ray Photoelectron Spectroscopy Studies of Some Cobalt(II) Nitrate Complexes. *Inorganica Chim. Acta* **1989**, 159 (2), 191–195. [https://doi.org/10.1016/S0020-1693\(00\)80566-6](https://doi.org/10.1016/S0020-1693(00)80566-6).
- (43) van der Heide, P. A. W. Systematic X-Ray Photoelectron Spectroscopic Study of La_{1-x}Sr_x-Based Perovskite-Type Oxides. *Surf. Interface Anal.* **2002**, 33 (5), 414–425. <https://doi.org/10.1002/sia.1227>.
- (44) Vasquez, R. P. X-Ray Photoelectron Spectroscopy Study of Sr and Ba Compounds. *J. Electron Spectros. Relat. Phenomena* **1991**, 56 (3), 217–240. [https://doi.org/10.1016/0368-2048\(91\)85005-E](https://doi.org/10.1016/0368-2048(91)85005-E).
- (45) Chen, Y.; Jung, W.; Cai, Z.; Kim, J. J.; Tuller, H. L.; Yildiz, B. Impact of Sr Segregation on the Electronic Structure and Oxygen Reduction Activity of SrTi_{1-x}Fe_xO₃ Surfaces. *Energy Environ. Sci.* **2012**, 5 (7), 7979. <https://doi.org/10.1039/c2ee21463f>.
- (46) Jiang, S. P.; Love, J. G. Origin of the Initial Polarization Behavior of Sr-Doped LaMnO₃ for O₂ Reduction in Solid Oxide Fuel Cells. *Solid State Ionics* **2001**, 138 (3–4), 183–190. [https://doi.org/10.1016/S0167-2738\(00\)00806-7](https://doi.org/10.1016/S0167-2738(00)00806-7).
- (47) Jung, W.; Tuller, H. L. Investigation of Surface Sr Segregation in Model Thin Film Solid Oxide Fuel Cell Perovskite Electrodes. *Energy Environ. Sci.* **2012**, 5 (1), 5370. <https://doi.org/10.1039/c1ee02762j>.

- (48) Antao, S. M.; Hassan, I. The Orthorhombic Structure of CaCO_3 , SrCO_3 , PbCO_3 and BaCO_3 : Linear Structural Trends. *Can. Mineral.* **2009**, *47*, 1245–1255.
- (49) Kim, J.; Yin, X.; Tsao, K.; Fang, S.; Yang, H. $\text{Ca}_{2}\text{Mn}_{2}\text{O}_{5}$ as Oxygen-Deficient Perovskite Electrocatalyst for Oxygen Evolution Reaction. *J. Am. Chem. Soc.* **2014**, *136* (42), 14646–14649. <https://doi.org/10.1021/ja506254g>.
- (50) Hardin, W. G.; Mefford, J. T.; Slanac, D. a.; Patel, B. B.; Wang, X.; Dai, S.; Zhao, X.; Ruoff, R. S.; Johnston, K. P.; Stevenson, K. J. Tuning the Electrocatalytic Activity of Perovskites through Active Site Variation and Support Interactions. *Chem. Mater.* **2014**, *26* (11), 3368–3376. <https://doi.org/10.1021/cm403785q>.
- (51) Corrigan, D. a. The Catalysis of the Oxygen Evolution Reaction by Iron Impurities in Thin Film Nickel Oxide Electrodes. *J. Electrochem. Soc.* **1987**, *134* (2), 377. <https://doi.org/10.1149/1.2100463>.
- (52) Smith, R. D. L.; Prevot, M. S.; Fagan, R. D.; Zhang, Z.; Sedach, P. A.; Siu, M. K. J.; Trudel, S.; Berlinguette, C. P. Photochemical Route for Accessing Amorphous Metal Oxide Materials for Water Oxidation Catalysis. *Science* (80-.). **2013**, *340* (6128), 60–63. <https://doi.org/10.1126/science.1233638>.

Chapter 8: Effect of Selenium Content on Nickel Sulfoselenide-Derived Nickel (Oxy)hydroxide Electrocatalysts for Water Oxidation³

8.1 INTRODUCTION

As the development and implementation of renewable solar and wind power continues to increase, so too does the need for an efficient means of storing this intermittent energy to allow for efficient incorporation into existing power grids.¹ Much of the recent research on energy storage techniques has focused on technologies like batteries or chemical fuels, and among the most promising of these is the generation of hydrogen fuel via the electrolysis of water.² When produced using a clean source of electricity, the only products of the process are H₂ and O₂ gas, which can recombine to produce water and electricity when the fuel is later consumed in a fuel cell or through combustion. Although promising, this technology faces several hurdles to wide-scale implementation, and one of the largest is a need for affordable electrocatalysts to drive the water splitting reactions.

Both halves of the water splitting process require electrocatalysts to reduce the kinetic barriers to electrochemical reaction, but electrocatalysts for the oxygen evolution reaction (OER) are arguably of greater interest, as the OER is the current rate-limiting step for total water electrolysis. The standard benchmark electrocatalysts for the OER are typically costly IrO₂ and RuO₂,³ and thus research in the field has been focused on replacing these precious metal catalysts with more earth-abundant materials like Fe-, Co-,

³ This work was previously published: Wygant, B.R., Poterek, A.H., Burrow, J.N., Mullins, C.B. Effect of Selenium Content on Nickel Sulfoselenide-Derived Nickel (Oxy)hydroxide Electrocatalysts for Water Oxidation, *ACS Appl. Mater. Interfaces*, **2020**, <https://doi.org/10.1021/acsami.0c00425>. The author of the dissertation was responsible for the development, execution, and interpretation of XRD, XPS, SEM, and electrochemical experiments.

and Ni-based (oxy)hydroxide materials.⁴⁻⁶ Building on this body of work, a number of promising metal chalcogenide OER catalysts have recently been reported, as well.^{5,7-9} In an effort to further improve the catalytic performance of both (oxy)hydroxides and chalcogenides, researchers have modified the compositions of these materials to leverage the synergistic effects of different transition metals, like Fe and Co, and impact the chemical and electrochemical properties of the catalysts.^{6,8,10-12} Recent work has shown that many of these chalcogenide materials may act as pre-catalysts for the true metal (oxy)hydroxide OER active sites, and that the properties of the initial chalcogenide may have a direct impact on the final catalyst that forms.^{13,14} As such, researchers have recently begun to systematically incorporate multiple chalcogens into these materials to investigate the resulting effect on OER performance.^{15,16} These works suggest that the incorporation of multiple chalcogens can induce a number of beneficial effects, such as the creation of OER-active crystal lattice defects and improvements in charge conduction, but further work is needed to explore this topic in greater detail.

Toward this end, we have used hydrothermal synthesis to create a series of nickel sulfoselenide materials, and have investigated their use as OER electrocatalysts. Using a variety of analytical techniques, including X-ray diffraction (XRD), X-ray photoelectron spectroscopy (XPS), scanning and transmission electron microscopy (SEM and TEM), total reflectance X-ray fluorescence spectroscopy (TXRF), electrochemical impedance spectroscopy (EIS), and cyclic voltammetry (CV), we have explored the chemical properties of the materials prior to electrocatalysis to determine what effect the S/Se ratio has on the physical, chemical, and electrocatalytic properties of the materials. We also explored the relative stability of the materials, and determined that these nickel sulfoselenides are best classified as pre-catalysts that yield an active nickel (oxy)hydroxide OER electrocatalyst. Importantly, we find that the incorporation of Se

into Ni_3S_2 appears to improve the electrical conductivity and oxidative stability of the metal sulfide, and that the degree of surface oxidation prior to OER correlates well with catalytic performance. Based on our findings, we suggest that metal mixed-chalcogenides like the nickel sulfoselenides represent a promising family of pre-catalysts suitable for use OER electrocatalysis applications. These results open the door for further work in the field of mixed-chalcogenide electrocatalysts for a variety of reactions, and the development of advanced catalysts and pre-catalysts which may improve the affordability of industrial-scale, renewably-powered water splitting.

8.2 EXPERIMENTAL

8.2.1 NiS_xSe_y Electrocatalyst Synthesis

All of the NiS_xSe_y electrocatalysts were synthesized using the hydrothermal synthesis detailed here. 0.5 mmol of $\text{Ni}(\text{SO}_4)_4 \cdot 6\text{H}_2\text{O}$ (Acros Organics, 99%) were added to 50 mL of ultrapure water (18 M Ω), and magnetically stirred for 10 minutes, at which point 5 mmol of the chalcogen precursor was added and the resulting solution stirred for a further 10 minutes. Here, thiourea (Acros Organics, 99.9%) was used as the S source, and SeO_2 (Alfa Aesar, 99%) was used as a Se source; in all but the pure NiS_{100} , the total molar chalcogen content was equivalent to the Ni content, and by changing the thiourea/ SeO_2 ratio we controlled the S/Se ratio of the final product. Thus, for a 25% Se- NiS_xSe_y sample, 0.5 mmol of Ni sulfate was combined with 0.375 mmol thiourea and 0.125 mmol selenium oxide. In the case of the pure Ni_3S_2 , a 3:2 ratio of Ni sulfate/thiourea was used, as a 1:1 ratio produced an uneven mix of Ni_3S_2 and NiS_2 , rather than NiS .

After mixing of the chalcogen precursors was completed, 10 mL (55x molar equivalents) of hydrazine hydrate solution (Millipore-Sigma, 99%) was added dropwise

to the solution over approximately 5 minutes, and the resulting solution stirred for an additional 10 minutes. In the hydrothermal synthesis, the hydrazine acts as a thermally-activated reducing agent to produce H_2S and H_2Se , which can in turn produce the Ni chalcogenides. After mixing, the resulting solution was transferred to a Teflon hydrothermal reactor vessel (100 mL) and sealed in a hydrothermal autoclave. The vessel was heated in a muffle furnace at $5\text{ }^\circ\text{C}/\text{min}$ to $180\text{ }^\circ\text{C}$ and held for 20 hours before being allowed to cool to room temperature naturally, typically about 6 hours. Following cooling, the resulting metal chalcogenide powder was washed in water and centrifuged twice, followed by one more wash in ethanol to remove any unreacted precursors, then dried in a vacuum oven overnight at $80\text{ }^\circ\text{C}$. These dried powders were then collected and used as-synthesized in further characterizations. Of note, this synthesis was relatively robust, and showed similar products, crystallography and morphology, when scaled up to 3-times the Ni/chalcogen concentration while maintaining the total water and hydrazine hydrate volume.

8.2.2 Electrocatalyst Ink and Electrode Preparation

In a typical electrode fabrication, 0.5 mg of catalyst powder was suspended in 0.125 mL (4:1 g/mL) of a 4% Nafion (Millipore-Sigma)/isopropanol solution by sonication for 10 minutes. Following suspension, the 12 μL of ink was deposited onto a 0.2 cm^2 glassy carbon rotating disk electrode (RDE, Gamry) in 3 μL aliquots, each followed by drying, to produce a total loading of $0.24\text{ mg}/\text{cm}^2$. Once dried, the electrode was used for electrochemical testing.

8.2.3 Electrochemical Testing

To determine overall electrocatalyst performance, we performed cyclic voltammetry (CV) in approximately 40 mL of 1 M KOH solution (Fisher, ACS Certified) using a CHI 660D potentiostats (CH Instruments, Austin, TX). The NiS_xSe_y/glassy carbon RDE was used as the working electrode, a Pt wire was used as the counter electrode, and an Ag/AgCl reference electrode in saturated KCl solution (CH Instruments, Austin, TX) was used as the reference. In a typical experiment, three consecutive CV sweeps were made from 0.2-0.8 V vs Ag/AgCl (sat'd KCl) with 100% iR compensation at a scan rate of 20 mV/s. For each material, testing was performed in triplicate fashion; three separate electrodes were prepared, and 3 CVs were run on each prepared electrode. The third scan of all three of the electrodes was then employed to generate an average curve from which the overpotential at 10 mA/cm² (η_{10}) was measured. Electrochemical impedance spectroscopy (EIS) was performed on selected NiS_xSe_y samples at an alternating potential of 1.52 V vs. RHE with an amplitude of +/- 5 mV between 100 kHz and 0.1 Hz. After the initial EIS spectra was measured, all samples underwent chronopotentiometric testing at 10 mA/cm² for 10 minutes, and the EIS spectra was measured again. For long-term testing of the electrodes, chronopotentiometric experiments were performed by measuring the potential required to produce 10 mA/cm² of current as a function of time; the potential was later corrected using the measured resistance of the electrode prior to testing. During long-term testing, the RDE was rotated at approximately 300 rpm and slow stream of Ar gas was impinged on the surface to dislodge any O₂ bubbles generated during the experiment.

For rotating ring-disk electrode (RRDE) analysis of Faradaic efficiency, a glassy carbon disk electrode loaded with 0.24 mg/cm² of NiS_xSe_y catalyst was used as the working electrode, and a Pt ring electrode was used to reduce the O₂ generated at the disk

to H₂O₂ via a 2-electron process; a Ag/AgCl (sat'd KCl) reference electrode and Pt wire counter electrode completed the electrochemical cell, and a CHI 700E bipotentiostat (CH Instruments, Austin, TX) was used to perform the analysis. An Ar-sparged 0.1M KOH solution was used as the electrolyte for all experiments. All of the experiments were background corrected by measuring the ring current at 0.435 V vs RHE and holding the disk at the open-circuit potential over 2 minutes while rotating at 1600 rpm; the average ring current of the last 60 second of the experiment was then subtracted from subsequent ring current measurements. For Faradaic efficiency measurements, the NiS_xSe_y electrocatalyst was held at 1, 2, and 4 mA/cm² for 2 minutes with a rotation rate of 1600 rpm, while the ring was held at 0.435 V vs RHE. The average ring and disk currents from the last 60 seconds of the measurement were used to solve for equation 1, where ε is the Faradaic efficiency, i_r is the ring current, i_d is the disk current, and N is the collection efficiency of the ring (measured as 0.39 in this system). Tests for each electrocatalyst were performed in triplicate, and the average values reported.

Equation 8.1: $\varepsilon = \frac{2i_r}{Ni_d}$

8.2.4 Physical Characterization

Powder X-ray diffraction (XRD) was performed using a Spider (Rigaku) diffractometer with a Cu K α radiation source. Scanning electron microscopy (SEM) images were collected using an FEI Quanta 650 ESEM using a 20 kV accelerating voltage. X-ray photoelectron spectroscopy analysis was performed using a Kratos Axis Ultra photoelectron spectrometer using a monochromated Al K α excitation source with spectra corrected to the adventitious C 1s peak at 284.8 eV. High resolution transmission electron microscopy (HRTEM) and energy dispersive X-ray spectroscopy (EDX) mapping using scanning-transmission electron microscopy (STEM) were all performed

on a JEOL 2010F transmission electron microscope with an ultra-high resolution pole piece. The EDX mapping was conducted using an Oxford X-MaxN 80TLE solid state detector. Brunauer-Emmett-Teller (BET) surface area measurements were made using Kr adsorption in a bath of liquid nitrogen at 77K with a Quantachrome AutoSorb iQ volumetric gas adsorption analyzer (Anton Paar). Due to the low amount of metal chalcogenide produced during our synthesis and the inherently low surface area of the materials ($<50 \text{ m}^2/\text{g}$), Kr was used as the adsorbate gas for all catalysts. All samples were degassed at 120°C under vacuum prior to weighing to remove surface adsorbed species. Multi-point BET analysis was performed using Anton Paar's ASiQ WinTM software with a specified P_0 value of 2.63 Torr. ASiQ WinTM's "Micropore BET Assistant" was employed for optimal point selection for fitting to the BET equation to determine Kr-accessible surface areas. Total reflection X-ray fluorescence (TXRF) quantification of dissolved S, Se, and Ni in electrolyte solution was measured using a S2 Picofox spectrometer (Bruker Nano GmbH) with a Mo K excitation source. 0.995 mL of electrolyte solution was mixed with 5.0 μL of a Y solution, (TraceCERT, 1000 mg/L in nitric acid, Sigma Aldrich) to act as an internal standard. 10 μL of the resulting solution was dropped on to a quartz disk and dried at 70°C for 15 minutes, and the TXRF spectra was acquired over 300 s; three replicates were performed for each NiS_xSe_y catalyst studied. External calibration for quantification was performed using a commercial standard (TraceCERT Periodic Mix Table 1, SigmaAldrich). The background concentrations of each analyte in a sample of KOH electrolyte prior to testing was also measured, and the quantities measured in the tested samples were background corrected to these values.

8.3 RESULTS AND DISCUSSION

8.3.1 X-ray Diffraction Spectroscopy and Scanning Electron Microscopy

To determine what effect chalcogen-substitution has on the hydrothermal synthesis of our nickel sulfoselenide electrocatalysts, we used powder X-ray diffraction (XRD) to analyze differences in the crystal structures of a series of materials, ranging from pure nickel sulfide and nickel selenide compounds to a range of S/Se ratios. For simplicity, the composites will be named according to a standard formula NiS_xSe_y , where “x” equals the percentage of S relative to Ni, and “y” represents the percentage of Se. Therefore, a composite with 90% S and 10% Se would be referred to as $\text{NiS}_{90}\text{Se}_{10}$. The results, presented in **Figure 8.1**, show that these materials undergo a variety of changes as the S/Se ratio decreases from 9:1 to 1:1. By XRD, the Se-free material, NiS_{100} , is composed of a primary Ni_3S_2 phase and a minor NiS impurity phase, and both phases have been shown to be effective electrocatalysts with comparable OER overpotentials in previous studies.^{17–20} With the incorporation of 10%Se, we observe the formation of a discrete NiSe peak near 33° two theta, indicating that the Ni_3S_2 does not accommodate all of the Se in the crystal lattice, and resulting in the formation of an $\text{Ni}_3\text{S}_2/\text{NiSe}$ composite. At 25%Se incorporation, the Ni_3S_2 and NiSe phases become equally intense, and by 50%Se incorporation, the Ni_3S_2 becomes the impurity phase in a primarily NiSe composite. As a comparison to the Se-incorporated Ni_3S_2 composites, we also report a pure NiSe_{100} sample, which is composed primarily of NiSe, with a small Ni_3Se_2 impurity.

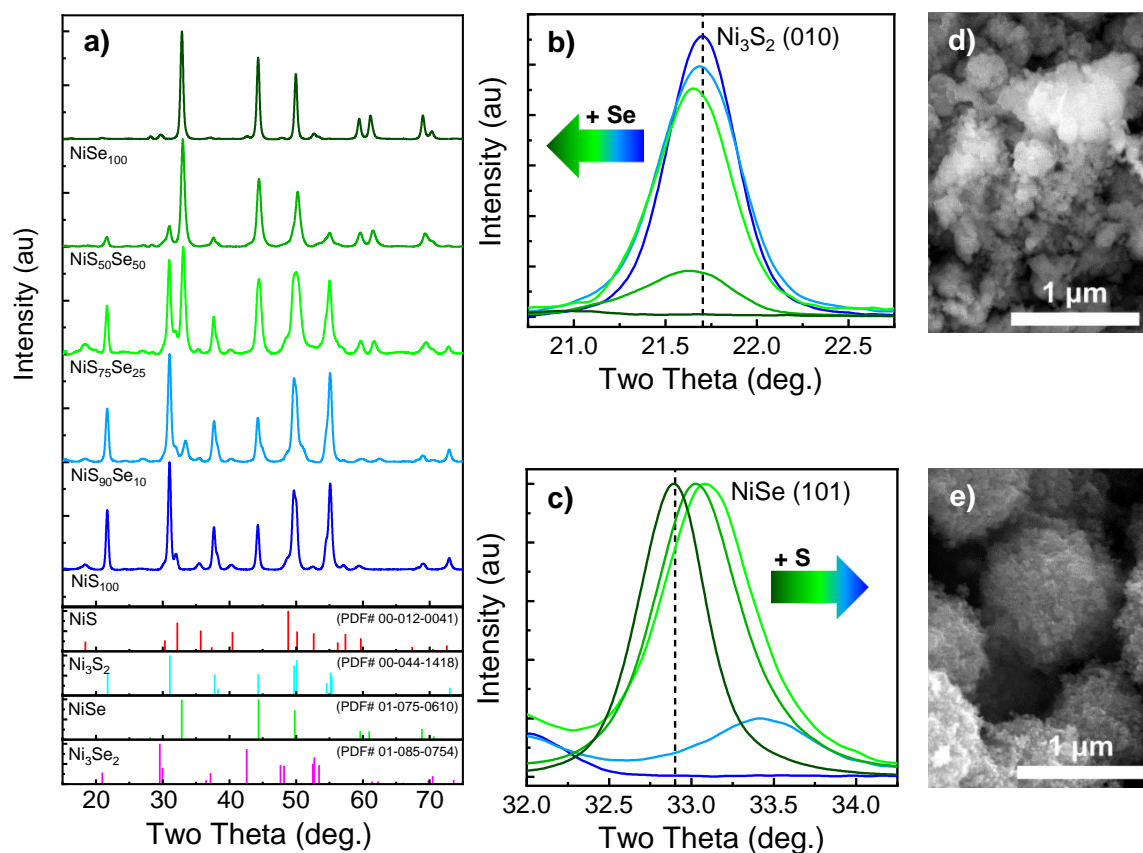


Figure 8.1: a) XRD spectra of a series of nickel sulfoselenide composite materials. The primary Ni_3S_2 phase is gradually replaced by NiSe as more Se is added to the composite. b) The Ni_3S_2 (010) peak shows a gradual shift to lower two theta with increasing Se content as more Se is incorporated into the lattice; (c) a similar effect occurs in the NiSe (101) peak, where increasing S-content causes a shift to higher two theta. SEM images of the NiS_{100} (d) and NiSe_{100} (e) shows both composites consist of agglomerated particles between 0.5 and 1 μm in diameter.

The formation of the NiSe impurity at an S/Se ratio of 9:1 indicates that much of the Se is likely segregated into a distinct NiSe phase during synthesis, and suggests that the incorporation of the much larger Se anion into the Ni_3S_2 lattice is not favorable.²¹ Despite this, the XRD spectra show that some of the Se does become incorporated into

the Ni_3S_2 phase. As seen in **Figure 8.1b**, there is a slight shift in the position of the Ni_3S_2 (010) peak at 21.7° to smaller two theta with increasing Se concentration, indicative of the incorporation of the larger anion into the crystal lattice. Likewise, a small quantity of S becomes incorporated into the selenide phase, and the NiSe_{100} (101) peak in at 32.9° (**Figure 8.1c**) exhibits a relatively large half degree shift to larger two theta as the composition becomes more S-rich.¹⁵ The magnitude of this shift, as well as the prominence of the NiSe product over Ni_3S_2 at low S/Se ratios, indicates that the smaller S^{2-} anion may be relatively easy to incorporate into the NiSe lattice, although the extent of that substitution is not further studied here.

The XRD spectra reveal that the final product of the hydrothermal synthesis is a Se-doped Ni_3S_2 and S-doped NiSe composite material, where the relative quantity of each component depends on the S/Se ratio. Previous studies of pure nickel sulfide and nickel selenide electrocatalysts have shown that both have good OER performance, with similar overpotentials when tested on high-surface area Ni foam electrodes.^{17,22} Importantly, however, the electrocatalysts presented in these two studies had dramatically different morphologies; the NiSe exhibited a nanowire morphology, while the Ni_3S_2 exhibited nanosheet morphology. Because significant differences in morphology and size can impact the comparison of electrocatalytic performance,¹⁴ we used SEM to study the morphology of our mixed NiS_xSe_y samples more closely and ensure that our synthetic procedure produced comparable products. As can be seen in **Figure 8.1d,e**, the materials are all composed primarily of roughly spherical particles, with diameters ranging from approximately 500 nm for the NiS_{100} material, to approximately 1 μm for the NiSe_{100} . Generally, it appears that the Ni_3S_2 -rich composites exhibit smaller particles than the NiSe-rich composites, but in all cases the particles appear to exhibit a degree of surface roughness (**Figure E.1,2**). The effect of any apparent roughness on the overall catalyst

surface area is small, however, as the Brunauer-Emmett-Teller (BET) surface areas of the composites measured using Kr adsorption measurements are all below 20 m²/g (**Figure E.3**). After comparing the SEM images, BET surface area measurements, and XRD spectra for all of the composites, we note a slight relationship between chalcogenide composition, morphology, and surface area. Low Se concentration (0 and 10% Se) leads to smaller Ni₃S₂ particles with larger surface areas, while increased Se-content (50 and 100%Se) appears to induce a transformation to the larger NiSe microspheres visible in the SEM in **Figures E.2d,e**. As evidenced by the XRD spectrum in **Figure 8.1**, NiS₇₅Se₂₅ appears to represent a transition between these two products, possessing both Ni₃S₂ and NiSe phases in abundance but generally possessing a more Ni₃S₂-like morphology; this combination appears to result in a material which breaks the trend in the relationship between BET surface area and Se-content. SEM images in **Figures E.1c, E.2c** show that the small Ni₃S₂-like particles present in the NiS₇₅Se₂₅ sample agglomerate more than the other composites, while there are also more micrometer-scale spherical NiSe particles visible as well. Together, both features may help to explain the anomalously-low BET surface area of the NiS₇₅Se₂₅ sample.

8.3.2 Electrochemical Characterization

Next, we used cyclic voltammetry to investigate the effects of these aforementioned differences in physiochemical properties on performance of the composites for the OER in alkaline solution. Using Nafion as a binder, we loaded the catalysts at 0.24 mg/cm² on a glassy carbon electrode for testing in a 1M KOH solution. As seen in **Figure 8.2a**, OER performance improves as Se is incorporated into the Ni₃S₂ composite. The overpotentials at 10 mA/cm² (η_{10}) of both the NiS₉₀Se₁₀ and the NiS₇₅Se₂₅ samples are approximately 40 mV lower than that of the Se-free NiS₁₀₀ sample. However,

further increasing the amount of Se to a 1:1 S/Se ratio results in an increase in overpotential to 412 mV, larger even than that of the pure NiSe₁₀₀ ($\eta_{10} = 386$ mV). A similar trend is likewise observed in measurements of mass activity for the catalysts at 300 mV and 400 mV of overpotential (**Figure E.4**), where the NiS₉₀Se₁₀ and NiS₇₅Se₂₅ samples showed notably better performance than the other composites tested. The measured η_{10} for all composites suggest that while pure Ni₃S₂ is a better catalyst for the OER than NiSe, the addition of moderate amounts of Se produces doped Ni₃S_{2-y}Se_y catalysts with notably improved OER performance and stability, indicated by the low η_{10} and the minimal change in overpotential over time in **Figure 8.2b**.

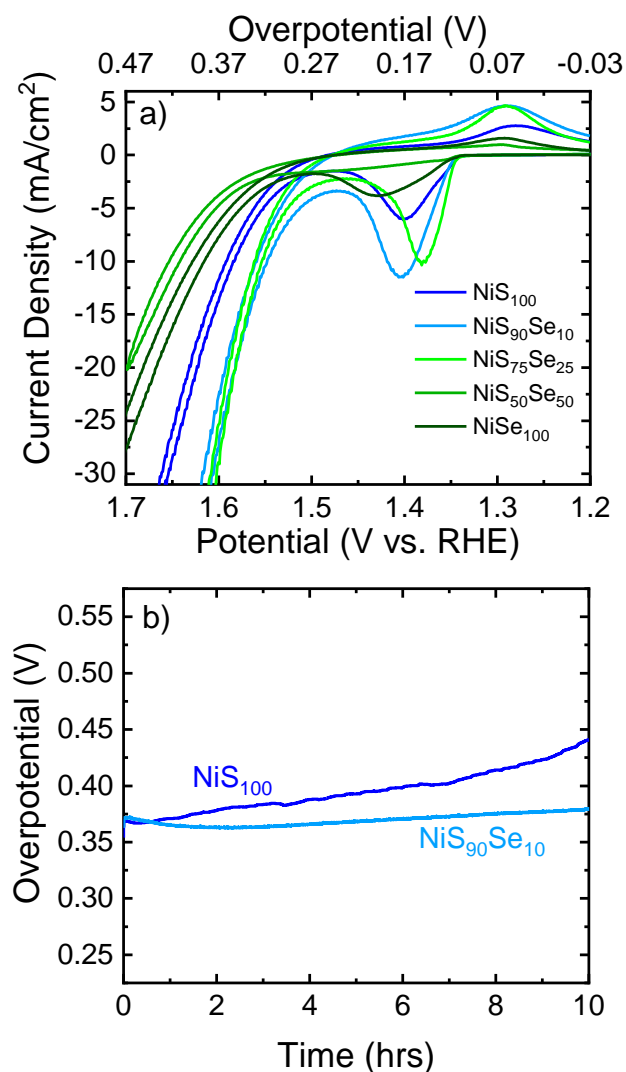


Figure 8.2: a) Averaged CVs of the NiSSe composites measured in 1M KOH. The addition of 10-25%Se significantly reduces the overpotential when compared to the pure sulfide or selenide, as well as the 50/50 mixture. b) Chronoamperomogram of the NiS₁₀₀ and NiS₉₀Se₁₀ composites at 10 mA/cm² over 10 hours of continuous use, showing the superior stability of the Se-incorporated material. All experiments were performed versus a Pt counter electrode with an Ag/AgCl(sat'd KCl) reference electrode.

The increase in overpotential with testing time for the NiS₁₀₀ sample may be due in part to oxidation of the metal chalcogenide surfaces with OER electrocatalysis.

Previous studies have shown that metal chalcogenides tend to exhibit oxidation under OER reaction conditions and that the factors that govern the extent of oxidation for different materials are relatively poorly understood at present.¹⁴ To explore if self-oxidative side reactions may occur at the catalyst surface during the OER, we used a rotating ring-disk electrode (RRDE) to calculate the Faradaic efficiency of the NiS₁₀₀, NiS₉₀Se₁₀, and NiSe₁₀₀ composites.²³ **Figure E.5** shows that over a range of applied j , the NiS₉₀Se₁₀ and NiSe₁₀₀ electrocatalysts showed higher Faradaic efficiency than the NiS₁₀₀ sample, which indicates that the presence of Se reduces Faradaic side reactions during OER. We note that errors on the order of +/- 10% are not uncommon with this technique,²³ and we believe that the greater than 100% efficiency observed for NiSe₁₀₀ at higher applied current densities (106% at 4 mA/cm²) is likely due to a systematic error present in our testing apparatus. As such systematic error is expected to be present in measurements for all three composites, we can make qualitative, if not quantitative, comparisons of the composites' Faradaic efficiencies. Total reflectance X-ray fluorescence (TXRF) analysis of the electrolytes used to test these composites for 6 hours at 10 mA/cm² appears to support these results as well. Analysis of three representative samples (NiS₁₀₀, NiS₉₀Se₁₀, and NiSe₁₀₀), showed less dissolved Ni in solution for the Se-containing electrocatalysts after testing (**Figure E.6**) than for the pure sulfide; as Ni is expected to be the binding site for OER catalysis, this helps explain the stability of our NiS₉₀Se₁₀ electrocatalyst. Sulfur was not observed in any samples, possibly due to *in situ* reduction at the counter electrode or to other systematic losses, and Se was observed in all samples, likely due to a small degree of surface contamination from the hydrothermal synthesis. We note that the significant quantity of Se detected in the electrolyte after testing the NiSe₁₀₀ sample may suggest chemical etching by KOH rather than electrochemical oxidative degradation, given the high measured Faradaic efficiency of

NiSe₁₀₀. Regardless, the decrease in the concentration of Ni in the electrolyte with increased Se content indicates that the addition of even small amounts of Se to the NiS_xSe_y composite can increase (electro)chemical stability, as previously observed when comparing the long-term testing in **Figure 8.2b**.

Notably, the addition of large amounts of S to a NiSe electrocatalyst actually decreased OER performance relative to an S-free material, despite the increased stability of Se-containing electrocatalysts at low Se concentrations. This result is significant because previous work on materials with a nominal NiSe crystal structure doped with S showed increased performance as the S/Se ratio decreased.¹⁵ Another study on an Se-doped NiS₂ material for the OER in neutral electrolyte showed that a 1:1 S/Se ratio was optimal, in marked contrast to the relatively poor performance of our NiS₅₀Se₅₀ sample.²⁴ Given that the materials in those previous studies were primarily NiSe and NiS₂, while the predominant crystal structure in our most efficient composites is Ni₃S₂, it appears that the effects of S- or Se-doping may differ noticeably between metal chalcogenides with different crystal structures. These differences may be due in part to the ease of defect formation in a given crystal structure upon heteroanion incorporation. Wang *et al.* previously showed that NiCoSe nanocrystals doped with S possessed more lattice defects than un-doped nanocrystals, which acted as nucleation sites for formation of the active NiCo(OH)₂ phase during catalysis.¹⁵ We postulate that the Se-incorporation evidenced in the XRD spectra may likewise induce defects in the Ni₃S₂ lattice, and may similarly help to form an active (oxy)hydroxide OER catalyst species. At moderate Se levels of 10% and 25%, Se incorporation appears to improve performance of predominantly Ni₃S₂ materials. However, above this observed threshold, increasing the Se ratio results instead in the formation of NiSe as the dominant crystalline product with residual S acting as the dopant. While NiSe-phase nanocrystals of a material with the same S/Se ratio were

shown to be efficient for OER,¹⁵ we observe that the production of defects might not have as significant of an effect in our micron-sized particles.

To more closely probe the fundamental differences in the intrinsic OER performance of these materials, we calculated the BET-derived current density ($\text{mA}/\text{cm}^2_{\text{BET}}$) by dividing the observed current densities ($\text{mA}/\text{cm}^2_{\text{RDE}}$) by the $0.24 \text{ mg}/\text{cm}^2_{\text{RDE}}$ loading and each electrocatalyst's BET specific surface area ($\text{SA}_{\text{BET}}, \text{cm}^2/\text{g}$) as determined by Kr adsorption (**Figure E.5**). These re-normalized performance curves are shown in **Figure E.6**, and both the gravimetric and BET-derived results are summarized in **Table 8.1**. After accounting for differences in SA_{BET} , the $\text{NiS}_{50}\text{Se}_{50}$ sample still shows the worst OER performance of all of the composites, while in contrast to the analysis based on RDE surface area, the $\text{NiS}_{75}\text{Se}_{25}$ catalyst shows higher geometric activity than the $\text{NiS}_{90}\text{Se}_{10}$ composite; this is in agreement with previous reports on low S/Se materials,¹⁵ as well as the mass activity measurements of the composites at higher overpotentials (**Figure E.4**). Further, the pure NiSe_{100} material shows a lower SA_{BET} -scaled overpotential than the pure NiS_{100} material, as previously observed by Nath and coworkers.⁷ Thus, our composites appear to show that, while the intrinsic performance of Se-rich nickel chalcogenides is superior to a point, the gravimetric performance of such composites is inhibited by their lower surface areas, which is likely caused by the formation of larger NiSe microspheres.

Sample	η_{10} , Gravimetric (V)	$\eta_{0.5}$, BET SA (V)	SA _{BET} (m ² /g)
NiS ₁₀₀	0.354	0.400	14.6
NiS ₉₀ Se ₁₀	0.318	0.368	17.3
NiS ₇₅ Se ₂₅	0.324	0.341	10.6
NiS ₅₀ Se ₅₀	0.412	0.462	12.7
NiSe ₁₀₀	0.386	0.377	5.67

Table 8.1 Gravimetric overpotential, BET-derived overpotential, and BET surface areas of NiS_xSe_y composites

Several factors may explain the improved intrinsic activity observed in the Se-containing composites. As previously mentioned, it may be due in part to the presence of lattice defects in the Ni₃S₂ material induced by the substitution of Se for S, as evidenced in **Figure 8.1b**. Alternatively, metal selenides are known to be more electronically conductive than metal sulfides, and thus the inclusion of Se may improve the conductivity of the resulting composite. Higher electrical conductivity and faster electron transfer within the catalyst might reduce resistive losses and improve catalyst performance. To determine if differences in electrical conductivity may be playing a role in the performance difference, we studied the electrochemical impedance spectroscopy (EIS) spectra of characteristic NiS_xSe_y electrocatalysts and related this to the previously-measured OER performance. Nyquist plots of the catalysts in **Figure E.8** show that the pristine, untested NiS₁₀₀ electrocatalyst has a significantly larger semicircle than either the NiS₉₀Se₁₀ or NiSe₁₀₀ materials. This indicates that the inclusion of just 10% Se into the Ni₃S₂ material significantly improved the conductivity of the material, making it greater even than that of a pure nickel selenide and likely contributing to the enhanced electrocatalytic performance observed in **Figure 8.2a**. Because subsequent surface oxidation may decrease electrocatalyst conductivity and impact measured performance, we also recorded the EIS spectra of the samples after 10 minutes of testing at 10 mA/cm².

For all materials, the semicircles in the Nyquist plots increased in diameter after testing (**Figure E.8**), an indication of reduced conductivity that can be attributed to the surface oxidation suggested by the measurements of Faradaic efficiency. Among the three samples, NiS₉₀Se₁₀ showed a much smaller loss of conductivity than either the NiS₁₀₀ or NiSe₁₀₀, in good agreement with the low η_{10} and high stability of the material. In contrast, both the pure sulfide and selenide materials show much larger semicircles that are indicative of lower conductivities. The NiSe₁₀₀ in particular shows a very large decrease in conductivity after testing that ultimately results in poorer conductivity than the NiS₁₀₀ sample; this agrees well with the relatively poor electrocatalytic performance previously demonstrated. In addition to the lower surface area of the catalyst, this evidence of decreased conductivity may explain its relatively low performance when compared to pure sulfur and 10% Se materials. Together, our EIS results suggest that conductivity, in addition to catalyst surface area, plays a significant role in OER electrocatalysis, and that the inclusion of small quantities of Se into Ni₃S₂ significantly improves the conductivity of the resulting material.

8.3.3 X-ray Photoelectron Spectroscopy

We next analyzed the chemical composition of the as-synthesized materials with X-ray photoelectron spectroscopy (XPS) and energy-dispersive X-ray spectroscopy (EDX) to more-fully explore the improved performance of the NiS_xSe_y electrocatalysts. Using XPS deconvolution and EDX quantification, we calculated the S/Se ratios of our catalysts (**Figure E.9a**) and found that the relative amount of each chalcogen agrees well with the theoretical values for the desired compositions. While the NiS₉₀Se₁₀ (S/Se theo. = 9.0) material shows a relatively low S/Se ratio of approximately 5.3 from XPS, this may be due to surface oxidation of the materials following synthesis. Such surface

oxidation is supported by the much higher S/Se value of 7.5 obtained via EDX (which has a much larger probe depth and is not as sensitive to surface oxidation). Indeed, closer analysis of the O 1s spectra for all materials (**Figure E.9b**) shows a significant hydroxide peak near 531 eV, which likewise indicates that the surface has oxidized even before testing. Notably, as the S/Se ratio decreases, so does the quantity of oxidized material at the composite surface, as can be seen in both the chalcogen (S 2s/Se 3s) and oxygen (O 1s) spectra for the NiS₁₀₀, NiS₉₀Se₁₀, and NiSe₁₀₀ materials in **Figures 8.3b,c** and for all other samples in **Figure E.9b,c**. In all cases, the S 2s and Se 3s spectra contain both a primary metal sulfide/selenide peak (226.2 eV for S and 228.9 eV for Se) and an accompanying oxidized S or Se peak approximately 3 – 3.5 eV higher. All Se-containing composites show less oxidation than the pure NiS₁₀₀ sample, and within the Se-containing samples, NiS₉₀Se₁₀ and NiS₇₅Se₂₅ show the smallest quantity of oxidized material (**Figure E.9d**). Similarly, as the S/Se ratio decreases, the Ni/Ni-X peak in the Ni 2p 3/2 spectra becomes more pronounced and shifts from 853.1 eV for NiS₁₀₀ to a value of approximately 852.3 eV for NiSe₁₀₀ (**Figure 8.3a**), as indicated by the dashed line. Combined, analysis of these spectra suggest the presence of a more metallic and less-oxidized surface for Se-containing composites. Differences in the Ni spectra of nickel sulfide, selenide, and telluride materials have been previously regarded as an indicator of the improved resistance to oxidation exhibited by the Se and Te materials.^{7,25} Thus, an increase in metallic character with increasing Se-incorporation for 10% and 25% composites not only agrees with the increasing quantity of NiSe visible in the XRD spectra, but may also indicate that the composite material is more resistant to oxidation than the pure Ni₃S₂ electrocatalyst.

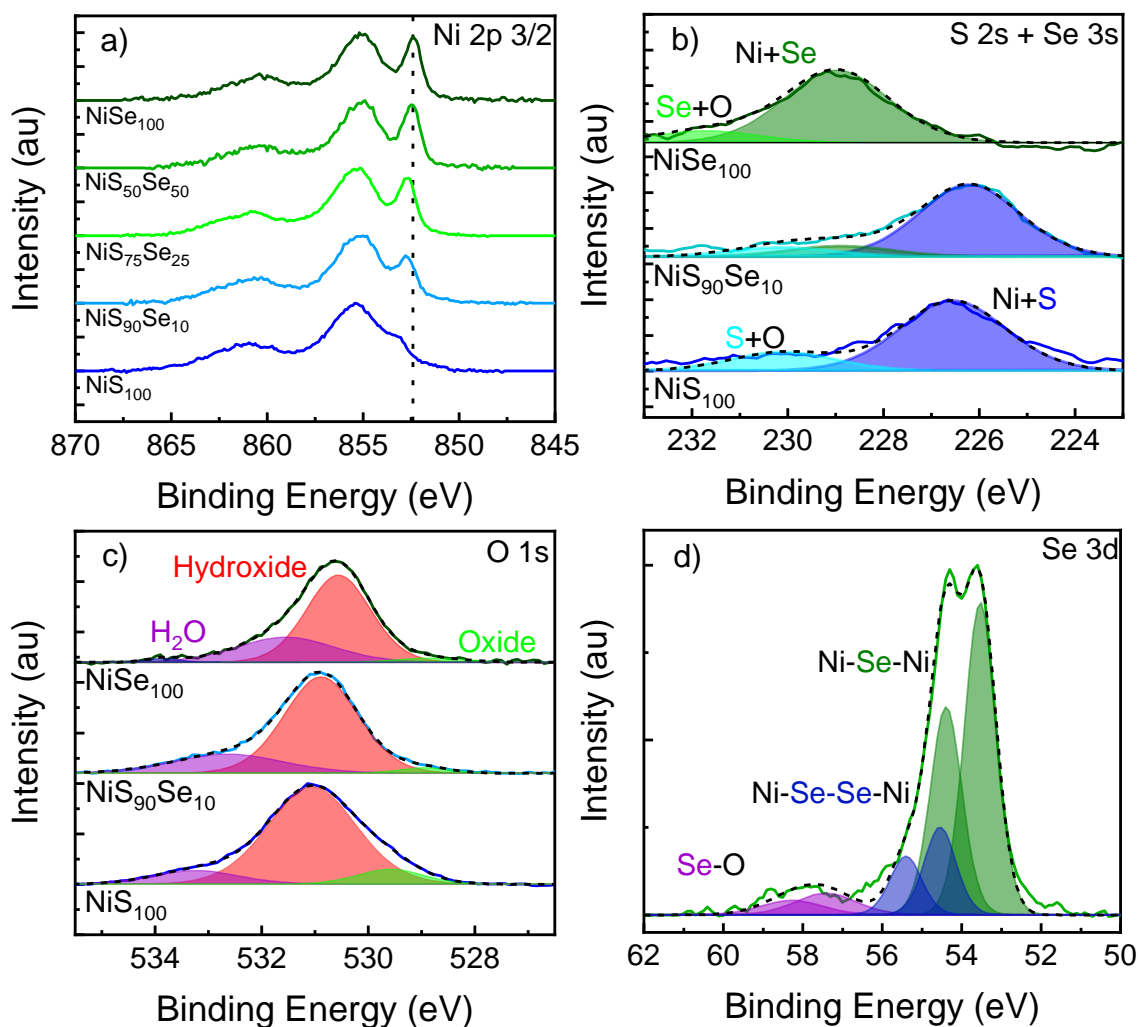


Figure 8.3: a) Ni 2p 3/2 XPS spectra of all NiSSe composites, showing a gradual shift to lower binding energies with increasing Se-content, indicating a more metallic character b) XPS spectra of the S 2s and Se 3s regions for the NiS_{100} , $\text{NiS}_{90}\text{Se}_{10}$, and NiSe_{100} samples. The addition of Se results in a decreased quantity of oxidized chalcogen at the surface. c) O 1s XPS spectra for the NiS_{100} , $\text{NiS}_{90}\text{Se}_{10}$, and NiSe_{100} composites, showing the contributions from surface hydroxides (red), oxides (green), and adsorbed water (purple). The addition of Se reduces the quantity of NiO_x species at the surface. d) Se 3d spectra for the $\text{NiS}_{50}\text{Se}_{50}$ composite, showing contributions from single and dichalcogenide bonds, as well as oxidized selenium species.

In agreement with the higher oxidation resistance of Se species, closer inspection of the Se 3d region for all composites (**Figure 8.3d, E.9d**) shows only a small degree of oxidized Se is present, and that the predominant Se species present is typically assigned to nickel selenide compounds, with a 3d 5/2 peak at approximately 53 eV.²⁶ As previously noted by Cui and coworkers on Co chalcogenide OER catalysts, selenides and tellurides tend to be more resistant to oxidation than corresponding sulfides.²⁷ Theoretical evidence of this can be observed when comparing Pourbaix diagrams for pure sulfide, selenide, and telluride materials (**Figure E.10**).^{28–30} In general, both Ni₃Se₂ and Ni₃Te₂ appear to be more stable than Ni₃S₂ across a wide range of pH and potential, although we do note that they are all expected to oxidize under OER conditions. Regardless, this data suggests that these materials possess a greater intrinsic stability, possibly due to the more metallic character of the material indicated by the Ni 2p region. In addition to the primary metal selenide peak, fitting of the spectrum reveals a second doublet of Se 3d peaks, however, with the 5/2 peak located at approximately 54.5 eV. This peak is more reduced than that of elemental Se,³¹ and therefore may instead be evidence of the surface presence of cubic NiSe₂, which exhibits a Se-Se bond.³² Previous work has shown that the S 2p spectra of S-rich molybdenum sulfides likewise exhibits both a lower binding energy (BE) peak, representative of direct Mo-S-Mo bonds, and a higher BE peak, representative of Mo-S-S-Mo bonds.³³ The existence of NiSe₂ agrees well with the observed XPS spectra, and we can infer from the lack of associated peaks in XRD that this phase is likely in low abundance and may in fact only exist at the surface. Typically, the NiSe₂ phase accounted for approximately 20-25% of the total selenide species at the surface for all the Se-containing materials. As there does not appear to be any correlation between the presence of NiSe₂ and improved OER performance, we do not think it plays a significant role in the observed differences in η_{10} .

Instead, OER performance is more closely related to the percentage of oxidized chalcogen present at the material surface prior to testing. By quantifying the amount of oxidized S and Se species in **Figure E.9b**, and then comparing this percentage to the η_{10} for each sample, we find similar changes in both the overpotential and the extent of surface oxidation as level of Se incorporation changes (**Figure E.11**). Both the Ni₃S₂-rich and the NiSe-rich composites show a clear decrease in η_{10} with decreasing S-O and Se-O species, and given that a material's surface species either contribute directly to the OER catalytic processes or indirectly influence the formation of other active sites and the overall electrical conductivity of the material, small changes in initial surface chemistry of an electrocatalyst can have significant impact on its OER performance. Previous work on a series of Ni-Se compounds showed that a previously-oxidized NiO catalyst performed worse than a fresh NiSe catalyst which was oxidized during testing,³⁴ and other studies have shown that the type of oxidized surface species can play a large role in catalytic performance. For example, our group has previously shown that nickel sulfide catalysts fully oxidized to an amorphous hydroxide exhibited better OER performance than initially oxidized materials,³⁵ and Cui and coworkers showed similar results on a series of Co-based chalcogenides.³⁶ Thus, we hypothesize that, in agreement with prior studies demonstrating the stability of Se-compounds towards oxidation,²⁵ the introduction of Se into the Ni₃S₂ lattice mitigates oxidation of the surface prior to testing and may induce lattice strain (evidenced in **Figure 8.1b**) which creates more active sites for the OER. While S-incorporation into NiSe particles may also induce this defect/nucleation site effect, the presence of an excess of S (with its inherently lower resistance to oxidation) may result in more adverse surface oxidation on these composites even prior to catalysis. Further, our particles are much larger than those of Wang *et al.*,¹⁵

and thus lattice defects may have less of an overall effect on the OER than surface oxidation for the larger NiS₅₀Se₅₀ particles.

8.3.4 Transmission Electron Microscopy

To study this oxidation behavior with much higher resolution, we used high-resolution transmission electron microscopy (HRTEM) and EDX mapping to examine catalyst oxidation before and after OER testing. To prepare materials for this comparison, chronopotentiometric stability experiments were performed on both composites, with the results reported in **Figure 8.2b**. Electrode stability was tested at a current density of 10 mA/cm², and initially both the NiS₁₀₀ and NiS₉₀Se₁₀ composites exhibited similar overpotentials near 375 mV. As the experiment progressed, however, the overpotential for the NiS₁₀₀ sample increased by approximately 20% over 10 hours, while the NiS₉₀Se₁₀ electrocatalyst did not exhibit any notable increase. The samples were run until failure, and the NiS₁₀₀ sample failed after approximately 11 hours, while the NiS₉₀Se₁₀ sample failed after approximately 22 hours (**Figure E.12**). This result agrees with our hypothesis regarding the stabilizing effect of the incorporated Se and is comparable to previously reported stabilities from Zeng *et al.* in neutral electrolyte.²⁴ Following testing, the electrocatalysts were removed from the GC electrode via sonication and studied using HRTEM.

HRTEM analysis of the NiS₁₀₀ material prior to testing shows that the micron-scale particles observed in the SEM images (**Figure E.1a**) are agglomerates of crystalline particles roughly 50 nm in diameter (**Figure E.13**), with additional crystalline particles less than 10 nm in diameter (**Figure E.14**). Fast Fourier transform (FFT) analysis of the HRTEM images shows that the crystalline interior of the particles is composed of a mixture of NiS and Ni₃S₂ (**Figure E.14**), in agreement with the XRD spectrum. Of note,

the HRTEM shows the presence of a sub-10 nm layer of mostly amorphous material surrounding the particle, which EDX mapping confirms to be O-rich (**Figure E.14b**). This O-rich region also corresponds to the NiO species found in HRTEM, which indicates that the NiS₁₀₀ catalyst exhibits both crystalline and amorphous oxide formation prior to OER testing; such oxidation corresponds to the hydroxide and oxide peaks observed in the O 1s XPS spectrum of the material. In contrast, HRTEM images of the as-synthesized NiS₉₀Se₁₀ (**Figure E.15a**) show a much thinner amorphous layer on the imaged particles (**Figure E.15c**). Lattice measurements show that these particles are composed primarily of NiS, Ni₃S₂, and NiSe phases, with evidence of NiOOH in the particle at spot 1, without any clear indication of NiO; this is in agreement with the previously-discussed XPS results (**Figure 8.2b**). Similarly, the lower degree of oxidation visible in the EDX map of the composite (**Figure E.15b**) indicates a diffuse amount of O in the material that, while most visible at the edges of the particles, is not as concentrated as in the NiS₁₀₀ composite. Overall, this data supports our hypothesis regarding the increased resistance to oxidation exhibited by the NiS_xSe_y composite materials.

After stability testing, both NiS₁₀₀ and NiS₉₀Se₁₀ materials showed the formation of a clearly oxidized shell of material surrounding an un-oxidized core (**Figure 8.4b,d**), while also maintaining a homogeneous distribution of Ni, S, and Se in the un-oxidized regions (**Figures E.16,17**). Such behavior has been previously observed in other Ni sulfide-based electrocatalysts, with both amorphous and crystalline metal (oxy)hydroxides observed as surface products.^{35,37} While the oxidized layer in the tested NiS₁₀₀ sample shows particles with clearly visible crystal lattices (**Figure 8.4c**), the surface of the tested NiS₉₀Se₁₀ sample appears to be much more disordered (**Figure 8.4e**). Similarly, the thickness of the resulting oxide layer appears to differ with Se-incorporation. From EDX mapping, the depth of the oxidized layer on the NiS₁₀₀ sample

appears to have doubled with OER testing, from ~10 nm to approximately 20 nm over 10 hours of testing. The $\text{NiS}_{90}\text{Se}_{10}$ sample also experiences growth, but only from 1-2 nm to 10 nm and over a much longer exposure of roughly 20 hours. Comparing the two samples, the slower rate of oxidation exhibited by the $\text{NiS}_{90}\text{Se}_{10}$ sample appears to be further evidence of the stabilizing effect of Se-incorporation.

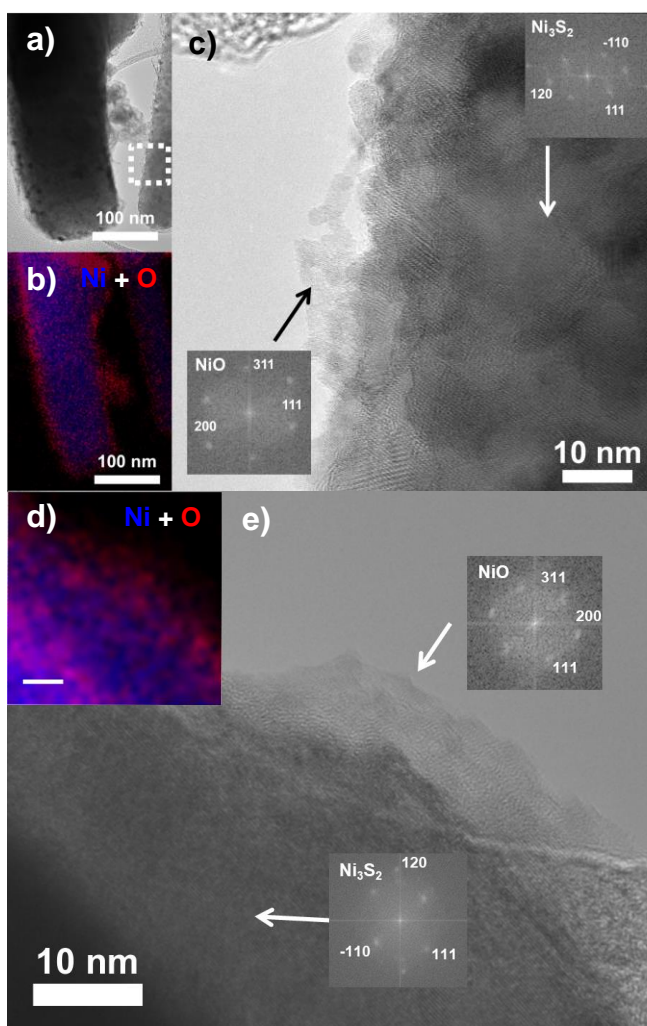


Figure 8.4: TEM image of post-OER NiS_{100} (a) with accompanying EDX mapping (b) showing the formation of an oxidized shell approximately 20 nm thick surrounding an un-oxidized interior. HRTEM shows that the oxidized region appears relatively crystalline, and composed of NiO , while the interior is composed of Ni_3S_2 . EDX mapping of the $\text{NiS}_{90}\text{Se}_{10}$ material (d, scale bar 10 nm) shows a similarly oxidized surface, that is much thinner (10 nm) with HRTEM and FFT (e) likewise corresponding to NiO at the surface and Ni_3S_2 in the bulk. This oxide appears less particulate than then NiS_{100} material, however.

The formation of an apparent core-shell particle after OER testing is interesting, as there is significant evidence to suggest that metal chalcogenides, and sulfides in particular, are inherently unstable under alkaline OER reaction conditions.^{5,27,35} Frequently, post-OER analysis shows that these materials are completely oxidized after testing,³⁵ although it appears as though the deliberate incorporation of metals like Fe or Co may inhibit this;⁶ we believe that the Se in our materials may be inducing a similar effect. Additionally, many previous reports on nickel sulfides explored NiS and NiS₂ compounds rather than the Ni₃S₂ material present here. Work from Nath and coworkers has shown that both Ni₃Te₂ and Ni₃Se₂ possess superior oxidative stability when compared to other telluride and selenide phases,^{7,25} thus, it is possible that Ni₃S₂ may likewise possess increased stability toward surface oxidation as compared to NiS or NiS₂ even before the addition of Se. Therefore, we suggest the minimal oxidation of NiS₉₀Se₁₀ observed after long-term testing is a result of enhanced oxidative resistance due to both Se-incorporation and this Ni₃S₂ phase. Regarding performance and stability, Se-incorporation likely induces the formation of a more defective, active amorphous oxidized layer at the surface and increases the conductivity of the material as compared to an Se-free material. The increased conductivity of the material may also help explain the improved stability of the NiS₉₀Se₁₀ material. Due to the increased conductivity and OER performance of the electrocatalyst, less internal resistive loss occurs and lower overpotentials are required to drive the OER forward, reducing the likelihood of parasitic side reactions like self-oxidation. Our measurements of Faradaic efficiency (**Figure E.5**) show that NiS₁₀₀ shows reduced efficiency for the OER at higher applied current densities (and larger overpotentials) when compared to the NiS₉₀Se₁₀, providing support for this hypothesis. In this way, the Se-incorporation would increase the stability of the material by increasing conductivity, and thereby indirectly mitigate undesired reactions.

Combined with the likely-higher intrinsic stability of the Ni_3S_2 phase and the lattice defects in the particles, this could explain why $\text{NiS}_{90}\text{Se}_{10}$ shows the best performance of all materials studied here, as it combines proper crystal phase, active lattice defects, and increased conductivity to improve electrocatalytic performance and minimize damage to the catalyst.

8.4 CONCLUSIONS

In summary, we have used a scalable hydrothermal synthesis to create series of nickel sulfoselenide materials for use as OER electrocatalysts in alkaline solution. Through this method, we created composites consisting primarily of Se-modified Ni_3S_2 from precursor mixtures with low Se concentrations, while a S-modified NiSe phase became more abundant with increasing precursor Se concentration. The predominant products and the relative extents of Se- or S-incorporation were monitored by XRD, while interrogation by XPS and EDX confirmed that the desired overall S/Se ratio was achieved. SEM and HRTEM measurements revealed that the synthesized materials were micron-sized clusters of smaller nanocrystals, and Kr surface adsorption analysis determined that all of the materials possessed similar BET surface areas ($< 20 \text{ m}^2/\text{g}$). Surface chemistry analysis with XPS suggested that Se addition appeared to reduce the extent of oxidation in the composites, resulting in more hydroxide than oxide species on the surface. OER overpotential measurements showed that Se-modified Ni_3S_2 possessed superior catalytic ability and stability when compared to the other composites, with $\text{NiS}_{90}\text{Se}_{10}$ having an η_{10} of 318 mV and stable performance over 20 hours. Improvement in electrocatalytic performance was correlated to a decrease in the amount of oxidized S or Se (determined via XPS) decreased, leading us to conclude that Se-incorporation may promote the formation of lattice defects that lead to fewer, but more active initial

(oxy)hydroxide species, which in turn act as the true OER electrocatalyst material. Further, EIS spectra shows that Se-incorporation leads to a more conductive material, and this increase in conductivity may also improve electrocatalytic performance and stability by reducing the overpotential needed to perform OER and thus reduce undesired side reactions like self-oxidation, as supported by Faradaic efficiency measurements. This is further supported by HRTEM and EDX analyses, which show clear differences in the type and extent of oxidized products that form on NiS₁₀₀ and NiS₉₀Se₁₀ electrocatalysts before and after long-term OER testing, indicating a lower extent of oxidation in Se-containing Ni₃S₂ materials. Together, our results suggest that mixed chalcogenides represent an exciting new class of OER pre-catalysts where differences in chalcogen composition can impact the physicochemical and electrochemical properties of both the as-synthesized metal chalcogenide and the final electrocatalytically-active metal (oxy)hydroxide. Further exploration of these exciting materials to better understand their structure-property-performance relationships should allow for rational engineering of efficient earth-abundant Ni electrocatalysts with enhanced performance and stability. With lower associated material and operating costs, widespread implementation of renewably-powered water electrolysis technologies could become a viable solution for sustainable hydrogen production for carbon-free fuels and industrial feedstocks.

8.5 REFERENCES

- (1) Denholm, P.; O'Connell, M.; Brinkman, G.; Jorgenson, J. Overgeneration from Solar Energy in California: A Field Guide to the Duck Chart (NREL/TP-6A20-65023). Tech. Rep. 2015, No. November, 46.
- (2) You, B.; Sun, Y. Innovative Strategies for Electrocatalytic Water Splitting. *Acc. Chem. Res.* **2018**, *51* (7), 1571–1580. <https://doi.org/10.1021/acs.accounts.8b00002>.

- (3) Gorlin, Y.; Jaramillo, T. F. A Bifunctional Nonprecious Metal Catalyst for Oxygen Reduction and Water Oxidation. *J. Am. Chem. Soc.* **2010**, *132* (39), 13612–13614. <https://doi.org/10.1021/ja104587v>.
- (4) Batchellor, A. S.; Boettcher, S. W. Pulse-Electrodeposited Ni-Fe (Oxy)Hydroxide Oxygen Evolution Electrocatalysts with High Geometric and Intrinsic Activities at Large Mass Loadings. *ACS Catal.* **2015**, *5* (11), 6680–6689. <https://doi.org/10.1021/acscatal.5b01551>.
- (5) Zhu, Y.; Chen, H. C.; Hsu, C. S.; Lin, T. S.; Chang, C. J.; Chang, S. C.; Tsai, L. D.; Chen, H. M. Operando Unraveling of the Structural and Chemical Stability of P-Substituted CoSe₂ Electrocatalysts toward Hydrogen and Oxygen Evolution Reactions in Alkaline Electrolyte. *ACS Energy Lett.* **2019**, *4* (4), 987–994. <https://doi.org/10.1021/acsenenergylett.9b00382>.
- (6) Zhou, M.; Weng, Q.; Zhang, X.; Wang, X.; Xue, Y.; Zeng, X.; Bando, Y.; Golberg, D. In Situ Electrochemical Formation of Core–Shell Nickel–Iron Disulfide and Oxyhydroxide Heterostructured Catalysts for a Stable Oxygen Evolution Reaction and the Associated Mechanisms. *J. Mater. Chem. A* **2017**, *5* (9), 4335–4342. <https://doi.org/10.1039/C6TA09366C>.
- (7) De Silva, U.; Masud, J.; Zhang, N.; Hong, Y.; Liyanage, W. P. R.; Asle Zaeem, M.; Nath, M. Nickel Telluride as a Bifunctional Electrocatalyst for Efficient Water Splitting in Alkaline Medium. *J. Mater. Chem. A* **2018**, *6* (17), 7608–7622. <https://doi.org/10.1039/C8TA01760C>.
- (8) Zhang, J. Y.; Lv, L.; Tian, Y.; Li, Z.; Ao, X.; Lan, Y.; Ji, J.; Wang, C. Rational Design of Cobalt-Iron Selenides for Highly Efficient Electrochemical Water Oxidation. *ACS Appl. Mater. Interfaces* **2017**, *9* (39), 33833–33840. <https://doi.org/10.1021/acsami.7b08917>.
- (9) Jiang, N.; Tang, Q.; Sheng, M.; You, B.; Jiang, D. E.; Sun, Y. Nickel Sulfides for Electrocatalytic Hydrogen Evolution under Alkaline Conditions: A Case Study of Crystalline NiS, NiS₂, and Ni₃S₂ Nanoparticles. *Catal. Sci. Technol.* **2016**, *6* (4), 1077–1084. <https://doi.org/10.1039/c5cy01111f>.
- (10) Yu, J.; Cheng, G.; Luo, W. Ternary Nickel-Iron Sulfide Microflowers as a Robust Electrocatalyst for Bifunctional Water Splitting. *J. Mater. Chem. A* **2017**, *5* (30), 15838–15844. <https://doi.org/10.1039/c7ta04438k>.
- (11) Du, X.; Ma, G.; Zhang, X. Experimental and Theoretical Understanding on Electrochemical Activation Processes of Nickel Selenide for Excellent Water-Splitting Performance: Comparing the Electrochemical Performances with M-NiSe (M = Co, Cu, and V). *ACS Sustain. Chem. Eng.* **2019**, *7* (23), 19257–19267. <https://doi.org/10.1021/acssuschemeng.9b05514>.
- (12) Du, X.; Su, H.; Zhang, X. Metal-Organic Framework-Derived Cu-Doped Co₉S₈ Nanorod Array with Less Low-Valence Co Sites as Highly Efficient Bifunctional

- Electrodes for Overall Water Splitting. *ACS Sustain. Chem. Eng.* **2019**, 7 (19), 16917–16926. <https://doi.org/10.1021/acssuschemeng.9b04739>.
- (13) Jin, S. Are Metal Chalcogenides, Nitrides, and Phosphides Oxygen Evolution Catalysts or Bifunctional Catalysts? *ACS Energy Lett.* **2017**, 2 (8), 1937–1938. <https://doi.org/10.1021/acsenergylett.7b00679>.
 - (14) Wygant, B. R.; Kawashima, K.; Mullins, C. B. Catalyst or Precatalyst? The Effect of Oxidation on Transition Metal Carbide, Pnictide, and Chalcogenide Oxygen Evolution Catalysts. *ACS Energy Lett.* **2018**, 3 (12), 2956–2966. <https://doi.org/10.1021/acsenergylett.8b01774>.
 - (15) Wang, M.; Dang, Z.; Prato, M.; Shinde, D. V.; De Trizio, L.; Manna, L. Ni–Co–S–Se Alloy Nanocrystals: Influence of the Composition on Their in Situ Transformation and Electrocatalytic Activity for the Oxygen Evolution Reaction. *ACS Appl. Nano Mater.* **2018**, 1 (10), 5753–5762. <https://doi.org/10.1021/acsanm.8b01418>.
 - (16) Hu, C.; Zhang, L.; Zhao, Z. J.; Li, A.; Chang, X.; Gong, J. Synergism of Geometric Construction and Electronic Regulation: 3D Se-(NiCo)S_x/(OH)_x Nanosheets for Highly Efficient Overall Water Splitting. *Adv. Mater.* **2018**, 30 (12), 1–8. <https://doi.org/10.1002/adma.201705538>.
 - (17) Zhang, J.; Li, Y.; Zhu, T.; Wang, Y.; Cui, J.; Wu, J.; Xu, H.; Shu, X.; Qin, Y.; Zheng, H.; et al. 3D Coral-Like Ni₃S₂ on Ni Foam as a Bifunctional Electrocatalyst for Overall Water Splitting. *ACS Appl. Mater. Interfaces* **2018**, 10 (37), 31330–31339. <https://doi.org/10.1021/acsaami.8b09361>.
 - (18) Khan, N. A.; Rashid, N.; Junaid, M.; Zafar, M. N.; Faheem, M.; Ahmad, I. NiO/NiS Heterostructures: An Efficient and Stable Electrocatalyst for Oxygen Evolution Reaction. *ACS Appl. Energy Mater.* **2019**, 2 (5), 3587–3594. <https://doi.org/10.1021/acsaem.9b00317>.
 - (19) Zhou, W.; Wu, X. J.; Cao, X.; Huang, X.; Tan, C.; Tian, J.; Liu, H.; Wang, J.; Zhang, H. Ni₃S₂ Nanorods/Ni Foam Composite Electrode with Low Overpotential for Electrocatalytic Oxygen Evolution. *Energy Environ. Sci.* **2013**, 6 (10), 2921–2924. <https://doi.org/10.1039/c3ee41572d>.
 - (20) Zhu, W.; Yue, X.; Zhang, W.; Yu, S.; Zhang, Y.; Wang, J.; Wang, J. Nickel Sulfide Microsphere Film on Ni Foam as an Efficient Bifunctional Electrocatalyst for Overall Water Splitting. *Chem. Commun.* **2016**, 52 (7), 1486–1489. <https://doi.org/10.1039/c5cc08064a>.
 - (21) Shannon, R. D. Revised Effective Ionic Radii and Systematic Studies of Interatomic Distances in Halides and Chalcogenides. *Acta Crystallographica Section A*. **1976**, pp 751–767. <https://doi.org/10.1107/S0567739476001551>.
 - (22) Tang, C.; Cheng, N.; Pu, Z.; Xing, W.; Sun, X. NiSe Nanowire Film Supported on Nickel Foam: An Efficient and Stable 3D Bifunctional Electrode for Full Water

- Splitting. *Angew. Chemie Int. Ed.* **2015**, *54* (32), 9351–9355. <https://doi.org/10.1002/anie.201503407>.
- (23) McCrory, C. C. L.; Jung, S.; Peters, J. C.; Jaramillo, T. F. Benchmarking Heterogeneous Electrocatalysts for the Oxygen Evolution Reaction. *J. Am. Chem. Soc.* **2013**, *135* (45), 16977–16987. <https://doi.org/10.1021/ja407115p>.
 - (24) Zeng, L.; Sun, K.; Chen, Y.; Liu, Z.; Chen, Y.; Pan, Y.; Zhao, R.; Liu, Y.; Liu, C. Neutral-PH Overall Water Splitting Catalyzed Efficiently by a Hollow and Porous Structured Ternary Nickel Sulfoselenide Electrocatalyst. *J. Mater. Chem. A* **2019**, *7* (28), 16793–16802. <https://doi.org/10.1039/c9ta05601g>.
 - (25) Swesi, A. T.; Masud, J.; Nath, M. Nickel Selenide as a High-Efficiency Catalyst for Oxygen Evolution Reaction. *Energy Environ. Sci.* **2016**, *9* (5), 1771–1782. <https://doi.org/10.1039/C5EE02463C>.
 - (26) Mandale, A. B.; Badrinarayanan, S.; Date, S. K.; Sinha, A. P. B. Photoelectron-Spectroscopic Study of Nickel, Manganese and Cobalt Selenides. *J. Electron Spectros. Relat. Phenomena* **1984**, *33* (1), 61–72. [https://doi.org/10.1016/0368-2048\(84\)80006-7](https://doi.org/10.1016/0368-2048(84)80006-7).
 - (27) Chen, W.; Liu, Y.; Li, Y.; Sun, J.; Qiu, Y.; Liu, C.; Zhou, G.; Cui, Y. In Situ Electrochemically Derived Nanoporous Oxides from Transition Metal Dichalcogenides for Active Oxygen Evolution Catalysts. *Nano Lett.* **2016**, *16* (12), 7588–7596. <https://doi.org/10.1021/acs.nanolett.6b03458>.
 - (28) Persson, K. A.; Waldwick, B.; Lazic, P.; Ceder, G. Prediction of Solid-Aqueous Equilibria: Scheme to Combine First-Principles Calculations of Solids with Experimental Aqueous States. *Phys. Rev. B - Condens. Matter Mater. Phys.* **2012**, *85* (23), 1–12. <https://doi.org/10.1103/PhysRevB.85.235438>.
 - (29) Jain, A.; Ong, S. P.; Hautier, G.; Chen, W.; Richards, W. D.; Dacek, S.; Cholia, S.; Gunter, D.; Skinner, D.; Ceder, G.; et al. Commentary: The Materials Project: A Materials Genome Approach to Accelerating Materials Innovation. *APL Mater.* **2013**, *1* (1), 011002. <https://doi.org/10.1063/1.4812323>.
 - (30) Singh, A. K.; Zhou, L.; Shinde, A.; Suram, S. K.; Montoya, J. H.; Winston, D.; Gregoire, J. M.; Persson, K. A. Electrochemical Stability of Metastable Materials. *Chem. Mater.* **2017**, *29* (23), 10159–10167. <https://doi.org/10.1021/acs.chemmater.7b03980>.
 - (31) Moulder, J. F.; Stickle, W. F.; Sobol, P. E.; Bomben, K. D. Handbook of X-Ray Photoelectron Spectroscopy; 1979; Vol. 3. <https://doi.org/10.1002/sia.740030412>.
 - (32) Fan, H.; Zhang, M.; Zhang, X.; Qian, Y. Hydrothermal Growth of NiSe 2 Tubular Microcrystals Assisted by PVA. *J. Cryst. Growth* **2009**, *311* (20), 4530–4534. <https://doi.org/10.1016/j.jcrysgro.2009.08.005>.

- (33) Mabayoje, O.; Liu, Y.; Wang, M.; Shoola, A.; Ebrahim, A. M.; Frenkel, A. I.; Mullins, C. B. Electrodeposition of MoS₂ x Hydrogen Evolution Catalysts from Sulfur-Rich Precursors . *ACS Appl. Mater. Interfaces* **2019**, *11* (36), 32879–32886. <https://doi.org/10.1021/acsami.9b07277>.
- (34) Xu, K.; Ding, H.; Lv, H.; Tao, S.; Chen, P.; Wu, X.; Chu, W.; Wu, C.; Xie, Y. Understanding Structure-Dependent Catalytic Performance of Nickel Selenides for Electrochemical Water Oxidation. *ACS Catal.* **2017**, *7* (1), 310–315. <https://doi.org/10.1021/acscatal.6b02884>.
- (35) Mabayoje, O.; Shoola, A.; Wygant, B. R.; Mullins, C. B. The Role of Anions in Metal Chalcogenide Oxygen Evolution Catalysis: Electrodeposited Thin Films of Nickel Sulfide as “Pre-Catalysts.” *ACS Energy Lett.* **2016**, *1* (1), 195–201. <https://doi.org/10.1021/acsenergylett.6b00084>.
- (36) Chen, W.; Wang, H.; Li, Y.; Liu, Y.; Sun, J.; Lee, S.; Lee, J.-S.; Cui, Y. In Situ Electrochemical Oxidation Tuning of Transition Metal Disulfides to Oxides for Enhanced Water Oxidation. *ACS Cent. Sci.* **2015**, 150715073040007. <https://doi.org/10.1021/acscentsci.5b00227>.
- (37) Xu, X.; Song, F.; Hu, X. A Nickel Iron Diselenide-Derived Efficient Oxygen-Evolution Catalyst. *Nat. Commun.* **2016**, *7* (1), 12324. <https://doi.org/10.1038/ncomms12324>.

Chapter 9: Conclusions and Future Work

9.1 CONCLUSIONS OF PRESENTED WORK

Renewable energy sources like solar power offer the potential for abundant, inexpensive energy, but improvements in our understanding of the materials that make harnessing and storing this energy possible are essential to making this potential reality. Through our work presented here, we have explored both halves of the problem and offered insight into how the underlying chemistry of materials used in photovoltaic devices and as electrocatalysts for the oxygen evolution reaction (OER) impacts electrochemical performance and material stability. Regarding photovoltaics, in Chapters 2 and 3 we conducted an in-depth analysis of the moisture-induced degradation chemistry of the quasi-2D Ruddlesden-Popper phase (RPP) perovskite *n*-butylammonium methylammonium lead iodide (nBA-MAPI) using a combination of analytical techniques such as time-of-flight secondary ion mass spectrometry (ToF-SIMS) and confocal fluorescence microscopy (CFM). We showed that the quasi-2D perovskite is more stable than the related 3D methylammonium lead triiodide (MAPI), due to the formation of a passivating layer of more thermodynamically-stable low-*n* RPP perovskite at the surface of the RPP film. This layer forms through a unique disproportionation process and reduces the interaction of the bulk film with moisture, reducing the rate at which the material degrades. This process cannot occur in the 3D material, thus the chemical composition of nBA-MAPI explains the greater stability of quasi-2D perovskites. Additionally, we showed that the formation of this passivation layer is accompanied by the growth of small crystallites of the same low-*n* RPP material, both at the surface and within the interior of the RPP film. Using atomic force microscopy and CFM, we probe the growth and development of these crystallites, and propose a mechanism to explain

their growth which is linked to the disproportionation previously observed. These results indicate that disproportionation of RPP perovskites, while beneficial, must be carefully controlled to limit undesired physical changes.

In Chapter 4, we expand our investigation of RPP perovskites to include an *n*-hexylammonium-based material (hexyl-MAPI) and compare its performance and stability to that of the previously studied *n*-butylammonium-based perovskite (here referred to as butyl-MAPI rather than nBA-MAPI) to better understand how the chemical composition of RPP perovskites affects their degradation chemistry under humid conditions. Using both photoluminescence (PL) spectroscopy and ToF-SIMS, we found that the hexyl-MAPI is more stable than butyl-MAPI when comparing devices made with both Ag and Au contacts, correlating to less disproportionation of the hexyl-MAPI during moisture exposure. Further, we show that the halide mobility of the stable $n = 2$ RPP perovskite phase in hexyl-MAPI is lower than that of the same phase in butyl-MAPI. This result has significant implications for device stability, as together with ToF-SIMS measurements, it indicates that the rate of iodide leaching from the perovskite is directly related to the overall stability of the material. This result helps explain the increased stability of the hexyl-MAPI devices, and further shows the importance of chemical composition when fabricating new perovskite PV materials.

Following our investigation of organolead halide perovskite stability we next explored how chemical composition affects the transition metal oxides and chalcogenides used as electrocatalysts for the OER in total water electrolysis. In Chapter 5, we found that the addition of both Sc and Fe to a strontium cobalt oxide (SCO) perovskite forces the lattice to adopt a more tetragonal crystal structure, and in doing so showed the crystal structure of the material does not determine its OER performance. Instead, the choice of metal added has a much larger impact, with Fe significantly reducing the OER

overpotential of an Fe-SCO catalyst compared to either Sc-SCO or undoped SCO. Based on electrochemical measurements and characterization using X-ray photoelectron spectroscopy (XPS) and transmission electron microscopy (TEM), we concluded that the presence of redox-active Fe improves the OER performance of SCO by buffering the overall oxidation state of the oxide material during OER.

Building on this evidence of the importance of chemical composition in OER electrocatalyst materials, in Chapter 6 we choose to explore how altering the relative ratio of two anionic species affects the performance of a nickel sulfoselenide catalyst. X-ray diffraction spectroscopy shows that during hydrothermal synthesis, some Se is incorporated into the crystal lattice of the nickel sulfide materials, in addition to the concurrent synthesis of a S-incorporated nickel selenide phase. Electrochemical tests show that the Se-incorporated nickel sulfides have improved OER performance and lower electrical resistance due to the Se-addition. Further study using TEM and energy dispersive X-ray spectroscopy shows that while both the pure sulfide and composite sulfoselenide materials undergo oxidation during OER, the sulfoselenide materials are more resistant to this oxidation and therefore more stable. Importantly, however, we found that the resulting nickel (oxy)hydroxide at the surface of both materials is the true electrocatalyst species, while the initial metal chalcogenides are best thought of pre-catalysts.

9.2 FUTURE DIRECTIONS

The results of our work suggest that additional research in the following areas may help improve the performance of both organolead halide perovskites and transition metal-based OER electrocatalysts. For the quasi-2D perovskites, the formation of the small crystallites we observed is likely a result of the inhomogeneous composition of

RPP thin films as a function of depth, creating films with a n -phase gradient and low- n nuclei deep in the film bulk. Thus, homogenization of these films may inhibit the formation of these crystallites following exposure to moisture, increasing the mechanical and chemical stability of the films. Alteration of the hot casting method used to create the RPP perovskite thin films may offer one means to control film composition, as may changing the chemical composition of the material. Our work on hexyl- and butyl-MAPI shows that even a simple change in composition can dramatically affect the chemical stability of the final RPP perovskite, and investigation of new alkylammonium species beyond n -butylammonium and n -hexylammonium may allow for even more dramatic changes in stability. Likewise, mixing of different alkylammonium species in a single material may also induce significant changes to material stability. This could be achieved by mixing multiple alkylammonium species into a single precursor solution, such as a 50/50 hexyl/butyl-MAPI, or by replicating the synthesis of the 2D/3D MAPI in Chapter 2 using an RPP perovskite thin film rather than the 3D MAPI previously investigated. The result would be a composite quasi-2D perovskite, with a surface passivation layer composed of one alkylammonium species and a bulk composed of another, likely possessing unique chemical properties.

In the field of OER electrocatalysts, much work remains to be done if we are to understand the transformation of a metal chalcogenide pre-catalyst into a metal (oxy)hydroxide electrocatalyst. The role that the initial chalcogenide composition plays on the rate of self-oxidation is still not well understood, and carefully controlled *in situ* studies using techniques like Raman spectroscopy and even ambient pressure XPS may offer details into how the process proceeds. Likewise, how chalcogenide composition affects the properties of the final (oxy)hydroxide is poorly understood as well, and surface sensitive techniques like XPS, TEM, and ToF-SIMS may be useful in probing for

the presence of chalcogenide species left within the (oxy)hydroxide layer, in addition to other chemical differences that may impact performance. Building on these more fundamental studies, our work with nickel sulfoselenide materials shows that metal mixed chalcogenide materials represent an exciting new class of OER pre-catalyst, where the relative ratio of the different chalcogenide species can make a significant impact on chemical properties and electrochemical performance in the resulting electrocatalyst. The similar chemistry of the Group 16 elements (O, S, Se, Te) suggests that a wide variety of mixed chalcogenide materials are possible, opening the door to the tuning of chemical composition and the rational design of improved metal chalcogenide pre-catalysts for the OER. Hydrothermal synthesis offers a simple, broadly applicable method for synthesizing these materials, as described in Chapter 6, but other techniques like mechanochemical synthesis and electrodeposition may also be useful in creating these materials.

In all, the future of renewable energy production and storage is bright, and many paths exist to further improve the materials that currently make these processes possible and to discover new materials for future applications. Through careful control of chemical composition, we believe it is possible to understand, and therefore exercise control over, the underlying processes that impact the performance and stability of both photovoltaic and electrocatalytic materials, thus enabling advances to a variety of electrochemical materials for renewable energy applications.

Appendix A: Supporting Information for Chapter 3

A.1 SUPPLEMENTAL DISCUSSIONS

A.1.1 Hydrophobicity of quasi-2D perovskite materials

Density functional theory (DFT) studies have shown that the enhanced van der Waals interactions of the longer alkyl chain on the A' linker molecule (*n*-butylammonium, or nBA, here and phenylethylammonium in previous work) help to stabilize quasi-2D perovskite phases with lower *n*.¹ This increases the desorption energy of the molecule relative to methylammonium (MA), and acts to stabilize the otherwise unprotected PbI₂ surface. While not directly cited in this work, it is also reasonable that the relative hydrophobicity of the A' alkyl chain, which is related to the relative strength of the van der Waals interactions, will also decrease the interaction of water at the exposed surface. A stable, low-*n* nBA-MAPI phase would have a proportionally higher quantity of hydrophobic nBA relative to a higher-*n* phase, potentially making the effect more pronounced. In 2D/3D MAPI systems treated with both butylammonium and octylammonium, such an increase in hydrophobicity with the presence of long alkyl chains has previously been observed.² The authors observed an increasing contact angle as the length of the alkyl chain on the alkylammonium cation increased (methyl to butyl to octyl), and this was positively correlated with increased stability in both XRD measurements and device performance. Other works have also mentioned the increased hydrophobicity of these molecules, but usually only note in passing that it protects the interior of the perovskite from water diffusion by inhibiting the migration of water into the film interior.^{3–5}

Thus, while the effect of hydrophobicity is undoubtedly important, it is difficult to fully disentangle from the increased thermodynamic stability of the alkyl chain-rich low-

n phases. Furthermore, hydrophobicity will almost certainly be directly impacted by the crystallographic orientation of the quasi-2D perovskites in the films and their predominant surface; this can be demonstrated in two distinct cases. In Case I, hot casting of the quasi-2D perovskites films has been shown by us and others⁵ to create films where the perovskite sheets are stacked orthogonally to the substrate; each sheet is expected to terminate in a methylammonium-terminated edge and possess long planes of A' perpendicular to the substrate (**Figure A.6b**). Conversely, the theoretical calculations by Quan *et al.* were performed on surfaces that would be terminated almost exclusively in A' linker molecules, and thus such crystals would be oriented parallel to the substrate (Case II). An example of this can be found in a work studying the thermal stability of such perovskites treated to create a 2D/3D structure similar to the system that we present; the authors propose that the crystals grains will be coated in a uniform layer of the linker molecule.⁶

Assuming idealized surfaces for Case I and II on a pure 2D perovskite, and ignoring low- n phase stability and our proposed disproportionation momentarily, diffusion of water into the films would almost certainly occur at very different rates. In Case I, water would diffuse more slowly along, or completely fail to penetrate into, the long planes of nBA molecules perpendicular to the substrate, as has been previously suggested.^{4,5} Unfortunately, it seems equally probable that water would then simply penetrate into the depth of the film through the relatively unprotected methylammonium-terminated sheet edges, offsetting this advantage. Case II would prevent this attack from the top edge almost entirely, offering a hydrophobic surface with which water would be unlikely to interact strongly. Extrapolating from Case I, moisture related damage would then need to travel laterally from the edge of the film to the center, and thus the apparent rate of degradation would be much slower when compared to Case I, as the distance from

edge-to-center is much larger than from surface-to-center. The trade-off, however, is that this surface coating of nBA would be expected slow charge transfer out of the perovskite, and indeed, may explain some of the slow carrier mobility measured in such films.^{5,7} Work on nanoparticle-based systems has shown that charge transfer will still occur, but would likely be slower than in Case I.⁸ In summary, in Case I water diffusion would be inhibited in the lateral plane of the perovskite, but unimpeded in the vertical direction; in Case II, diffusion of moisture would be limited in the vertical plane, but unhindered in the lateral plane of the film.

Finally, with these two examples in hand, we can attempt to apply these principles to our particular 2D and 2D/3D systems and predict what effect hydrophobicity may have. Starting with the 2D/3D system, based on the ToF-SIMS profile in **Figure A.17c** and previous work on similar systems,⁶ there is a sub-10 nm layer of nBA-MAPI at the surface of the film, oriented as in Case II, and a thin surface coating of nBA on some portion of the 3D MAPI grain boundaries throughout the film depth. Together, this would inhibit water diffusion through the cell both laterally and vertically. For the 2D film, XRD evidence suggests that the dominant orientation for the film must be similar to that in Case I, and that while water diffusion through the film would be lower than in pure 3D MAPI, it will still suffer from attacks to the vertical sheet edges. We postulate that a thin layer of nBA could substitute for the MAPI on the extreme outer edge of the perovskite sheet, increasing stability as in Case II, but there is no way to determine this definitively. Instead, in such a case, it is very likely that the increased thermodynamic stability is imparting the increased resistance to moisture.

A.1.2 Spectroscopic and physical effects of nBA-MAPI disproportionation

PL spectroscopy has been used to probe the existence and relative location of various n -phases within quasi-2D perovskite thin films,^{7,9-12} but care must be taken to account for the electronic band structure of these materials. Due to the effects of quantum confinement on the perovskite chromophore, adjacent (n) and ($n-1$) perovskites will form type II heterojunctions, leading to rapid energy transfer from low- to high- n species.^{7,9,10} Steady-state PL experiments show that the front of hot-cast perovskite films, such as those used in this study, have a predominately high- n character, and a back with predominately low- n character; this allows electrons and holes to be separated within the film under illumination.¹⁰ Transient absorption (TA) and time-resolved PL of the films show that the typical steady-state spectra hide the presence of low- n species at or near the surface, however.^{7,9} Sargent and coworkers have shown that the PL spectra of these films at sufficiently short time scales (>5 ns) show the presence of $n = 2, 3$, and 4 species, but that due to the type II band alignment of the perovskites, photogenerated carriers produced in the low- n layers are rapidly shuttled to the bulk 2D perovskite phase. There, they eventually undergo radiative recombination via PL and produce the characteristic steady-state spectrum with a single peak near 1.75 eV. Thus, in order to observe an increase in PL for $n = 3$ and other intermediate n phases that we see in our degraded nBA-MAPI film (**Figure 2.3c**), something must be inhibiting the migration of carriers in our film.

To investigate if film topography could have an effect on this inhibition, we probed the surface of the nBA-MAPI film using atomic force microscopy (AFM) before and after exposure. For the fresh film, we observe a relatively flat surface (RMS 23.9 nm) composed of flat crystal grains ranging from 100 nm to 1 μ m in diameter (**Figure A.11a**). Based upon the work of Yuan *et al.* it is likely that these grains may consist of a variety

of different n -phases, or may themselves each be a separate phase,⁹ but together they represent a disordered layer with an inhomogeneous energy surface (**Figure A.11c,e**). After 8 hours of exposure to humidity, the surface looks remarkably similar on the whole, but now also features distinct crystal-like structures which appear to be growing normal to the surface (**Figure A.11b**). This orientation and their small size may explain why they are not clearly indicated by the XRD in **Figure A.5**. While many are visible at the site of grain boundaries, there are a number of crystals that appear to have grown from within the center of the larger perovskite grains. The crystals have an average thickness of 110 nm, range in length from 100 nm to almost a micron, and generally project slightly from the surface of the film (>20 nm). Regarding the identity of these new structures, bulk quasi-2D perovskite single crystals are known to crystalize as large flat plates,¹³ but more importantly, the morphology of these new structures is very similar to that observed by Li *et al.* when they grew low- n perovskite crystals on the surface of a PbI_2 film.¹² In agreement with this, the WAXS spectra of an nBA-MAPI film (**Figure A.12b,c**) exposed to moisture for 8 hours shows the formation of clear rings near $q_y = 0.6 \text{ \AA}^{-1}$, which we can index to the $n = 4$ (060) and $n = 2$ (020) reflections.¹³ The appearance of these rings in the WAXS coincides with the formation of the randomly oriented platelet-structures in the AFM, making it very likely that these structures are composed of low- n nBA-MAPI phases. Based on these results, we hypothesize that as the nBA-MAPI degrades, the surface undergoes some degree of structural reorganization to reduce entropy in the film and produces discrete structures composed of low- n nBA-MAPI perovskite phases. Concurrently, some areas of the initial disordered layer are preserved, possibly growing in thickness as degradation slowly proceeds toward the interior of the film (**Figure A.11d**). We propose this degraded surface layer likely acts as a protective coating which slows this degradation of the bulk perovskite film, however, in agreement with our

electrochemical results. Together, these structural and crystallographic changes are consistent with the enhanced stability of low- n perovskite phases first reported by Sargent and coworkers.¹

These discreet low- n structures may also help explain the increased PL intensity for low- n species that we observe in our steady state experiments. As these structures form and likely degrade from the outside in, they would naturally create structures with a low- n surface surrounding a higher- n interior. Based on reported band positions and relative band structures for these quasi-2D perovskites, this could give rise to one of two distinct quantum well-like band structures within these platelets.^{14,15} In the first case, given the band structure first reported by Cao *et al.* for n -butylammonium-based quasi-2D perovskites,¹⁴ the various adjacent n -phases would form a series of type II heterojunctions. As can be seen in **Figure A.11f**, carriers photogenerated inside the structure would tend to flow downhill to the high- n phases at the core (here composed largely of $n = 3$ and 4) and become trapped, eventually recombining and emitting PL at the wavelengths we observe in **Figure 2.3b**. Additionally, 3D MAPI produced as a byproduct of degradation at the outside of these structures could likewise collect electrons from neighboring phases, producing the increase in 3D MAPI PL that we observe. Meanwhile, holes would migrate to the low- n edges of the structures and become caught in shallow trap states.⁷ Once trapped, they would eventually recombine by largely non-radiative trap-assisted processes, as previously observed for most trapped carriers in organolead halide perovskites.¹⁶ Transfer of electrons to high- n phases and holes to low- n phases has been observed in several studies using ultrafast transient absorption spectroscopy,^{7,9,12,17–20} and such transfer agrees well with the relative band alignments these groups propose using ultraviolet photoelectron spectroscopy (UPS).

In the second case, recent work from Kahn *et al.* has suggested that when an n and $n+1$ phase are adjacent to each other, a type I heterojunction forms instead of the previously proposed type II heterojunction.¹⁵ From density functional theory (DFT), they find that these perovskites possess a low density of states near the valence band maximum that makes accurate determination of the exact position of the valence band maximum and conduction band minimum difficult using UPS alone.^{15,21} Further, they show that the two band edges are composed primarily of Pb and I states, indicating that neither the butylammonium spacers nor the methylammonium inside the perovskite lattice will have a significant impact on the electronic structure near the band edges.^{15,21,22} Together, this suggests altogether different band structure will form within the platelets at the surface, presented here in **Figure A.11g**. In this configuration, electrons will still collect in the interior of the crystals, as in the previous case, but holes will no longer collect at the outer edges of the platelet. Instead, the holes will also transfer to the higher- n phases within of the interior along with the electrons. This would provide a ready source of both electrons and holes for radiative recombination, and agrees with the increased PL we observe for our films. While more investigation is needed to definitively determine whether a type I or type II heterojunction is formed in these quasi-2D materials, it seems probable that either band alignment would result in the electronic isolation of $n = 2, 3$, and 4 phases produced by degradation within the surface crystallites. This isolation prevents the extraction of photogenerated-charges into the high- n phases of the bulk and allows us to observe the formation of these phases via degradation in the PL spectra of our films.

A.1.3 Water diffusion and damage at the perovskite/PEDOT:PSS interface

There are two interfaces at which the perovskite absorber layer can interact with the outside environment: the top where it contacts C_{60} , and the bottom where it contacts PEDOT:PSS. Either interface could be damaged by water which has diffused there, and must be considered when assessing stability. Regarding the top (C_{60} /perovskite) interface, the largest chemical changes visible in the ToF-SIMS profiles occur at this interface. As seen in **Figure 2.6a,c**, MAPI shows clear formation of new inorganic (PbI_2^-) and organic (C_2N^-) and CH_2^-) peaks here, and both the nBA-MAPI and 2D/3D MAPI show more notable peak broadening at this interface when compared to the back interface (perovskite/PEDOT). Further, when comparing the relative stabilities of the MAPI and 2D/3D MAPI devices, it is apparent that the surface treatment appears to have significantly improved the stability of this 3D perovskite. While the depth profile in **Figure A.17a** does show some degree of penetration into the film by the nBA^+ along grain boundaries, the primary peak is still at the surface of the film, and thus the protection likely comes strongly from there. Finally, in the PL spectra of the nBA-MAPI film (**Figure 2.3b**), the most significant changes occur in the front-side spectra rather than the back. Thus, the experimental results strongly suggest that the top interface is of significant importance when studying degradation in these devices, and it is for this reason that we chose to focus much of our analysis on this interface.

Regarding the bottom interface with the PEDOT:PSS layer, it is both possible and probable that some degree of damage does occur here, but evidence for the extent of this damage is not as clear as for the top. ToF-SIMS depth profiles in **Figure 2.6** show slight variations in some of the organic species at the back interface, but the changes are not as significant as those at the top. Further, as mentioned above, all changes to the inorganic species appear to occur at the upper surface, with little to no change occurring near the

PEDOT. This observation may be due, in part, the relative amount of water which is traveling to each interface during exposure, which is related to both the type and quantity of material through which the water must diffuse. While diffusion through the C₆₀ is expected to be slow due to the hydrophobicity of the molecule, the diffusion path itself is extremely short (~50-200 nm). Conversely, water has been calculated to have a relatively high diffusion constant of $5 \times 10^{-6} \text{ cm}^2/\text{s}$ in PEDOT:PSS²³ but must diffuse across approximately 0.75 - 1 cm to reach the active device area from the unprotected outer edge of the substrate. Thus, new water arriving at the interface would take on the order of 20 hours to travel the 1 cm distance from the substrate edge to the device area in the center. This is significantly slower than the rate of degradation exhibited by the 3D MAPI film, and is thus unlikely to be the source of degradation in this film, or by extension the other films.

Finally, we also note that, as previously discussed, the 3D MAPI and 2D/3D MAPI films differ only in the nBA surface treatment and yet exhibit very different electrochemical degradation rates. As the two films are thus expected to have very similar perovskite/PEDOT:PSS interfaces, this clearly suggests that this interface cannot be the dominant source of water-based degradation, and supports analysis of the top interface with C₆₀. Further studies on alternative hole transport materials, such as P3HT and NiO would be interesting, and may provide a more nuanced view of the choice of substrate on the moisture stability of both 2D and 3D perovskites.

A.2 TABLES

	V_{OC} (V)	J_{SC} (mA/cm ²)	PCE (%)	FF
MAPI	-0.63 +/- 0.08 (-0.746)	-11.1 +/- 0.7 (-11.6)	4.26 +/- 0.63 (5.27)	0.61 +/- 0.03 (0.61)
nBA-MAPI	-0.80 +/- 0.07 (-0.881)	-9.47 +/- 1.2 (-10.0)	4.73 +/- 0.85 (5.83)	0.63 +/- 0.06 (0.66)
2D/3D MAPI	-0.54 +/- 0.03 (-0.578)	-13.3 +/- 0.6	4.4 +/- 1.1 (5.4)	0.61 +/- 0.14 (0.71)

Table A.1: Performance metrics from electrochemical tests of MAPI, nBA-MAPI, and 2D/3D MAPI devices. Average values from a single batch of devices are reported with a standard deviation, while champion device values are included in parentheses.

A.3 FIGURES

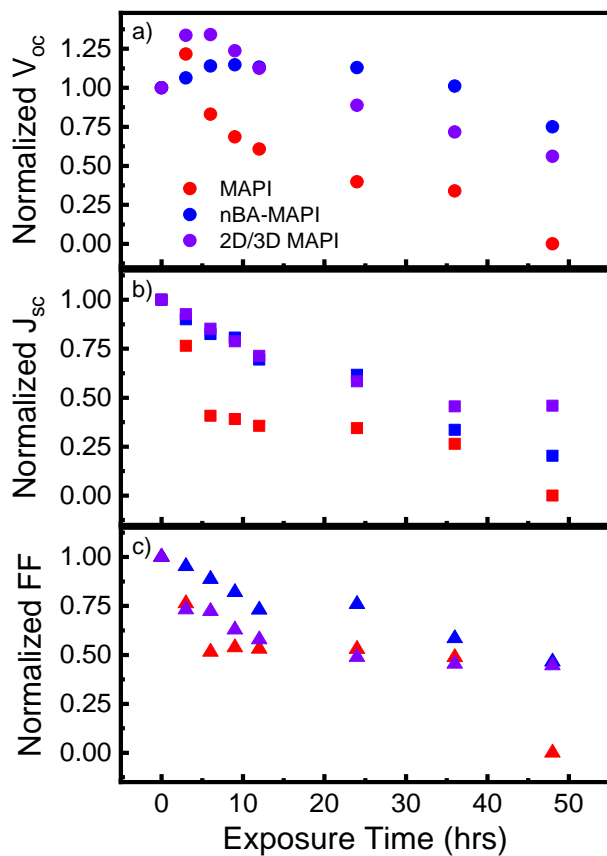


Figure A.1 Normalized (a) open-circuit potential, (b) short-circuit current, and (c) fill factor values for MAPI, nBA-MAPI, and 2D/3D MAPI devices exposed to 78% relative humidity over time. For all three metrics, the 2D-containing perovskites show slower degradation.

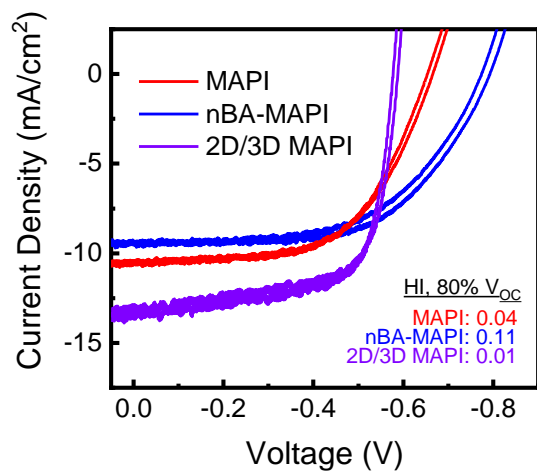


Figure A.2 Cyclic voltammograms of characteristic perovskite devices before exposure to humidity showing the performance of the three types of perovskite material. A hysteresis index (HI) at 80% of the maximum V_{oc} for each cell is provided, demonstrating the low degree of hysteresis between the forward and reverse scans.

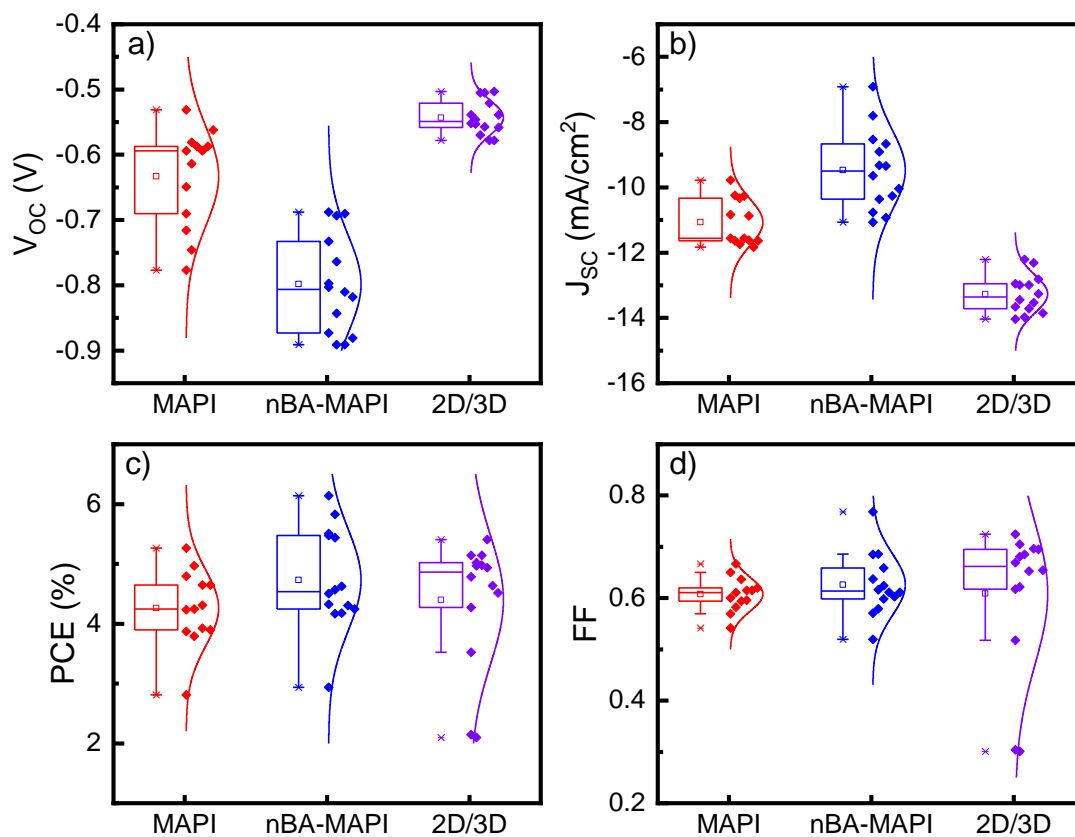


Figure A.3 Statistical distributions for the a) V_{oc} , b) J_{sc} , c) PCE, and d) FF at $t = 0$ hrs for all cells tested. Two partially shorted devices are responsible for the outlier values in the FF and PCE of the 2D/3D devices, which would otherwise distribution similar to those for MAPI and nBA-MAPI.

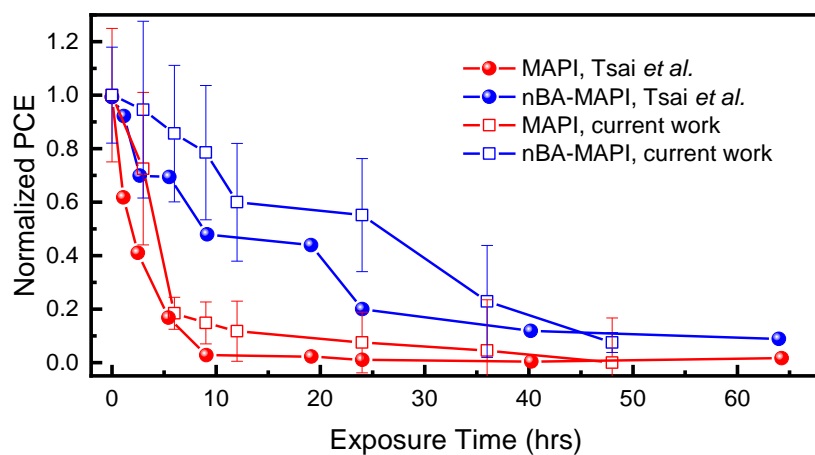


Figure A.4 Normalized PCE values for MAPI and nBA-MAPI devices exposed to a humid environment as reported by Tsai *et al.* (ref. 5), compared to similar devices reported in the current work. Within error, the devices presented here show similar degradation kinetics and trends to those reported previously, indicating the degradation process is similar in both.

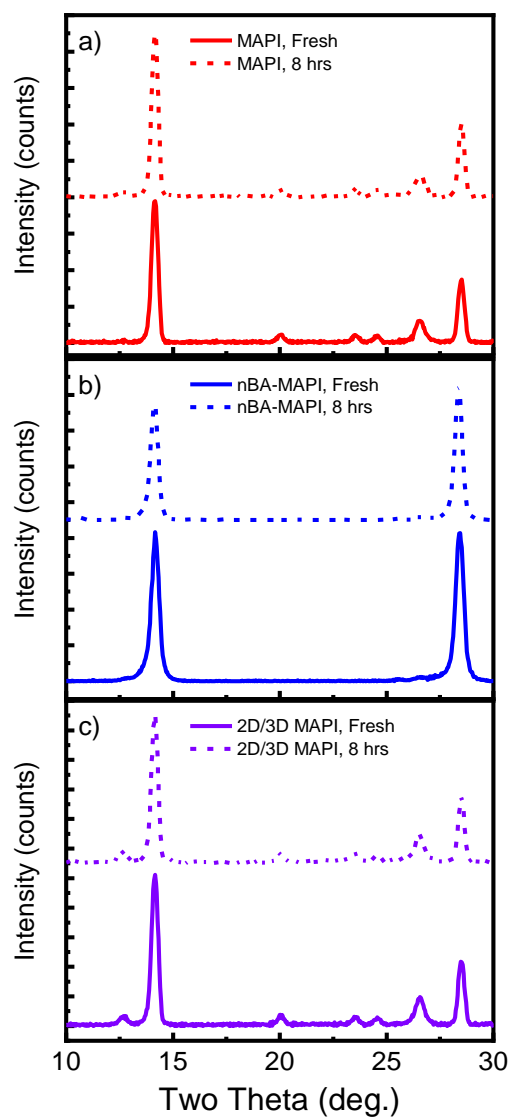


Figure A.5 XRD spectra for (a) MAPI, (b) nBA-MAPI, and (c) 2D/3D MAPI films before and after exposure to 78%RH for 8 hours. Little crystallographic change is observed for any of the films tested.

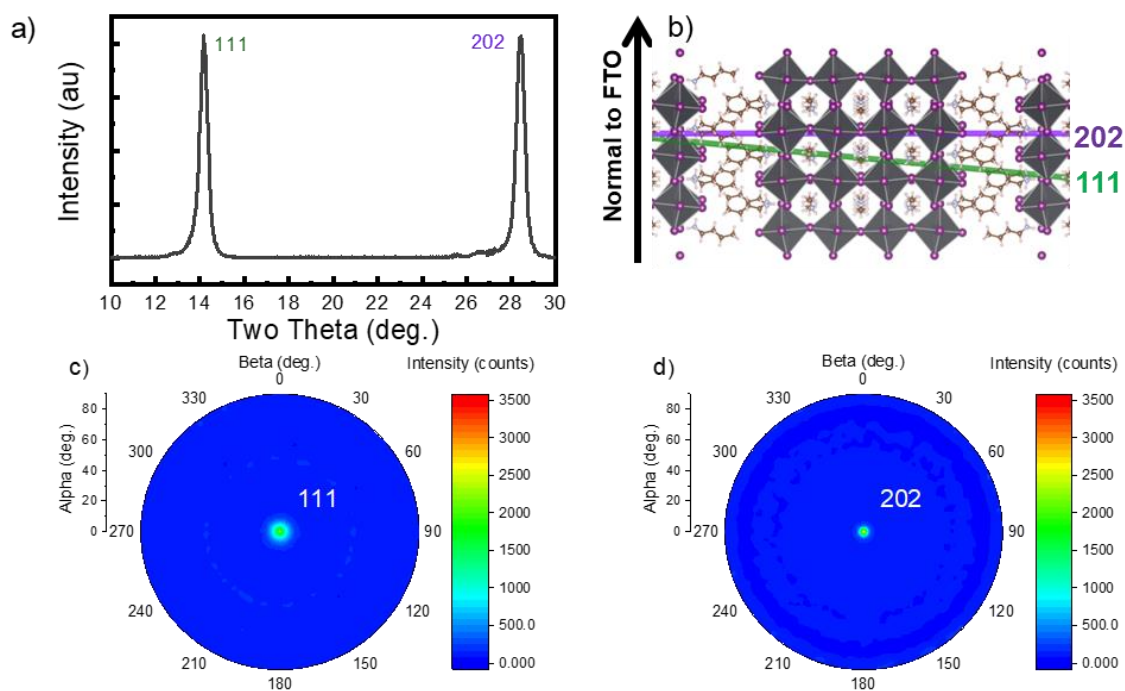


Figure A.6 a) XRD spectra for a fresh nBA-MAPI film, with the 111 and 202 peaks labeled. b) graphic of an nBA-MAPI film with an orientation normal to the FTO substrate, as would be expected from a hot-cast film. Both the 111 and 202 planes have a significant horizontal component. Pole figure measurements for the 111 (c) and 202 (d) peaks, with a sharp central peak demonstrating the good agreement with the orientation of image b).

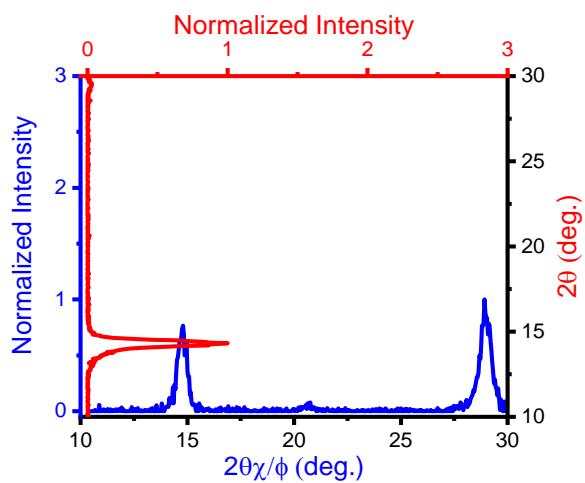


Figure A.7 In-plane (y-axis) and grazing incidence (x-axis) X-ray diffraction spectra from a fresh nBA-MAPI film. The lack of the 202 peak on the y-axis indicates a well-ordered film.

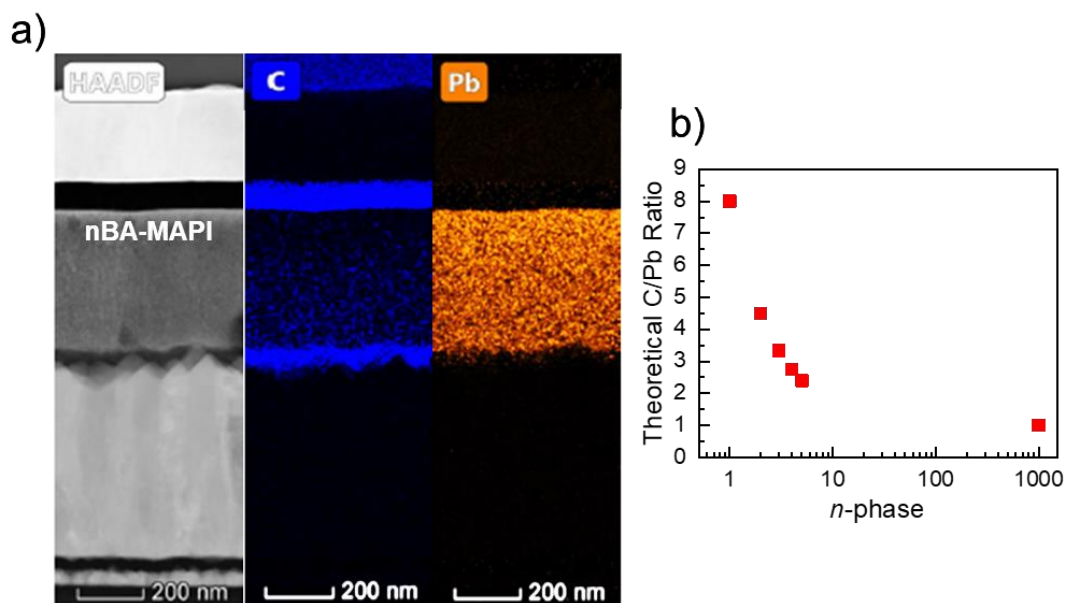


Figure A.8 a) Cross-sectional HAADF (left) image of a nBA-MAPI device, with the perovskite in the center of the cross section. Accompanying EDX elemental maps of C (blue) and Pb (orange), showing a gradient in both elements as a function of depth. b) Theoretical C/Pb elemental ratio based on the stoichiometric ratios of both elements in various n -phases of the nBA-MAPI perovskite, showing that the ratio would increase as n decreases.

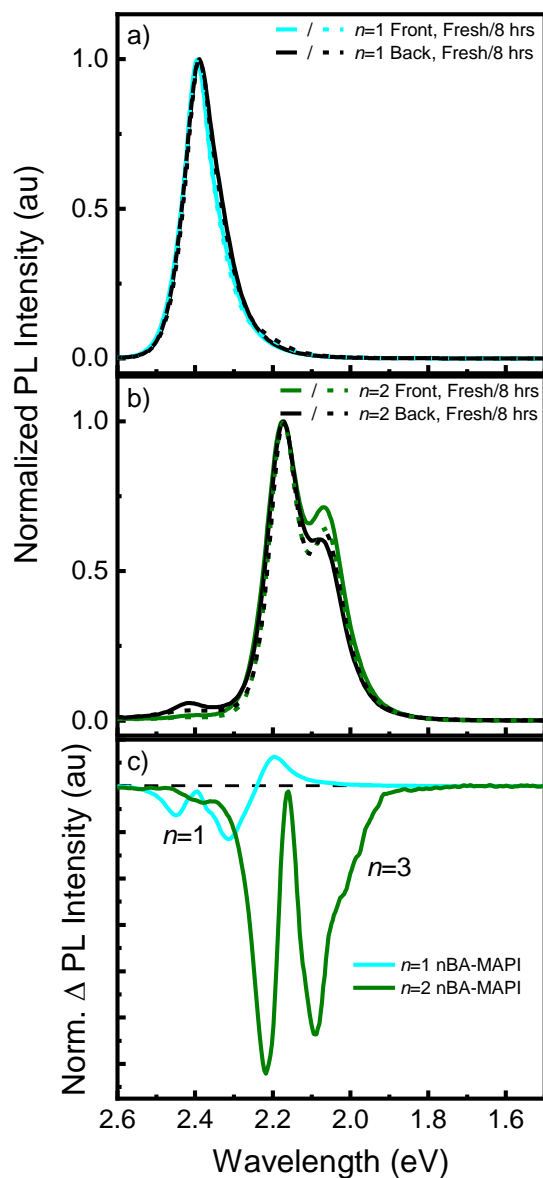


Figure A.9 Normalized fluorescence spectra for the front and back of nominally a) $n = 1$ and b) $n = 2$ films, before and after exposure to 78% relative humidity for 8 hours. c) Normalized difference plot for the front-side spectra for both films. After exposure, the $n = 1$ film shows a slight shift toward lower emission energies, while the $n = 2$ film shows both the loss of $n = 1$ and 3 from the surface, as well as a general peak narrowing for the $n = 2$ peak.

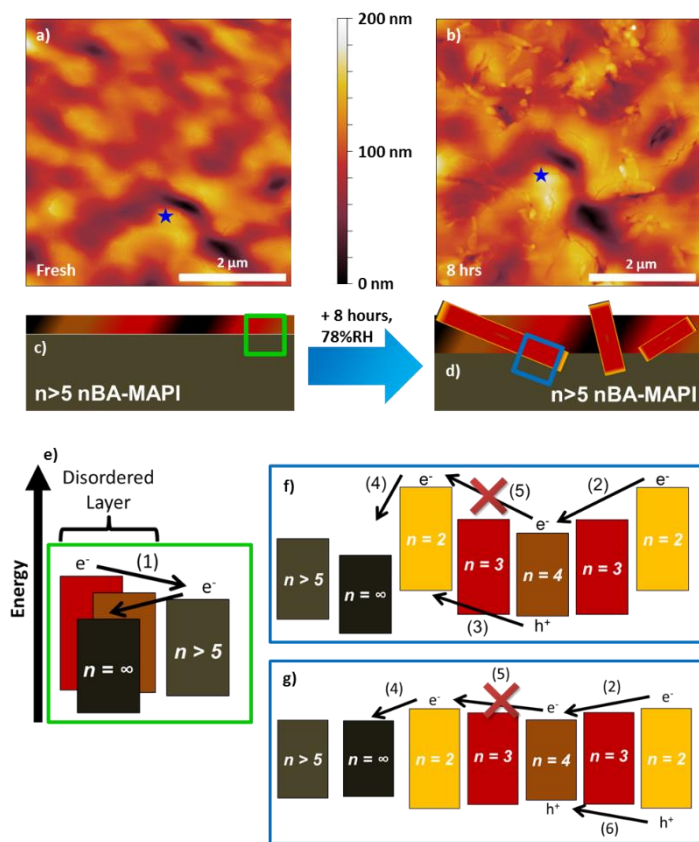


Figure A.10 AFM images of an nBA-MAPI film a) before and b) after 8 hours of exposure to a 78%RH environment. For reference, the blue star indicates the same location in each image. New elongated structures are observed to form on the surface of the film, and are likely discrete crystals of low- n perovskite. c) Schematic of the cross section of the fresh nBA-MAPI film, showing a disordered surface layer composed of various low- n phases atop a bulk of high- n nBA-MAPI. d) Schematic of the cross section of the same film following moisture exposure, showing an increase in the thickness of the disordered surface, as well as the formation of the localized structures observed in b). e) Simplified energy diagram for c), showing electron transfer both from the low- n phases of the surface to the bulk, and from the bulk to 3D MAPI within the disordered surface (1). f) Simplified energy diagram showing the preferential motion of electrons (2) and holes (3) generated within the type II heterojunction well structure, as well as possible charge transfer from the surface to the bulk (4). Generally, however, photogenerated electrons will be trapped in the interior, unable to escape (5). g) Simplified energy diagram for a type I heterojunction well, with similar electron transfer to the type II well. Here, hole transfer also flows to the higher- n interior (6), where radiative recombination could occur.

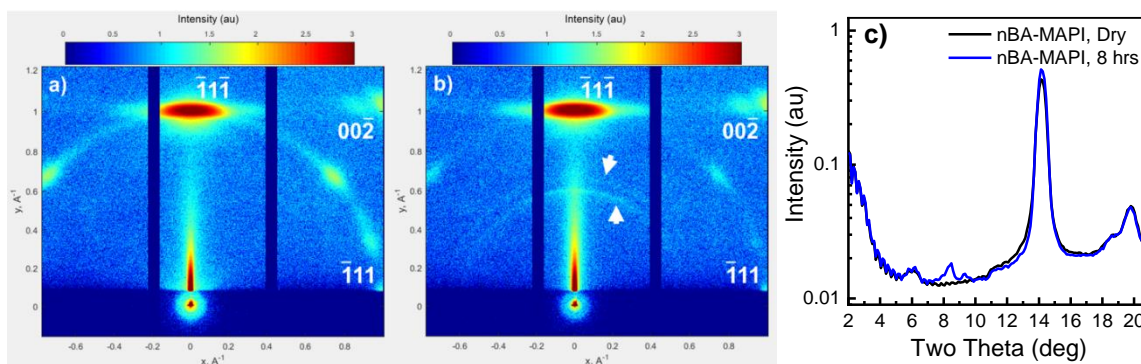


Figure A.11 Wide angle x-ray scattering spectra for a) fresh and b) 8 hour-exposed nBA-MAPI films on FTO. Bragg diffraction spots for a well-oriented perovskite lattice have been assigned based on previous reports. Following exposure, two diffraction rings (marked with white arrows) appear, indicative of the formation of randomly-oriented low- n perovskites in the film. c) intensity plot vs two theta generated from the WAXS spectra, clearly showing the formation of the two peaks near 8-9° two theta which can be indexed to $n = 2,4$ phases. The small feature near 6° is an instrumental artifact, and is independent of the film.

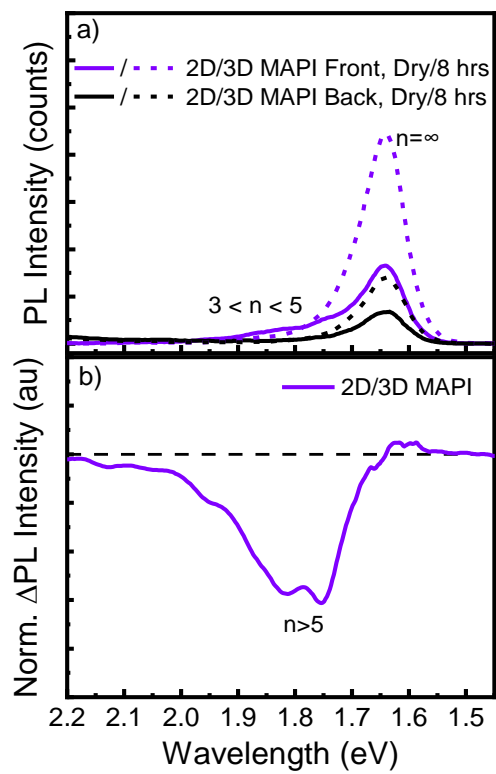


Figure A.12 a) Fluorescence spectra for the front and back of a bare 2D/3D MAPI film, before and after exposure to 78% relative humidity for 8 hours. The primary peak is at 1.65 eV, and a broad shoulder near 1.8 eV indicates the presence of nBA-MAPI phases. b) Normalized difference plot for the front of a 2D/3D MAPI film, showing the loss of the shoulder near 1.8 eV following exposure.

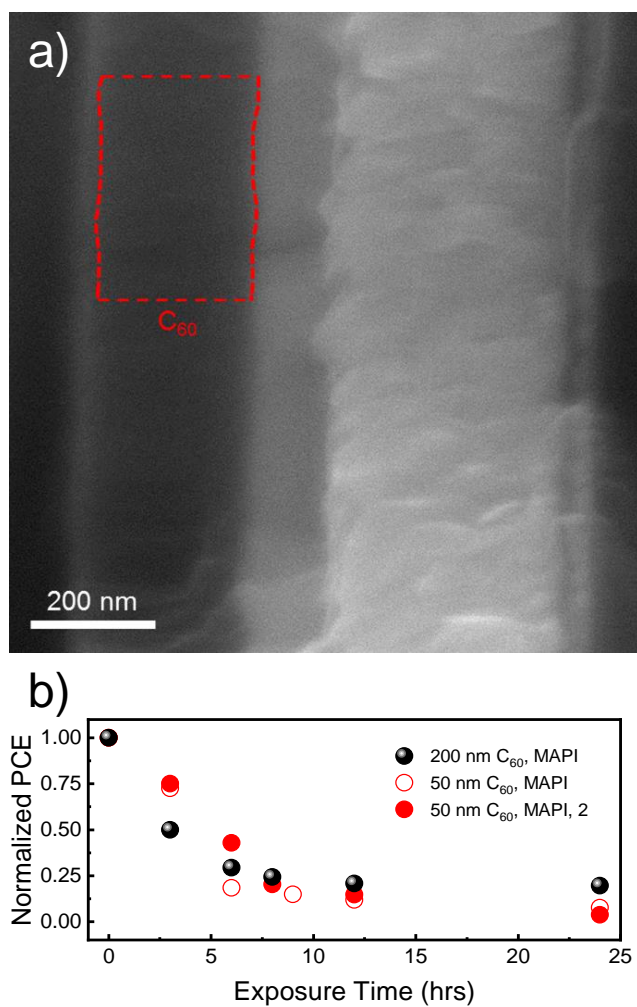


Figure A.13 a) cross sectional SEM image of a 200 nm C_{60} MAPI device, with the C_{60} layer outlined in red. b) Normalized PCE for two batches of our typical 50 nm C_{60} MAPI devices (red) and the 200 nm C_{60} device (black).

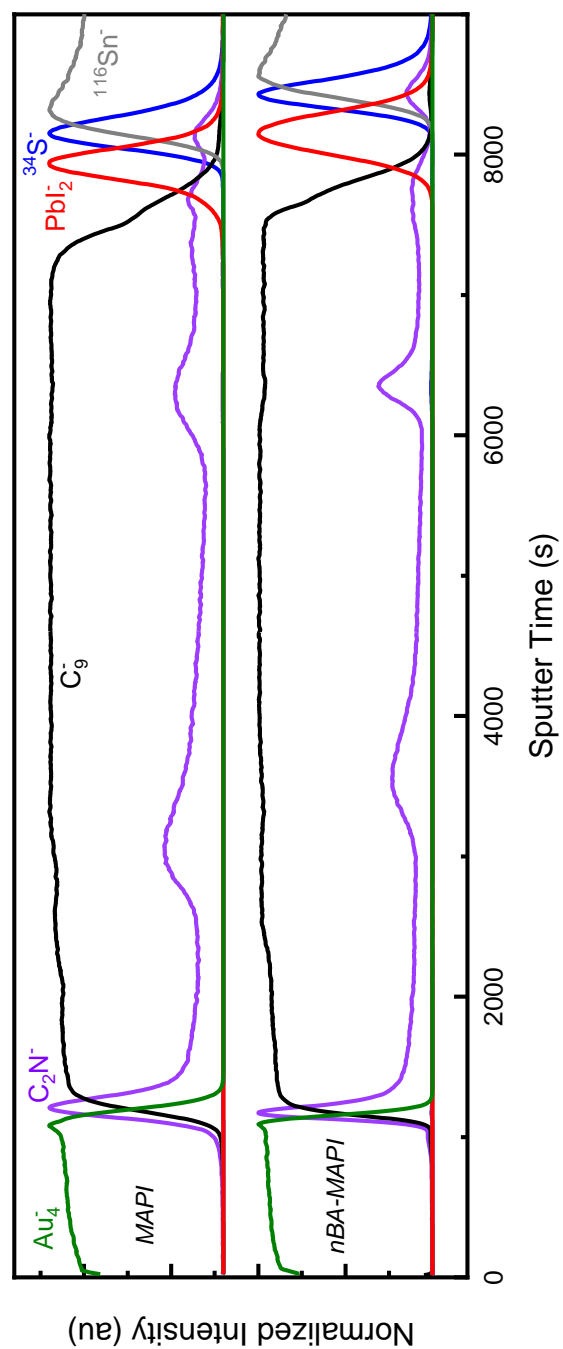


Figure A.14 Full negative-mode ToF-SIMS depth profiles for fresh 200 nm C₆₀ MAPI (top) and nBA-MAPI (bottom) with characteristic species chosen to represent different materials.

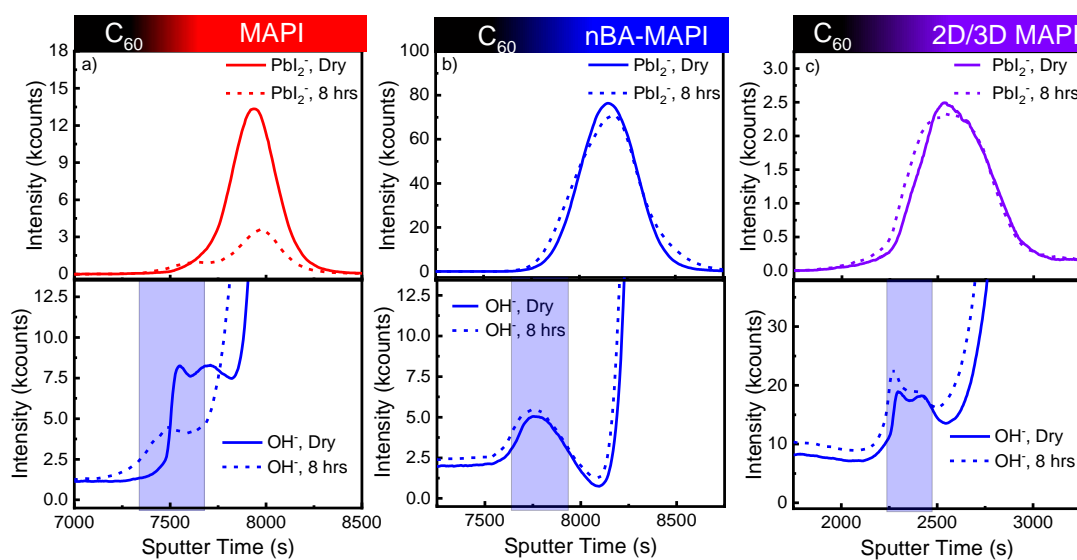


Figure A.15 Negative-mode ToF-SIMS depth profiles of (a) MAPI, (b), nBA-MAPI, and (c) 2D/3D MAPI devices, before and after exposure to humidity, near the C_{60} /perovskite interface; the blue box represents the hydration region in each device. The top profiles show the changes to the perovskite (PbI_2^-) with exposure; nBA-MAPI and 2D/3D MAPI show little change, while MAPI shows the formation of a new peak in the hydration region and a significant decrease in intensity due to hydration damage. The bottom profiles show changes to the hydrated species (OH^-) before and after exposure to humidity. The FWHM of the OH^- peak after exposure is used to determine the hydration region (blue). nBA-MAPI (b) and 2D/3D MAPI (c) show only a slight increase in OH^- , while MAPI shows a large decrease, indicating loss of hydrated species with exposure.

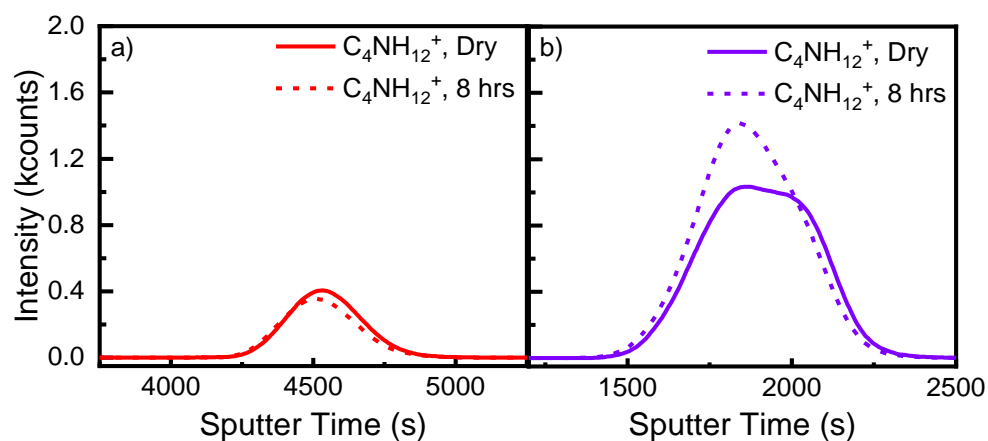


Figure A.16 Positive-mode ToF-SIMS depth profiles for the $\text{C}_4\text{NH}_{12}^+$ species representing *n*-butylammonium in (a) MAPI and (b) 2D/3D MAPI devices. The larger signal and dynamic nature of the signal with humidity in b) indicates that the signal is likely a product of *n*-butylammonium; the peak near 1750 s after exposure agrees with the formation of an nBA-MAPI layer following hydration.

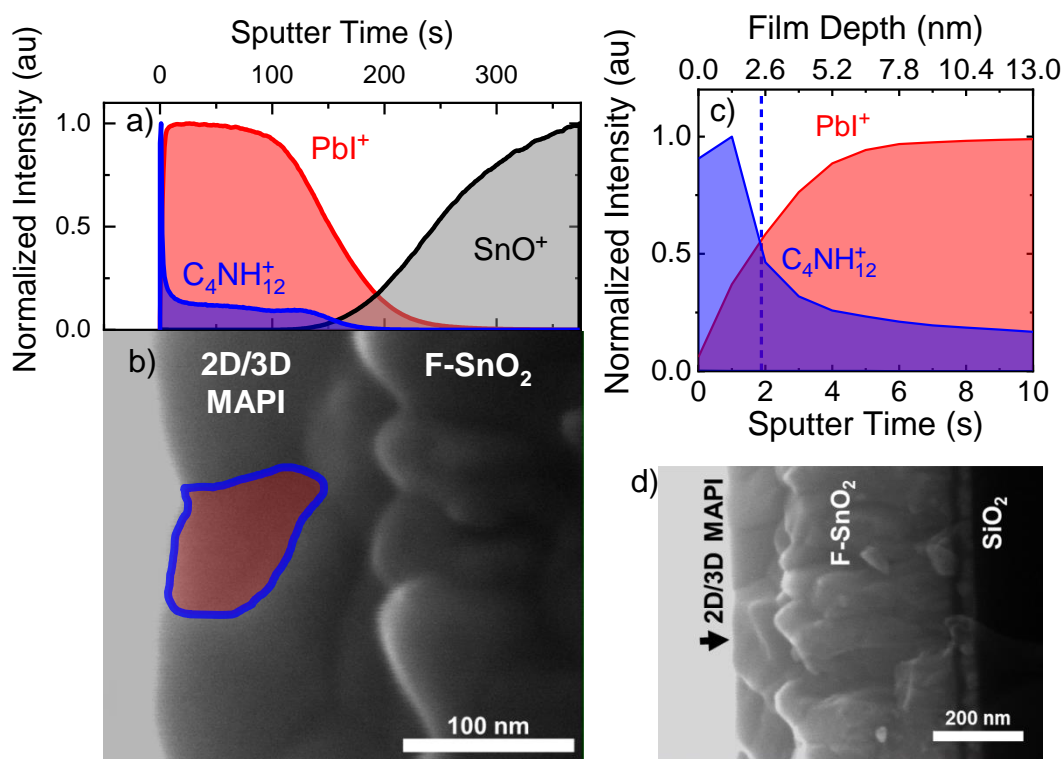


Figure A.17 a) Positive mode ToF-SIMS depth profiles for $\text{C}_4\text{NH}_{12}^+$ (representing *n*-butylammonium), PbI^+ (representing 3D MAPI), and SnO^+ (representing FTO) for a bare 2D/3D MAPI film, showing a sharp *n*-butylammonium peak at the surface of the film that tapers off into the film. b) Corresponding cross sectional SEM image of a 2D/3D MAPI film on FTO. The blue lines represent the nBA-MAPI at the film surface and the coating on the grain boundaries of the 3D MAPI crystals (red). c) Depth profile of the first 10 seconds (~13 nm) of the 2D/3D MAPI film, showing a nBA-MAPI film thickness of roughly 2.5 nm. d) Full cross sectional SEM image of the 2D/3D MAPI film.

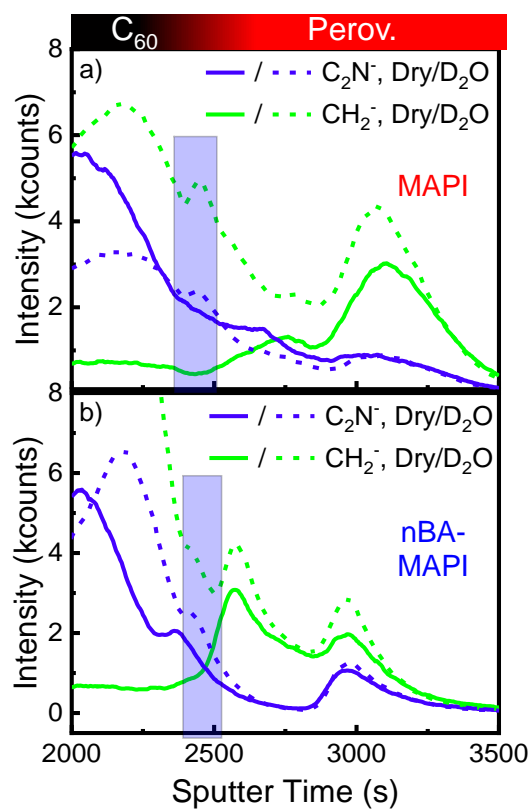


Figure A.18 ToF-SIMS depth profiles of N- and H-containing (C_2N^- and CH_2^- , respectively) organic species in (a) MAPI and (b) nBA-MAPI devices following exposure to D_2O vapor near the C_{60} /Perovskite interface; the blue box represents the hydration region. The MAPI sample shows clear formation of a peak in both species inside the hydration region, in agreement with the formation of degraded hydrated-MAPI species at the interface.

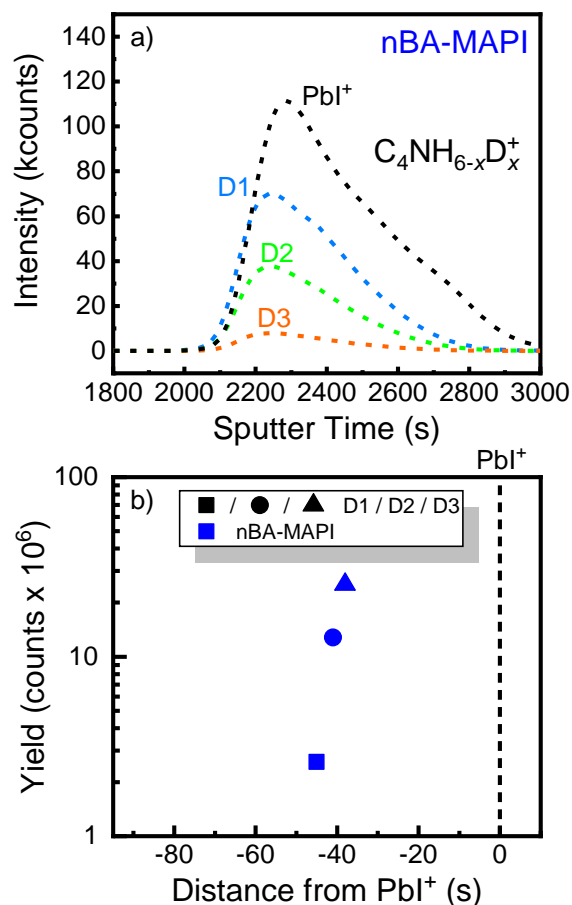


Figure A.19 a) Deuterated *n*-butylammonium derivatives ($D = 1-3$, i.e. $D1 = C_4NH_{11}D^+$) and PbI^+ for an nBA-MAPI device exposed to D_2O vapor for 1 hour. The total ion counts, and therefore abundance, of the derivatives decreases as the level of deuteriation increases. b) Total integrated yield of the deuterated *n*-butylammonium derivatives as a function of distance of each derivative's peak from the PbI^+ peak ($t = 0$). The relatively large distance from the center of the perovskite layer indicates a low degree of water penetration into the material.

A.4 REFERENCES

- (1) Quan, L. N.; Yuan, M.; Comin, R.; Voznyy, O.; Beauregard, E. M.; Hoogland, S.; Buin, A.; Kirmani, A. R.; Zhao, K.; Amassian, A.; Kim, D. H.; Sargent, E. H. Ligand-Stabilized Reduced-Dimensionality Perovskites. *J. Am. Chem. Soc.* 2016, 138 (8), 2649–2655. <https://doi.org/10.1021/jacs.5b11740>.
- (2) Koh, T. M.; Shanmugam, V.; Guo, X.; Lim, S. S.; Filonik, O.; Herzig, E. M.; Müller-Buschbaum, P.; Swamy, V.; Chien, S. T.; Mhaisalkar, S. G.; Mathews, N. Enhancing Moisture Tolerance in Efficient Hybrid 3D/2D Perovskite Photovoltaics. *J. Mater. Chem. A* 2018, 2122–2128. <https://doi.org/10.1039/C7TA09657G>.
- (3) Qing, J.; Liu, X. K.; Li, M.; Liu, F.; Yuan, Z.; Tiukalova, E.; Yan, Z.; Duchamp, M.; Chen, S.; Wang, Y.; Bai, S.; Liu, J. M.; Snaith, H. J.; Lee, C. S.; Sum, T. C.; Gao, F. Aligned and Graded Type-II Ruddlesden–Popper Perovskite Films for Efficient Solar Cells. *Adv. Energy Mater.* 2018, 8 (21), 1–8. <https://doi.org/10.1002/aenm.201800185>.
- (4) Zhou, N.; Shen, Y.; Li, L.; Tan, S.; Liu, N.; Zheng, G.; Chen, Q.; Zhou, H. Exploration of Crystallization Kinetics in Quasi Two-Dimensional Perovskite and High Performance Solar Cells. *J. Am. Chem. Soc.* 2018, 140 (1), 459–465. <https://doi.org/10.1021/jacs.7b11157>.
- (5) Tsai, H.; Nie, W.; Blancon, J.-C.; Stoumpos, C. C.; Asadpour, R.; Harutyunyan, B.; Neukirch, A. J.; Verduzco, R.; Crochet, J. J.; Tretiak, S.; Pedesseau, L.; Even, J.; Alam, M. A.; Gupta, G.; Lou, J.; Ajayan, P. M.; Bedzyk, M. J.; Kanatzidis, M. G.; Mohite, A. D. High-Efficiency Two-Dimensional Ruddlesden–Popper Perovskite Solar Cells. *Nature* 2016, 536 (7616), 312–316. <https://doi.org/10.1038/nature18306>.
- (6) Lin, Y.; Bai, Y.; Fang, Y.; Chen, Z.; Yang, S.; Zheng, X.; Tang, S.; Liu, Y.; Zhao, J.; Huang, J. Enhanced Thermal Stability in Perovskite Solar Cells by Assembling 2D/3D Stacking Structures. *J. Phys. Chem. Lett.* 2018, 9 (3), 654–658. <https://doi.org/10.1021/acs.jpclett.7b02679>.
- (7) Proppe, A. H.; Quintero-Bermudez, R.; Tan, H.; Voznyy, O.; Kelley, S. O.; Sargent, E. H. Synthetic Control over Quantum Well Width Distribution and Carrier Migration in Low-Dimensional Perovskite Photovoltaics. *J. Am. Chem. Soc.* 2018, 140 (8), 2890–2896. <https://doi.org/10.1021/jacs.7b12551>.
- (8) Bouduban, M. E. F.; Burgos-Caminal, A.; Ossola, R.; Teuscher, J.; Moser, J. E. Energy and Charge Transfer Cascade in Methylammonium Lead Bromide Perovskite Nanoparticle Aggregates. *Chem. Sci.* 2017, 8 (6), 4371–4380. <https://doi.org/10.1039/c6sc05211h>.
- (9) Yuan, M.; Quan, L. N.; Comin, R.; Walters, G.; Sabatini, R.; Voznyy, O.; Hoogland, S.; Zhao, Y.; Beauregard, E. M.; Kanjanaboos, P.; Lu, Z.; Kim, D. H.;

- Sargent, E. H. Perovskite Energy Funnels for Efficient Light-Emitting Diodes. *Nat. Nanotechnol.* 2016, 11 (10), 872–877. <https://doi.org/10.1038/nnano.2016.110>.
- (10) Liu, J.; Leng, J.; Wu, K.; Zhang, J.; Jin, S. Observation of Internal Photoinduced Electron and Hole Separation in Hybrid Two-Dimensional Perovskite Films. *J. Am. Chem. Soc.* 2017, 139 (4), 1432–1435. <https://doi.org/10.1021/jacs.6b12581>.
 - (11) Wang, J.; Leng, J.; Liu, J.; He, S.; Wang, Y.; Wu, K.; Jin, S. Engineered Directional Charge Flow in Mixed Two-Dimensional Perovskites Enabled by Facile Cation-Exchange. *J. Phys. Chem. C* 2017, 121 (39), 21281–21289. <https://doi.org/10.1021/acs.jpcc.7b08535>.
 - (12) Li, L.; Zhou, N.; Chen, Q.; Shang, Q.; Zhang, Q.; Wang, X.; Zhou, H. Unraveling the Growth of Hierarchical Quasi-2D/3D Perovskite and Carrier Dynamics. *J. Phys. Chem. Lett.* 2018, 9 (5), 1124–1132. <https://doi.org/10.1021/acs.jpclett.7b03294>.
 - (13) Stoumpos, C. C.; Cao, D. H.; Clark, D. J.; Young, J.; Rondinelli, J. M.; Jang, J. I.; Hupp, J. T.; Kanatzidis, M. G. Ruddlesden-Popper Hybrid Lead Iodide Perovskite 2D Homologous Semiconductors. *Chem. Mater.* 2016, 28 (8), 2852–2867. <https://doi.org/10.1021/acs.chemmater.6b00847>.
 - (14) Cao, D. H.; Stoumpos, C. C.; Farha, O. K.; Hupp, J. T.; Kanatzidis, M. G. 2D Homologous Perovskites as Light-Absorbing Materials for Solar Cell Applications. *J. Am. Chem. Soc.* 2015, 137 (24), 7843–7850. <https://doi.org/10.1021/jacs.5b03796>.
 - (15) Silver, S.; Dai, Q.; Li, H.; Brédas, J. L.; Kahn, A. Quantum Well Energetics of an $n = 2$ Ruddlesden–Popper Phase Perovskite. *Adv. Energy Mater.* 2019, 9, 1901005, 1–7. <https://doi.org/10.1002/aenm.201901005>.
 - (16) Chen, Z.; Li, Z.; Zhang, C.; Jiang, X. F.; Chen, D.; Xue, Q.; Liu, M.; Su, S.; Yip, H. L.; Cao, Y. Recombination Dynamics Study on Nanostructured Perovskite Light-Emitting Devices. *Adv. Mater.* 2018, 30 (38), 1–9. <https://doi.org/10.1002/adma.201801370>.
 - (17) Shang, Q.; Wang, Y.; Zhong, Y.; Mi, Y.; Qin, L.; Zhao, Y.; Qiu, X.; Liu, X.; Zhang, Q. Unveiling Structurally Engineered Carrier Dynamics in Hybrid Quasi-Two-Dimensional Perovskite Thin Films toward Controllable Emission. *J. Phys. Chem. Lett.* 2017, 8 (18), 4431–4438. <https://doi.org/10.1021/acs.jpclett.7b01857>.
 - (18) Quan, L. N.; Zhao, Y.; García De Arquer, F. P.; Sabatini, R.; Walters, G.; Voznyy, O.; Comin, R.; Li, Y.; Fan, J. Z.; Tan, H.; Pan, J.; Yuan, M.; Bakr, O. M.; Lu, Z.; Kim, D. H.; Sargent, E. H. Tailoring the Energy Landscape in Quasi-2D Halide Perovskites Enables Efficient Green-Light Emission. *Nano Lett.* 2017, 17 (6), 3701–3709. <https://doi.org/10.1021/acs.nanolett.7b00976>.

- (19) Proppe, A. H.; Elkins, M. H.; Voznyy, O.; Pensack, R. D.; Zapata, F.; Besteiro, L. V.; Quan, L. N.; Quintero-Bermudez, R.; Todorovic, P.; Kelley, S. O.; Govorov, A. O.; Gray, S. K.; Infante, I.; Sargent, E. H.; Scholes, G. D. Spectrally Resolved Ultrafast Exciton Transfer in Mixed Perovskite Quantum Wells. *J. Phys. Chem. Lett.* 2019, 10 (3), 419–426. <https://doi.org/10.1021/acs.jpcllett.9b00018>.
- (20) Liu, J.; Leng, J.; Wu, K.; Zhang, J.; Jin, S. Observation of Internal Photoinduced Electron and Hole Separation in Hybrid Two-Dimensional Perovskite Films. *J. Am. Chem. Soc.* 2017, 139 (4), 1432–1435. <https://doi.org/10.1021/jacs.6b12581>.
- (21) Silver, S.; Yin, J.; Li, H.; Brédas, J. L.; Kahn, A. Characterization of the Valence and Conduction Band Levels of $n = 1$ 2D Perovskites: A Combined Experimental and Theoretical Investigation. *Adv. Energy Mater.* 2018, 8 (16), 1–7. <https://doi.org/10.1002/aenm.201703468>.
- (22) Endres, J.; Egger, D. A.; Kulbak, M.; Kerner, R. A.; Zhao, L.; Silver, S. H.; Hodes, G.; Rand, B. P.; Cahen, D.; Kronik, L.; Kahn, A. Valence and Conduction Band Densities of States of Metal Halide Perovskites: A Combined Experimental-Theoretical Study. *J. Phys. Chem. Lett.* 2016, 7 (14), 2722–2729. <https://doi.org/10.1021/acs.jpcllett.6b00946>.
- (23) Feron, K.; Nagle, T. J.; Rozanski, L. J.; Gong, B. B.; Fell, C. J. Spatially Resolved Photocurrent Measurements of Organic Solar Cells: Tracking Water Ingress at Edges and Pinholes. *Sol. Energy Mater. Sol. Cells* 2013, 109, 169–177. <https://doi.org/10.1016/j.solmat.2012.10.027>.

Appendix B: Supporting Information for Chapter 4

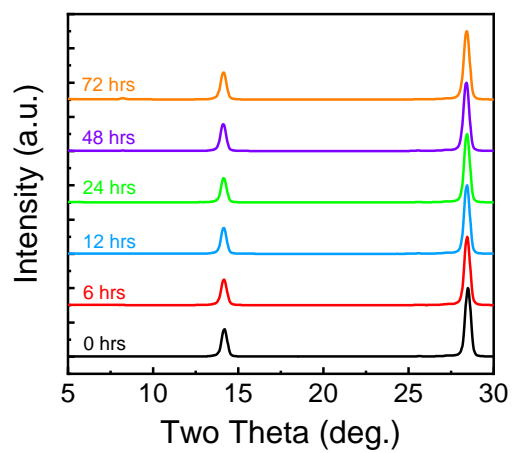


Figure B.1 XRD spectra of an nBA-MAPI film over 72 hours of moisture exposure at 78%RH.

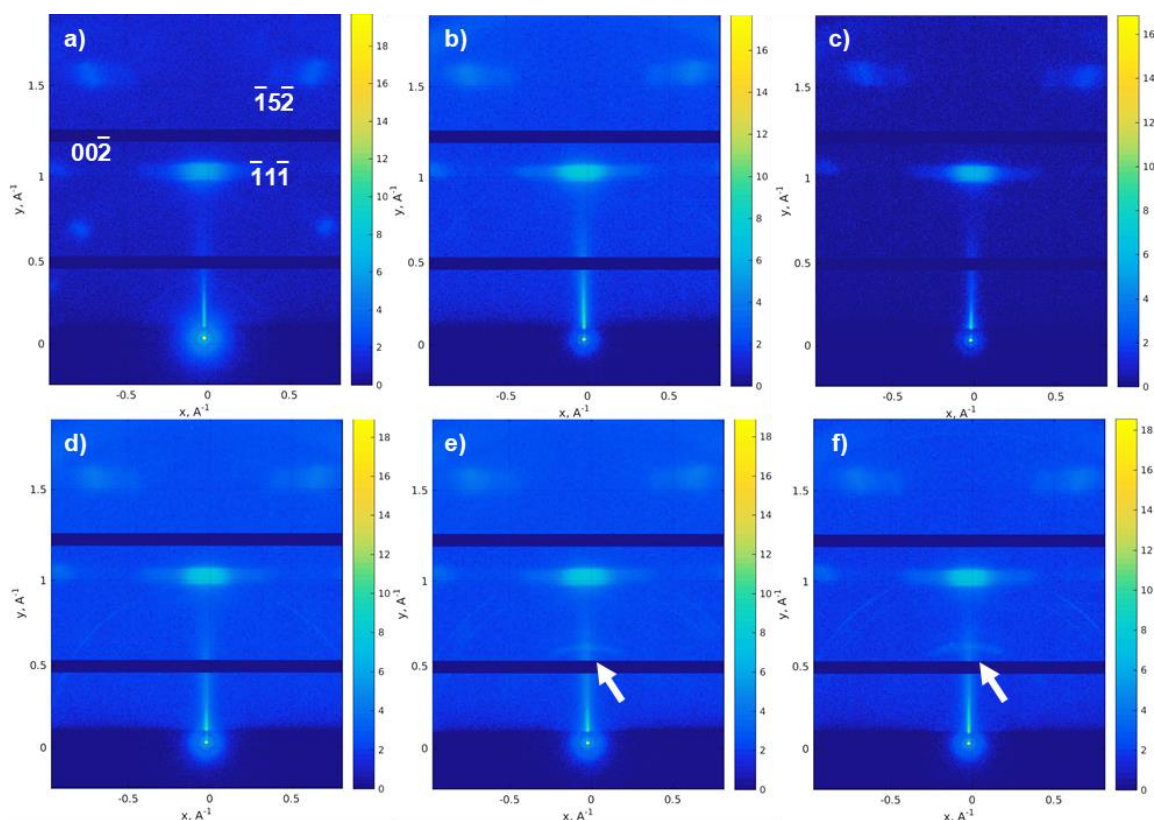


Figure B.2 WAXS spectra of nBA-MAPI films at a) 0 hours, b) 6 hours, c) 12 hours, d) 24 hours, e) 48 hours, and f) 72 hours of exposure to 78%RH. All samples show well-oriented crystal structures, as indicated by the clear spots for the $(0\ 0\ -2)$, $(-1\ 5\ -2)$, and $(-1\ 1\ -1)$ reflections. Spectra after 48 hours of exposure (e and f) show the formation of rings at low- q (indicated by white arrows), indicating the formation of un-oriented low- n perovskite phases after sufficient exposure.

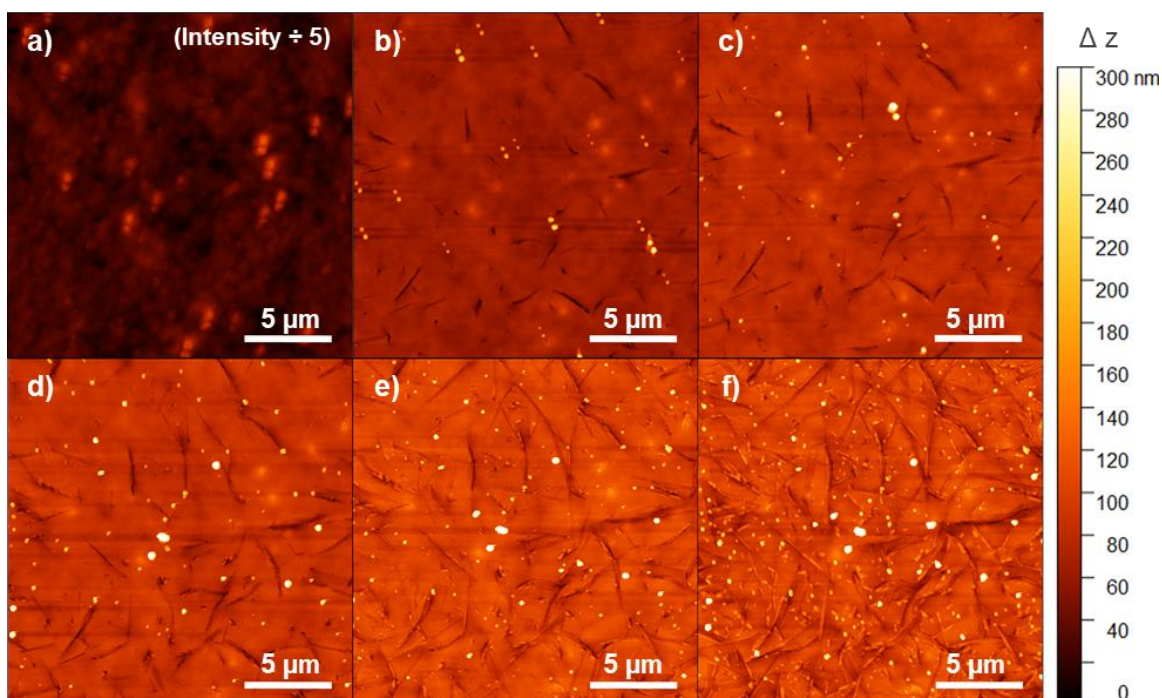


Figure B.3 AFM images of a single area of an nBA-MAPI film acquired *in situ* over a) 0 hours, b) 6 hours, c) 12 hours, d) 24 hours, e) 48 hours, and f) 72 hours of exposure to 78%RH. Cracks initially form in the surface of the film after just 6 hours of exposure (b), and grow over time. Crystalline structures also appear between b) and c), and likewise continue to grow, covering the surface after 72 hours (f).

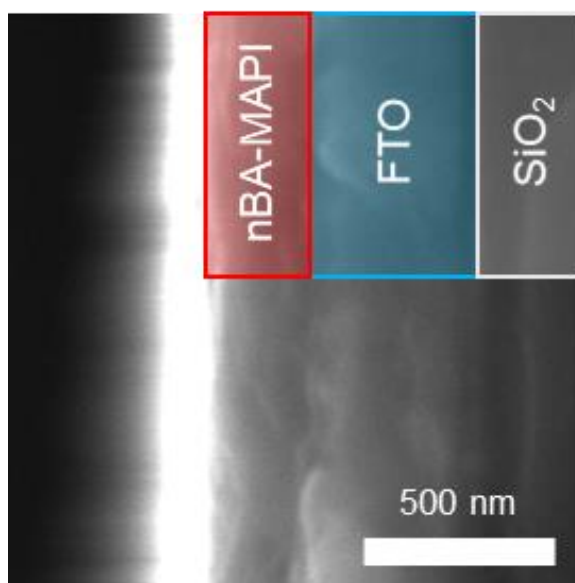


Figure B.4 Cross-sectional SEM image of a typical nBA-MAPI film showing an average thickness of roughly 350 nm.

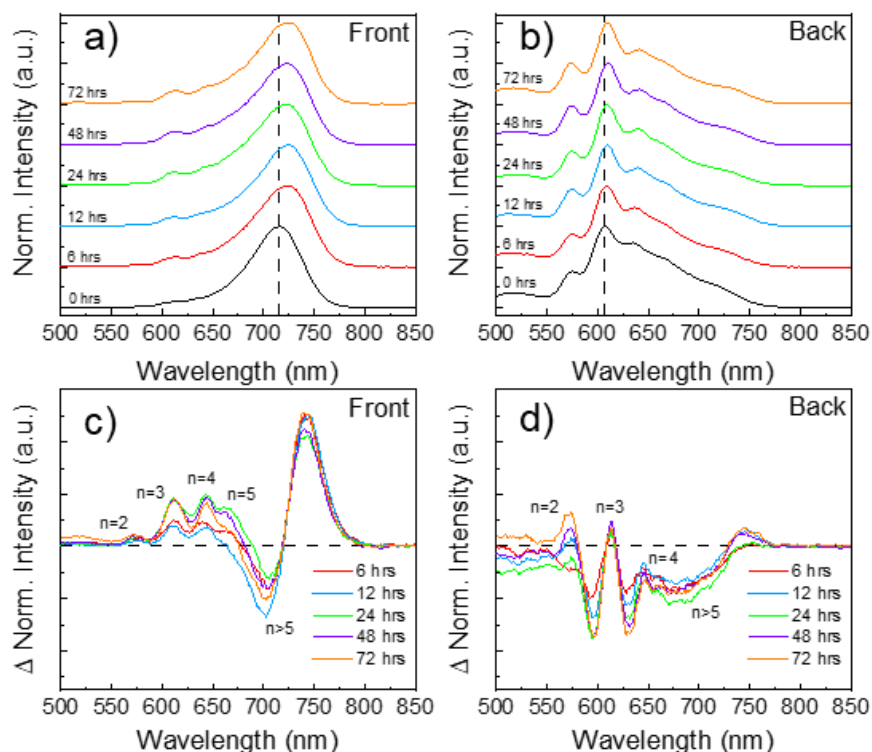


Figure B.5 PL spectra taken from the front (a) and back (b) of an nBA-MAPI film over the course of 72 hours of exposure to 78%RH. New peaks in the 575 to 650 nm range, corresponding to $n = 2$ -5 phases, appear on the front side (a) after exposure, and the primary peak at 715 nm shifts to 725 nm. Similar, but smaller spectral changes are observed in b). Normalized PL difference plots from the front (c) and back (d) of the same film, showing the formation of low- n species and a 3D-like species concurrent with the loss of the $n > 5$ species with exposure.

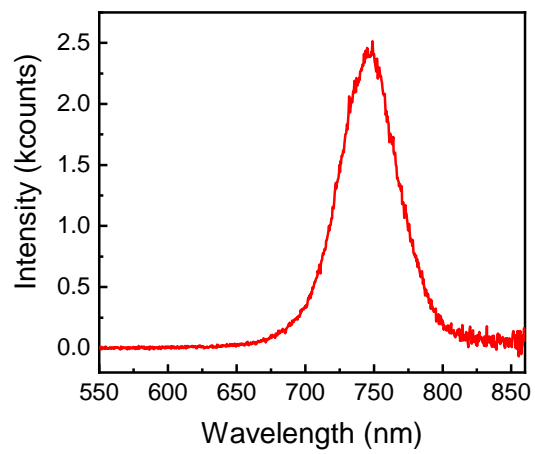


Figure B.6 Point fluorescence spectrum from an nBA-MAPI film showing a strong peak near 750 nm.

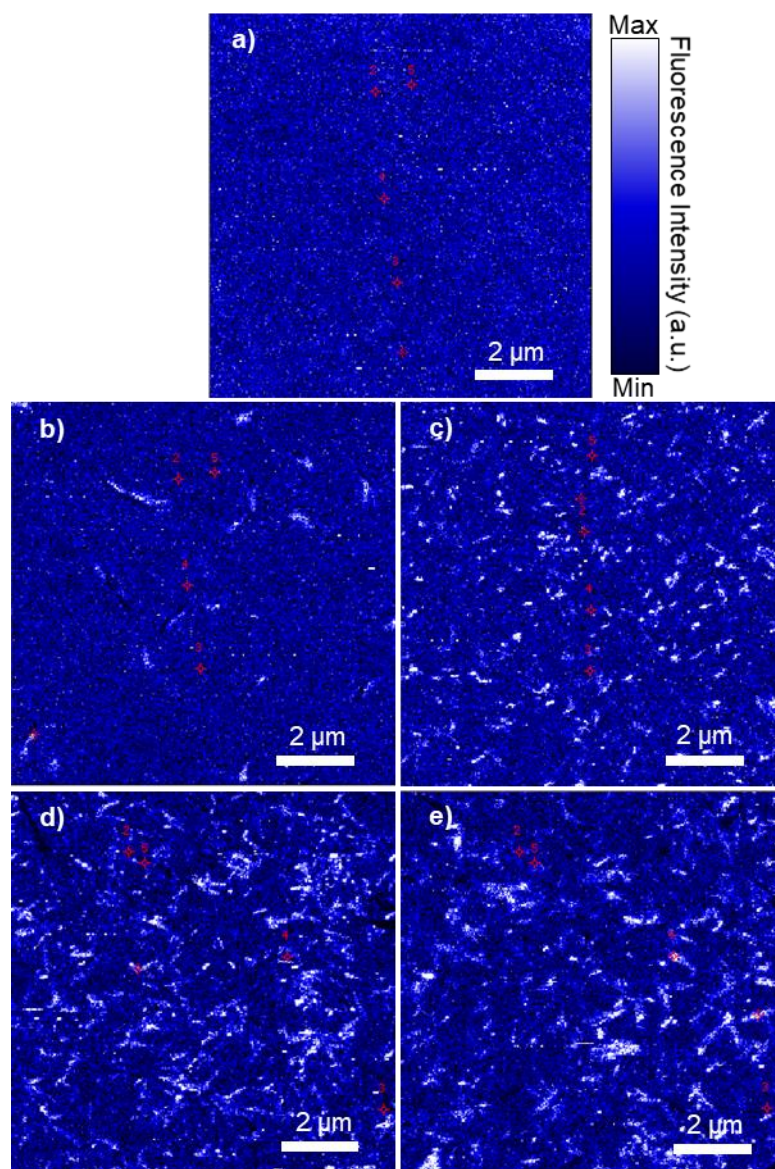


Figure B.7 CFM images of a nBA-MAPI films at a) 0 hours, b) 12 hours, c) 24 hours, d) 48 hours, and e) 72 hours of exposure to 78%RH with a 740 nm short-pass filter. After 12 hours (b) fluorescence from elongated structures on the film is observed, and the size and surface density of these structures increases with exposure. The red crosshairs and numbers are artifacts from the imaging software.

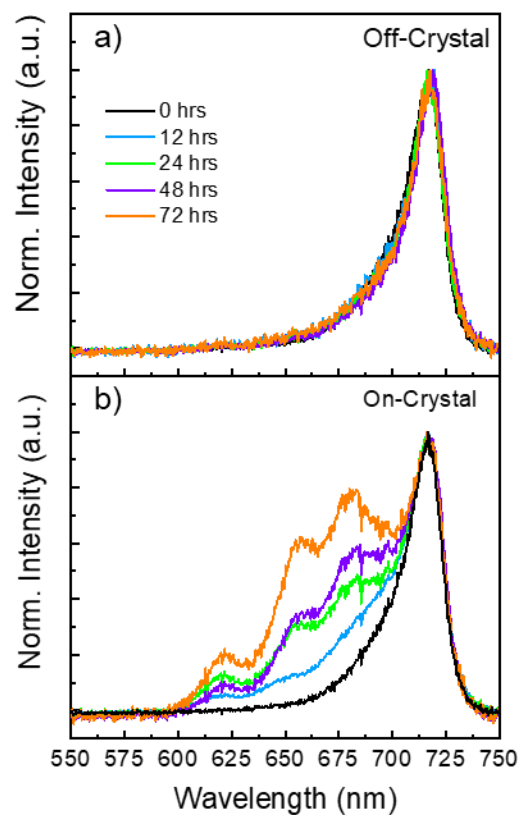


Figure B.8 Average normalized point fluorescence spectra from CFM of areas off- (a) and on-crystal (b) taken from nBA-MAPI films exposed to 78%RH over 72 hours. In a) only the shoulder of the large peak at 750 nm can be observed for all samples. In b), there is a clear increase in peaks at 620, 660, and 680 nm with exposure time, corresponding to formation of $n=3$, 4, and 5 peaks, respectively.

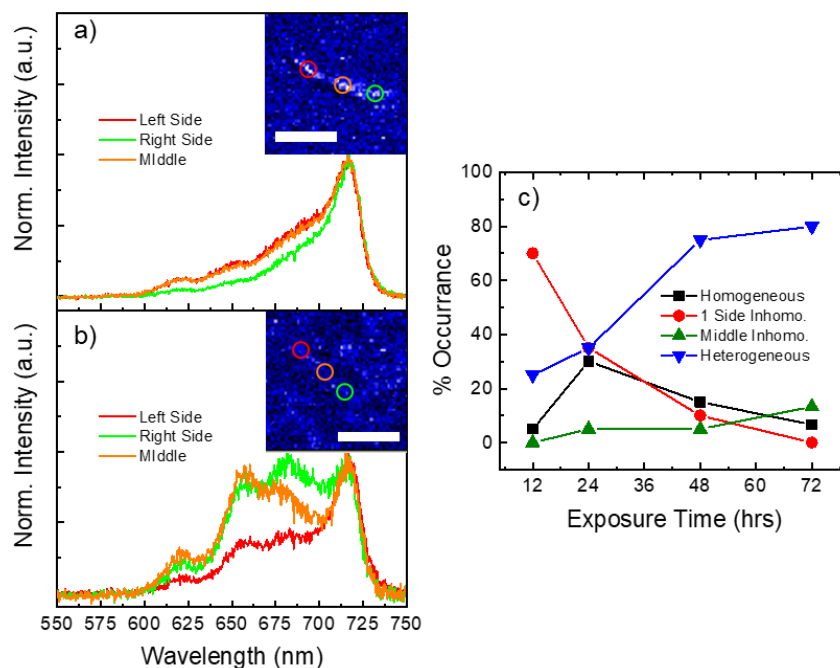


Figure B.9 Point fluorescence spectra taken from three different locations of the same nBA-MAPI crystal using CFM at a) 12 hours and b) 72 hours of exposure to 78% RH, demonstrating differences in crystal homogeneity. The inset image in each provides an example of the locations sampled for each spectrum. Scale bar equal to 1 μm . c) Plot showing the prevalence of different levels of crystal homogeneity in nBA-MAPI crystals over 72 hours of exposure. Over time, the overall homogeneity of the crystals decreases as spectra from different locations of the crystals begin to show varying quantities of different n -phases.

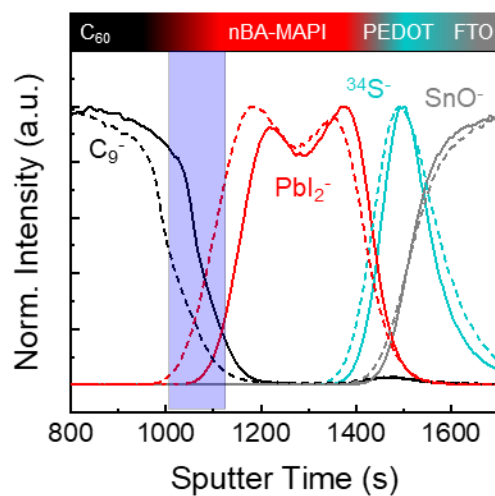


Figure B.10 ToF-SIMS depth profile of various species from fresh (solid line) and exposed (dashed line) model PV devices. Exposed devices were left exposed to 78% RH for 24 hours prior to analysis. After exposure, the perovskite layer (PbI_2^-) shows an increase in width at the C_{60} interface, largely corresponding the hydration layer that has built up here (blue shaded region) and indicating moisture-related changes in the material.

Appendix C: Supporting Information for Chapter 5

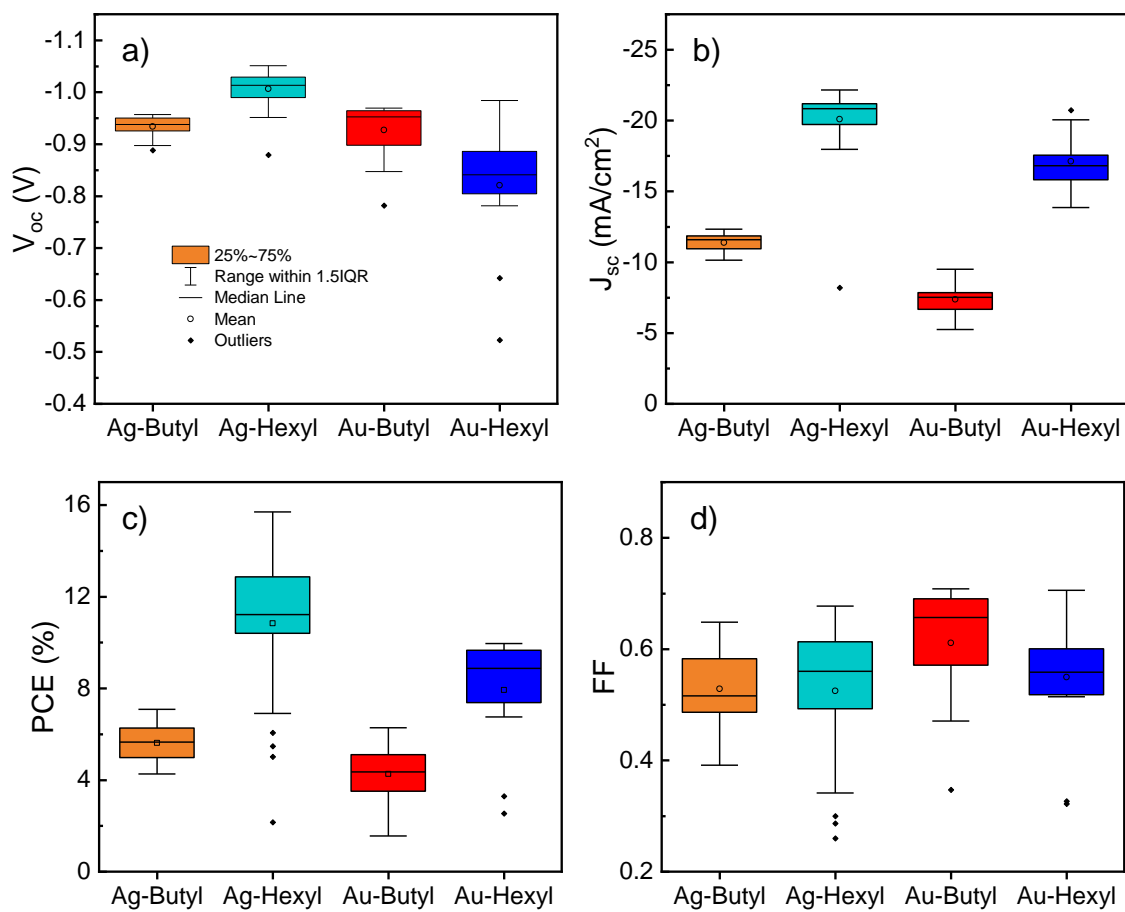


Figure C.1 Average (a) V_{oc} , (b) J_{sc} , (c) PCE, and (d) FF of all butyl- and hexyl-MAPI devices with both Ag and Au contacts.

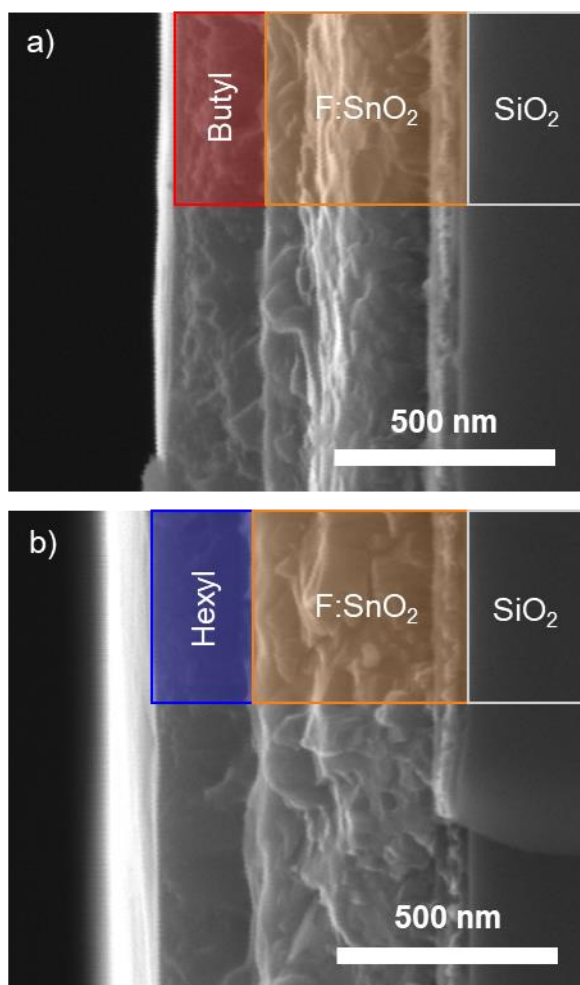


Figure C.2 Cross sectional SEM image of (a) butyl-MAPI and (b) hexyl-MAPI films.

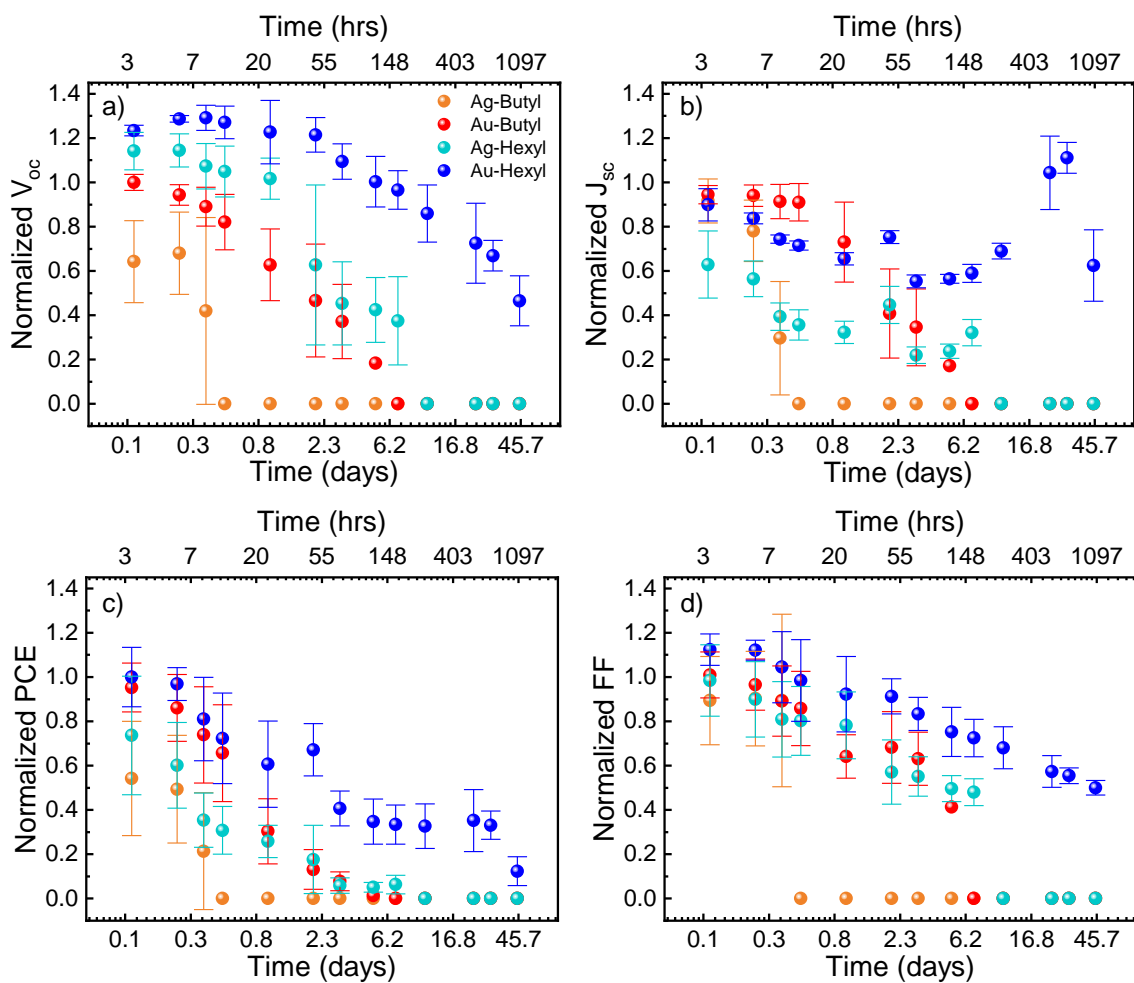


Figure C.3 Normalized (a) V_{oc} , (b) J_{sc} , (c) PCE, and (d) FF of butyl- and hexyl-MAPI devices fabricated using Au and Ag contacts exposed to 78%RH.

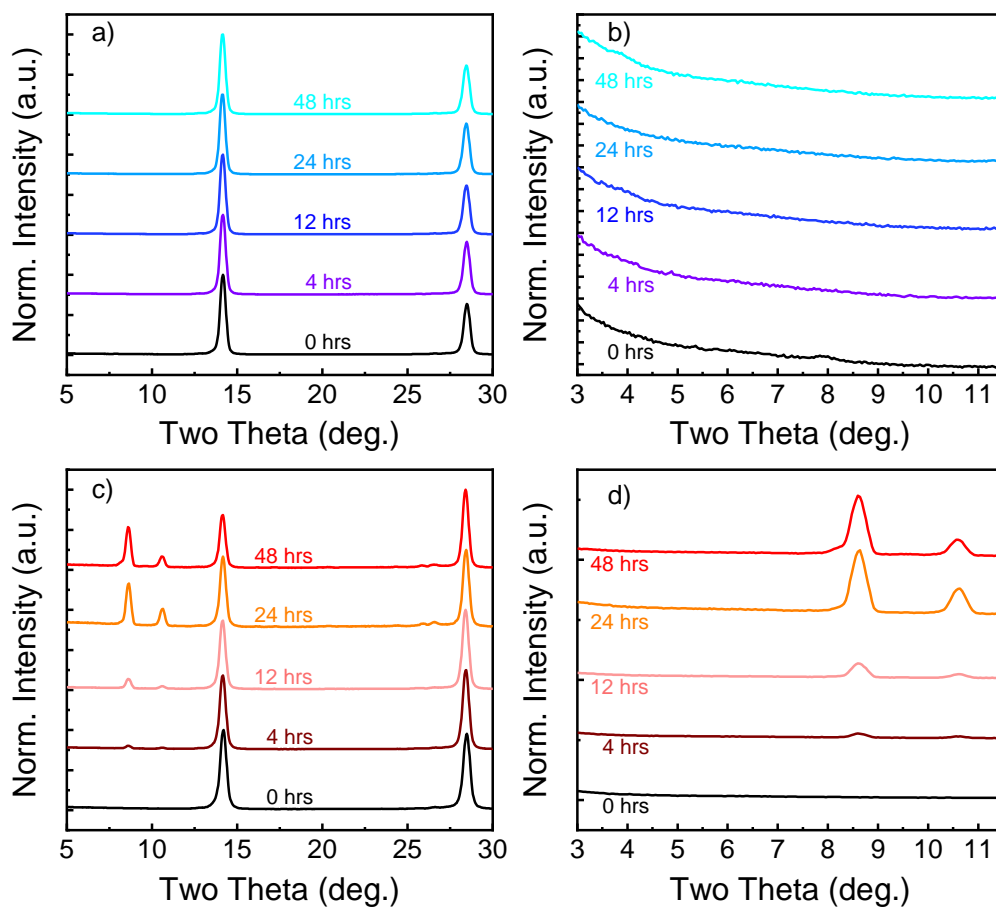


Figure C.4 Full XRD spectra of (a) hexyl-MAPI and (c) butyl-MAPI films exposed to 78%RH over 48 hours. Low-angle XRD spectra of (b) hexyl-MAPI and (d) butyl-MAPI films exposed to humidity. As exposure time progresses, the butyl-MAPI films exhibit the growth of low- n peaks below $2\theta = 12^\circ$, while hexyl-MAPI does not.

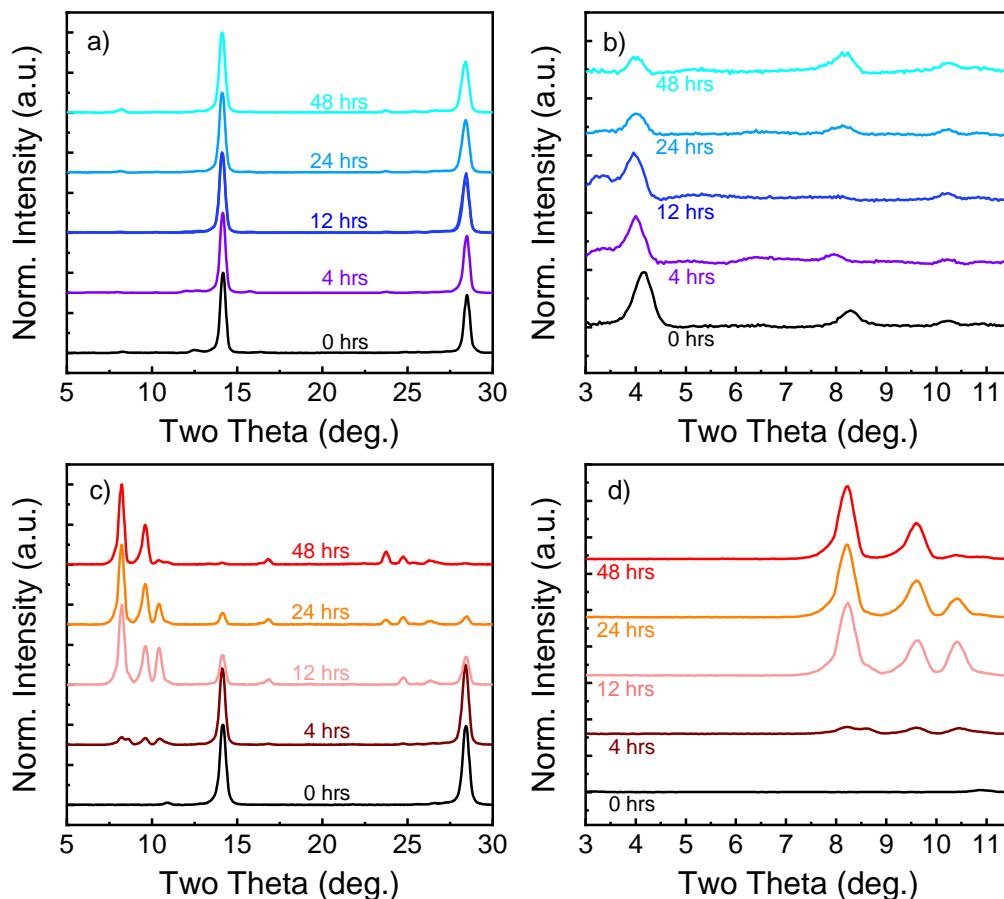


Figure C.5 Full XRD spectra of (a) Ag-hexyl and (c) Ag-butyl devices exposed to 78%RH over 48 hours. Low-angle XRD spectra of (b) Ag-hexyl and (d) Ag-butyl devices exposed to humidity. As exposure time progresses, the Ag-butyl devices exhibit the growth of low- n peaks below $2\theta = 12^\circ$ and the near complete loss of the original diffraction peaks, while hexyl-MAPI does not. Weak low- n peaks are visible in (b), likely indicating the formation of some low- n species during fabrication.

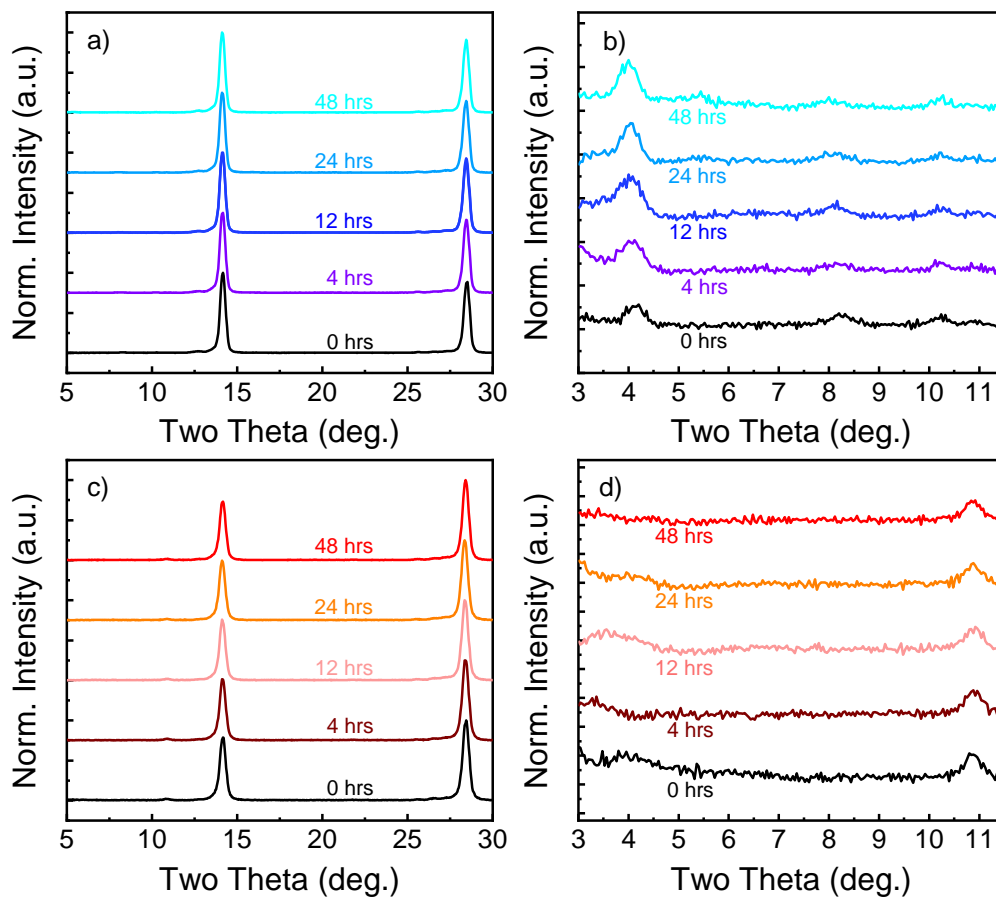


Figure C.6 Full XRD spectra of (a) Au-hexyl and (c) Au-butyl devices exposed to 78%RH over 48 hours. Low-angle XRD spectra of (b) Au-hexyl and (d) Au-butyl devices exposed to humidity. Both hexyl- and butyl-MAPI show low- n peaks below $2\theta = 12^\circ$ formed during fabrication, but these peaks do not grow with exposure time.

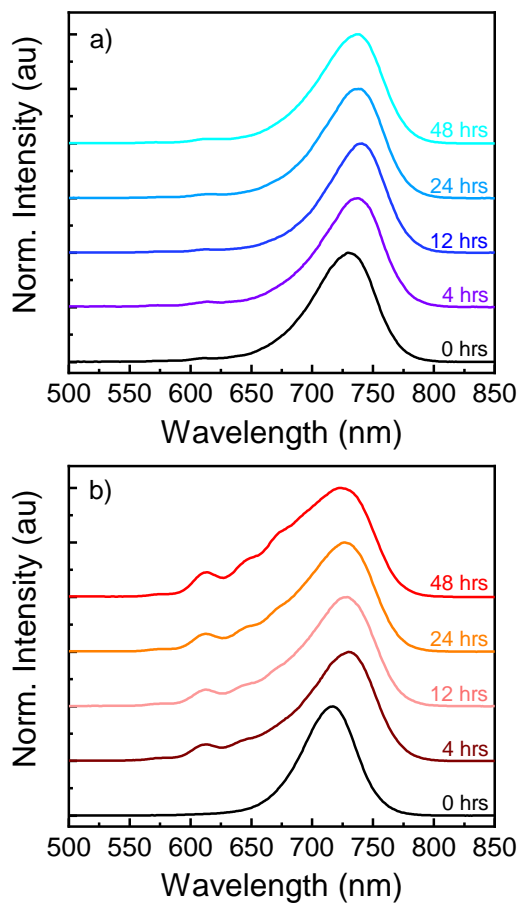


Figure C.7 Normalized PL spectra of (a) hexyl-MAPI and (b) butyl-MAPI films over 48 hours of exposure to 78% RH. Both the hexyl- and butyl-MAPI films shows a slight (~ 10 nm) red-shift of the primary peak, but the butyl-MAPI film also shows clear formation of low- n peaks from 700 – 600 nm.

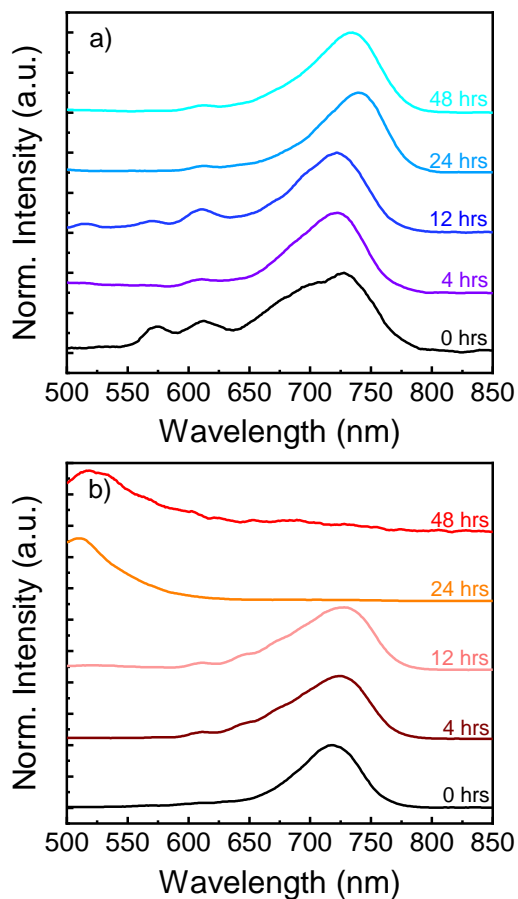


Figure C.8 Normalized PL spectra of (a) Ag-hexyl and (b) Ag-butyl devices over 48 hours of exposure to 78% RH. Both the hexyl- and butyl-MAPI devices shows a slight (~ 10 nm) red-shift of the primary peak, but the butyl-MAPI film also shows clear formation of low- n peaks from 700 – 550 nm up to 12 hours. Afterwards, the film shows only a broad emission below 550 nm. The hexyl-MAPI film showed a decrease in the relative intensity of low- n peaks with exposure with time.

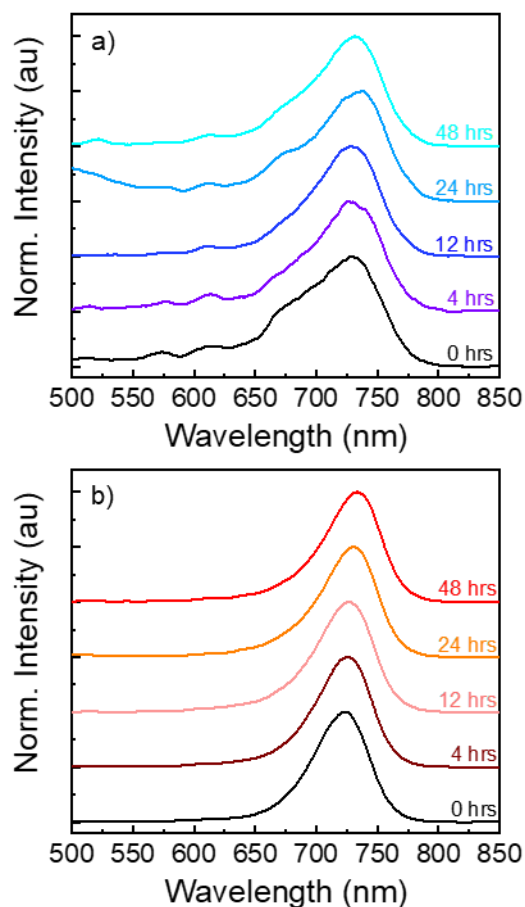


Figure C.9 Normalized PL spectra of (a) Au-hexyl and (b) Au-butyl devices over 48 hours of exposure to 78% RH. Both the hexyl- and butyl-MAPI devices shows a slight (~ 10 nm) red-shift of the primary peak, but the hexyl-MAPI device shows a decrease in the relative intensity of the low- n peaks from 700 – 550 nm. In contrast, the butyl-MAPI device shows almost no change.

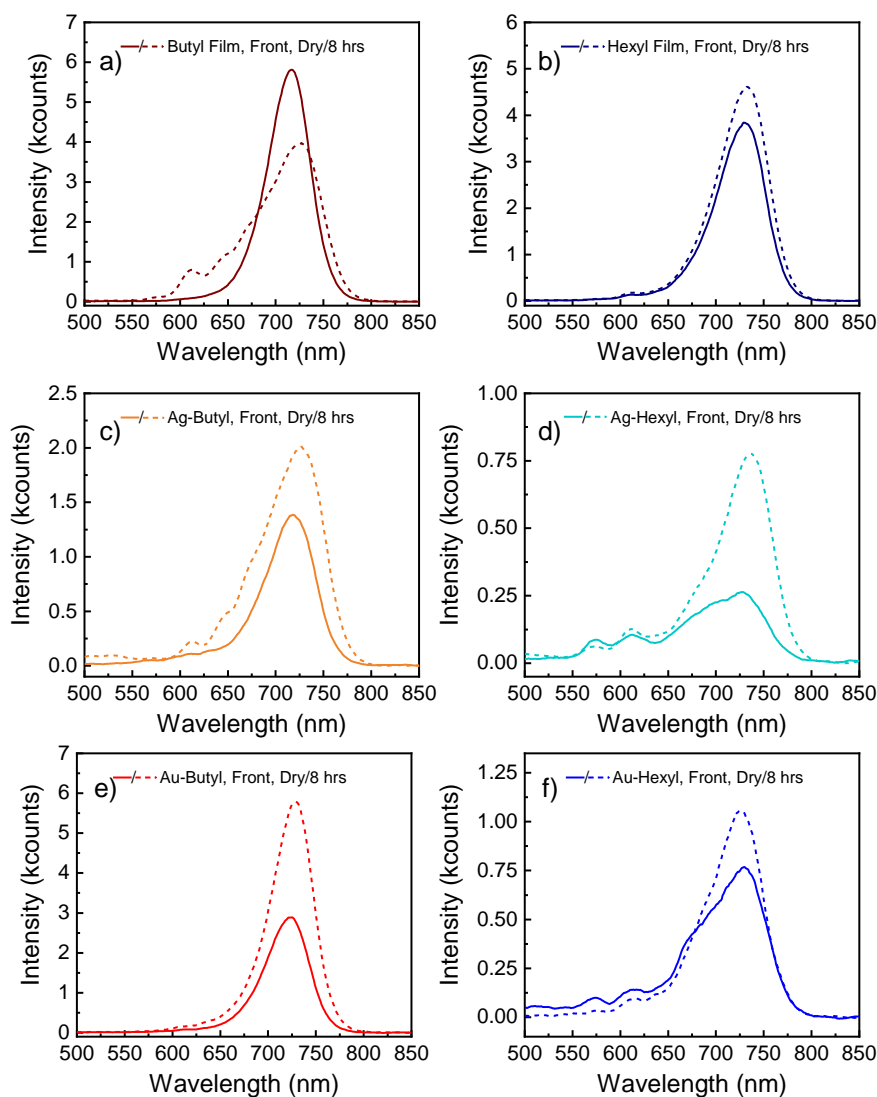


Figure C.10 PL spectra of a (a) butyl-MAPI film, (b) hexyl-MAPI film, (c) Ag-butyl device, (d) Ag-hexyl device, (e) Au-butyl device, and (f) Au-hexyl device before and after exposure to 78% RH for 8 hours. The hexyl-MAPI film shows a slight increase in the $n > 5$ peak with exposure, likely due to passivation of the surface, while the butyl-MAPI film shows a decrease in the primary $n > 5$ peak and an increase in the low- n peaks below 700 nm, likely due to disproportionation of the perovskite. All of the devices show an increase in PL intensity with moisture exposure, indicating decreased quenching of carriers by the C_{60} due to the formation of a low- n passivation layer at the surface of the film. Low- n features are observed prior to degradation in (d) and (f), but do not appear to grow larger following degradation.

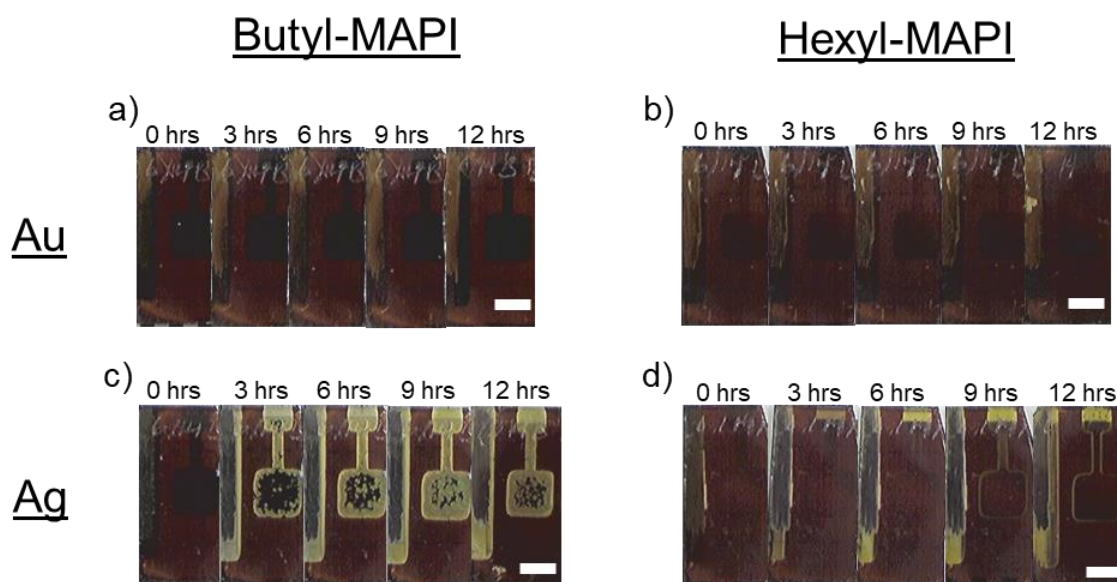


Figure C.11 Photographs of the backs of (a) Au-butyl, (b) Au-hexyl, (c) Ag-butyl, and (d) Ag-hexyl devices over the course of 12 hours of exposure to 78% RH. Both (a) and (b) show little change to the devices over the time period, while (d) shows the formation of a thin strip of yellow material around the outer edges of the Ag contacts only. (c) shows the formation of a large quantity of yellow material around the outer edges of the contacts, as well as some areas in the interior after just 3 hours. The degradation continues over the next 9 hours, until almost the entire device is yellow. Of interest, the yellow material only forms in areas directly under or adjacent to the Ag electrode. The scale bar indicates 0.5 cm.

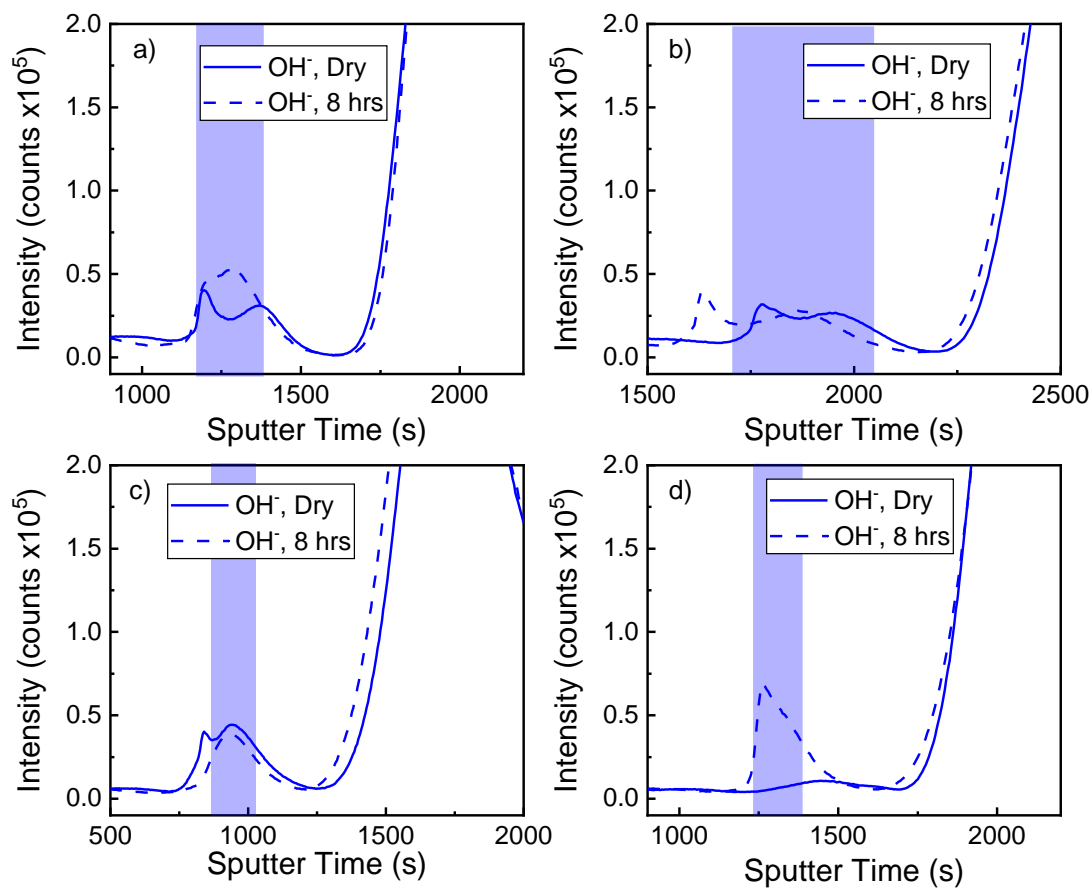


Figure C.12 OH^- depth profiles of (a) Ag-butyl, (b) Au-butyl, (c) Ag-hexyl, and (d) Au-hexyl devices before and after 8 hours of exposure to 78% RH. The hydration region for each device is defined as the FWHM of the OH^- peak at the C_{60} /perovskite interface following exposure.

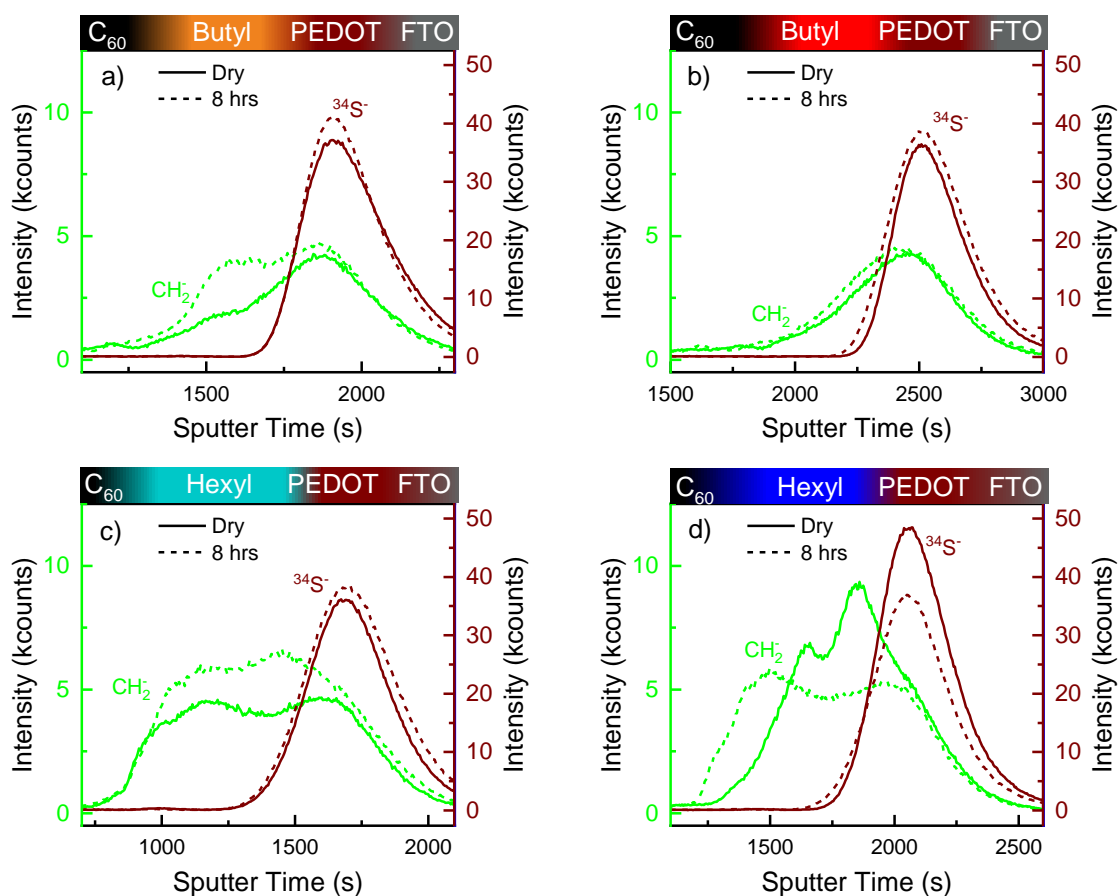


Figure C.13 CH_2^- and $^{34}\text{S}^-$ depth profiles for (a) Ag-butyl, (b) Au-butyl, (c) Ag-hexyl, and (d) Au-hexyl devices before and after moisture exposure. The colored bars on top of each profile show the relative location of the peaks within the larger device. In all cases, there is a CH_2^- peak on the bottom (rightward) side of the perovskite layer that corresponds with the organics in the PEDOT (indicated by the $^{34}\text{S}^-$ species).

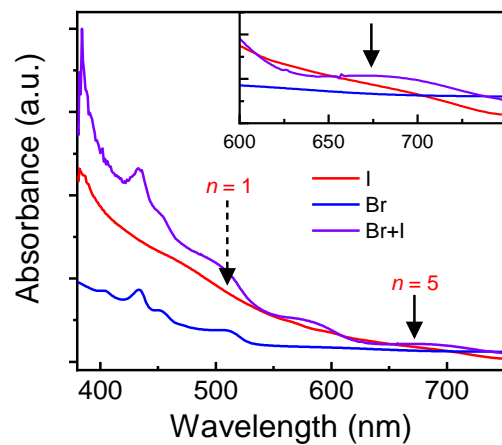


Figure C.14 UV-Vis spectra of $n = 5$ films of butyl-MAPI (red), butyl-MAPBr (blue), and a paired butyl iodo/bromo set (purple). The iodo $n = 5$ band gap (arrow in inset) is poorly defined in the paired sample, as is the $n = 1$ feature.

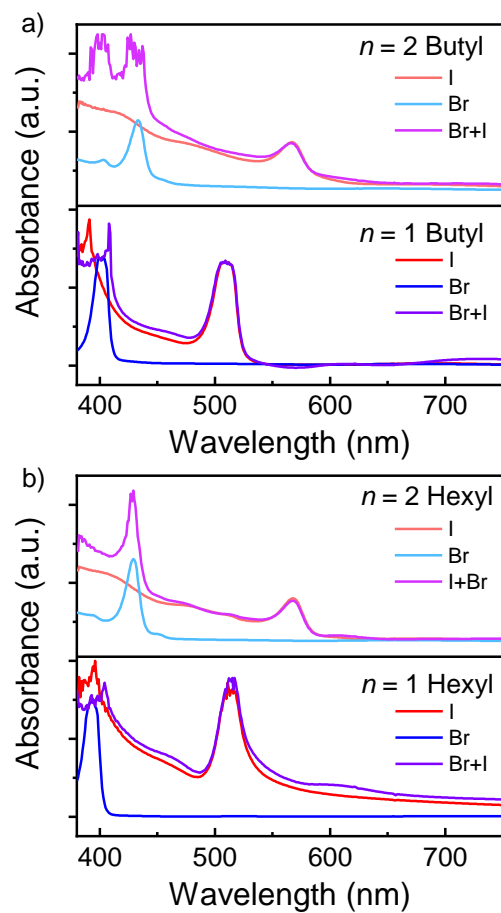


Figure C.15 UV-Vis spectra of $n = 2$ (top) and 1 (bottom) films of (a) butyl-MAPI and (b) hexyl-MAPI. The spectra include single iodo (red) and bromo (blue) materials, as well as a paired set of iodo/bromo films (purple).

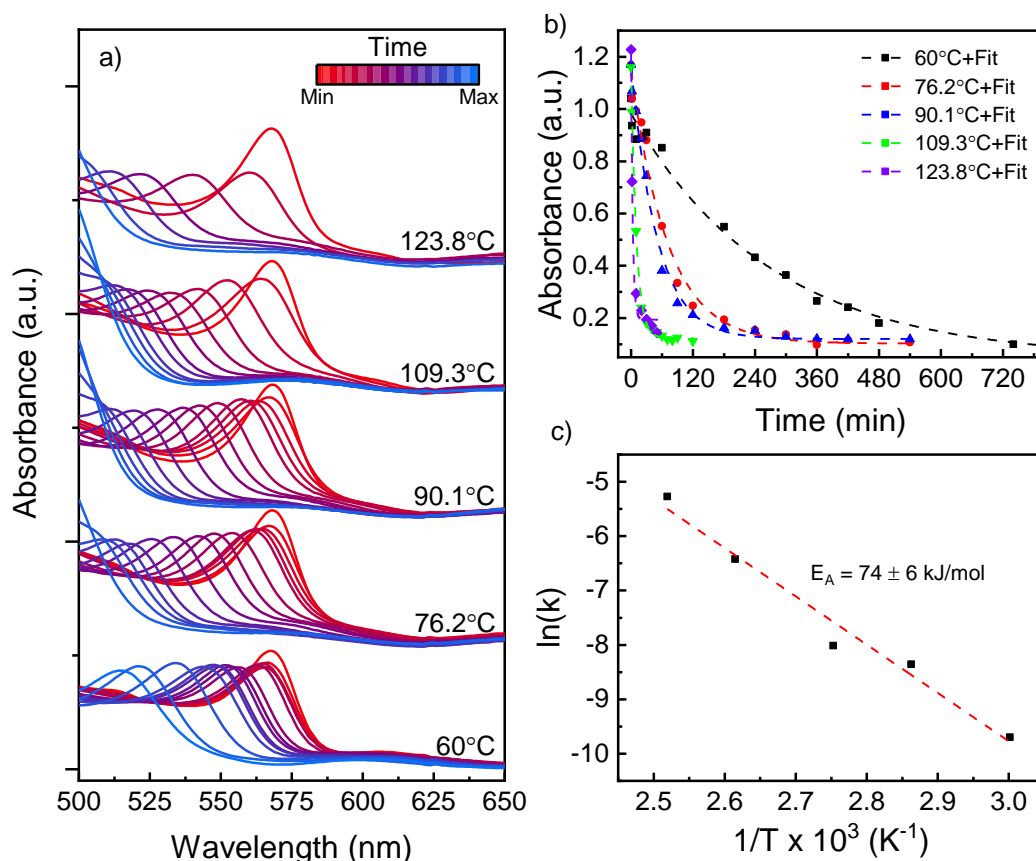


Figure C.16 a) UV-Vis spectra of $n = 2$ hexyl-MAPI iodo/bromo pairs held at several temperatures over time. b) Decay in the intensity of the iodo UV-Vis peak near 575 nm in (a) measured over time; each point corresponds to a spectrum in (a). The data is fit to first order decay (line). c) Arrhenius plot derived from decay constants calculated using the data in (b), providing the activation energy of halide migration in the material.

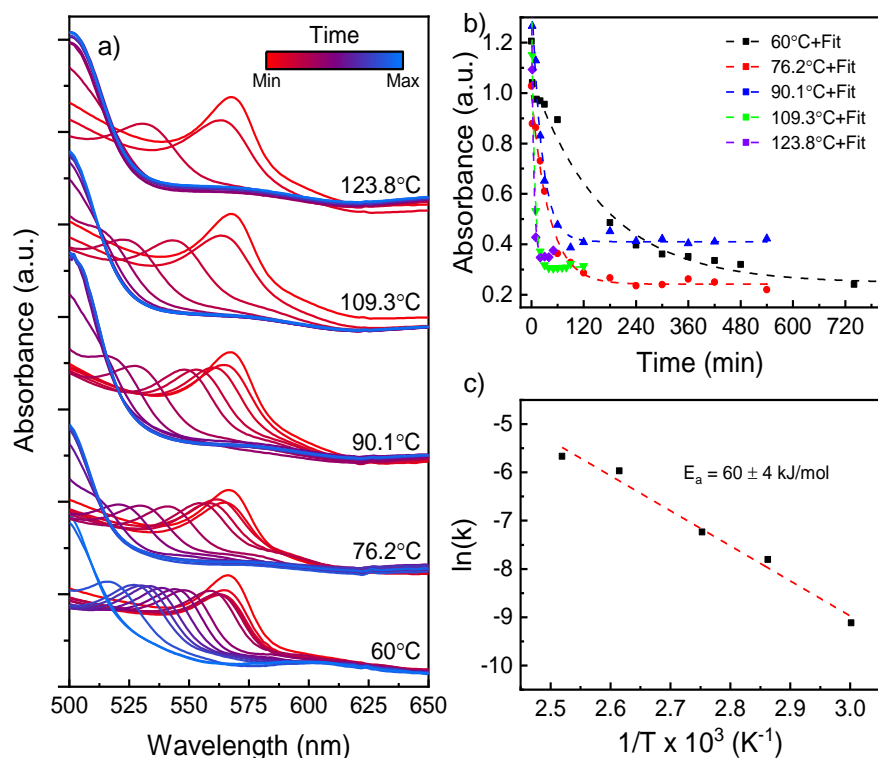


Figure C.17 a) UV-Vis spectra of $n = 2$ butyl-MAPI iodo/bromo pairs held at several temperatures over time. b) Decay in the intensity of the iodo UV-Vis peak near 575 nm in (a) measured over time; each point corresponds to a spectrum in (a). The data is fit to first order decay (line). c) Arrhenius plot derived from decay constants calculated using the data in (b), providing the activation energy of halide migration in the material.

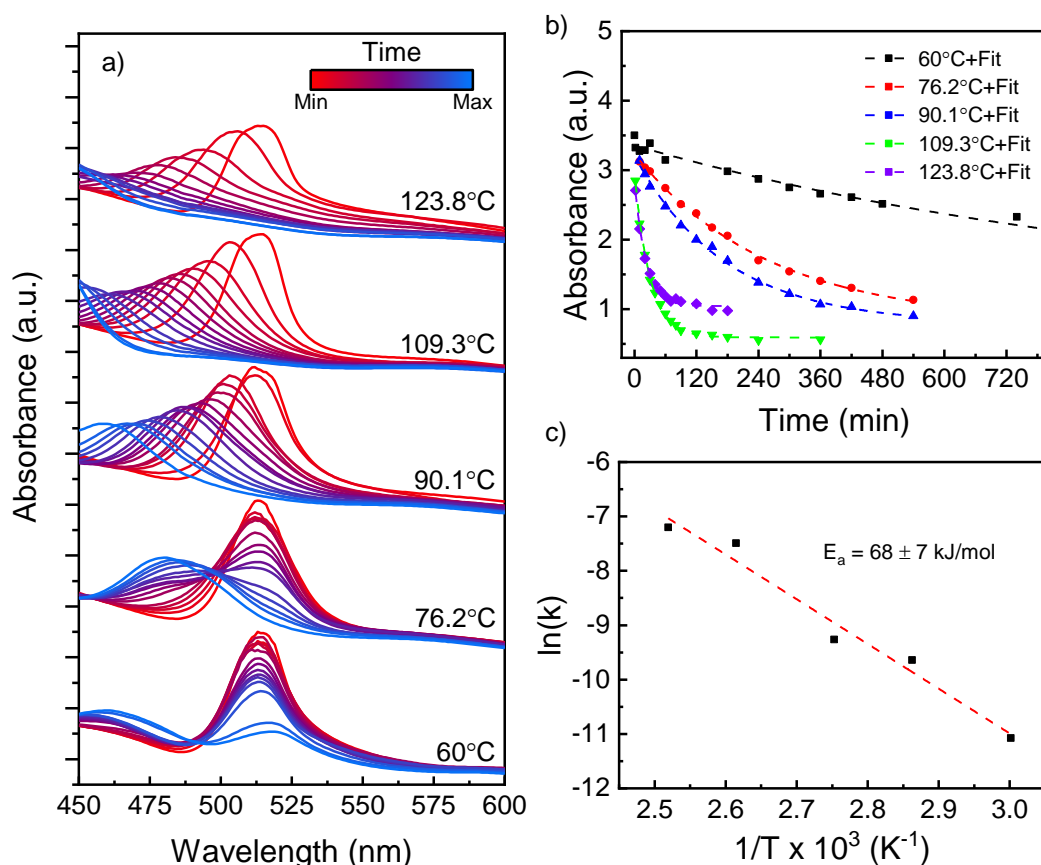


Figure C.18 a) UV-Vis spectra of $n = 1$ hexyl-MAPI iodo/bromo pairs held at several temperatures over time. b) Decay in the intensity of the iodo UV-Vis peak near 510 nm in (a) measured over time; each point corresponds to a spectrum in (a). The data is fit to first order decay (line). c) Arrhenius plot derived from decay constants calculated using the data in (b), providing the activation energy of halide migration in the material.

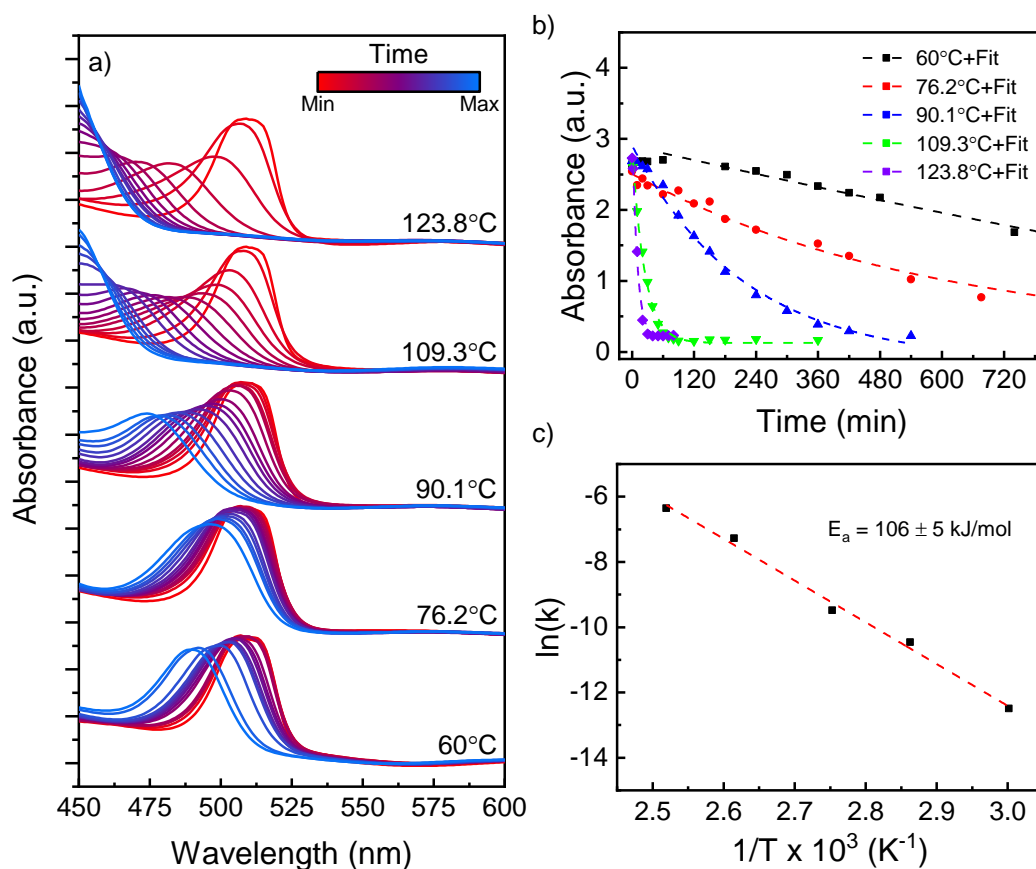


Figure C.19 a) UV-Vis spectra of $n = 1$ butyl-MAPI iodo/bromo pairs held at several temperatures over time. b) Decay in the intensity of the iodo UV-Vis peak near 510 nm in (a) measured over time; each point corresponds to a spectrum in (a). The data is fit to first order decay (line). c) Arrhenius plot derived from decay constants calculated using the data in (b), providing the activation energy of halide migration in the material.

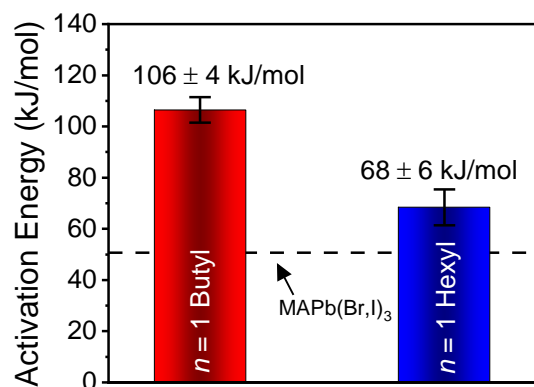


Figure C.20 Activation energies for halide mobility in *n* = 1 butyl- and hexyl-MAPI perovskite determined by UV-Vis spectroscopy. The dashed line represents the previously reported activation energy of a 3D perovskite.

Appendix D: Supporting Information for Chapter 7

D.1 TABLES

Sample	t
UnSCO	1.002
1%Fe-SCO	1.002
5%Fe-SCO	1.001
10%Fe-SCO	1.000
1%Sc-SCO	1.001
5%Sc-SCO	0.996
10%Sc-SCO	0.989

Table D.1 Tolerance values for the seven selected SCO samples examined in this study. t shows a transition to unity with increasing concentrations of both Fe and Sc dopants.

Sample	Percent Fe/Sc (%)	Binding Energy (eV)
1%Fe-SCO	1.14	711.9
5%Fe-SCO	3.78	712.2
10%Fe-SCO	9.10	712.9
1%Sc-SCO	3.95	402.7
5%Sc-SCO	5.18	402.9
10%Sc-SCO	13.61	401.6

Table D.2 Atomic percentage of Fe and Sc dopants as measured using XPS, and the binding energy of the 2p $3/2$ peaks both elements.

Sample	Binding Energy (eV)	FWHM
1%Fe-SCO	780.2	2.49
5%Fe-SCO	781.5	3.20
10%Fe-SCO	781.2	3.37

Table D.3 FWHM and Co 2p 3/2 binding energies for the Fe-SCO samples. As iron concentration increases, the FWHM of the peak increases as well.

Sample	Mass Activity (mA/mg)
$\text{SrCo}_{0.9}\text{Fe}_{0.1}\text{O}_{3-\delta}$	6.5
LaNiO_3^*	90.0
$\text{LaNi}_{0.75}\text{Fe}_{0.25}\text{O}_3^*$	82.0
LaCoO_3^*	100.0
LaMnO_3^*	92

Table D.4 OER mass activities of several perovskites. LaNiO_3 , $\text{LaNi}_{0.75}\text{Fe}_{0.25}\text{O}_3$, LaCoO_3 , and LaMnO_3 are all supported on N-doped carbon on a glassy carbon rotating disk electrode.

D.2 FIGURES

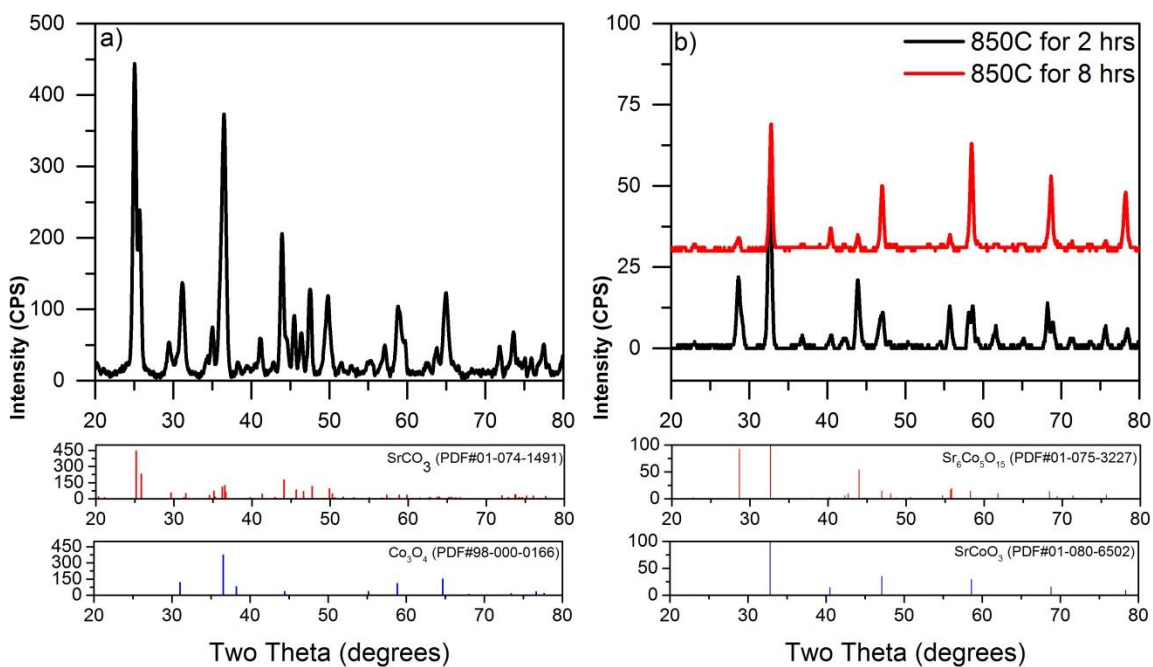


Figure D.1. XRD spectra of a) SCO precursor annealed for 4.5 hours at 450°C, b) SCO precursor annealed at 850°C for 2 and 8 hours

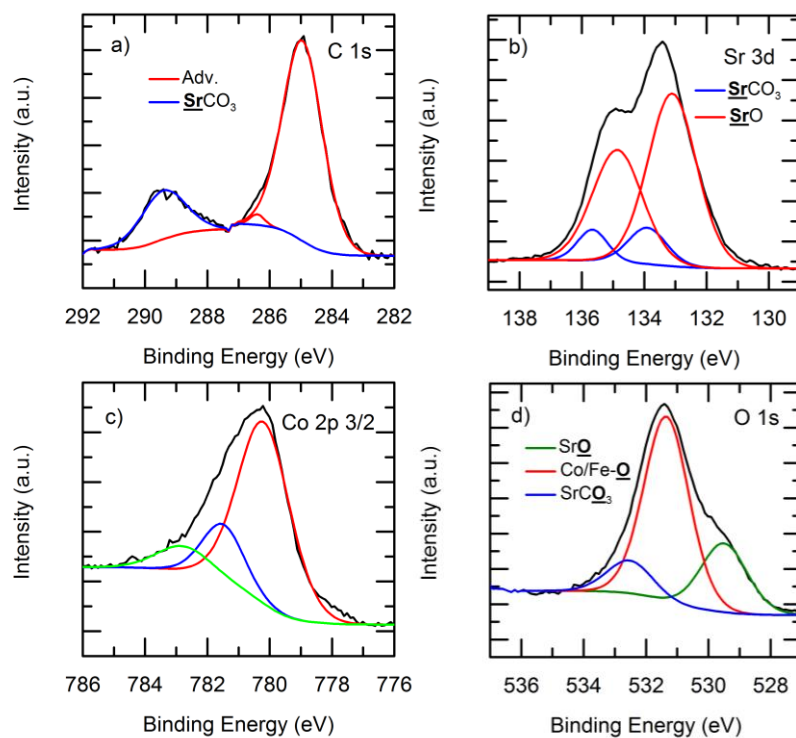


Figure D.2. XPS spectra and fitted peaks for the 1%Fe-SCO sample. a) Spectra of the carbon 1s peak. b) Spectra of the strontium 3d 5/2 and 3/2 peaks. c) Spectra of the cobalt 2p peak. d) Spectra of the oxygen 1s peak.

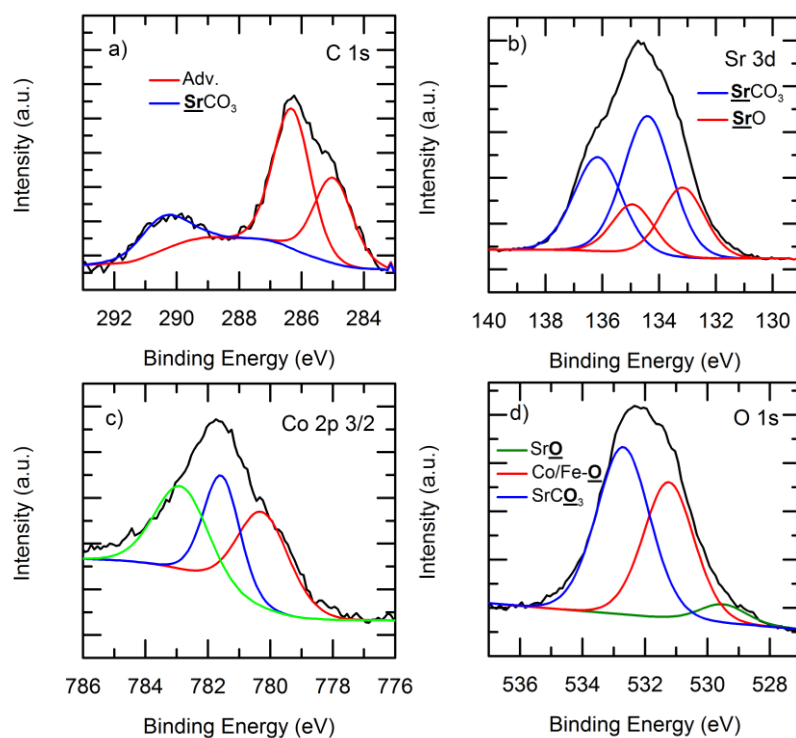


Figure D.3. XPS spectra and fitted peaks for the 5%Fe-SCO sample. a) Spectra of the carbon 1s peak. b) Spectra of the strontium 3d 5/2 and 3/2 peaks. c) Spectra of the cobalt 2p peak. d) Spectra of the oxygen 1s peak.

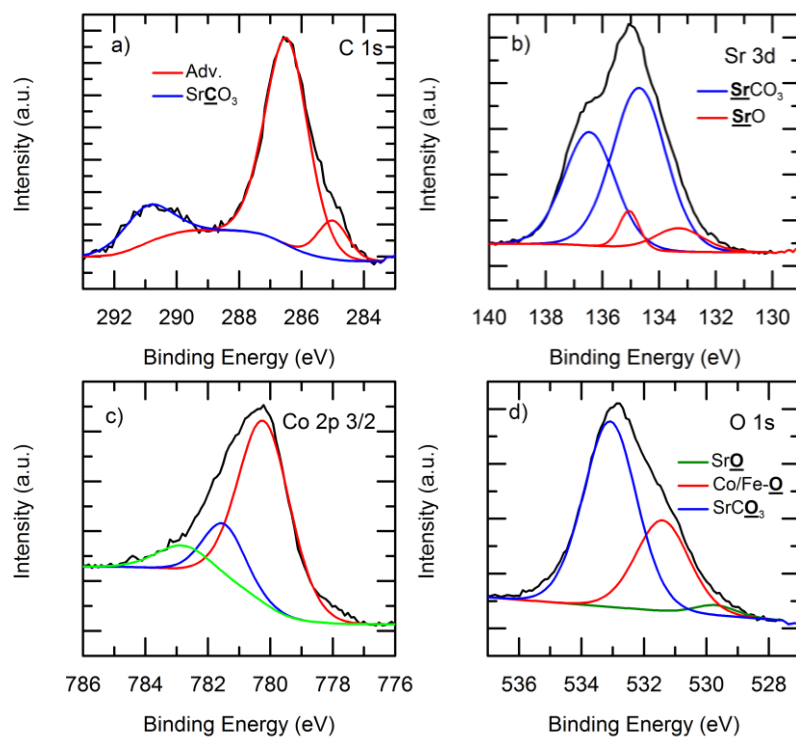


Figure D.4. XPS spectra and fitted peaks for the 1%Sc-SCO sample. a) Spectra of the carbon 1s peak. b) Spectra of the strontium 3d 5/2 and 3/2 peaks. c) Spectra of the cobalt 2p peak. d) Spectra of the oxygen 1s peak.

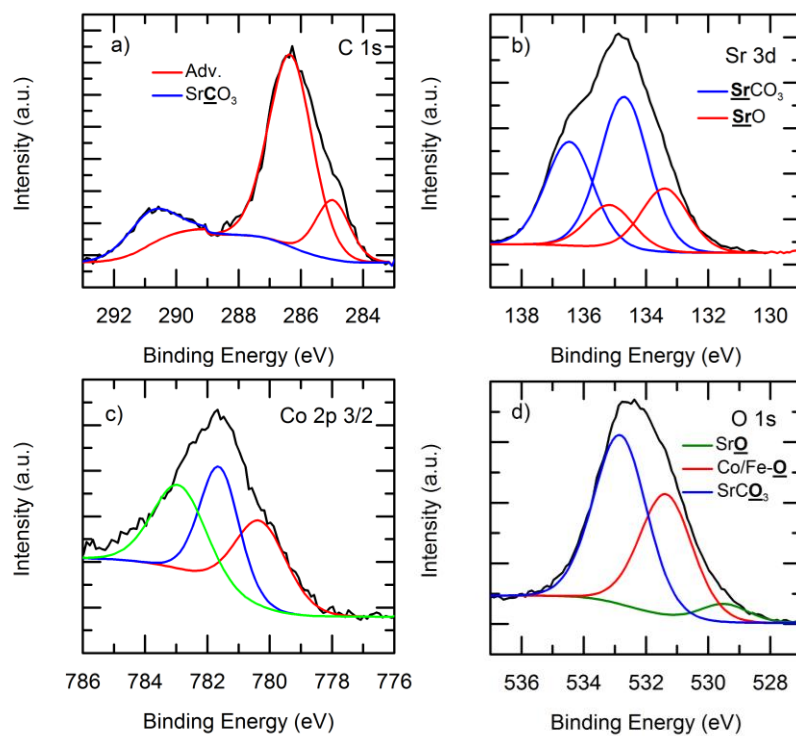


Figure D.5. XPS spectra and fitted peaks for the 5%Sc-SCO sample. a) Spectra of the carbon 1s peak. b) Spectra of the strontium 3d 5/2 and 3/2 peaks. c) Spectra of the cobalt 2p peak. d) Spectra of the oxygen 1s peak.

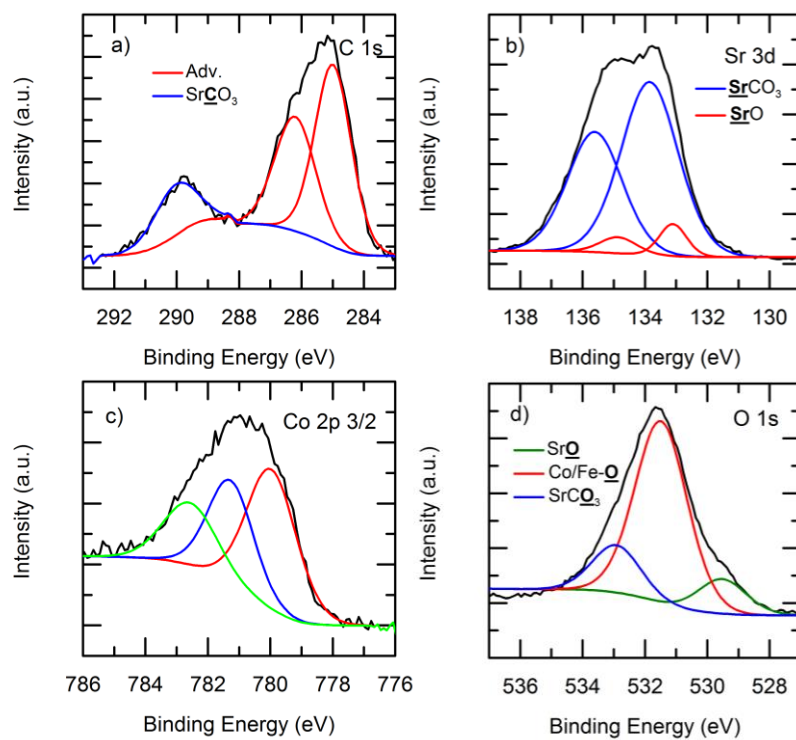


Figure D.6. XPS spectra and fitted peaks for the 10%Sc-SCO sample. a) Spectra of the carbon 1s peak. b) Spectra of the strontium 3d 5/2 and 3/2 peaks. c) Spectra of the cobalt 2p peak. d) Spectra of the oxygen 1s peak.

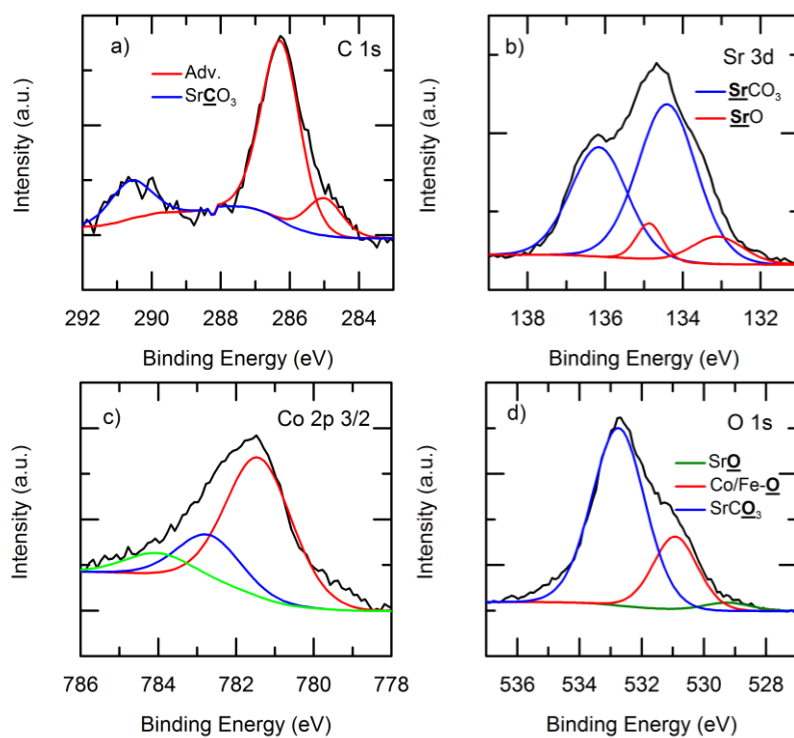


Figure D.7. XPS spectra and fitted peaks for the UnSCO sample. a) Spectra of the carbon 1s peak. b) Spectra of the strontium 3d 5/2 and 3/2 peaks. c) Spectra of the cobalt 2p peak. d) Spectra of the oxygen 1s peak.

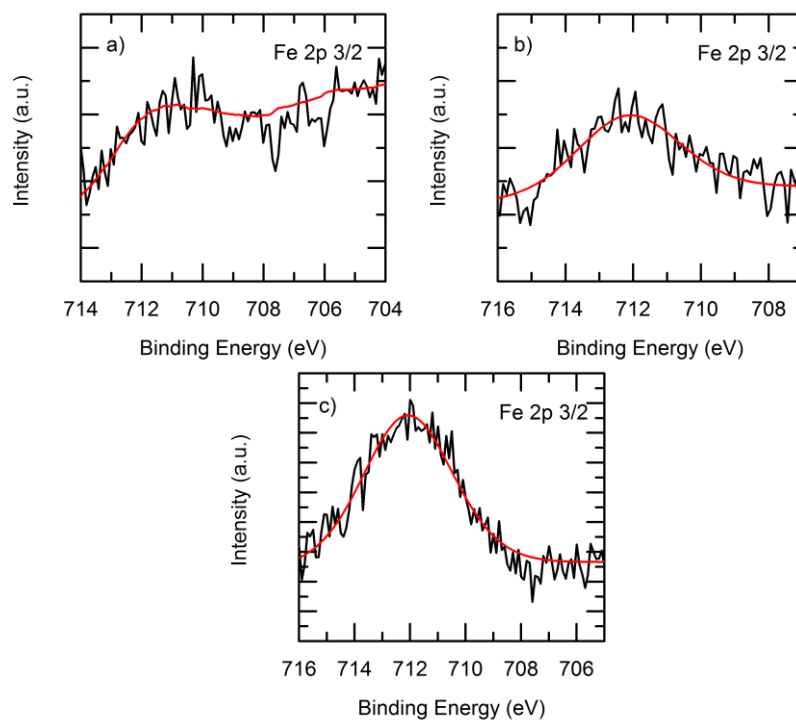


Figure D.8. XPS spectra and fitted peaks for the Fe 2p $3/2$ peaks of the Fe-SCO samples.
a) 1%Fe-SCO b) 5%Fe-SCO c) 10%Fe-SCO

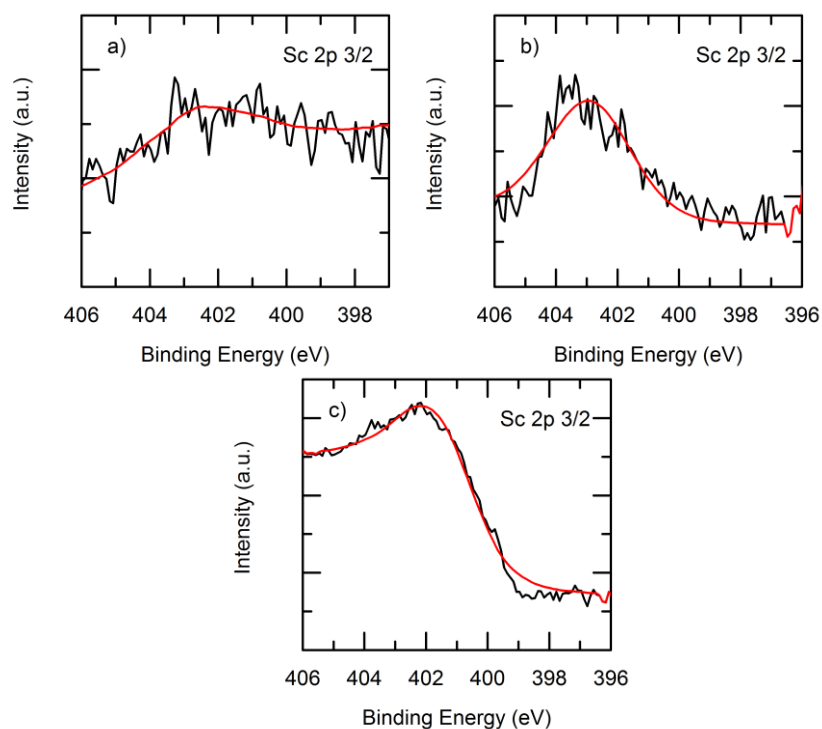


Figure D.9. XPS spectra and fitted peaks for the Sc 2p 3/2 peaks of the Sc-SCO samples.
a) 1%Sc-SCO b) 5%Sc-SCO c) 10%Sc-SCO

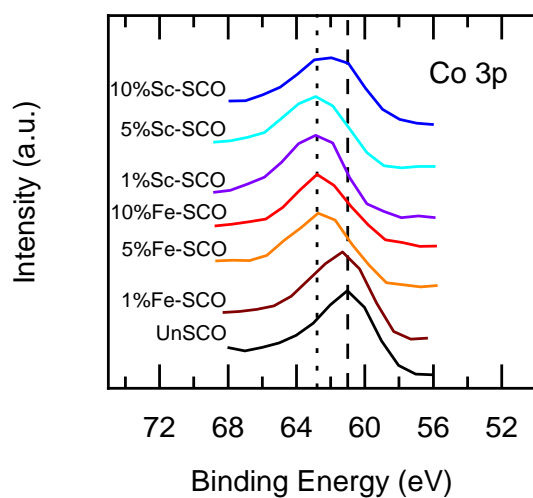


Figure D.10. XPS spectra of the Co 3p region in all SCO samples. The dashed line lies on 61.0 eV, the dotted line lies on 62.8 eV

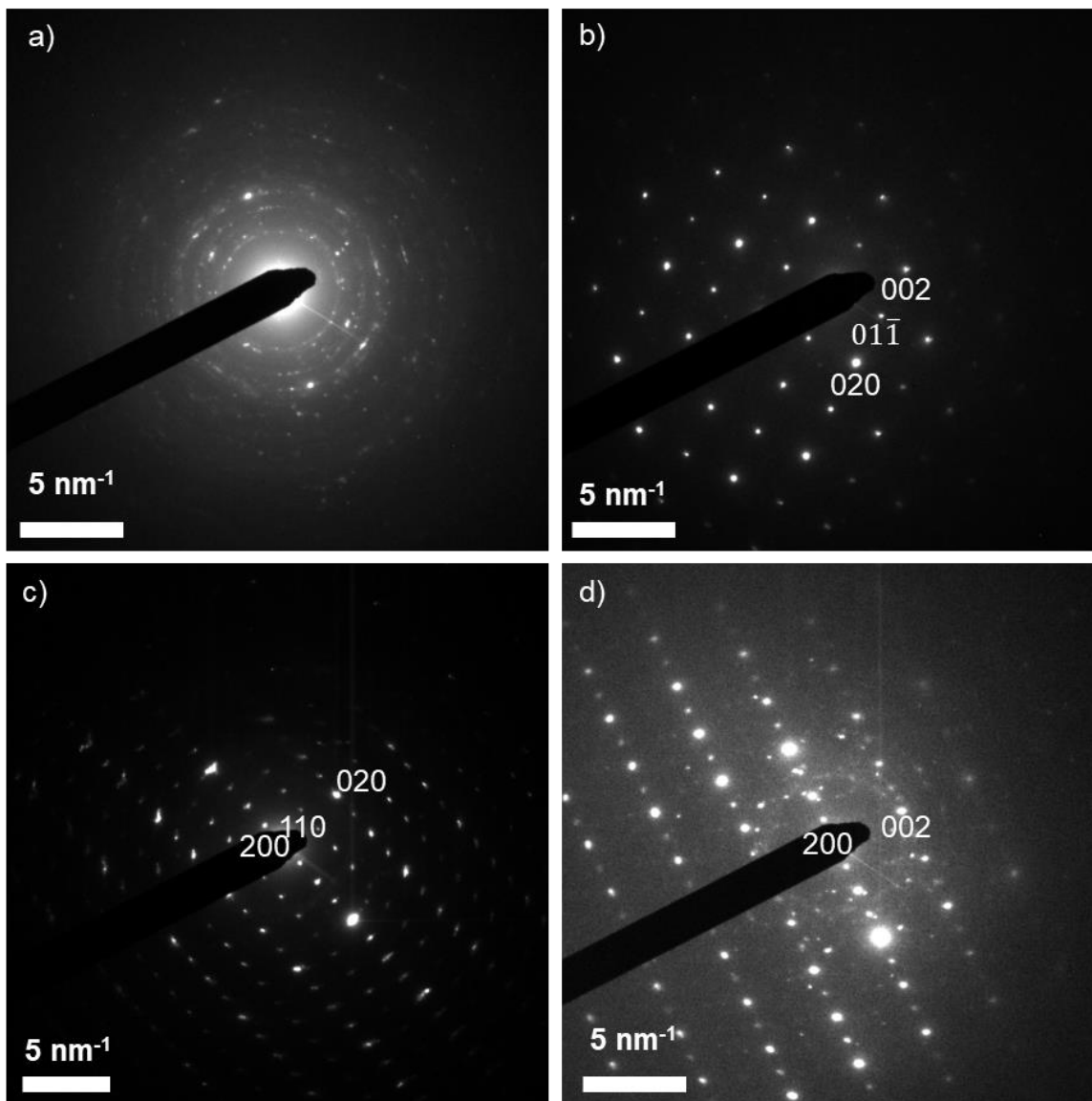


Figure D.11. Selected area electron diffraction patterns of a) undoped-SCO, b) 5%Fe-SCO, c) 10%Fe-SCO), and d) 10% Sc-SCO showing the polycrystalline nature of the undoped material. The other diffraction patterns have been indexed as orthorhombic $\text{SrCoO}_{2.5}$

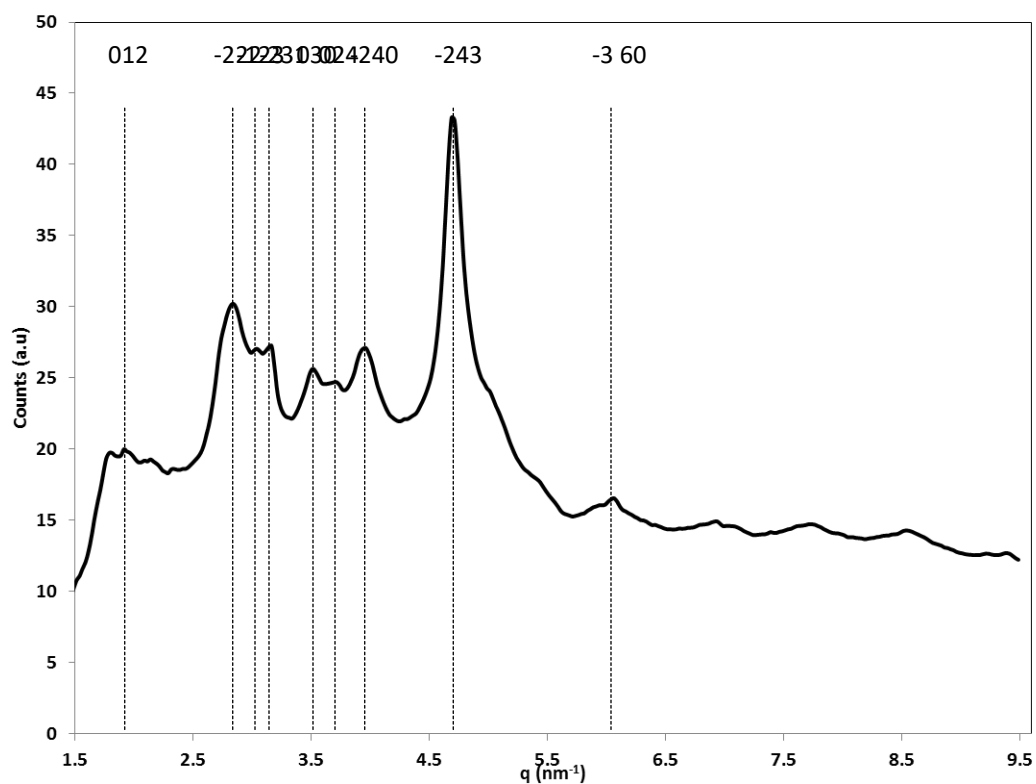


Figure D.12. Radial distribution plot of the SAED in Figure D.X1 for undoped-SCO integrated over 360° indexed as trigonal $\text{Sr}_6\text{Co}_5\text{O}_{15}$.

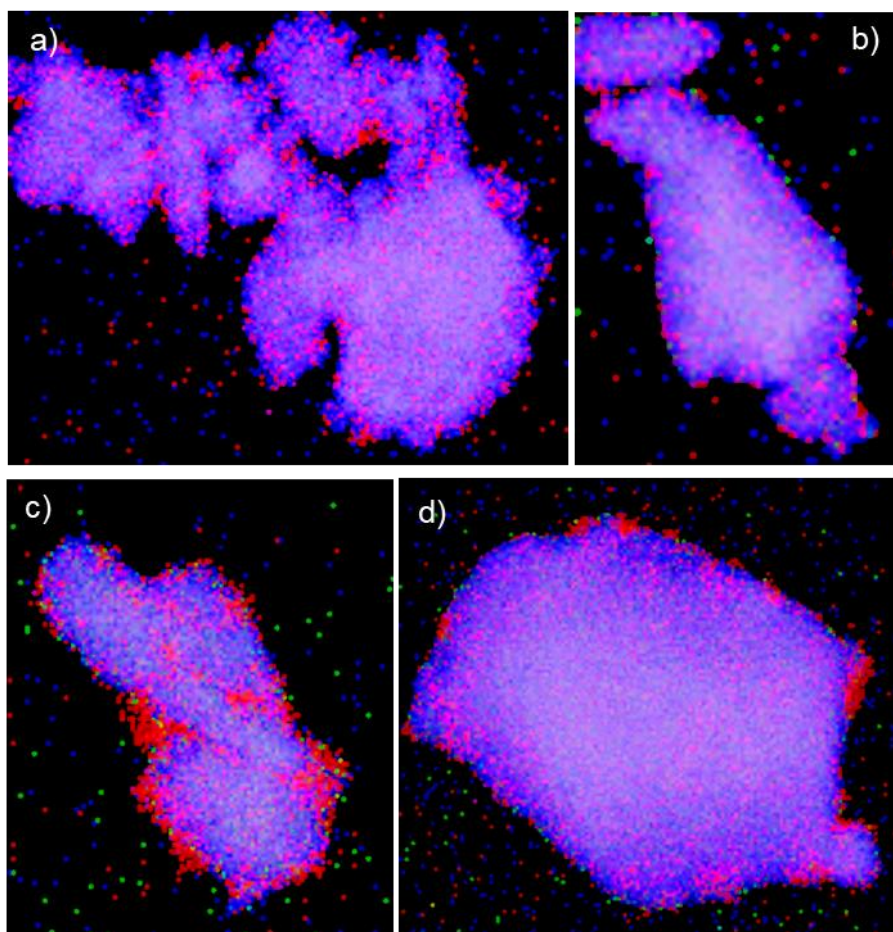


Figure D.13. Electron dispersive X-ray spectroscopy maps of a) UnSCO, b) 5%Fe-SCO, c) 10%Fe-SCO, and d) 10% Sc-SCO. Cobalt is blue, strontium is red, and the dopant (Fe or Sc) is green

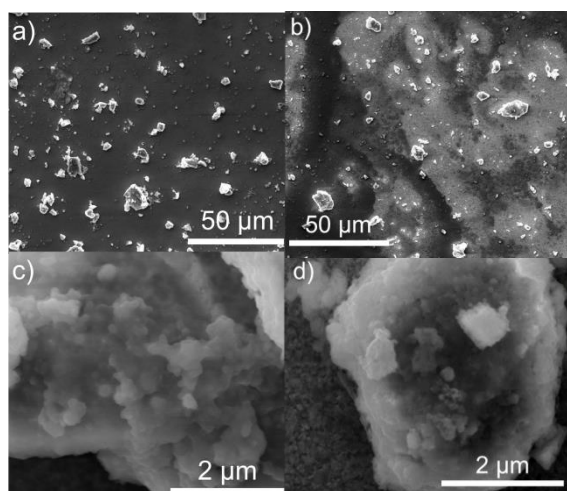


Figure D.14. SEM images of a) 10%Fe-SCO and b) undoped SCO microparticle catalyst on conductive FTO substrate. Surface morphology for the c) 10%Fe-SCO and d) undoped SCO microparticles both appear rough, and composed of sintered microparticles.

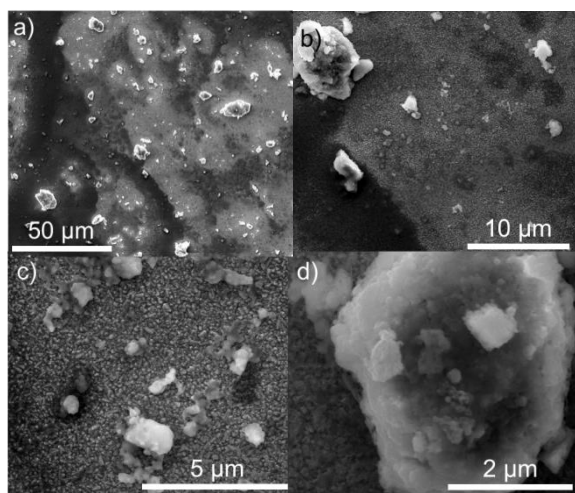


Figure D.15. SEM images of UnSCO Electrode

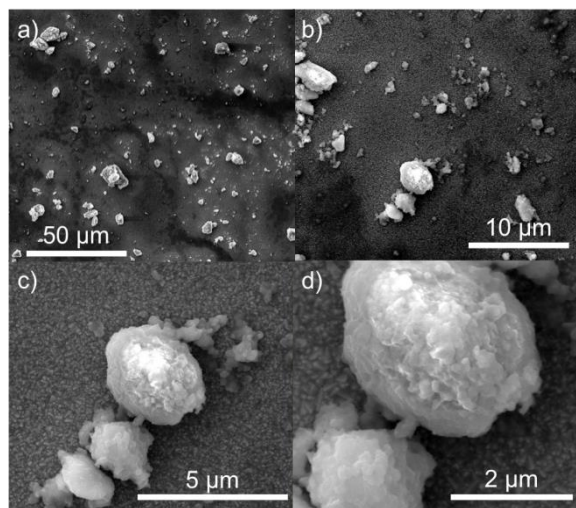


Figure D.16. SEM images of 1%Fe-SCO Electrode

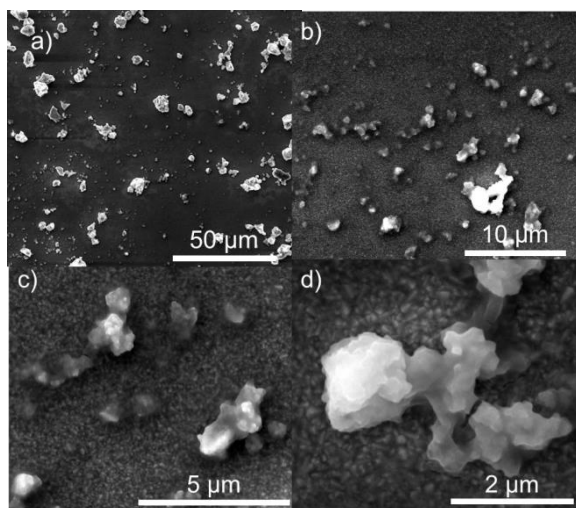


Figure D.17. SEM images of 5%Fe-SCO Electrode

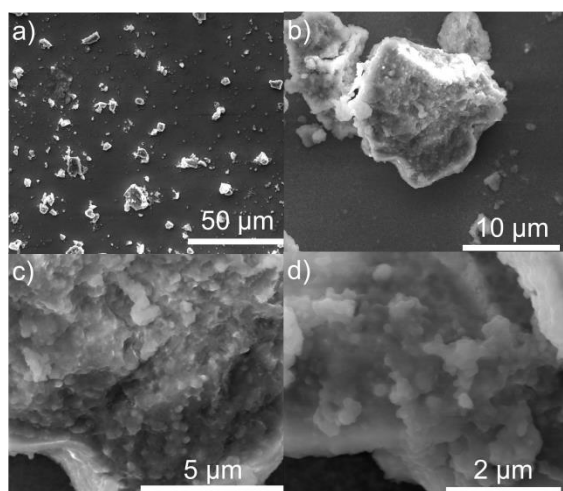


Figure D.18. SEM images of 10%Fe-SCO Electrode

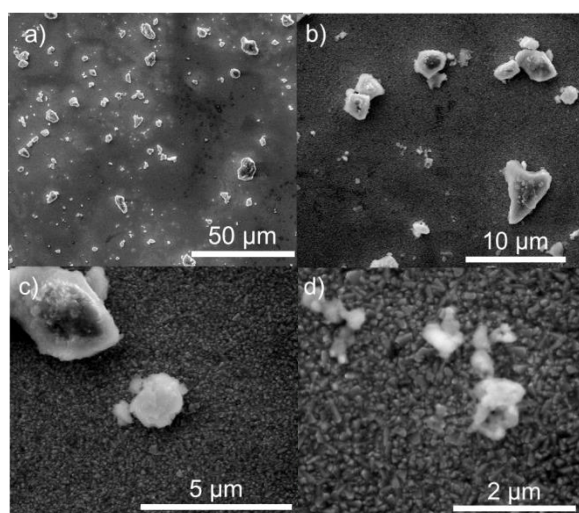


Figure D.19. SEM images of 1%Sc-SCO Electrode

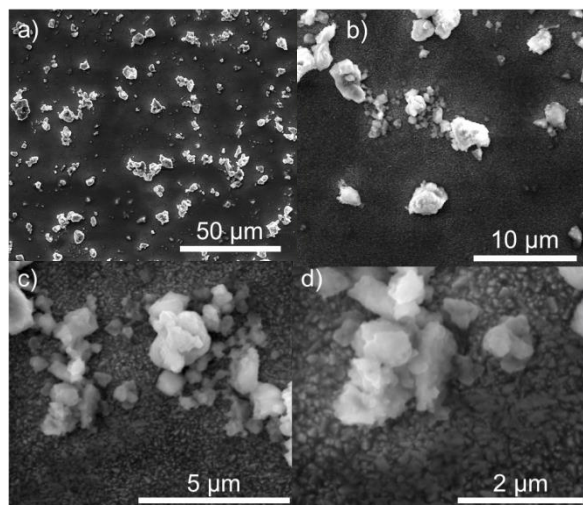


Figure D.20. SEM images of 5%Sc-SCO Electrode

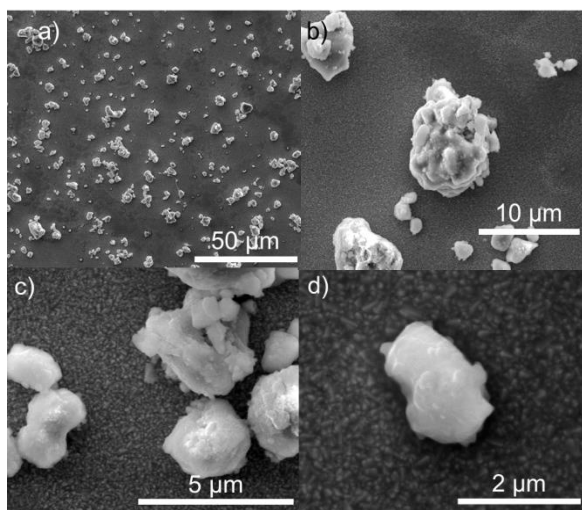


Figure D.21. SEM images of 10%Sc-SCO Electrode

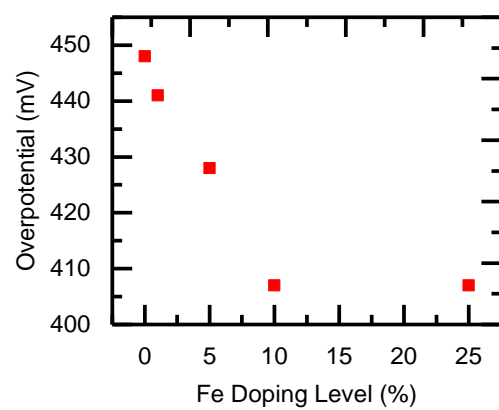


Figure D.22. Plot of measured overpotential at 10 mA/cm² versus [Fe] in several Fe-doped SCO electrodes

Appendix E: Supporting Information for Chapter 8

E.1 FIGURES

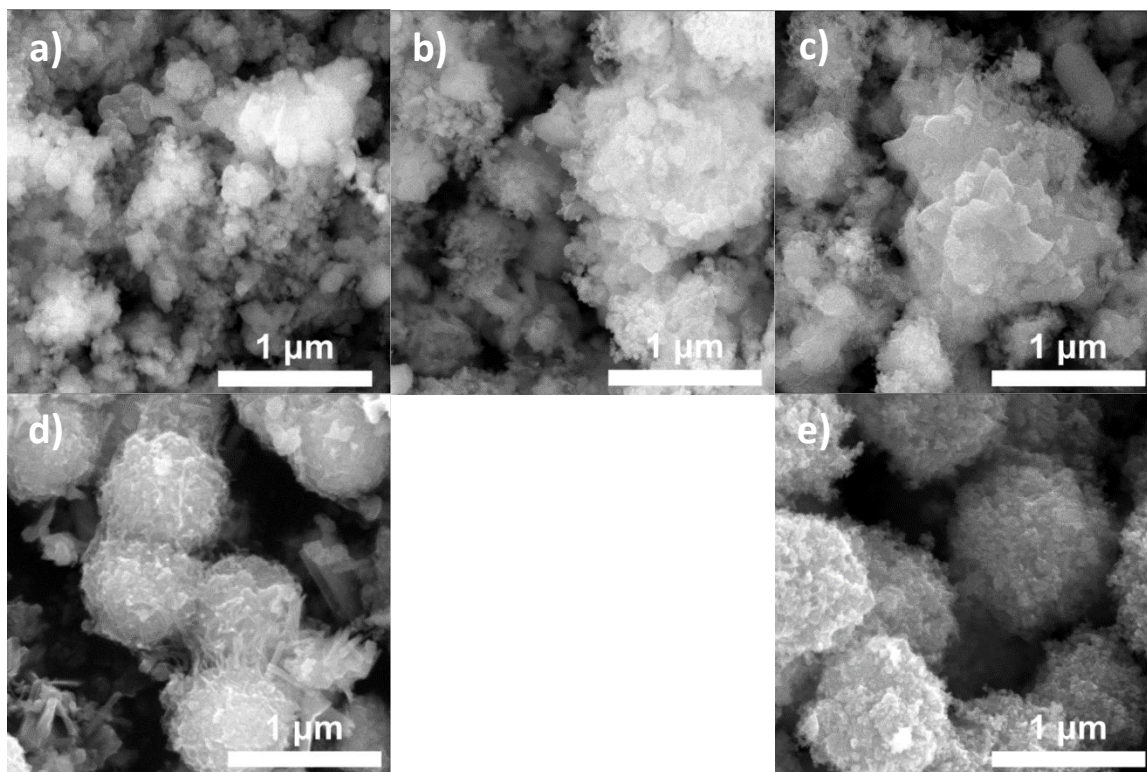


Figure E.1: Higher-magnification SEM images of a) NiS_{100} , b) $\text{NiS}_{10}\text{Se}_{10}$, c) $\text{NiS}_{75}\text{Se}_{25}$, d) $\text{NiS}_{50}\text{Se}_{50}$, and e) NiSe_{100} NiSSe composite materials. All materials show primarily spherical particle-like morphologies, with particle size tending to increase as Se-content increases, ultimately resulting in roughly 1 micron-diameter microspheres of NiSe material for the NiSe_{100} composite.

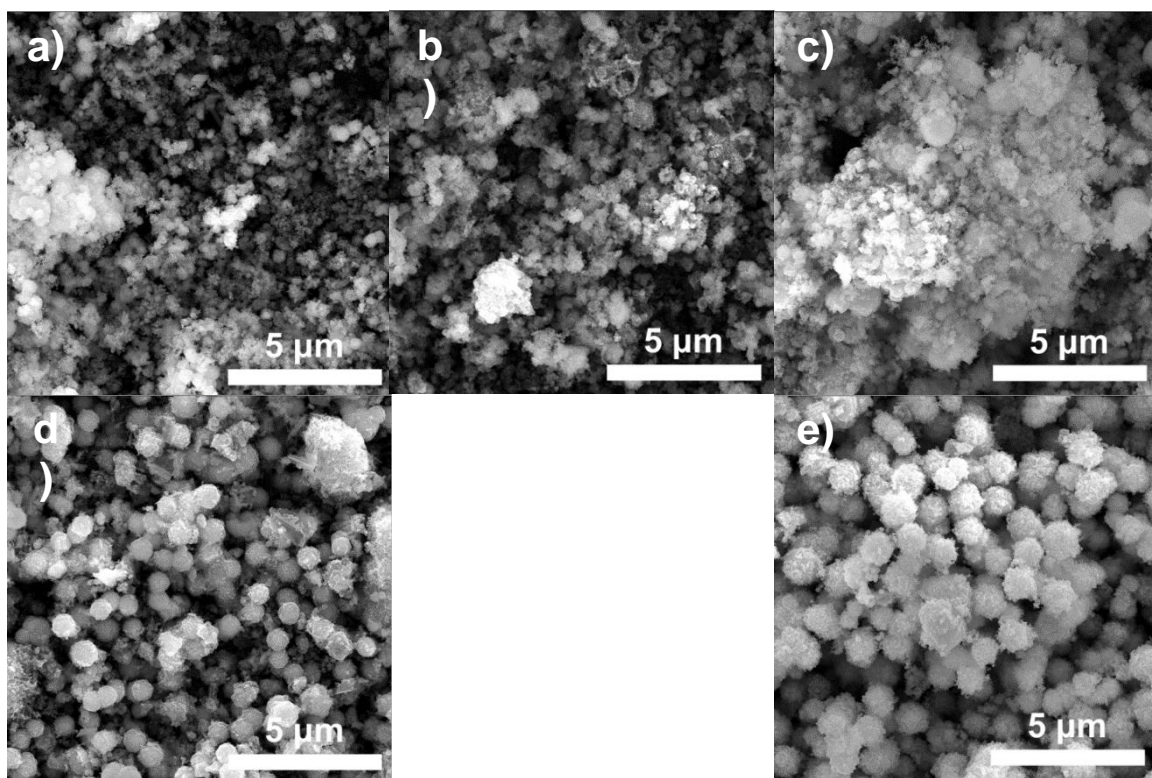


Figure E.2: Lower-magnification SEM images of a) NiS_{100} , b) $\text{NiS}_{10}\text{Se}_{10}$, c) $\text{NiS}_{75}\text{Se}_{25}$, d) $\text{NiS}_{50}\text{Se}_{50}$, and e) NiSe_{100} NiSSe composite materials. S-rich composites tend to show larger polydispersity in particle size, frequently forming micron-scale agglomerates from much smaller particles. The Se-rich materials tend to be composed of much more uniform particles.

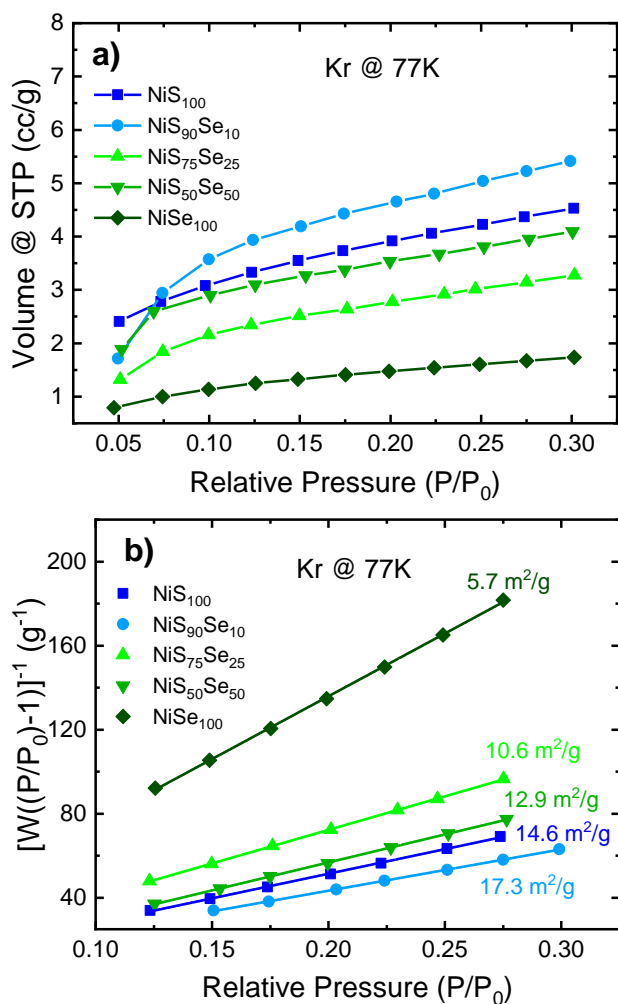


Figure E.3: a) Krypton uptakes at 77K over the classical BET relative pressure range and b) the resulting multi-point BET plot for extraction of surface area from adsorption analysis by linear regression (solid lines), with all samples showing excellent fits ($r > 0.9998$).

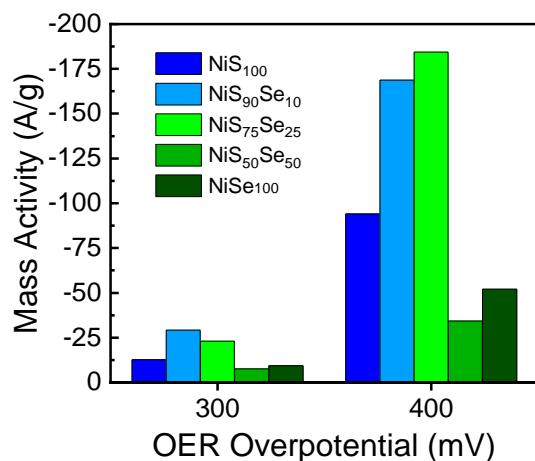


Figure E.4: Mass activity of NiS_xSe_y composites measured at 300 mV and 400 mV of overpotential. A total catalyst mass of 48 μ g was used for all measurements.

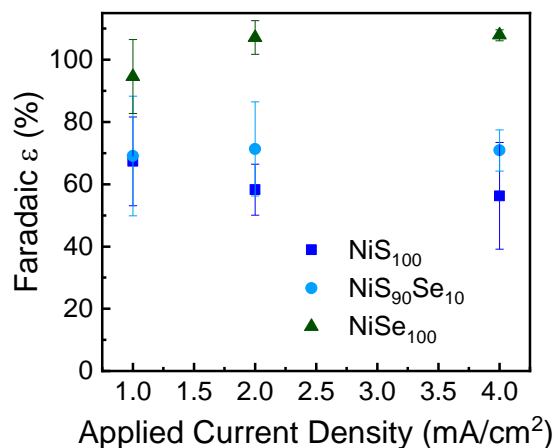


Figure E.5: RRDE-derived Faradaic efficiency of NiS₁₀₀, NiS₉₀Se₁₀, and NiSe₁₀₀ electrocatalysts over a range of applied current densities. All measurements were performed in Ar-sparged 0.1M KOH solution at a rotation rate of 1600 rpm. The Pt ring electrode was held at 0.435V vs. RHE while the glassy carbon disk was held at 1.0, 2.0, and 4.0 mA/cm².

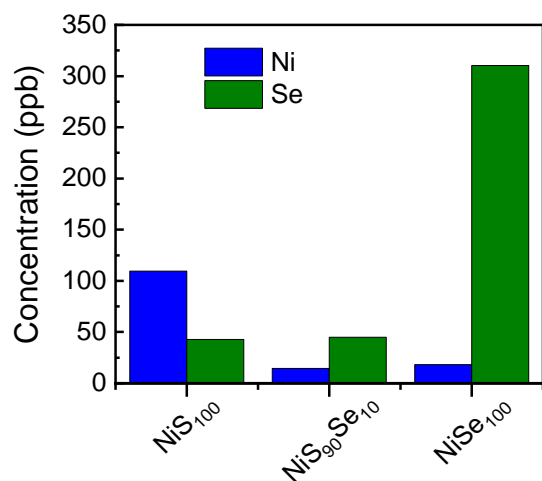


Figure E.6: Dissolved Ni and Se content of 1 M KOH electrolyte solution for after 6 hours of OER electrocatalysis at 10 mA/cm^2 using NiS₁₀₀, NiS₉₀Se₁₀, and NiSe₁₀₀. The addition of Se to the composite correlates to reduced Ni dissolution with OER testing.

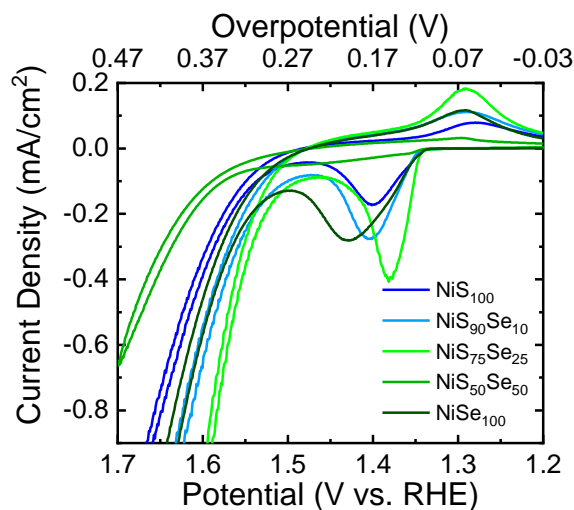


Figure E.7: CVs of the NiSSe composites performed in 1M KOH solution, with OER-derived current normalized by BET surface areas to better determine the intrinsic performance of each material. Here, the NiS₇₅Se₂₅ composite shows superior performance. All measurements were made vs a Pt counter electrode using an Ag/AgCl(sat'd KCl) reference electrode, using a 20 mV/s sweep rate.

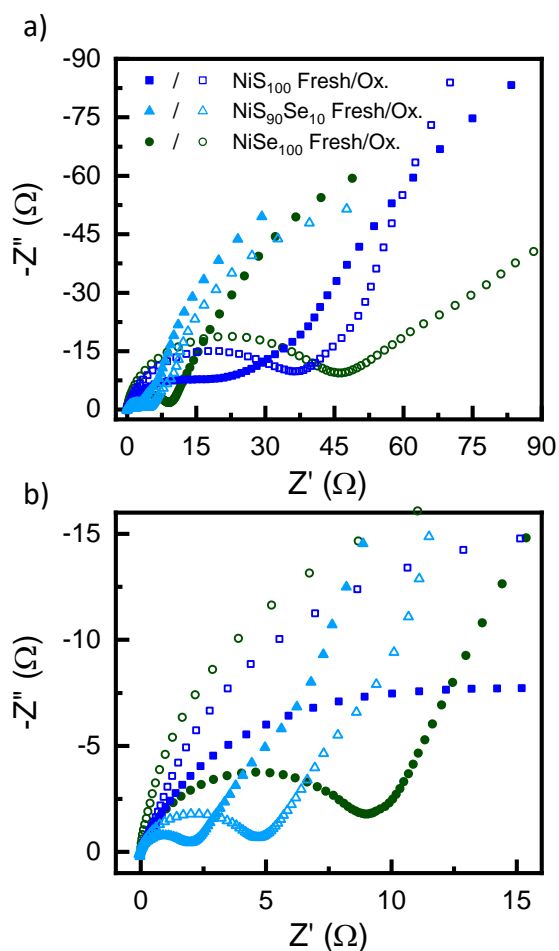


Figure E.8: Full (a) and low-Ohm region (b) EIS spectra of NiS_{100} , $\text{NiS}_{90}\text{Se}_{10}$, and NiSe_{100} electrocatalysts before (fresh) and after electrochemical surface oxidation (ox.), recorded from 0.1Hz to 100kHz at 1.52V vs. RHE. Se-containing samples show the lowest R_{CT} prior to oxidation, while the $\text{NiS}_{90}\text{Se}_{10}$ sample shows the lowest R_{CT} after testing at 10 mA/cm^2 for 30 minutes, indicating increased resistance to oxidation compared to pure S and Se materials. Samples were tested in a 1M KOH solution with a Pt wire counter electrode and an Ag/AgCl (sat'd KCl) reference electrode.

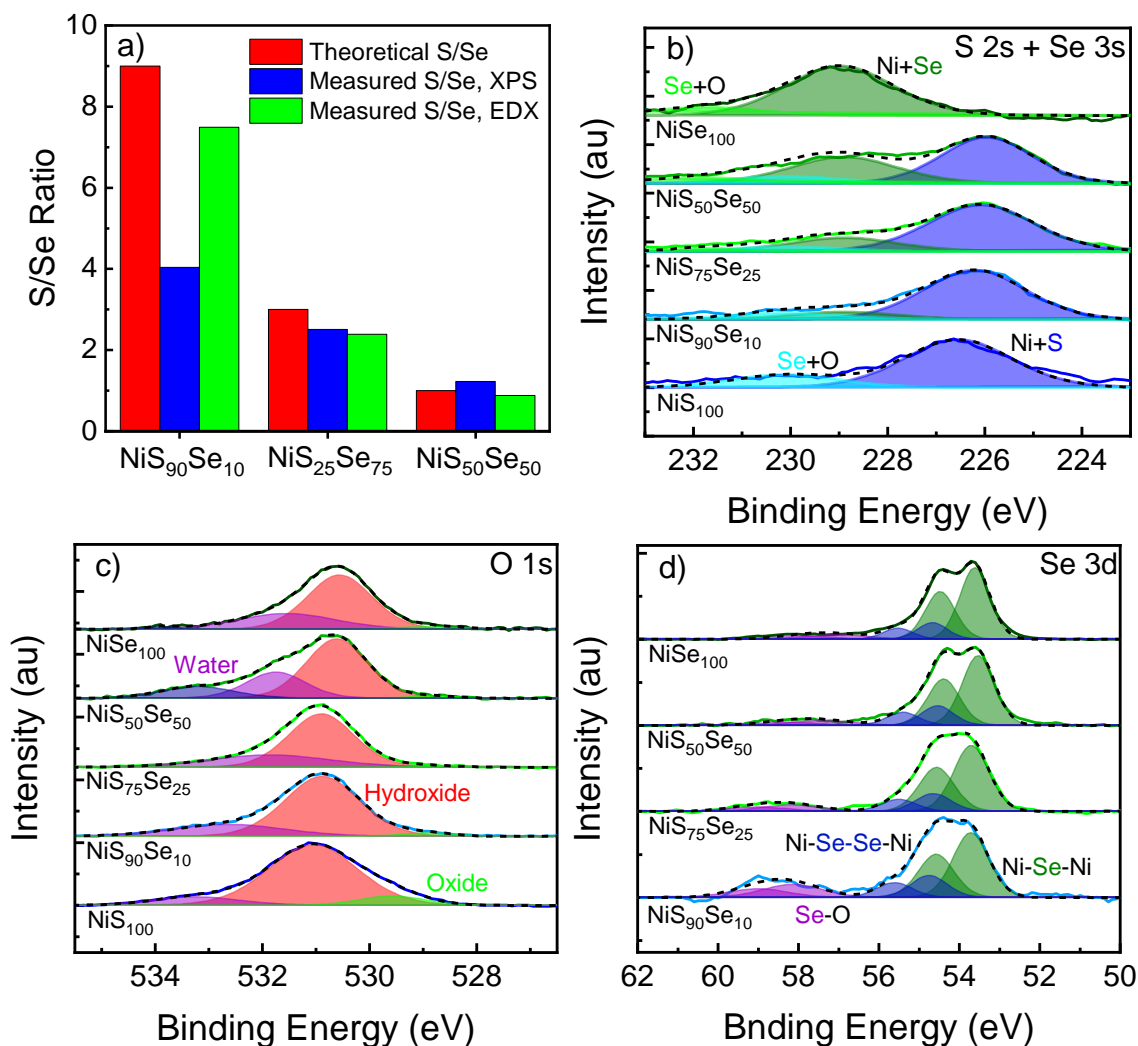


Figure E.9: a) Relative ratio of S/Se calculated from the fitted peaks in (b) and from EDX measurements made during SEM, indicating generally good agreement between the theoretical quantity of each species and the measured quantity. The NiS₉₀Se₁₀ S/Se ratio from XPS may be skewed due to preferential oxidation of S at the surface, as indicated by the higher value when measured using EDX. b) S 2s and Se 3s region for all NiSSe composites, showing fitted peaks for Ni-S, Ni-Se, and oxidized chalcogen species. c) O 1s region for all NiSSe composites, showing the surface oxygen species are primarily OH⁻, with small quantities of NiO_x present at high Se-contents, as well as several adsorbed water peaks. d) Se 3d spectra for all NiSSe composites, showing peak fits for the monoselenide (green), di-selenide (blue), and oxidized selenium (purple) species.

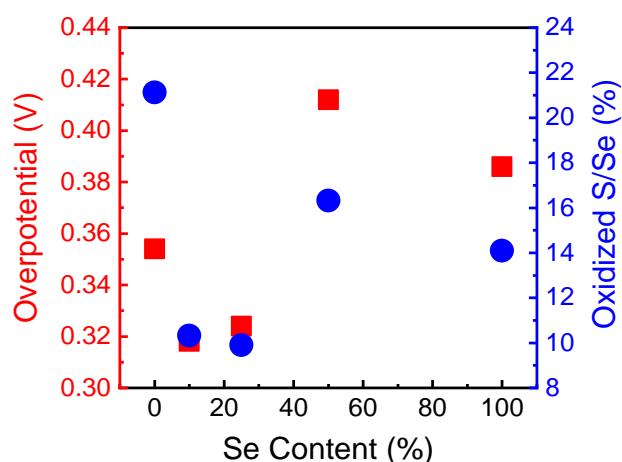


Figure E.11: Comparison of the observed overpotential at 10 mA/cm^2 for each composite (red) with the percentage of oxidized S or Se (blue). This shows that as the Se content increases in S-rich materials, the amount of oxidized chalcogen and the overpotential both decrease in a similar fashion.

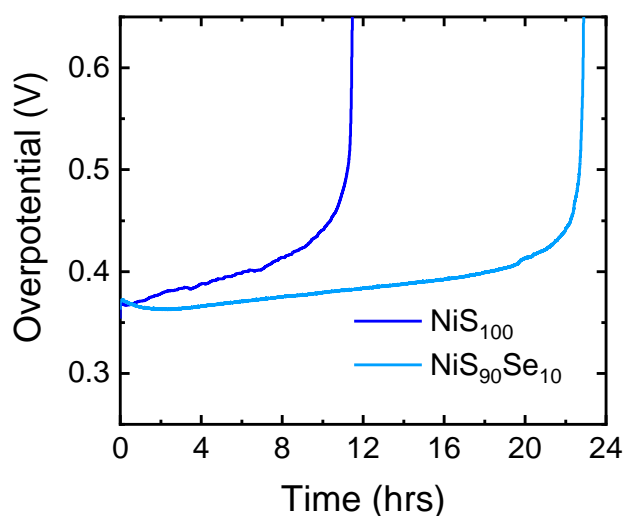


Figure E.12: Chronoamperogram of the NiS₁₀₀ and NiS₉₀Se₁₀ composites at 10 mA/cm^2 until material failure, as indicated by the sharp increase in overpotential, showing the superior stability of the Se-incorporated material. The experiments were performed versus a Pt counter electrode with an Ag/AgCl(sat'd KCl) reference electrode, with N₂ sparging to remove accumulated bubbles.

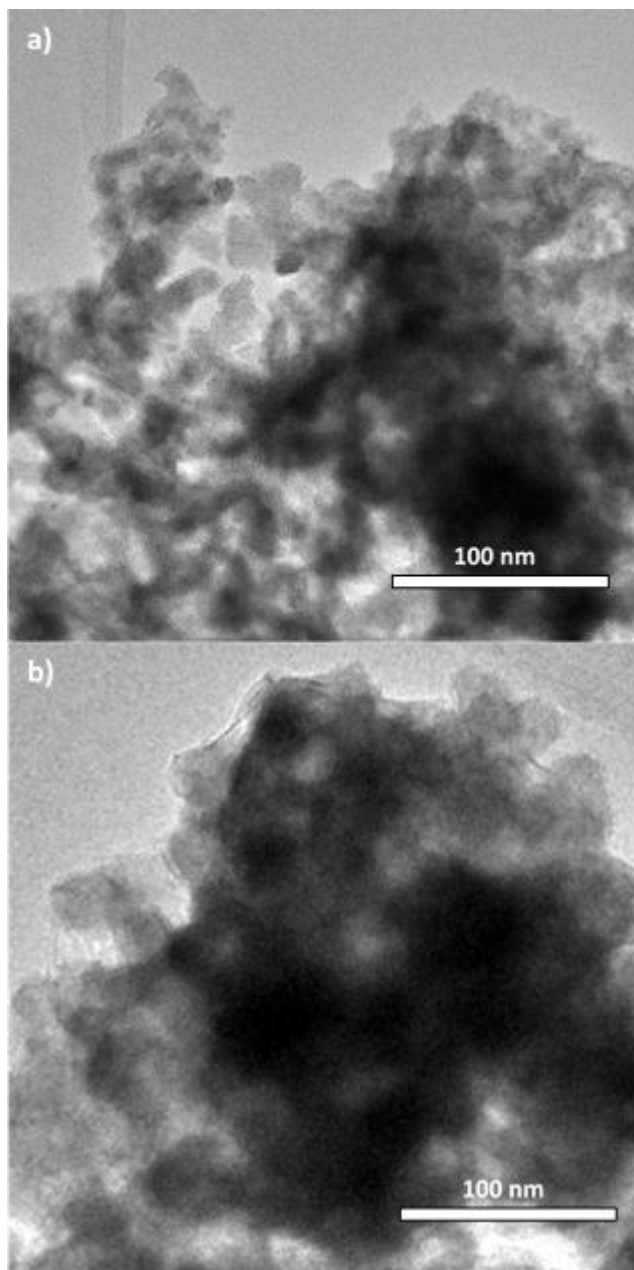


Figure E.13: TEM images of a) NiS_{100} and b) $\text{NiS}_{90}\text{Se}_{10}$ as-synthesized, showing that both materials appear to be agglomerates composed of smaller nanoparticles.

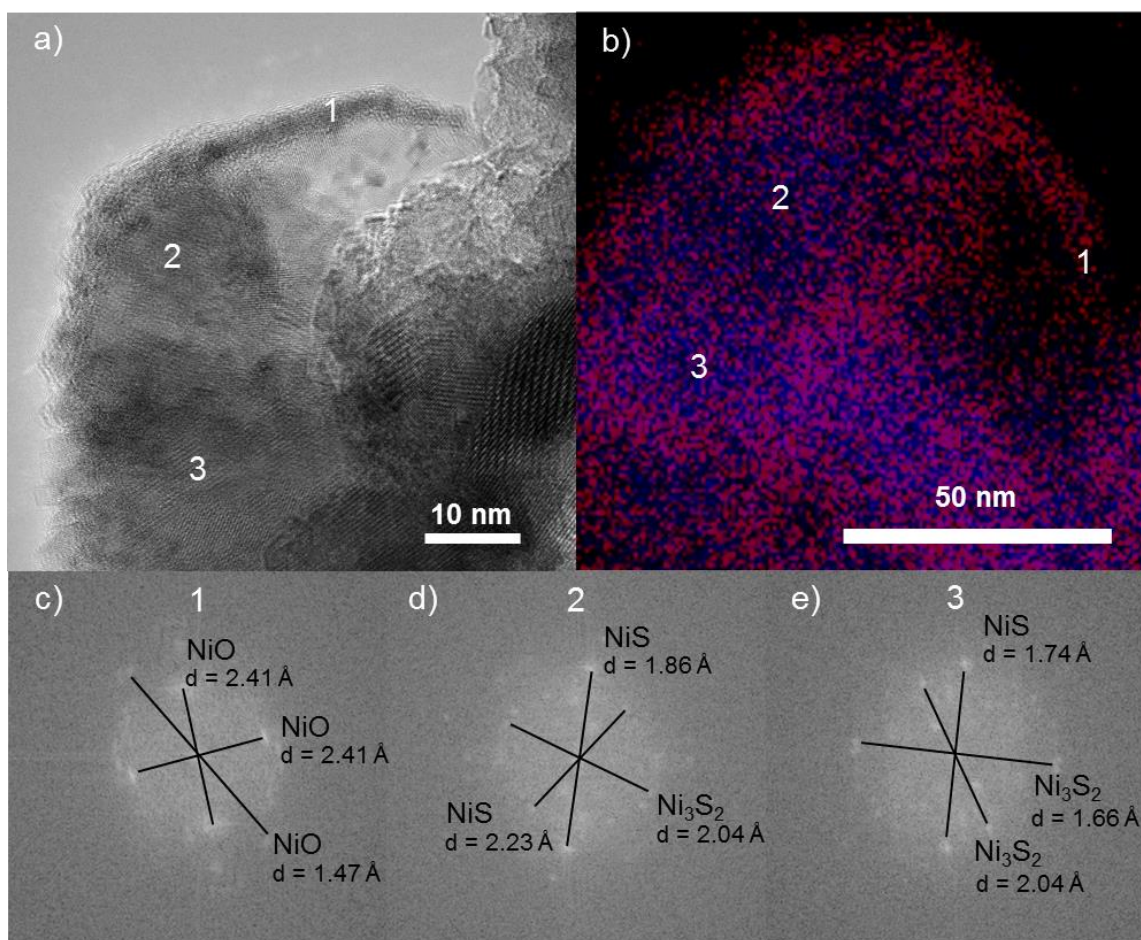


Figure E.14: a) HRTEM image of as-synthesized NiS_{100} and b) an EDX map of Ni and O from the same region demonstrating the large degree of oxidation natively present at the surface of this material. FFT from the oxidized surface shows d-spacing corresponding to NiO (c), while FFT from the interior of the particle corresponds to NiS and Ni_3S_2 (d,e).

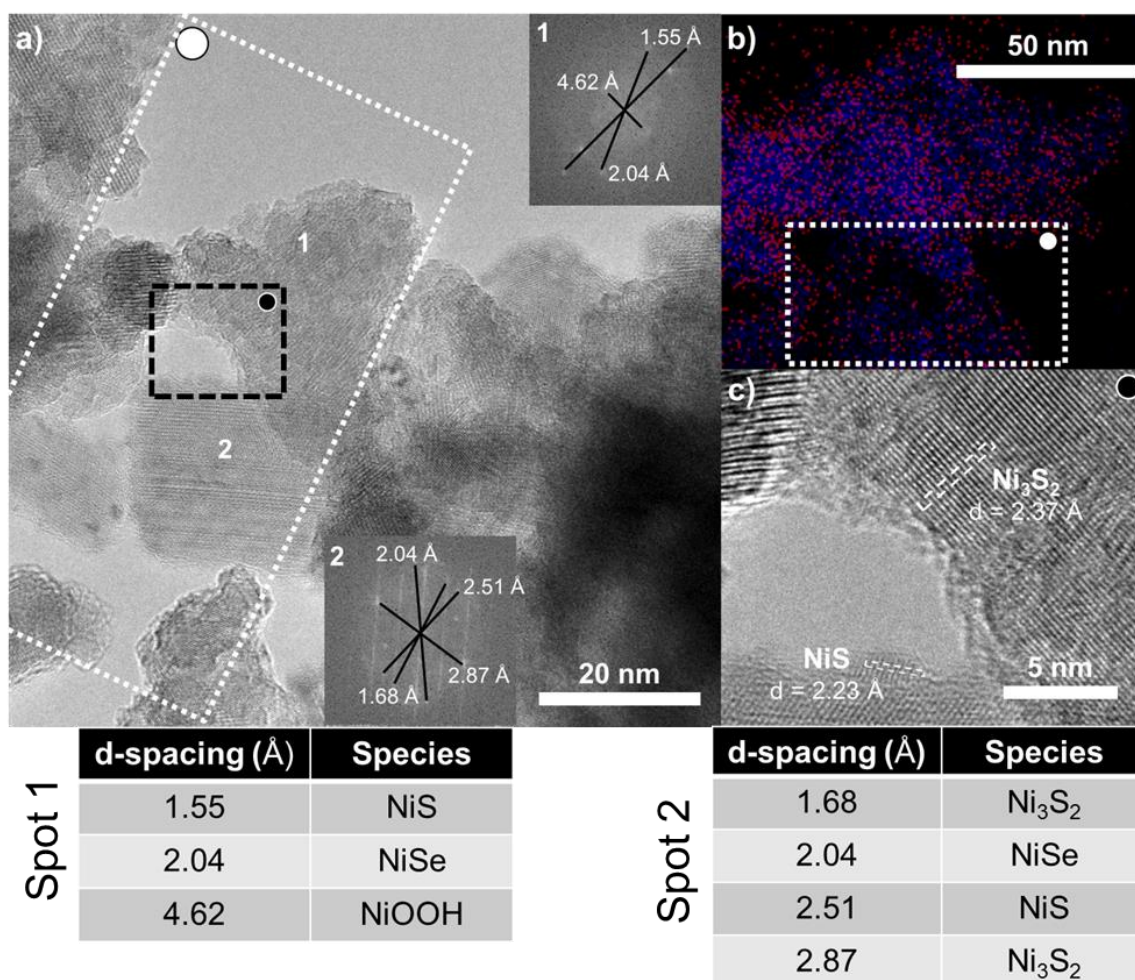


Figure E.15: a) HRTEM image of as-synthesized NiS₉₀Se₁₀ and b) an EDX map of Ni and O from the region within the white box, demonstrating a small degree of oxidation is natively present on the surface of the material. FFT from Spot 1 shows d-spacings corresponding to NiSe, NiS, and some NiOOH, while FFT from Spot 2 shows primarily metal chalcogenide character. Lattice fringes from the area inside the black box (c) can be indexed to Ni₃S₂ and NiS, in agreement with the FFT. There appears to be relatively little amorphous oxide/hydroxide on this sample, and the metal chalcogenide lattice extends to the surface of the particle.

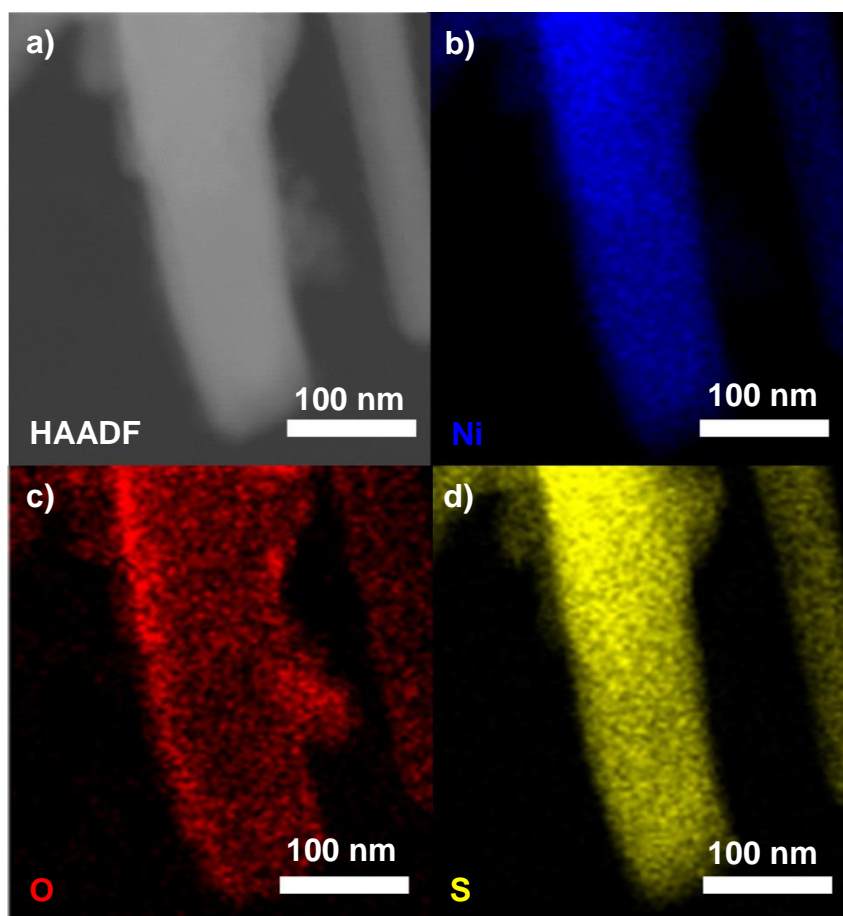


Figure E.16: a) HAADF image of the NiS_{100} composite after OER testing, with corresponding EDX maps for b) Ni, c) O, and d) S. There is a roughly 20 nm-thick layer of O-rich material surrounding the NiS_{100} material, and both Ni and S are evenly distributed in the interior.

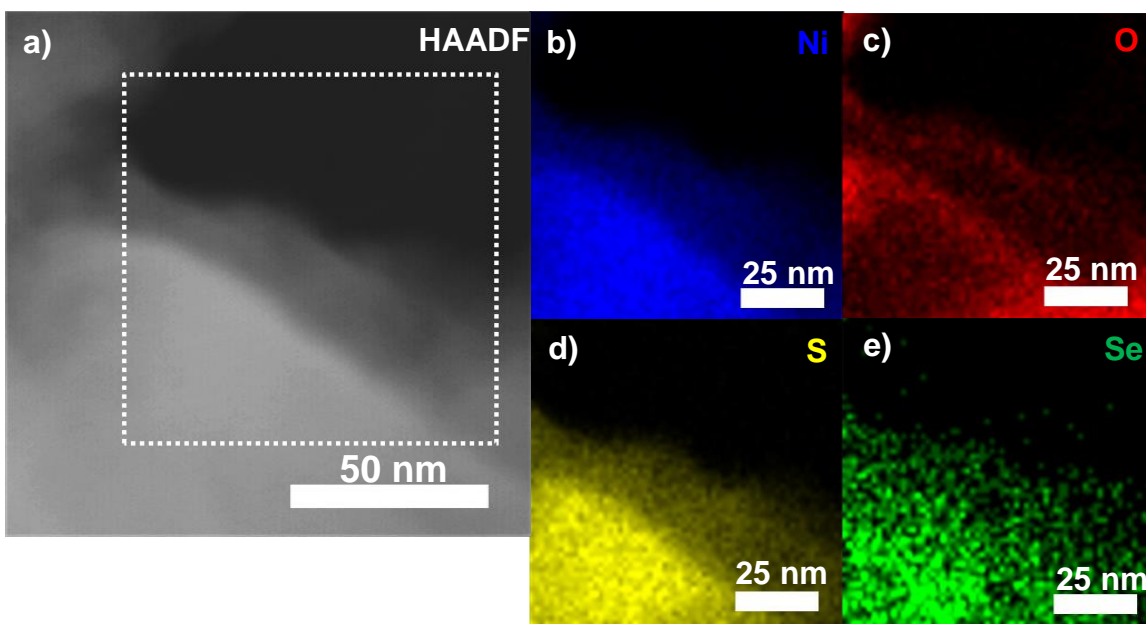


Figure E.17: a) HAADF image of the $\text{NiS}_{90}\text{Se}_{10}$ composite after OER testing, with corresponding EDX maps for b) Ni, c) O, d) S, and e) Se. There is a roughly 10 nm-thick layer of O-rich material surrounding the $\text{NiS}_{90}\text{Se}_{10}$ material, and what appears to be multiple planes of material, as evidenced by multiple O-rich edges. Ni, S, and Se appear to be evenly mixed in the particle.

E.2 REFERENCES

- (1) Persson, K. A.; Waldwick, B.; Lazic, P.; Ceder, G. Prediction of Solid-Aqueous Equilibria: Scheme to Combine First-Principles Calculations of Solids with Experimental Aqueous States. *Phys. Rev. B - Condens. Matter Mater. Phys.* **2012**, 85 (23), 1–12. <https://doi.org/10.1103/PhysRevB.85.235438>.
- (2) Jain, A.; Ong, S. P.; Hautier, G.; Chen, W.; Richards, W. D.; Dacek, S.; Cholia, S.; Gunter, D.; Skinner, D.; Ceder, G.; Persson, K.A. Commentary: The Materials Project: A Materials Genome Approach to Accelerating Materials Innovation. *APL Mater.* **2013**, 1 (1), 011002. <https://doi.org/10.1063/1.4812323>.
- (3) Singh, A. K.; Zhou, L.; Shinde, A.; Suram, S. K.; Montoya, J. H.; Winston, D.; Gregoire, J. M.; Persson, K. A. Electrochemical Stability of Metastable Materials. *Chem. Mater.* **2017**, 29 (23), 10159–10167. <https://doi.org/10.1021/acs.chemmater.7b03980>.

Works Cited

- Akbulatov, A. F.; Frolova, L. A.; Griffin, M. P.; Gearba, I. R.; Dolocan, A.; Vanden Bout, D. A.; Tsarev, S.; Katz, E. A.; Shestakov, A. F.; Stevenson, K. J.; et al. Effect of Electron-Transport Material on Light-Induced Degradation of Inverted Planar Junction Perovskite Solar Cells. *Adv. Energy Mater.* 2017, 7 (19), 1700476. <https://doi.org/10.1002/aenm.201700476>.
- Annual Energy Outlook 2020 with projections to 2050 www.eia.gov/aeo (accessed Apr 2, 2020).
- Antao, S. M.; Hassan, I. The Orthorhombic Structure of CaCO_3 , SrCO_3 , PbCO_3 and BaCO_3 : Linear Structural Trends. *Can. Mineral.* 2009, 47, 1245–1255.
- Batchellor, A. S.; Boettcher, S. W. Pulse-Electrodeposited Ni-Fe (Oxy)Hydroxide Oxygen Evolution Electrocatalysts with High Geometric and Intrinsic Activities at Large Mass Loadings. *ACS Catal.* 2015, 5 (11), 6680–6689. <https://doi.org/10.1021/acscatal.5b01551>.
- Beal, R. E.; Slotcavage, D. J.; Leijtens, T.; Bowering, A. R.; Belisle, R. A.; Nguyen, W. H.; Burkhard, G. F.; Hoke, E. T.; McGehee, M. D. Cesium Lead Halide Perovskites with Improved Stability for Tandem Solar Cells. *J. Phys. Chem. Lett.* 2016, 7 (5), 746–751. <https://doi.org/10.1021/acs.jpclett.6b00002>.
- Belisle, R. A.; Bush, K. A.; Bertoluzzi, L.; Gold-Parker, A.; Toney, M. F.; McGehee, M. D. Impact of Surfaces on Photoinduced Halide Segregation in Mixed-Halide Perovskites. *ACS Energy Lett.* 2018, 3 (11), 2694–2700. <https://doi.org/10.1021/acsenenergylett.8b01562>.
- Benck, J. D.; Hellstern, T. R.; Kibsgaard, J.; Chakthranont, P.; Jaramillo, T. F. Catalyzing the Hydrogen Evolution Reaction (HER) with Molybdenum Sulfide Nanomaterials. *ACS Catal.* 2014, 4 (11), 3957–3971. <https://doi.org/10.1021/cs500923c>.
- Biesinger, M. C.; Payne, B. P.; Grosvenor, A. P.; Lau, L. W. M.; Gerson, A. R.; Smart, R. S. C. Resolving Surface Chemical States in XPS Analysis of First Row Transition Metals, Oxides and Hydroxides: Cr, Mn, Fe, Co and Ni. *Appl. Surf. Sci.* 2011, 257 (7), 2717–2730. <https://doi.org/10.1016/j.apsusc.2010.10.051>.
- Billing, D. G.; Lemmerer, A. Synthesis, Characterization and Phase Transitions in the Inorganic-Organic Layered Perovskite-Type Hybrids $[(\text{C}_n\text{H}_{2n} + 1\text{NH}_3)_2\text{PbI}_4]$, $n = 4, 5$ and 6. *Acta Crystallogr. Sect. B Struct. Sci.* 2007, 63 (5), 735–747. <https://doi.org/10.1107/S0108768107031758>.
- Bockris, J. O. The Electrocatalysis of Oxygen Evolution on Perovskites. *Journal of The Electrochemical Society*. 1984, p 290. <https://doi.org/10.1149/1.2115565>.

- Bouduban, M. E. F.; Burgos-Caminal, A.; Ossola, R.; Teuscher, J.; Moser, J. E. Energy and Charge Transfer Cascade in Methylammonium Lead Bromide Perovskite Nanoparticle Aggregates. *Chem. Sci.* 2017, 8 (6), 4371–4380. <https://doi.org/10.1039/c6sc05211h>.
- Bryant, D.; Aristidou, N.; Pont, S.; Sanchez-molina, I.; Chotchunangatchaval, T.; Wheeler, S.; Durrant, R.; Haque, S. A. Environmental Science Light and Oxygen Induced Degradation Limits the Operational Stability of Methylammonium Lead Triiodide Perovskite Solar Cells †. *Energy Environ. Sci.* 2016, 9, 1655–1660. <https://doi.org/10.1039/C6EE00409A>.
- Bush, K. A.; Palmstrom, A. F.; Yu, Z. J.; Boccard, M.; Cheacharoen, R.; Mailoa, J. P.; McMeekin, D. P.; Hoyer, R. L. Z.; Bailie, C. D.; Leijtens, T.; et al. 23.6%-Efficient Monolithic Perovskite/Silicon Tandem Solar Cells with Improved Stability. *Nat. Energy* 2017, 2 (4), 17009. <https://doi.org/10.1038/nenergy.2017.9>.
- Cao, D. H.; Stoumpos, C. C.; Farha, O. K.; Hupp, J. T.; Kanatzidis, M. G. 2D Homologous Perovskites as Light-Absorbing Materials for Solar Cell Applications. *J. Am. Chem. Soc.* 2015, 137 (24), 7843–7850. <https://doi.org/10.1021/jacs.5b03796>.
- Cheacharoen, R.; Rolston, N.; Harwood, D.; Bush, K. A.; Dauskardt, R. H.; McGehee, M. D. Design and Understanding of Encapsulated Perovskite Solar Cells to Withstand Temperature Cycling. *Energy Environ. Sci.* 2018, 11 (1), 144–150. <https://doi.org/10.1039/c7ee02564e>.
- Chemelewski, W. D.; Lee, H. C.; Lin, J. F.; Bard, A. J.; Mullins, C. B. Amorphous FeOOH Oxygen Evolution Reaction Catalyst for Photoelectrochemical Water Splitting. *J. Am. Chem. Soc.* 2014, 136 (7), 2843–2850. <https://doi.org/10.1021/ja411835a>.
- Chen, A. Z.; Shiu, M.; Ma, J. H.; Alpert, M. R.; Zhang, D.; Foley, B. J.; Smilgies, D. M.; Lee, S. H.; Choi, J. J. Origin of Vertical Orientation in Two-Dimensional Metal Halide Perovskites and Its Effect on Photovoltaic Performance. *Nat. Commun.* 2018, 9 (1), 1–7. <https://doi.org/10.1038/s41467-018-03757-0>.
- Chen, D.; Chen, C.; Zhang, Z.; Baiyee, Z. M.; Ciucci, F.; Shao, Z. Compositional Engineering of Perovskite Oxides for Highly Efficient Oxygen Reduction Reactions. *ACS Appl. Mater. Interfaces* 2015, 7 (16), 8562–8571. <https://doi.org/10.1021/acsami.5b00358>.
- Chen, J.; Lee, D.; Park, N. G. Stabilizing the Ag Electrode and Reducing J-V Hysteresis through Suppression of Iodide Migration in Perovskite Solar Cells. *ACS Appl. Mater. Interfaces* 2017, 9 (41), 36338–36349. <https://doi.org/10.1021/acsami.7b07595>.

- Chen, S.; Qiao, S. Z. Hierarchically Porous Nitrogen-Doped Graphene-NiCo₂O₄ Hybrid Paper as an Advanced Electrocatalytic Water-Splitting Material. *ACS Nano* 2013, 7 (11), 10190–10196. <https://doi.org/10.1021/nn404444r>.
- Chen, W.; Liu, Y.; Li, Y.; Sun, J.; Qiu, Y.; Liu, C.; Zhou, G.; Cui, Y. In Situ Electrochemically Derived Nanoporous Oxides from Transition Metal Dichalcogenides for Active Oxygen Evolution Catalysts. *Nano Lett.* 2016, 16 (12), 7588–7596. <https://doi.org/10.1021/acs.nanolett.6b03458>.
- Chen, W.; Wang, H.; Li, Y.; Liu, Y.; Sun, J.; Lee, S.; Lee, J.-S.; Cui, Y. In Situ Electrochemical Oxidation Tuning of Transition Metal Disulfides to Oxides for Enhanced Water Oxidation. *ACS Cent. Sci.* 2015, 150715073040007. <https://doi.org/10.1021/acscentsci.5b00227>.
- Chen, Y.; Jung, W.; Cai, Z.; Kim, J. J.; Tuller, H. L.; Yildiz, B. Impact of Sr Segregation on the Electronic Structure and Oxygen Reduction Activity of SrTi_{1-x}FexO₃ Surfaces. *Energy Environ. Sci.* 2012, 5 (7), 7979. <https://doi.org/10.1039/c2ee21463f>.
- Chen, Z.; Li, Z.; Zhang, C.; Jiang, X. F.; Chen, D.; Xue, Q.; Liu, M.; Su, S.; Yip, H. L.; Cao, Y. Recombination Dynamics Study on Nanostructured Perovskite Light-Emitting Devices. *Adv. Mater.* 2018, 30 (38), 1–9. <https://doi.org/10.1002/adma.201801370>.
- Chou, H.; Ismach, A.; Ghosh, R.; Ruoff, R. S.; Dolocan, A. Revealing the Planar Chemistry of Two-Dimensional Heterostructures at the Atomic Level. *Nat. Commun.* 2015, 6 (May), 7482. <https://doi.org/10.1038/ncomms8482>.
- Christians, J. A.; Miranda Herrera, P. A.; Kamat, P. V. Transformation of the Excited State and Photovoltaic Efficiency of CH₃NH₃PbI₃ Perovskite upon Controlled Exposure to Humidified Air. *J. Am. Chem. Soc.* 2015, 137 (4), 1530–1538. <https://doi.org/10.1021/ja511132a>.
- Corrigan, D. a. The Catalysis of the Oxygen Evolution Reaction by Iron Impurities in Thin Film Nickel Oxide Electrodes. *J. Electrochem. Soc.* 1987, 134 (2), 377. <https://doi.org/10.1149/1.2100463>.
- De Koninck, M.; Poirier, S.; Marsan, B. Cu_xCo_{3-x}O₄ Used as Bifunctional Electrocatalyst. *Journal of The Electrochemical Society.* 2007, p A381. <https://doi.org/10.1149/1.2454366>.
- De Silva, U.; Masud, J.; Zhang, N.; Hong, Y.; Liyanage, W. P. R.; Asle Zaeem, M.; Nath, M. Nickel Telluride as a Bifunctional Electrocatalyst for Efficient Water Splitting in Alkaline Medium. *J. Mater. Chem. A* 2018, No. March. <https://doi.org/10.1039/C8TA01760C>.
- Denholm, P.; O'Connell, M.; Brinkman, G.; Jorgenson, J. Overgeneration from Solar Energy in California: A Field Guide to the Duck Chart (NREL/TP-6A20-65023); 2015.

- Draguta, S.; Sharia, O.; Yoon, S. J.; Brennan, M. C.; Morozov, Y. V.; Manser, J. M.; Kamat, P. V.; Schneider, W. F.; Kuno, M. Rationalizing the Light-Induced Phase Separation of Mixed Halide Organic-Inorganic Perovskites. *Nat. Commun.* 2017, 8 (1). <https://doi.org/10.1038/s41467-017-00284-2>.
- Du, X.; Ma, G.; Zhang, X. Experimental and Theoretical Understanding on Electrochemical Activation Processes of Nickel Selenide for Excellent Water-Splitting Performance: Comparing the Electrochemical Performances with M-NiSe (M = Co, Cu, and V). *ACS Sustain. Chem. Eng.* 2019, 7 (23), 19257–19267. <https://doi.org/10.1021/acssuschemeng.9b05514>.
- Du, X.; Su, H.; Zhang, X. Metal-Organic Framework-Derived Cu-Doped Co₉S₈ Nanorod Array with Less Low-Valence Co Sites as Highly Efficient Bifunctional Electrodes for Overall Water Splitting. *ACS Sustain. Chem. Eng.* 2019, 7 (19), 16917–16926. <https://doi.org/10.1021/acssuschemeng.9b04739>.
- Dunlap-Shohl, W. A.; Zhou, Y.; Padture, N. P.; Mitzi, D. B. Synthetic Approaches for Halide Perovskite Thin Films. *Chem. Rev.* 2019, 119 (5), 3193–3295. <https://doi.org/10.1021/acs.chemrev.8b00318>.
- Eisele, D. M.; Knoester, J.; Kirstein, S.; Rabe, J. P.; Vanden Bout, D. A. Uniform Exciton Fluorescence from Individual Molecular Nanotubes Immobilized on Solid Substrates. *Nat. Nanotechnol.* 2009, 4 (10), 658–663. <https://doi.org/10.1038/nnano.2009.227>.
- Elacqua, E.; Geberth, G. T.; Vanden Bout, D. A.; Weck, M. Synthesis and Folding Behaviour of Poly(p-Phenylene Vinylene)-Based β -Sheet Polychromophores. *Chem. Sci.* 2019, 10 (7), 2144–2152. <https://doi.org/10.1039/c8sc05111a>.
- Elmelund, T.; Scheidt, R. A.; Seger, B.; Kamat, P. V. Bidirectional Halide Ion Exchange in Paired Lead Halide Perovskite Films with Thermal Activation. *ACS Energy Lett.* 2019, 4 (8), 1961–1969. <https://doi.org/10.1021/acsenenergylett.9b01280>.
- Endres, J.; Egger, D. A.; Kulbak, M.; Kerner, R. A.; Zhao, L.; Silver, S. H.; Hodes, G.; Rand, B. P.; Cahen, D.; Kronik, L.; Kahn, A. Valence and Conduction Band Densities of States of Metal Halide Perovskites: A Combined Experimental-Theoretical Study. *J. Phys. Chem. Lett.* 2016, 7 (14), 2722–2729. <https://doi.org/10.1021/acs.jpclett.6b00946>.
- Eperon, G. E.; Stranks, S. D.; Menelaou, C.; Johnston, M. B.; Herz, L. M.; Snaith, H. J. Formamidinium Lead Trihalide: A Broadly Tunable Perovskite for Efficient Planar Heterojunction Solar Cells. *Energy Environ. Sci.* 2014, 7 (3), 982. <https://doi.org/10.1039/c3ee43822h>.
- Esswein, A. J.; Surendranath, Y.; Reece, S. Y.; Nocera, D. G. Highly Active Cobalt Phosphate and Borate Based Oxygen Evolving Catalysts Operating in Neutral and Natural Waters. *Energy Environ. Sci.* 2011, 4 (2), 499. <https://doi.org/10.1039/c0ee00518e>.

- Fan, H.; Zhang, M.; Zhang, X.; Qian, Y. Hydrothermal Growth of NiSe 2 Tubular Microcrystals Assisted by PVA. *J. Cryst. Growth* 2009, 311 (20), 4530–4534. <https://doi.org/10.1016/j.jcrysgro.2009.08.005>.
- Feng, J.; Gong, C.; Gao, H.; Wen, W.; Gong, Y.; Jiang, X.; Zhang, B.; Wu, Y.; Wu, Y.; Fu, H.; et al. Single-Crystalline Layered Metal-Halide Perovskite Nanowires for Ultrasensitive Photodetectors. *Nat. Electron.* 2018, 1 (7), 404–410. <https://doi.org/10.1038/s41928-018-0101-5>.
- Feron, K.; Nagle, T. J.; Rozanski, L. J.; Gong, B. B.; Fell, C. J. Spatially Resolved Photocurrent Measurements of Organic Solar Cells: Tracking Water Ingress at Edges and Pinholes. *Sol. Energy Mater. Sol. Cells* 2013, 109, 169–177. <https://doi.org/10.1016/j.solmat.2012.10.027>.
- Gao, M.; Sheng, W.; Zhuang, Z.; Fang, Q.; Gu, S.; Jiang, J.; Yan, Y. Efficient Water Oxidation Using Nanostructured ??-Nickel-Hydroxide as an Electrocatalyst. *J. Am. Chem. Soc.* 2014, 136 (19), 7077–7084. <https://doi.org/10.1021/ja502128j>.
- Gaoke, Z.; Ying, L.; Xia, Y.; Yanping, W.; Shixi, O.; Hangxing, L. Comparison of Synthesis Methods, Crystal Structure and Characterization of Strontium Cobaltite Powders. *Mater. Chem. Phys.* 2006, 99 (1), 88–95. <https://doi.org/10.1016/j.matchemphys.2005.09.078>.
- Gil-Escrig, L.; Momblona, C.; La-Placa, M. G.; Boix, P. P.; Sessolo, M.; Bolink, H. J. Vacuum Deposited Triple-Cation Mixed-Halide Perovskite Solar Cells. *Adv. Energy Mater.* 2018, 8 (14), 1–6. <https://doi.org/10.1002/aenm.201703506>.
- Goldschmidt, V. M. Die Gesetze Der Krystallochemie. *Naturwissenschaften* 1926, 14 (21), 477–485. <https://doi.org/10.1007/BF01507527>.
- Gong, M.; Li, Y.; Wang, H.; Liang, Y.; Wu, J. Z.; Zhou, J.; Wang, J.; Regier, T.; Wei, F.; Dai, H. An Advanced Ni-Fe Layered Double Hydroxide Electrocatalyst for Water Oxidation. *J. Am. Chem. Soc.* 2013, 135 (23), 8452–8455. <https://doi.org/10.1021/ja4027715>.
- Gorlin, Y.; Jaramillo, T. F. A Bifunctional Nonprecious Metal Catalyst for Oxygen Reduction and Water Oxidation. *J. Am. Chem. Soc.* 2010, 132 (39), 13612–13614. <https://doi.org/10.1021/ja104587v>.
- Grancini, G.; Roldán-Carmona, C.; Zimmermann, I.; Mosconi, E.; Lee, X.; Martineau, D.; Nabey, S.; Oswald, F.; De Angelis, F.; Graetzel, M.; et al. One-Year Stable Perovskite Solar Cells by 2D/3D Interface Engineering. *Nat. Commun.* 2017, 8, 15684. <https://doi.org/10.1038/ncomms15684>.
- Griffin, M. P.; Gearba, R.; Stevenson, K. J.; Vanden Bout, D. A.; Dolocan, A. Revealing the Chemistry and Morphology of Buried Donor/Acceptor Interfaces in Organic Photovoltaics. *J. Phys. Chem. Lett.* 2017, 8 (13), 2764–2773. <https://doi.org/10.1021/acs.jpcllett.7b00911>.

- Grosvenor, a. P.; Kobe, B. a.; Biesinger, M. C.; McIntyre, N. S. Investigation of Multiplet Splitting of Fe 2p XPS Spectra and Bonding in Iron Compounds. *Surf. Interface Anal.* 2004, 36 (12), 1564–1574. <https://doi.org/10.1002/sia.1984>.
- Habas, S. E.; Platt, H. A. S.; Van Hest, M. F. A. M.; Ginley, D. S. Low-Cost Inorganic Solar Cells: From Ink to Printed Device. *Chem. Rev.* 2010, 110 (11), 6571–6594. <https://doi.org/10.1021/cr100191d>.
- Hardin, W. G.; Mefford, J. T.; Slanac, D. a.; Patel, B. B.; Wang, X.; Dai, S.; Zhao, X.; Ruoff, R. S.; Johnston, K. P.; Stevenson, K. J. Tuning the Electrocatalytic Activity of Perovskites through Active Site Variation and Support Interactions. *Chem. Mater.* 2014, 26 (11), 3368–3376. <https://doi.org/10.1021/cm403785q>.
- Harrison, W. T. a.; Hegwood, S. L.; Jacobson, A. J. A Powder Neutron Diffraction Determination of the Structure of Sr₆Co₅O₁₅, Formerly Described as the Low-Temperature Hexagonal Form of SrCoO₃?X . *J. Chem. Soc. Chem. Commun.* 1995, No. 19, 1953. <https://doi.org/10.1039/c39950001953>.
- Harvey, S. P.; Li, Z.; Christians, J. A.; Zhu, K.; Luther, J. M.; Berry, J. J. Probing Perovskite Inhomogeneity beyond the Surface: TOF-SIMS Analysis of Halide Perovskite Photovoltaic Devices. *ACS Appl. Mater. Interfaces* 2018, 10 (34), 28541–28552. <https://doi.org/10.1021/acsami.8b07937>.
- He, P.; Faulkner, L. R. Intelligent, Automatic Compensation of Solution Resistance. *Anal. Chem.* 1986, 58 (3), 517–523. <https://doi.org/10.1021/ac00294a004>.
- Horowitz, K. A. W.; Fu, R.; Sun, X.; Silverman, T.; Woodhouse, M.; Alam, M. A.; Horowitz, K. A. W.; Fu, R.; Sun, X.; Silverman, T.; et al. An Analysis of the Cost and Performance of Photovoltaic Systems as a Function of Module Area. *Natl. Renew. Energy Lab.* 2017, No. April.
- Hsu, H. Y.; Ji, L.; Ahn, H. S.; Zhao, J.; Yu, E. T.; Bard, A. J. A Liquid Junction Photoelectrochemical Solar Cell Based on P-Type MeNH₃PbI₃ Perovskite with 1.05 v Open-Circuit Photovoltage. *J. Am. Chem. Soc.* 2015, 137 (46), 14758–14764. <https://doi.org/10.1021/jacs.5b09758>.
- Hu, C.; Zhang, L.; Zhao, Z. J.; Li, A.; Chang, X.; Gong, J. Synergism of Geometric Construction and Electronic Regulation: 3D Se-(NiCo)S_x/(OH)_x Nanosheets for Highly Efficient Overall Water Splitting. *Adv. Mater.* 2018, 30 (12), 1–8. <https://doi.org/10.1002/adma.201705538>.
- Hu, Z.; Shao, B.; Geberth, G. T.; Vanden Bout, D. A. Effects of Molecular Architecture on Morphology and Photophysics in Conjugated Polymers: From Single Molecules to Bulk. *Chem. Sci.* 2018, 9 (5), 1101–1111. <https://doi.org/10.1039/c7sc03465b>.
- International Energy Outlook 2019 with projections to 2050 www.eia.gov/ieo (accessed Apr 2, 2020).

- Jain, A.; Ong, S. P.; Hautier, G.; Chen, W.; Richards, W. D.; Dacek, S.; Cholia, S.; Gunter, D.; Skinner, D.; Ceder, G.; Persson, K.A. Commentary: The Materials Project: A Materials Genome Approach to Accelerating Materials Innovation. *APL Mater.* 2013, 1 (1), 011002. <https://doi.org/10.1063/1.4812323>.
- Jansson, E. T.; Lai, Y.; Santiago, J. G.; Zare, R. N. Rapid Hydrogen – Deuterium Exchange in Liquid Droplets. *J. Am. Chem. Soc.* 2017, 139 (20), 6851–6854. <https://doi.org/10.1021/jacs.7b03541>.
- Jena, A. K.; Kulkarni, A.; Miyasaka, T. Halide Perovskite Photovoltaics: Background, Status, and Future Prospects. *Chem. Rev.* 2019, 119 (5), 3036–3103. <https://doi.org/10.1021/acs.chemrev.8b00539>.
- Jeon, T. H.; Choi, W.; Park, H. Cobalt–Phosphate Complexes Catalyze the Photoelectrochemical Water Oxidation of BiVO₄ Electrodes. *Physical Chemistry Chemical Physics*. 2011, p 21392. <https://doi.org/10.1039/c1cp23135a>.
- Jiang, N.; Tang, Q.; Sheng, M.; You, B.; Jiang, D. E.; Sun, Y. Nickel Sulfides for Electrocatalytic Hydrogen Evolution under Alkaline Conditions: A Case Study of Crystalline NiS, NiS₂, and Ni₃S₂ Nanoparticles. *Catal. Sci. Technol.* 2016, 6 (4), 1077–1084. <https://doi.org/10.1039/c5cy01111f>.
- Jiang, S. P.; Love, J. G. Origin of the Initial Polarization Behavior of Sr-Doped LaMnO₃ for O₂ Reduction in Solid Oxide Fuel Cells. *Solid State Ionics* 2001, 138 (3–4), 183–190. [https://doi.org/10.1016/S0167-2738\(00\)00806-7](https://doi.org/10.1016/S0167-2738(00)00806-7).
- Jin, S. Are Metal Chalcogenides, Nitrides, and Phosphides Oxygen Evolution Catalysts or Bifunctional Catalysts? *ACS Energy Lett.* 2017, 2 (8), 1937–1938. <https://doi.org/10.1021/acsenergylett.7b00679>.
- Jung, W.; Tuller, H. L. Investigation of Surface Sr Segregation in Model Thin Film Solid Oxide Fuel Cell Perovskite Electrodes. *Energy Environ. Sci.* 2012, 5 (1), 5370. <https://doi.org/10.1039/c1ee02762j>.
- Kaltenbrunner, M.; Adam, G.; Glowacki, E. D.; Drack, M.; Schwödiauer, R.; Leonat, L.; Apaydin, D. H.; Groiss, H.; Scharber, M. C.; White, M. S.; et al. Flexible High Power-per-Weight Perovskite Solar Cells with Chromium Oxide–Metal Contacts for Improved Stability in Air. *Nat. Mater.* 2015, 14 (10), 1032–1039. <https://doi.org/10.1038/nmat4388>.
- Kanan, M. W.; Nocera, D. G. In Situ Formation of an Oxygen-Evolving Catalyst in Neutral Water Containing Phosphate and Co²⁺. *Science* 2008, 321 (5892), 1072–1075. <https://doi.org/10.1126/science.1162018>.
- Kato, Y.; Ono, L. K.; Lee, M. V.; Wang, S.; Raga, S. R.; Qi, Y. Silver Iodide Formation in Methyl Ammonium Lead Iodide Perovskite Solar Cells with Silver Top Electrodes. *Adv. Mater. Interfaces* 2015, 2 (13), 2–7. <https://doi.org/10.1002/admi.201500195>.

- Khan, N. A.; Rashid, N.; Junaid, M.; Zafar, M. N.; Faheem, M.; Ahmad, I. NiO/NiS Heterostructures: An Efficient and Stable Electrocatalyst for Oxygen Evolution Reaction. *ACS Appl. Energy Mater.* 2019, 2 (5), 3587–3594. <https://doi.org/10.1021/acsaem.9b00317>.
- Kim, H. S.; Hagfeldt, A.; Park, N. G. Morphological and Compositional Progress in Halide Perovskite Solar Cells. *Chem. Commun.* 2019, 55 (9), 1192–1200. <https://doi.org/10.1039/c8cc08653b>.
- Kim, H.-S.; Lee, C.-R.; Im, J.-H.; Lee, K.-B.; Moehl, T.; Marchioro, A.; Moon, S.-J.; Humphry-Baker, R.; Yum, J.-H.; Moser, J. E.; et al. Lead Iodide Perovskite Sensitized All-Solid-State Submicron Thin Film Mesoscopic Solar Cell with Efficiency Exceeding 9%. *Sci. Rep.* 2012, 2, 1–7. <https://doi.org/10.1038/srep00591>.
- Kim, J.; Yin, X.; Tsao, K.; Fang, S.; Yang, H. Ca₂Mn₂O₅ as Oxygen-Deficient Perovskite Electrocatalyst for Oxygen Evolution Reaction. *J. Am. Chem. Soc.* 2014, 136 (42), 14646–14649. <https://doi.org/10.1021/ja506254g>.
- Kim, K. X-Ray-Photoelectron Spectroscopic Studies of the Electronic Structure of CoO. *Phys. Rev. B* 1975, 11 (15), 2177–2185.
- Koh, T. M.; Shanmugam, V.; Guo, X.; Lim, S. S.; Filonik, O.; Herzig, E. M.; Müller-Buschbaum, P.; Swamy, V.; Chien, S. T.; Mhaisalkar, S. G.; Mathews, N. Enhancing Moisture Tolerance in Efficient Hybrid 3D/2D Perovskite Photovoltaics. *J. Mater. Chem. A* 2018, 2122–2128. <https://doi.org/10.1039/C7TA09657G>.
- Kojima, A.; Teshima, K.; Shirai, Y.; Miyasaka, T. Organometal Halide Perovskites as Visible-Light Sensitizers for Photovoltaic Cells. *J. Am. Chem. Soc.* 2009, 131 (17), 6050–6051. <https://doi.org/10.1021/ja809598r>.
- Le Toquin, R.; Paulus, W.; Cousson, A.; Prestipino, C.; Lamberti, C. Time-Resolved in Situ Studies of Oxygen Intercalation into SrCoO_{2.5}, Performed by Neutron Diffraction and X-Ray Absorption Spectroscopy. *J. Am. Chem. Soc.* 2006, 128 (40), 13161–13174. <https://doi.org/10.1021/ja063207m>.
- Lee, D. U.; Kim, B. J.; Chen, Z. One-Pot Synthesis of a Mesoporous NiCo₂O₄ Nanoplatelet and Graphene Hybrid and Its Oxygen Reduction and Evolution Activities as an Efficient Bi-Functional Electrocatalyst. *J. Mater. Chem. A* 2013, 1 (15), 4754. <https://doi.org/10.1039/c3ta01402a>.
- Lee, Y.; Suntivich, J.; May, K. J.; Perry, E. E.; Shao-Horn, Y. Synthesis and Activities of Rutile IrO₂ and RuO₂ Nanoparticles for Oxygen Evolution in Acid and Alkaline Solutions. *Journal of Physical Chemistry Letters*. 2012, pp 399–404. <https://doi.org/10.1021/jz2016507>.
- Leguy, A. M. A.; Hu, Y.; Campoy-Quiles, M.; Alonso, M. I.; Weber, O. J.; Azarhoosh, P.; van Schilfgaarde, M.; Weller, M. T.; Bein, T.; Nelson, J.; et al. Reversible

- Hydration of $\text{CH}_3\text{NH}_3\text{PbI}_3$ in Films, Single Crystals, and Solar Cells. *Chem. Mater.* 2015, 27 (9), 3397–3407. <https://doi.org/10.1021/acs.chemmater.5b00660>.
- Li, J.; Dong, Q.; Li, N.; Wang, L. Direct Evidence of Ion Diffusion for the Silver-Electrode-Induced Thermal Degradation of Inverted Perovskite Solar Cells. *Adv. Energy Mater.* 2017, 7 (14), 1–8. <https://doi.org/10.1002/aenm.201602922>.
- Li, L.; Zhou, N.; Chen, Q.; Shang, Q.; Zhang, Q.; Wang, X.; Zhou, H. Unraveling the Growth of Hierarchical Quasi-2D/3D Perovskite and Carrier Dynamics. *J. Phys. Chem. Lett.* 2018, 9 (5), 1124–1132. <https://doi.org/10.1021/acs.jpcllett.7b03294>.
- Li, Z.; Chen, Z.; Yang, Y.; Xue, Q.; Yip, H. L.; Cao, Y. Modulation of Recombination Zone Position for Quasi-Two-Dimensional Blue Perovskite Light-Emitting Diodes with Efficiency Exceeding 5%. *Nat. Commun.* 2019, 10 (1), 1–10. <https://doi.org/10.1038/s41467-019-09011-5>.
- Lin, W. C.; Chang, H. Y.; Abbasi, K.; Shyue, J. J.; Burda, C. 3D In Situ ToF-SIMS Imaging of Perovskite Films under Controlled Humidity Environmental Conditions. *Adv. Mater. Interfaces* 2017, 4 (2), 1–9. <https://doi.org/10.1002/admi.201600673>.
- Lin, Y.; Bai, Y.; Fang, Y.; Chen, Z.; Yang, S.; Zheng, X.; Tang, S.; Liu, Y.; Zhao, J.; Huang, J. Enhanced Thermal Stability in Perovskite Solar Cells by Assembling 2D/3D Stacking Structures. *J. Phys. Chem. Lett.* 2018, 9 (3), 654–658. <https://doi.org/10.1021/acs.jpcllett.7b02679>.
- Lin, Y.; Fang, Y.; Zhao, J.; Shao, Y.; Stuard, S. J.; Nahid, M. M.; Ade, H.; Wang, Q.; Shield, J. E.; Zhou, N.; et al. Unveiling the Operation Mechanism of Layered Perovskite Solar Cells. *Nat. Commun.* 2019, 10 (1), 1–11. <https://doi.org/10.1038/s41467-019-08958-9>.
- Liu, J.; Leng, J.; Wu, K.; Zhang, J.; Jin, S. Observation of Internal Photoinduced Electron and Hole Separation in Hybrid Two-Dimensional Perovskite Films. *J. Am. Chem. Soc.* 2017, 139 (4), 1432–1435. <https://doi.org/10.1021/jacs.6b12581>.
- Liu, N.; Liu, P.; Ren, H.; Xie, H.; Zhou, N.; Gao, Y.; Li, Y.; Zhou, H.; Bai, Y.; Chen, Q. Probing Phase Distribution in 2D Perovskites for Efficient Device Design. *ACS Appl. Mater. Interfaces* 2020, 12 (2), 3127–3133. <https://doi.org/10.1021/acsami.9b17047>.
- Mabayoje, O.; Liu, Y.; Wang, M.; Shoola, A.; Ebrahim, A. M.; Frenkel, A. I.; Mullins, C. B. Electrodeposition of MoS_x Hydrogen Evolution Catalysts from Sulfur-Rich Precursors. *ACS Appl. Mater. Interfaces* 2019, 11 (36), 32879–32886. <https://doi.org/10.1021/acsami.9b07277>.
- Mabayoje, O.; Shoola, A.; Wygant, B. R.; Mullins, C. B. The Role of Anions in Metal Chalcogenide Oxygen Evolution Catalysis: Electrodeposited Thin Films of Nickel Sulfide as “Pre-Catalysts.” *ACS Energy Lett.* 2016, 1 (1), 195–201. <https://doi.org/10.1021/acsenergylett.6b00084>.

- Mabayoje, O.; Shoola, A.; Wygant, B. R.; Mullins, C. B. The Role of Anions in Metal Chalcogenide Oxygen Evolution Catalysis: Electrodeposited Thin Films of Nickel Sulfide as “Pre-Catalysts.” *ACS Energy Lett.* 2016, 1 (1), 195–201. <https://doi.org/10.1021/acsenergylett.6b00084>.
- Man, I. C.; Su, H. Y.; Calle-Vallejo, F.; Hansen, H. a.; Martínez, J. I.; Inoglu, N. G.; Kitchin, J.; Jaramillo, T. F.; Nørskov, J. K.; Rossmeisl, J. Universality in Oxygen Evolution Electrocatalysis on Oxide Surfaces. *ChemCatChem* 2011, 3 (7), 1159–1165. <https://doi.org/10.1002/cctc.201000397>.
- Mandale, A. B.; Badrinarayanan, S.; Date, S. K.; Sinha, A. P. B. Photoelectron-Spectroscopic Study of Nickel, Manganese and Cobalt Selenides. *J. Electron Spectros. Relat. Phenomena* 1984, 33 (1), 61–72. [https://doi.org/10.1016/0368-2048\(84\)80006-7](https://doi.org/10.1016/0368-2048(84)80006-7).
- Matsumoto, Y.; Yamada, S.; Nishida, T.; Sato, E. Oxygen Evolution on La(1-x)Sr_xFe(1-y)O₃ Series Oxides. *J. Electrochem. Soc.* 1980, 127 (11), 2360–2364.
- May, K. J.; Carlton, C. E.; Stoerzinger, K. a.; Risch, M.; Suntivich, J.; Lee, Y. L.; Grimaud, A.; Shao-Horn, Y. Influence of Oxygen Evolution during Water Oxidation on the Surface of Perovskite Oxide Catalysts. *J. Phys. Chem. Lett.* 2012, 3 (22), 3264–3270. <https://doi.org/10.1021/jz301414z>.
- McCrory, C. C. L.; Jung, S.; Ferrer, I. M.; Chatman, S. M.; Peters, J. C.; Jaramillo, T. F. Benchmarking Hydrogen Evolving Reaction and Oxygen Evolving Reaction Electrocatalysts for Solar Water Splitting Devices. *J. Am. Chem. Soc.* 2015, 137 (13), 4347–4357. <https://doi.org/10.1021/ja510442p>.
- Mills, A.; Russell, T. Comparative Study of New and Established Heterogeneous Oxygen Catalysts. *J. Chem. Soc. Faraday Trans.* 1991, 87 (8), 1245. <https://doi.org/10.1039/ft9918701245>.
- Mosconi, E.; Azpiroz, J. M.; De Angelis, F. Ab Initio Molecular Dynamics Simulations of Methylammonium Lead Iodide Perovskite Degradation by Water. *Chem. Mater.* 2015, 27 (13), 4885–4892. <https://doi.org/10.1021/acs.chemmater.5b01991>.
- Moulder, J. F.; Stickle, W. F.; Sobol, P. E.; Bomben, K. D. Handbook of X-Ray Photoelectron Spectroscopy; 1979; Vol. 3. <https://doi.org/10.1002/sia.740030412>.
- Muturo, E.; Crumlin, E. J.; Biegalski, M. D.; Christen, H. M.; Shao-Horn, Y. Enhanced Oxygen Reduction Activity on Surface-Decorated Perovskite Thin Films for Solid Oxide Fuel Cells. *Energy Environ. Sci.* 2011, 4 (9), 3689. <https://doi.org/10.1039/c1ee01245b>.
- Myae Soe, C. M.; Nagabhushana, G. P.; Shivaramaiah, R.; Tsai, H.; Nie, W.; Blancon, J. C.; Melkonyan, F.; Cao, D. H.; Traoré, B.; Pedesseau, L.; et al. Structural and Thermodynamic Limits of Layer Thickness in 2D Halide Perovskites. *Proc. Natl.*

- Acad. Sci. U. S. A. 2019, 116 (1), 58–66. <https://doi.org/10.1073/pnas.1811006115>.
- Nagai, T.; Ito, W.; Sakon, T. Relationship between Cation Substitution and Stability of Perovskite Structure in SrCoO₃-??-Based Mixed Conductors. *Solid State Ionics* 2007, 177 (39–40), 3433–3444. <https://doi.org/10.1016/j.ssi.2006.10.022>.
- Nakagawa, T.; Beasley, C. a.; Murray, R. W. Efficient Electro-Oxidation of Water near Its Reversible Potential by a Mesoporous IrO_x Nanoparticle Film. *J. Phys. Chem. C* 2009, 113 (30), 12958–12961. <https://doi.org/10.1021/jp9060076>.
- NREL. Best Research-Cell Efficiencies <https://www.nrel.gov/pv/assets/pdfs/pv-efficiency-chart.20181221.pdf>.
- Osterloh, F. E. Inorganic Nanostructures for Photoelectrochemical and Photocatalytic Water Splitting. *Chem. Soc. Rev.* 2013, 42 (6), 2294–2320. <https://doi.org/10.1039/C2CS35266D>.
- Paritmongkol, W.; Dahod, N. S.; Stollmann, A.; Mao, N.; Settens, C.; Zheng, S. L.; Tisdale, W. A. Synthetic Variation and Structural Trends in Layered Two-Dimensional Alkylammonium Lead Halide Perovskites. *Chem. Mater.* 2019, 31 (15), 5592–5607. <https://doi.org/10.1021/acs.chemmater.9b01318>.
- Persson, K. A.; Waldwick, B.; Lazic, P.; Ceder, G. Prediction of Solid-Aqueous Equilibria: Scheme to Combine First-Principles Calculations of Solids with Experimental Aqueous States. *Phys. Rev. B - Condens. Matter Mater. Phys.* 2012, 85 (23), 1–12. <https://doi.org/10.1103/PhysRevB.85.235438>.
- Postorino, P.; Malavasi, L. Pressure-Induced Effects in Organic-Inorganic Hybrid Perovskites. *J. Phys. Chem. Lett.* 2017, 8 (12), 2613–2622. <https://doi.org/10.1021/acs.jpclett.7b00347>.
- Prochowicz, D.; Runjhun, R.; Tavakoli, M. M.; Yadav, P.; Saski, M.; Alanazi, A. Q.; Kubicki, D. J.; Kaszkur, Z.; Zakeeruddin, S. M.; Lewiński, J.; et al. Engineering of Perovskite Materials Based on Formamidinium and Cesium Hybridization for High-Efficiency Solar Cells. *Chem. Mater.* 2019, 31 (5), 1620–1627. <https://doi.org/10.1021/acs.chemmater.8b04871>.
- Proppe, A. H.; Elkins, M. H.; Voznyy, O.; Pensack, R. D.; Zapata, F.; Besteiro, L. V.; Quan, L. N.; Quintero-Bermudez, R.; Todorovic, P.; Kelley, S. O.; Govorov, A. O.; Gray, S. K.; Infante, I.; Sargent, E. H.; Scholes, G. D. Spectrally Resolved Ultrafast Exciton Transfer in Mixed Perovskite Quantum Wells. *J. Phys. Chem. Lett.* 2019, 10 (3), 419–426. <https://doi.org/10.1021/acs.jpclett.9b00018>.
- Proppe, A. H.; Quintero-Bermudez, R.; Tan, H.; Voznyy, O.; Kelley, S. O.; Sargent, E. H. Synthetic Control over Quantum Well Width Distribution and Carrier Migration in Low-Dimensional Perovskite Photovoltaics. *J. Am. Chem. Soc.* 2018, 140 (8), 2890–2896. <https://doi.org/10.1021/jacs.7b12551>.

- Qing, J.; Liu, X. K.; Li, M.; Liu, F.; Yuan, Z.; Tiukalova, E.; Yan, Z.; Duchamp, M.; Chen, S.; Wang, Y.; Bai, S.; Liu, J. M.; Snaith, H. J.; Lee, C. S.; Sum, T. C.; Gao, F. Aligned and Graded Type-II Ruddlesden–Popper Perovskite Films for Efficient Solar Cells. *Adv. Energy Mater.* 2018, 8 (21), 1–8. <https://doi.org/10.1002/aenm.201800185>.
- Qiu, J.; Xia, Y.; Zheng, Y.; Hui, W.; Gu, H.; Yuan, W.; Yu, H.; Chao, L.; Niu, T.; Yang, Y.; et al. 2D Intermediate Suppression for Efficient Ruddlesden–Popper (RP) Phase Lead-Free Perovskite Solar Cells. *ACS Energy Lett.* 2019, 4 (7), 1513–1520. <https://doi.org/10.1021/acsenenergylett.9b00954>.
- Quan, L. N.; Yuan, M.; Comin, R.; Voznyy, O.; Beauregard, E. M.; Hoogland, S.; Buin, A.; Kirmani, A. R.; Zhao, K.; Amassian, A.; Kim, D. H.; Sargent, E. H. Ligand-Stabilized Reduced-Dimensionality Perovskites. *J. Am. Chem. Soc.* 2016, 138 (8), 2649–2655. <https://doi.org/10.1021/jacs.5b11740>.
- Quan, L. N.; Zhao, Y.; García De Arquer, F. P.; Sabatini, R.; Walters, G.; Voznyy, O.; Comin, R.; Li, Y.; Fan, J. Z.; Tan, H.; Pan, J.; Yuan, M.; Bakr, O. M.; Lu, Z.; Kim, D. H.; Sargent, E. H. Tailoring the Energy Landscape in Quasi-2D Halide Perovskites Enables Efficient Green-Light Emission. *Nano Lett.* 2017, 17 (6), 3701–3709. <https://doi.org/10.1021/acs.nanolett.7b00976>.
- Quintero-Bermudez, R.; Gold-Parker, A.; Proppe, A. H.; Munir, R.; Yang, Z.; Kelley, S. O.; Amassian, A.; Toney, M. F.; Sargent, E. H. Compositional and Orientational Control in Metal Halide Perovskites of Reduced Dimensionality. *Nat. Mater.* 2018, 17 (10), 900–907. <https://doi.org/10.1038/s41563-018-0154-x>.
- Reier, T.; Oezaslan, M.; Strasser, P. Electrocatalytic Oxygen Evolution Reaction (OER) on Ru, Ir, and Pt Catalysts: A Comparative Study of Nanoparticles and Bulk Materials. *ACS Catal.* 2012, 2 (8), 1765–1772. <https://doi.org/10.1021/cs3003098>.
- Riedinger, A.; Ott, F. D.; Mule, A.; Mazzotti, S.; Knüsel, P. N.; Kress, S. J. P.; Prins, F.; Erwin, S. C.; Norris, D. J. An Intrinsic Growth Instability in Isotropic Materials Leads to Quasi-Two-Dimensional Nanoplatelets. *Nat. Mater.* 2017, 16 (7), 743–748. <https://doi.org/10.1038/nmat4889>.
- Rong, Y.; Hu, Y.; Mei, A.; Tan, H.; Saidaminov, M. I.; Seok, S. Il; McGehee, M. D.; Sargent, E. H.; Han, H. Challenges for Commercializing Perovskite Solar Cells. *Science* (80-.). 2018, 361 (6408). <https://doi.org/10.1126/science.aat8235>.
- Ruggeri, E.; Anaya, M.; Gałkowski, K.; Delport, G.; Kosasih, F. U.; Abfalterer, A.; Mackowski, S.; Ducati, C.; Stranks, S. D. Controlling the Growth Kinetics and Optoelectronic Properties of 2D/3D Lead–Tin Perovskite Heterojunctions. *Adv. Mater.* 2019, 1905247, 1–9. <https://doi.org/10.1002/adma.201905247>.
- Samu, G. F.; Scheidt, R. A.; Kamat, P. V.; Janáky, C. Electrochemistry and Spectroelectrochemistry of Lead Halide Perovskite Films: Materials Science

- Aspects and Boundary Conditions. *Chem. Mater.* 2018, 30 (3), 561–569. <https://doi.org/10.1021/acs.chemmater.7b04321>.
- Seabold, J. A.; Choi, K. S. Efficient and Stable Photo-Oxidation of Water by a Bismuth Vanadate Photoanode Coupled with an Iron Oxyhydroxide Oxygen Evolution Catalyst. *J. Am. Chem. Soc.* 2012, 134 (4), 2186–2192. <https://doi.org/10.1021/ja209001d>.
- Shang, Q.; Wang, Y.; Zhong, Y.; Mi, Y.; Qin, L.; Zhao, Y.; Qiu, X.; Liu, X.; Zhang, Q. Unveiling Structurally Engineered Carrier Dynamics in Hybrid Quasi-Two-Dimensional Perovskite Thin Films toward Controllable Emission. *J. Phys. Chem. Lett.* 2017, 8 (18), 4431–4438. <https://doi.org/10.1021/acs.jpclett.7b01857>.
- Shannon, R. D. Revised Effective Ionic Radii and Systematic Studies of Interatomic Distances in Halides and Chalcogenides. *Acta Crystallographica Section A.* 1976, pp 751–767. <https://doi.org/10.1107/S0567739476001551>.
- Shirayama, M.; Kato, M.; Miyadera, T.; Sugita, T.; Fujiseki, T.; Hara, S.; Kadowaki, H.; Murata, D.; Chikamatsu, M.; Fujiwara, H. Degradation Mechanism of CH₃NH₃PbI₃ Perovskite Materials upon Exposure to Humid Air. *J. Appl. Phys.* 2016, 119 (11), 115501. <https://doi.org/10.1063/1.4943638>.
- Silver, S.; Dai, Q.; Li, H.; Brédas, J. L.; Kahn, A. Quantum Well Energetics of an n = 2 Ruddlesden–Popper Phase Perovskite. *Adv. Energy Mater.* 2019, 9, 1901005, 1–7. <https://doi.org/10.1002/aenm.201901005>.
- Silver, S.; Yin, J.; Li, H.; Brédas, J. L.; Kahn, A. Characterization of the Valence and Conduction Band Levels of n = 1 2D Perovskites: A Combined Experimental and Theoretical Investigation. *Adv. Energy Mater.* 2018, 8 (16), 1–7. <https://doi.org/10.1002/aenm.201703468>.
- Singh, A. K.; Zhou, L.; Shinde, A.; Suram, S. K.; Montoya, J. H.; Winston, D.; Gregoire, J. M.; Persson, K. A. Electrochemical Stability of Metastable Materials. *Chem. Mater.* 2017, 29 (23), 10159–10167. <https://doi.org/10.1021/acs.chemmater.7b03980>.
- Singh, P.; Shiva, K.; Celio, H.; Goodenough, J. B. Eldfellite, NaFe(SO₄)₂: An Intercalation Cathode Host for Low-Cost Na-Ion Batteries. *Energy Environ. Sci.* 2015, 8 (10), 3000–3005. <https://doi.org/10.1039/C5EE02274F>.
- Smith, R. D. L.; Prévot, M. S.; Fagan, R. D.; Trudel, S.; Berlinguette, C. P. Water Oxidation Catalysis: Electrocatalytic Response to Metal Stoichiometry in Amorphous Metal Oxide Films Containing Iron, Cobalt, and Nickel. *J. Am. Chem. Soc.* 2013, 135 (31), 11580–11586. <https://doi.org/10.1021/ja403102j>.
- Smith, R. D. L.; Prevot, M. S.; Fagan, R. D.; Zhang, Z.; Sedach, P. A.; Siu, M. K. J.; Trudel, S.; Berlinguette, C. P. Photochemical Route for Accessing Amorphous Metal Oxide Materials for Water Oxidation Catalysis. *Science* (80-.). 2013, 340 (6128), 60–63. <https://doi.org/10.1126/science.1233638>.

- Soe, C. M. M.; Nie, W.; Stoumpos, C. C.; Tsai, H.; Blancon, J. C.; Liu, F.; Even, J.; Marks, T. J.; Mohite, A. D.; Kanatzidis, M. G. Understanding Film Formation Morphology and Orientation in High Member 2D Ruddlesden–Popper Perovskites for High-Efficiency Solar Cells. *Adv. Energy Mater.* 2018, 8 (1), 2–11. <https://doi.org/10.1002/aenm.201700979>.
- Spanopoulos, I.; Hadar, I.; Ke, W.; Tu, Q.; Chen, M.; Tsai, H.; He, Y.; Shekhawat, G.; Dravid, V. P.; Wasielewski, M. R.; et al. Uniaxial Expansion of the 2D Ruddlesden-Popper Perovskite Family for Improved Environmental Stability. *J. Am. Chem. Soc.* 2019, 141 (13), 5518–5534. <https://doi.org/10.1021/jacs.9b01327>.
- Stølen, S.; Bakken, E.; Mohn, C. E. Oxygen-Deficient Perovskites: Linking Structure, Energetics and Ion Transport. *Phys. Chem. Chem. Phys.* 2006, 8 (4), 429–447. <https://doi.org/10.1039/b512271f>.
- Stoumpos, C. C.; Cao, D. H.; Clark, D. J.; Young, J.; Rondinelli, J. M.; Jang, J. I.; Hupp, J. T.; Kanatzidis, M. G. Ruddlesden-Popper Hybrid Lead Iodide Perovskite 2D Homologous Semiconductors. *Chem. Mater.* 2016, 28 (8), 2852–2867. <https://doi.org/10.1021/acs.chemmater.6b00847>.
- Stoumpos, C. C.; Soe, C. M. M.; Tsai, H.; Nie, W.; Blancon, J. C.; Cao, D. H.; Liu, F.; Traoré, B.; Katan, C.; Even, J.; et al. High Members of the 2D Ruddlesden-Popper Halide Perovskites: Synthesis, Optical Properties, and Solar Cells of $(\text{CH}_3(\text{CH}_2)_3\text{NH}_3)_2(\text{CH}_3\text{NH}_3)_4\text{Pb}_5\text{I}_{16}$. *Chem* 2017, 2 (3), 427–440. <https://doi.org/10.1016/j.chempr.2017.02.004>.
- Strydom, C. A.; Strydom, H. J. X-Ray Photoelectron Spectroscopy Studies of Some Cobalt(II) Nitrate Complexes. *Inorganica Chim. Acta* 1989, 159 (2), 191–195. [https://doi.org/10.1016/S0020-1693\(00\)80566-6](https://doi.org/10.1016/S0020-1693(00)80566-6).
- Suntivich, J.; Gasteiger, H. a.; Yabuuchi, N.; Shao-Horn, Y. Electrocatalytic Measurement Methodology of Oxide Catalysts Using a Thin-Film Rotating Disk Electrode. *J. Electrochem. Soc.* 2010, 157 (8), B1263. <https://doi.org/10.1149/1.3456630>.
- Suntivich, J.; May, K. J.; Gasteiger, H. A.; Goodenough, J. B.; Shao-Horn, Y. A Perovskite Oxide Optimized for Oxygen Evolution Catalysis from Molecular Orbital Principles. *Science*. 2011, pp 1383–1385. <https://doi.org/10.1126/science.1212858>.
- Surendranath, Y.; Dincă, M.; Nocera, D. G. Electrolyte-Dependent Electrosynthesis and Activity of Cobalt-Based Water Oxidation Catalysts. *J. Am. Chem. Soc.* 2009, 131 (7), 2615–2620. <https://doi.org/10.1021/ja807769r>.
- Swesi, A. T.; Masud, J.; Nath, M. Nickel Selenide as a High-Efficiency Catalyst for Oxygen Evolution Reaction. *Energy Environ. Sci.* 2016, 9 (5), 1771–1782. <https://doi.org/10.1039/C5EE02463C>.

- Takeda, Y.; Kanamura, F.; Shimada, M.; Koizumi, M. The Crystal Structure of BaNiO₃. *Acta Crystallogr. Sect. B Struct. Crystallogr. Cryst. Chem.* 1976, 32 (8), 2464–2466. <https://doi.org/10.1107/S056774087600798X>.
- Takeda, Y.; Kanno, R.; Kondo, T.; Yamamoto, O.; Taguchi, H.; Shimada, M.; Koizumi, M. Properties Of SrMO_{3-?} (M=Fe, Co) as Oxygen Electrodes in Alkaline Solution. *Journal of Applied Electrochemistry.* 1982, pp 275–280. <https://doi.org/10.1007/BF00615092>.
- Tang, C.; Cheng, N.; Pu, Z.; Xing, W.; Sun, X. NiSe Nanowire Film Supported on Nickel Foam: An Efficient and Stable 3D Bifunctional Electrode for Full Water Splitting. *Angew. Chemie Int. Ed.* 2015, 54 (32), 9351–9355. <https://doi.org/10.1002/anie.201503407>.
- Tsai, H.; Nie, W.; Blancon, J.-C.; Stoumpos, C. C.; Asadpour, R.; Harutyunyan, B.; Neukirch, A. J.; Verduzco, R.; Crochet, J. J.; Tretiak, S.; Pedesseau, L.; Even, J.; Alam, M. A.; Gupta, G.; Lou, J.; Ajayan, P. M.; Bedzyk, M. J.; Kanatzidis, M. G.; Mohite, A. D. High-Efficiency Two-Dimensional Ruddlesden–Popper Perovskite Solar Cells. *Nature* 2016, 536 (7616), 312–316. <https://doi.org/10.1038/nature18306>.
- Turren-Cruz, S. H.; Saliba, M.; Mayer, M. T.; Juárez-Santiesteban, H.; Mathew, X.; Nienhaus, L.; Tress, W.; Erodici, M. P.; Sher, M. J.; Bawendi, M. G.; et al. Enhanced Charge Carrier Mobility and Lifetime Suppress Hysteresis and Improve Efficiency in Planar Perovskite Solar Cells. *Energy Environ. Sci.* 2018, 11 (1), 78–86. <https://doi.org/10.1039/c7ee02901b>.
- van der Heide, P. A. W. Systematic X-Ray Photoelectron Spectroscopic Study of La_{1-x}Sr_x-Based Perovskite-Type Oxides. *Surf. Interface Anal.* 2002, 33 (5), 414–425. <https://doi.org/10.1002/sia.1227>.
- Vasquez, R. P. X-Ray Photoelectron Spectroscopy Study of Sr and Ba Compounds. *J. Electron Spectros. Relat. Phenomena* 1991, 56 (3), 217–240. [https://doi.org/10.1016/0368-2048\(91\)85005-E](https://doi.org/10.1016/0368-2048(91)85005-E).
- Wang, H.; Bian, H.; Jin, Z.; Zhang, H.; Liang, L.; Wen, J.; Wang, Q.; Ding, L.; Liu, S. F. Cesium Lead Mixed-Halide Perovskites for Low-Energy Loss Solar Cells with Efficiency beyond 17%. *Chem. Mater.* 2019, 31 (16), 6231–6238. <https://doi.org/10.1021/acs.chemmater.9b02248>.
- Wang, H.; Lee, H.-W.; Deng, Y.; Lu, Z.; Hsu, P.-C.; Liu, Y.; Lin, D.; Cui, Y. Bifunctional Non-Noble Metal Oxide Nanoparticle Electrocatalysts through Lithium-Induced Conversion for Overall Water Splitting. *Nat. Commun.* 2015, 6 (1), 7261. <https://doi.org/10.1038/ncomms8261>.
- Wang, J.; Leng, J.; Liu, J.; He, S.; Wang, Y.; Wu, K.; Jin, S. Engineered Directional Charge Flow in Mixed Two-Dimensional Perovskites Enabled by Facile Cation-

- Exchange. *J. Phys. Chem. C* 2017, 121 (39), 21281–21289. <https://doi.org/10.1021/acs.jpcc.7b08535>.
- Wang, K.; Wu, C.; Yang, D.; Jiang, Y.; Priya, S. Quasi-Two-Dimensional Halide Perovskite Single Crystal Photodetector. *ACS Nano* 2018, 12 (5), 4919–4929. <https://doi.org/10.1021/acs.nano.8b01999>.
- Wang, M.; Dang, Z.; Prato, M.; Shinde, D. V.; De Trizio, L.; Manna, L. Ni–Co–S–Se Alloy Nanocrystals: Influence of the Composition on Their in Situ Transformation and Electrocatalytic Activity for the Oxygen Evolution Reaction. *ACS Appl. Nano Mater.* 2018, 1 (10), 5753–5762. <https://doi.org/10.1021/acsanm.8b01418>.
- Wang, N.; Cheng, L.; Ge, R.; Zhang, S.; Miao, Y.; Zou, W.; Yi, C.; Sun, Y.; Cao, Y.; Yang, R.; et al. Perovskite Light-Emitting Diodes Based on Solution- Processed Self-Organized Multiple Quantum Wells. *Nat. Photonics* 2016, 10 (11), 699–704. <https://doi.org/10.1038/nphoton.2016.185>.
- Wang, Z.; Lin, Q.; Chmiel, F. P.; Sakai, N.; Herz, L. M.; Snaith, H. J. Efficient Ambient-Air-Stable Solar Cells with 2D-3D Heterostructured Butylammonium-Caesium-Formamidinium Lead Halide Perovskites. *Nat. Energy* 2017, 2 (9), 1–10. <https://doi.org/10.1038/nenergy.2017.135>.
- Wei, J.; Li, H.; Zhao, Y.; Zhou, W.; Fu, R.; Leprince-Wang, Y.; Yu, D.; Zhao, Q. Suppressed Hysteresis and Improved Stability in Perovskite Solar Cells with Conductive Organic Network. *Nano Energy* 2016, 26, 139–147. <https://doi.org/10.1016/j.nanoen.2016.05.023>.
- Woodhouse, M.; Smith, B.; Ramdas, A.; Robert Margolis. Crystalline Silicon Photovoltaic Module Manufacturing Costs and Sustainable Pricing: 1H 2018 Benchmark and Cost Reduction Roadmap; 2019.
- Wygant, B. R.; Kawashima, K.; Mullins, C. B. Catalyst or Precatalyst? The Effect of Oxidation on Transition Metal Carbide, Pnictide, and Chalcogenide Oxygen Evolution Catalysts. *ACS Energy Lett.* 2018, 3 (12), 2956–2966. <https://doi.org/10.1021/acsenergylett.8b01774>.
- Wygant, B. R.; Ye, A. Z.; Dolocan, A.; Vu, Q.; Abbot, D. M.; Mullins, C. B. Probing the Degradation Chemistry and Enhanced Stability of 2D Organolead Halide Perovskites. *J. Am. Chem. Soc.* 2019, 141, 18170–18181. <https://doi.org/10.1021/jacs.9b08895>.
- Xing, J.; Yan, F.; Zhao, Y.; Chen, S.; Yu, H.; Zhang, Q.; Zeng, R.; Demir, H. V.; Sun, X.; Huan, A.; et al. High-Efficiency Light-Emitting Diodes of Organometal Halide Perovskite Amorphous Nanoparticles. *ACS Nano* 2016, 10 (7), 6623–6630. <https://doi.org/10.1021/acs.nano.6b01540>.
- Xu, K.; Ding, H.; Lv, H.; Tao, S.; Chen, P.; Wu, X.; Chu, W.; Wu, C.; Xie, Y. Understanding Structure-Dependent Catalytic Performance of Nickel Selenides

- for Electrochemical Water Oxidation. *ACS Catal.* 2017, 7 (1), 310–315. <https://doi.org/10.1021/acscatal.6b02884>.
- Xu, X.; Song, F.; Hu, X. A Nickel Iron Diselenide-Derived Efficient Oxygen-Evolution Catalyst. *Nat. Commun.* 2016, 7 (1), 12324. <https://doi.org/10.1038/ncomms12324>.
- Yan, L.; Niu, H. J.; Duong, G. V.; Suchomel, M. R.; Bacsá, J.; Chalker, P. R.; Hadermann, J.; van Tendeloo, G.; Rosseinsky, M. J. Cation Ordering within the Perovskite Block of a Six-Layer Ruddlesden-Popper Oxide from Layer-by-Layer Growth – Artificial Interfaces in Complex Unit Cells. *Chem. Sci.* 2011, 2 (2), 261–272. <https://doi.org/10.1039/C0SC00482K>.
- Yang, B.; Dyck, O.; Ming, W.; Du, M.; Das, S.; Rouleau, C. M.; Duscher, G.; Geohegan, D. B.; Xiao, K. Observation of Nanoscale Morphological and Structural Degradation in Perovskite Solar Cells by in Situ TEM. *ACS Appl. Mater. Interfaces* 2016, 8 (47), 32333–32340. <https://doi.org/10.1021/acsami.6b11341>.
- Yang, D.; Yang, R.; Priya, S.; Liu, S. (Frank). Recent Advances in Flexible Perovskite Solar Cells: Fabrication and Applications. *Angew. Chemie - Int. Ed.* 2019, 58 (14), 4466–4483. <https://doi.org/10.1002/anie.201809781>.
- Yao, T.; An, X.; Han, H.; Chen, J. Q.; Li, C. Photoelectrocatalytic Materials for Solar Water Splitting. *Adv. Energy Mater.* 2018, 8 (21), 1800210. <https://doi.org/10.1002/aenm.201800210>.
- You, B.; Sun, Y. Innovative Strategies for Electrocatalytic Water Splitting. *Acc. Chem. Res.* 2018, 51 (7), 1571–1580. <https://doi.org/10.1021/acs.accounts.8b00002>.
- Yu, J.; Cheng, G.; Luo, W. Ternary Nickel-Iron Sulfide Microflowers as a Robust Electrocatalyst for Bifunctional Water Splitting. *J. Mater. Chem. A* 2017, 5 (30), 15838–15844. <https://doi.org/10.1039/c7ta04438k>.
- Yuan, M.; Quan, L. N.; Comin, R.; Walters, G.; Sabatini, R.; Voznyy, O.; Hoogland, S.; Zhao, Y.; Beauregard, E. M.; Kanjanaboos, P.; Lu, Z.; Kim, D. H.; Sargent, E. H. Perovskite Energy Funnels for Efficient Light-Emitting Diodes. *Nat. Nanotechnol.* 2016, 11 (10), 872–877. <https://doi.org/10.1038/nnano.2016.110>.
- Yue, D.; You, F.; Darling, S. B. Domestic and Overseas Manufacturing Scenarios of Silicon-Based Photovoltaics: Life Cycle Energy and Environmental Comparative Analysis. *Sol. Energy* 2014, 105, 669–678. <https://doi.org/10.1016/j.solener.2014.04.008>.
- Zeng, L.; Sun, K.; Chen, Y.; Liu, Z.; Chen, Y.; Pan, Y.; Zhao, R.; Liu, Y.; Liu, C. Neutral-PH Overall Water Splitting Catalyzed Efficiently by a Hollow and Porous Structured Ternary Nickel Sulfoselenide Electrocatalyst. *J. Mater. Chem. A* 2019, 7 (28), 16793–16802. <https://doi.org/10.1039/c9ta05601g>.

- Zeng, P.; Ran, R.; Chen, Z.; Zhou, W.; Gu, H.; Shao, Z.; Liu, S. Efficient Stabilization of Cubic Perovskite $\text{SrCoO}_{3-\delta}$ by B-Site Low Concentration Scandium Doping Combined with Sol-Gel Synthesis. *J. Alloys Compd.* 2008, 455 (1–2), 465–470. <https://doi.org/10.1016/j.jallcom.2007.01.144>.
- Zhang, J. Y.; Lv, L.; Tian, Y.; Li, Z.; Ao, X.; Lan, Y.; Ji, J.; Wang, C. Rational Design of Cobalt-Iron Selenides for Highly Efficient Electrochemical Water Oxidation. *ACS Appl. Mater. Interfaces* 2017, 9 (39), 33833–33840. <https://doi.org/10.1021/acsami.7b08917>.
- Zhang, J.; Li, Y.; Zhu, T.; Wang, Y.; Cui, J.; Wu, J.; Xu, H.; Shu, X.; Qin, Y.; Zheng, H.; et al. 3D Coral-Like Ni_3S_2 on Ni Foam as a Bifunctional Electrocatalyst for Overall Water Splitting. *ACS Appl. Mater. Interfaces* 2018, 10 (37), 31330–31339. <https://doi.org/10.1021/acsami.8b09361>.
- Zhang, M.; de Respinis, M.; Frei, H. Time-Resolved Observations of Water Oxidation Intermediates on a Cobalt Oxide Nanoparticle Catalyst. *Nat. Chem.* 2014, 6 (4), 362–367. <https://doi.org/10.1038/nchem.1874>.
- Zhang, T.; Meng, X.; Bai, Y.; Xiao, S.; Hu, C.; Yang, Y.; Chen, H.; Yang, S. Profiling the Organic Cation-Dependent Degradation of Organolead Halide Perovskite Solar Cells. *J. Mater. Chem. A* 2017, 5 (3), 1103–1111. <https://doi.org/10.1039/C6TA09687E>.
- Zhang, W.; Xiong, J.; Li, J.; Daoud, W. A. Guanidinium Induced Phase Separated Perovskite Layer for Efficient and Highly Stable Solar Cells. *J. Mater. Chem. A* 2019, 7 (16), 9486–9496. <https://doi.org/10.1039/c9ta01893j>.
- Zhao, L.; Kerner, R. A.; Xiao, Z.; Lin, Y. L.; Lee, K. M.; Schwartz, J.; Rand, B. P. Redox Chemistry Dominates the Degradation and Decomposition of Metal Halide Perovskite Optoelectronic Devices. *ACS Energy Lett.* 2016, 1 (3), 595–602. <https://doi.org/10.1021/acsenergylett.6b00320>.
- Zhou, M.; Weng, Q.; Zhang, X.; Wang, X.; Xue, Y.; Zeng, X.; Bando, Y.; Golberg, D. In Situ Electrochemical Formation of Core–Shell Nickel–Iron Disulfide and Oxyhydroxide Heterostructured Catalysts for a Stable Oxygen Evolution Reaction and the Associated Mechanisms. *J. Mater. Chem. A* 2017, 5 (9), 4335–4342. <https://doi.org/10.1039/C6TA09366C>.
- Zhou, N.; Shen, Y.; Li, L.; Tan, S.; Liu, N.; Zheng, G.; Chen, Q.; Zhou, H. Exploration of Crystallization Kinetics in Quasi Two-Dimensional Perovskite and High Performance Solar Cells. *J. Am. Chem. Soc.* 2018, 140 (1), 459–465. <https://doi.org/10.1021/jacs.7b11157>.
- Zhou, W.; Wu, X. J.; Cao, X.; Huang, X.; Tan, C.; Tian, J.; Liu, H.; Wang, J.; Zhang, H. Ni_3S_2 Nanorods/Ni Foam Composite Electrode with Low Overpotential for Electrocatalytic Oxygen Evolution. *Energy Environ. Sci.* 2013, 6 (10), 2921–2924. <https://doi.org/10.1039/c3ee41572d>.

- Zhu, W.; Yue, X.; Zhang, W.; Yu, S.; Zhang, Y.; Wang, J.; Wang, J. Nickel Sulfide Microsphere Film on Ni Foam as an Efficient Bifunctional Electrocatalyst for Overall Water Splitting. *Chem. Commun.* 2016, 52 (7), 1486–1489. <https://doi.org/10.1039/c5cc08064a>.
- Zhu, Y.; Chen, H. C.; Hsu, C. S.; Lin, T. S.; Chang, C. J.; Chang, S. C.; Tsai, L. D.; Chen, H. M. Operando Unraveling of the Structural and Chemical Stability of P-Substituted CoSe₂ Electrocatalysts toward Hydrogen and Oxygen Evolution Reactions in Alkaline Electrolyte. *ACS Energy Lett.* 2019, 4 (4), 987–994. <https://doi.org/10.1021/acsenergylett.9b00382>.
- Zohar, A.; Kedem, N.; Levine, I.; Zohar, D.; Vilan, A.; Ehre, D.; Hodes, G.; Cahen, D. Impedance Spectroscopic Indication for Solid State Electrochemical Reaction in (CH₃NH₃)PbI₃ Films. *J. Phys. Chem. Lett.* 2016, 7 (1), 191–197. <https://doi.org/10.1021/acs.jpclett.5b02618>.
- Zou, X.; Zhang, Y. Noble Metal-Free Hydrogen Evolution Catalysts for Water Splitting. *Chem. Soc. Rev.* 2015, 44 (15), 5148–5180. <https://doi.org/10.1039/c4cs00448e>.